Bijel
a novel composite material from colloids on liquid-liquid interfaces

Eva M. Herzig

Thesis submitted for the degree of Doctor of Philosophy

School of Physics
University of Edinburgh

2008

Abstract

Composite materials generally consist of different components which individually exhibit an entirely different material behaviour than within the composite. Here, two immiscible liquids are stabilised with solid particles forming liquid-liquid emulsions. Solid stabilised emulsions, also known as Pickering emulsions, have been thoroughly studied and find application in many industrial sectors. In these emulsions one liquid is generally suspended within the other in the form of droplets. Inspired by computer simulations, it should be possible to create a bicontinuous network of two immiscible liquids also stabilised with jammed particles. This will result in an attractive new material which could find possible industrial applications, for example as microreactors. This potential **bi**continuous, **i**nterfacially **j**ammed **e**mulsion ge**l** was dubbed bijel.

Drawing together knowledge from different disciplines this thesis presents an experimental route to bijel formation. Accessing a certain type of phase separation called spinodal decomposition can be used to create a convoluted arrangement of bicontinuous interfaces. Liquid-liquid interfaces can be stabilised by exploiting the fact that solid particles can be irreversibly trapped at liquid-liquid interfaces. Once trapped, the presence of the particles demands a minimum interfacial area between the two liquids. If the particles are jammed against each other this will result in the stabilisation of the liquid-liquid interfaces.

To stabilise convoluted, bicontinuous interfaces in this way one type of particles must be able to concurrently stabilise two types of curvatures. Over the last three years it has been shown by several different research groups that this is possible.

This thesis examines different types of temperature and pressure quenches on binary liquid systems to reach spinodal decomposition in the presence of particles. At the same time the ability of the particles to collect on the interfaces created during such phase separations is tested. It is found that temperature quenches through the critical point can lead to reproducible bijel formation resulting in the first experimental presentation of bijels. Using confocal microscopy the bijel formation process is studied in detail and properties of this new material are examined. To obtain insight into the behaviour of slowly ageing soft materials x-ray photon correlation spectroscopy is separately carried out on droplet emulsions.

Declaration

I declare that this thesis has been composed entirely by myself and has not been submitted in any previous application for a degree. I have carried out the work presented, except where otherwise stated.

Eva M. Herzig
February 2008

Acknowledgements

I would like to thank my first supervisor Paul Clegg for his dedicated support and never-faltering enthusiasm during this project and my second supervisor Wilson Poon for valuable input throughout.

Stefan Egelhaaf has been a terrific mentor during my undergraduate degree and never doubted my ability to progress.

Without Danielle's support during the sleepless nights of the x-ray experiments the results would not have been as compelling. And I am glad to have worked with Kathryn White and Job Thijssen and hope they will bring bijels closer to our homes.

It was very helpful that I was able to discuss my results with Peter Pusey and Mark Sutton.

Without the excellent expertise of other staff here at the University of Edinburgh life would have been a lot more difficult. I would like to thank Andrew Schofield, Andrew Downie, George Gillies, Paul Harris and Eric Davidson.

I had the pleasure of collaborating with many people from different institutions and am particularly grateful to Hugh Vass, Aymeric Robert, Luca Cipelletti, Tommy Horozov and Bernie Binks.

My friends here in the Physics department, at the Counting House and elsewhere have been invaluable and I am very, very grateful for all their support and the fun times with them.

Most importantly, of course, my deepest thanks go to: Mum, Dad, Anna and Alex.

Contents

List of Figures

List of Tables

Chapter 1

Introduction

Bijel is short for **b**icontinuous **i**nterfacially **j**ammed **e**mulsion ge**l**. A bijel is a novel material with intriguing properties that has been hypothesised using computer simulations. In this thesis I present the first bijel formation in the laboratory and study the properties of bijels and that of related systems.

1.1 Composites in everyday life

It is of scientific and industrial interest to study bijels because they are part of a wider group called composite materials. Composites combine two types of materials, usually a flexible binder added to a stiff and strong reinforcing component which gives the composite material superior properties. Most importantly the strength and stiffness of composite materials can be carefully tuned to satisfy a vast range of requirements. This concept also occurs in nature. Wood for example consists of stiff cellulose held together by lignin. To add two different materials to combine their properties has been exploited long ago when building straw and mud houses. One of the most common composite materials these days is fibre glass [25]. Another large and much softer subsection of composite materials are solid-stabilised emulsions.

Various types of emulsions surround us in everyday life: milk, paint and various cosmetic creams are just a few examples. All of these products have small insoluble globules suspended in a surrounding liquid. In milk these are little fat globules in a water based liquid, in paint these are small droplets of adhesive coated by coloured particles dispersed in a thinning medium, while in creams it is usually little oil droplets in an aqueous solution. If oil and vinegar are added together when dressing a salad, the oil first forms several droplets floating on the vinegar but eventually all the oil merges together. To achieve a homogenously mixed salad dressing the merging of the oil droplets must be avoided. This can be achieved for example by adding mustard which contains a surfactant and acts as a stabiliser. The emulsions I examine in this thesis are stabilised with solid particles i.e. similar to the paint. To obtain a stable solid stabilised emulsion the particles need to be strongly trapped at the liquid-liquid interfaces. Solid particles have the property that if they are forced together they do not change their shape. Instead the stabilising particles jam together on the shrinking liquid-liquid interface of the emulsion droplets and prevent the system reaching equilibrium. At the same time the interface gains mechanical strength due to the jammed particles. Such arrested out-of-equilibrium samples are intriguing to study because they do not just depend on the current environmental parameters but are strongly history dependent. A substantial amount of work has been carried out on such solid stabilised emulsions studying in detail the influence of parameters like particle surface, volume fraction of particles, liquid-liquid volume ratios, types of liquids, mixing methods and more (see section 2.1). Additionally, the mechanical properties of such particle-laden interfaces have been examined in detail (see section 2.2) revealing solid-like properties of these interfaces.

1.2 A special emulsion: the bijel

Conventional emulsions generally occur in droplet form. In contrast, the postulated bijel has a significantly different morphology. Instead of individual oil

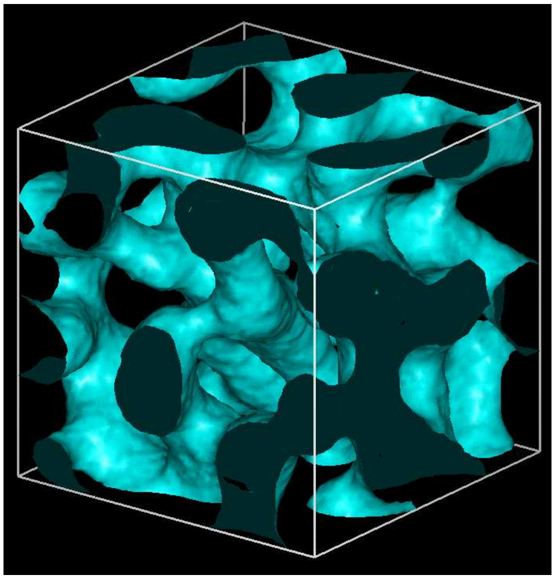

Figure 1.1: Example of a bicontinuous structure. From computer simulations [1].

droplets being dispersed in the majority phase, the bijel has a continuous channel system for each of the two liquids. Contrary to conventional droplet emulsions both liquid phases are now accessible and the liquids are no longer distinguishable as 'internal' and 'external' phases. Such a morphology is called bicontinuous and an example is shown in figure 1.1. Surfactant sponge phases, for instance, also have such a morphology [26]. However, in a bijel the interfaces between the two liquids are packed with small, spherical particles forming a static scaffold throughout the bijel. A surfactant sponge phase has in contrast very subtle walls and rearranges continuously over time.

The particles in the static scaffold are closely packed and lend the material stability. This is also the case for individual particle-covered droplets in conventional emulsions but in a bijel the sample spanning geometry creates a large scale integrity that allows load bearing properties. A collection of droplets, in contrast, will rearrange when a local load is applied. Similarly it is expected that creaming or sedimentation, the process which in a conventional emulsion determines the shelf life of the product, is reduced by the sample spanning geometry of the bijel.

The static particle scaffold within a bijel is also expected to allow the two participating liquids to remain mixed on the meso scale with the liquids in flow as well as at rest, whereas current techniques require a high pressure flow at all times to achieve such mixing. Although the particle-laden interfaces will be closely packed with particles there will still be interstices between particles with liquid-liquid interfaces. The size of these interstices can be determined by the particle size and shape and the two liquids can exchange molecules through this contact area. This is why the bijel is highly appealing for the use as a microreactor or possibly in fuel cells or in many other potential applications which is part of the motivation for investigating the formation process, material properties and the tuning possibilities.

The challenge is to create and observe such a material experimentally. The channels within the bijel will have a diameter of tens of microns while the stabilising particles will be submicron sized. It is impossible to produce such a system by manually arranging the building blocks. Instead a naturally evolving system is used to self-assemble a bijel.

1.3 Phase separation as means for self-assembly

If a system is in equilibrium not much rearrangement will occur because the system is very stable in this state. By changing its environment, however, for example by applying pressure, increasing the temperature or adding a new component, it is possible to bring the system out-of-equilibrium. Suddenly, the system is no longer stable and it will try to move towards its equilibrium again. Fascinatingly, this is very often attempted by a very definite process. Such controlled rearrangements into often highly ordered configurations occur widely in nature but are also exploited in industrial processes. For a binary-liquid mixture which prefers to be mixed at one temperature but not at another, demixing via a process known as 'spinodal decomposition' to reach equilibrium occurs in a very particular manner and can repeatedly and reproducibly create bicontinuous interfaces and will do so automatically as a response to, for example, changes in the temperature of the system

The experiments carried out in my thesis are based on this simple principle: particles present during liquid-liquid demixing trap and then jam on a convoluted interface, prevent further coarsening and therefore arrest a bicontinuous structure. However, the successful experimental realisation requires a very accurately tuned system which is experimentally very challenging. Two binary liquids undergo spinodal decomposition in a fraction of a second and only for a small range of liquid compositions in a selected temperature or pressure range. These regions must be experimentally accessible and the separation process also depends on the heating rate and any temperature gradients within the sample. If the stabilising particles have appropriate wetting conditions they will be very strongly trapped at liquid-liquid interfaces and successfully stabilise a bijel structure. However, only minor deviations from the ideal conditions can lead to preferred curvatures of the interfaces, rendering a stable bicontinuous geometry impossible. Therefore a basic system consisting of silica spheres and a low molecular weight binary liquid system is chosen here to systematically establish the essential experimental conditions for successful bijel formation. In future the use of components with product specific properties can be envisioned to optimise the bijel for potential applications.

1.4 Thesis layout

In the next chapter (chapter 2) I will introduce the relevant theory including the work of others carried out in this field of research, followed by the experimental methods and sample preparations used throughout the thesis in chapter 3. In the main part of the thesis I will show in chapter 4 the successful route to bijel formation via a critical temperature quench in the 2,6-lutidine/water system.

Chapter 5 and 6 show other attempts at reaching spinodal decomposition via deep, off-critical temperature and pressure quenches respectively. The limiting factors and the understanding gained during these experiments are discussed. In the last experimental chapter (chapter 7) I have examined the slow dynamics of a related droplet emulsion system using x-ray photon correlation spectroscopy (XPCS). In chapter 8 I will summarise the achieved experimental progress and make suggestions for further work.

Chapter 2

Theoretical background

There is currently great interest in soft composites that are arrested out-of-equilibrium. Here I study such a system that is based on emulsions and is fabricated via a novel route. In this chapter I describe the theory behind the emulsions, the properties of the interfaces and the kinetic route employed in fabrication.

2.1 Emulsions

If two liquids in contact do not mix an interface will exist between them with an associated energy cost. The system will assume a configuration in which the interfacial area is minimised to keep the associated energy cost as low as possible. Typically this would imply a flat interface with the lighter liquid sitting on top of the heavier liquid. However, in an emulsion droplets of the minority phase [1] are dispersed in the majority phase requiring a much larger amount of interface compared to the equilibrium configuration. Firstly, work needs to be put into the system to create these interfaces. Once interfaces are formed they need to be stabilised to obtain long-lived emulsions. This can

---

[1] The liquid with the smaller volume will usually be the dispersed phase and is called the minority phase while the phase with the larger volume is called the majority phase.

either be done by reducing the expensive cost of maintaining the liquid-liquid interfaces or by mechanically hindering the system from reverting to equilibrium, i.e. by preventing the coalescence of the emulsions droplets. Once stable emulsion droplets are obtained it is often desirable to have a homogeneous emulsion, i.e. sedimentation or creaming effects should be avoided. This can be achieved by reducing the size of the suspended droplets because then they move slower under the influence of gravity and the emulsion is homogeneous for longer. A common example is the homogenisation of cow's milk during which the fat globules are made smaller so no creamy layer forms on top of the milk. It is also possible to increase the viscosity of the majority phase to achieve an equivalent outcome.

A common way to lower the cost of the liquid-liquid interfaces is through the use of surfactants. Surfactants (surface active agents) are conventionally amphiphilic molecules with a hydrophilic head and a hydrophobic tail. These molecules prefer being situated on interfaces instead of being solely in one of the single phases because of their amphiphilic nature. If located at the interface their hydrophilic heads can sit in the water while their hydrophobic tails will stick into the oil phase therefore satisfying the preference of both parts of their bodies. Furthermore, by spreading on the interface the surfactant molecules exert a pressure throughout the interface which opposes the contracting tension of the interface [27] and therefore lowers the interfacial tension. Because the associated interfacial cost is dramatically lowered if the interfacial tension is near-zero, surfactant covered oil droplets can exist in water over a long time even though the multiple droplet surfaces can imply a very large liquid-liquid interface. Surfactant molecules can quickly adsorb and desorb from interfaces [28] so that droplets can rearrange and reform. When surfactants are found for example in water without oil they form micelles (all tails oriented into the centre while the heads form a water-liking surface). This ability makes them good for solubilisation [28] which is exploited in the detergent industry. It is possible to stabilise a wide oil/water ratio resulting in oil-in-water or water-in-oil emulsions. It is also possible to

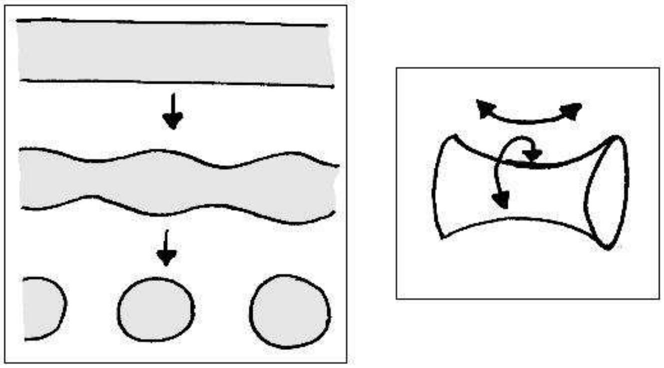

Figure 2.1: A liquid cylinder will undergo the Plateau-Rayleigh instability if the ratio between the length of the neck and its diameter exceed a certain value. It is then energetically favourable to form individual droplets. Before breaking these necks have two types of curvature as shown by the arrows on the right.

obtain bicontinuous structures in which both the oil and water domains extend over macroscopic distances in a convoluted manner [29]. It has been shown by conductivity experiments that the surfactants separate two continuous domains throughout the sample [30].

This bicontinuous, convoluted morphology is only achievable if fluid necks can be created. Such necks no longer have a constant mean curvature like spherical droplets. The mean curvature is defined as $H = \frac{1}{2}(\frac{1}{R_1} + \frac{1}{R_2})$, where R_1 and R_2 are the radii of the two circles described by the arrows on the right hand side of figure 2.1. If the surface area is minimised then $H = 0$. Another way of describing curvature is by using the Gaussian curvature $K = \frac{1}{R_1 R_2}$ which is zero if the surface is flat. Liquids cannot sustain surfaces that have non-zero mean curvature and therefore liquid necks will undergo the Plateau-Rayleigh instability (see figure 2.1) if the cylindrical area increases too much compared to the diameter which means that the neck breaks and retracts or droplets are formed instead, reducing the interfacial energy cost. The driving force behind this instability is the interfacial tension. Because the interfacial tension is so low when surfactants occupy the liquid-liquid interface such necks can be thermodynamically stable. However, a bicontinuous surfactant-stabilised structure will not be static over time but will continuously rearrange.

When emulsifying oil in water, for example, instead of decreasing the interfacial tension and therefore removing the drive for the system to coalesce, it is also possible to avoid the coarsening of the system by introducing a barrier to coalescence. A shell of solid particles, for instance, can act in this way. Solid particles can be trapped on interfaces because they reduce the area of the expensive liquid-liquid interface. Provided this trapping is strong enough these particles will not be expelled from the interface even if many of the particles are jammed closely together. If a droplet is fully covered with particles then this shell will prevent two such droplets from coalescing and renders such an emulsion stable for up to years [2]. These solid stabilised emulsions are also known as Pickering emulsions [31] although Ramsden actually first observed this phenomenon [32]. If the particles come into very close contact they can interact via Van-der-Waals interactions. If they are charged, they can stabilise droplets without being in physical contact with each other [33].

Leunissen et al [33] claim that PMMA particles can stabilise interfaces of liquids with a large dielectric constant difference solely by electrostatics without being interfacially trapped using the concept of image charges. However, from the microscopy images they show it is not evident that the particles are truly separated from the interface. Their system has an interfacial tension of about 10 mN/m and trapping at very large wetting angles shows significant changes in the trapping energy for minor changes in the wetting angle. A wetting angle of 177° would lead to a trapping energy of $G=\pi r^2\gamma(1-|\cos(\theta_w)|)^2=14\ k_BT$ while already for $\theta_w=176°$ results in a trapping of 46 k_BT for the system they are using ($r = 1\ \mu m$, $\gamma = 10$ mN/m). $\theta_w=180°$ would indicate no trapping. Furthermore, related computer simulations [34] show that for the particles to approach each other close enough near the interface counter ions are needed along the other side of this interface to cancel the electrostatic interactions. Although the experimental studies show the existence of such counter ions the existence of Wigner crystals inside the stabilised droplets show that the electrostatic interactions are not cancelled at the interface suggesting that possibly some interfacial trapping still occurs. Further experiments are necessary to clarify this ambiguity.

The stabilisation mechanism used in this thesis, however, is interfacial trapping. Solid particle stabilised droplet emulsions have been widely studied and a good review is given by Aveyard et al [2] and Zeng et al [35] and a detailed account on topics related to this field is given in a recent book published by Binks and Horozov [36].

The principles involved in particle stabilised emulsions can be extended to any other globular constituents like proteins, viruses or possibly bacteria, and is not restricted to solid materials like clay, polystyrene, silica or metals opening up a wide range of possible self-assembled biomaterials. Because I intend to study a novel system which intricately depends on many parameters I choose spherical, monodisperse Stöber silica, i.e. solid spheres to keep the system as simple as possible.

2.2 Solid particles on liquid-liquid interfaces

2.2.1 Trapping mechanisms

Solid particles can be energetically trapped at liquid-liquid interfaces because they replace some of the expensive liquid-liquid interface by their own presence. If the surface of the particles is chosen in such a way that it exhibits partial wettability with both liquids this will reduce the energy cost involved. The wetting properties of the particle are often quantified by the wetting angle, i.e. the three-phase contact angle as shown in figure 2.2. The contact angle is determined by the interfacial tension between particle and oil, γ_{po}, between particle and water, γ_{pw}, and of course by the liquid-liquid interfacial tension γ_{ow} using the Young's

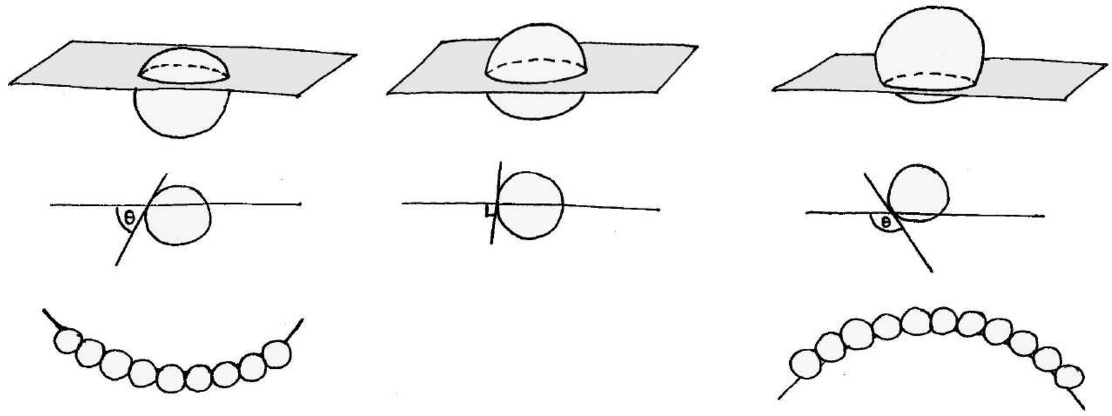

Figure 2.2: The wetting angle of a particle determines how much of the interfacial area is replaced by the particle. Three different cases are distinguished (from left to right): $\theta_{ow} < 90°$, $\theta_{ow} = 90°$ (neutral wetting) and $\theta_{ow} > 90°$. The wetting behaviour of particles also leads to a preferred curvature of particle stabilised interfaces [2].

equation [37]:

$$cos(\theta) = \frac{\gamma_{po} - \gamma_{pw}}{\gamma_{ow}}. \tag{2.1}$$

Provided the particles are small enough so that gravity effects can be neglected the reduction of energy due to the adsorption of a particle with radius r on a flat interface can be expressed as follows [2]:

$$\Delta_{int}G = \pi r^2 \gamma_{ow}(1 \pm cos(\theta_{ow})^2. \tag{2.2}$$

γ_{ow} is the interfacial tension between the two liquids and the contact angle θ_{ow} is related to the wettability of the particle (see figure 2.2) and determines the replaced liquid-liquid interfacial area. Assuming a particle size of 0.5 μm diameter and a typical interfacial tension of 1mN/m results in a trapping of 50 000 k_BT for neutrally wetting (θ_{ow}=90°) particles. This energy reduction is huge and implies that the particles, once at the interface, will be irreversibly trapped. However, the interfacial tension itself is not lowered as in the case of surfactants [38]. On the contrary, the interfacial tension is responsible for the strength of the particle trapping at the interface. Figure 2.2 also shows that for particles with non-neutral wetting, i.e. $\theta_{ow} < 90°$ or $\theta_{ow} > 90°$, a preferred curvature in the particle covered interfaces is induced [28]. If the wetting angle is lower or higher than 90°, one of the two liquids is preferred. Therefore the particle will expose a larger surface area to the preferred liquid as seen in the bottom row of figure 2.2. This generally dictates whether oil-in-water or water-in-oil emulsions are formed. However, this property is not absolute and the system can be forced to curve into the other direction under certain conditions [39, 40].

During the standard creation of Pickering emulsions two liquids with a very high interfacial tension are agitated mechanically. The interfaces will have a high interfacial tension throughout the emulsification procedure and particles once having approached an interface will be trapped upon it. Even if there is a large free energy reduction when a particle goes onto the interface, there are other phenomena which can hinder the attachment. For example, the line tension created upon reaching the interface can lead to an energy barrier which has to be overcome before irreversible trapping can occur. Also, the kinetics of forming a three-phase contact line and film thinning can lead to delays in the trapping. This has been carefully studied with regards to froth flotation [41]. Additionally, the speed of the moving interfaces during mixing can also have a significant effect on successful trapping, in an analogous way to West et al [42].

In parts of this project I use phase separation to emulsify two partially miscible liquids. In contrast to emulsification via mechanical agitation, creation of interfaces via spinodal decomposition creates interfaces whose interfacial tension is initially very low and increases over time. For polystyrene latex spheres in 2,6-lutidine/water system the spheres were observed to partition to the interface only below a certain wetting temperature T_w which is a few mK higher than the critical temperature T_c [43]. For nucleation processes it has already been observed in 1908 [44] that particles can accumulate on the interfaces during phase separation forming stable droplets. This has been reconfirmed by a more systematic study exploring the behaviour of silica stabilised alcohol/oil systems with a miscibility gap accessible by temperature for changes in temperature [45]. For phase boundaries in liquid crystal systems it has been found that particle trapping also depends on the speed with which the interfaces move [42] which could happen analogously for liquid-liquid interfaces during phase separation although the underlying mechanisms are not equivalent. It therefore needs to be explored how to trap the particles most efficiently on liquid-liquid interfaces created during spinodal decomposition which is necessary to create bijels via phase separation.

2.2.2 Mechanical material properties

A good way to characterise the mechanical properties of a material is to consider the relationship between the stress and strain. The stress is the load per unit area or the force distribution within the material while the strain is the associated extension of the material per unit length [46]. For a viscous fluid, it is the rate of change of strain that is important and the relationship will be

$$\sigma = \eta \frac{d\epsilon}{dt}, \tag{2.3}$$

where σ is the stress, ϵ is the strain and η the viscosity of the fluid [47]. In solids one distinguishes between the elastic regime and the plastic regime. In the elastic regime the strain increases linearly for an increasing stress with the resulting deformation being completely reversible [46]. This relationship can be described by Hooke's Law:

$$\sigma = E\epsilon. \tag{2.4}$$

Here E is the Young's modulus. The same relationship can also be written ϵ=Jσ where J is the compliance (J=$\frac{1}{E}$) [47]. Hooke's law will only hold for small stresses before it is violated. A material will only be elastic below a certain stress level. Once this is exceeded the material will behave plastically, i.e. the deformation will no longer be reversible but permanent. The limiting stress at which the response changes from elastic to plastic behaviour is called the yield stress. For real materials the liquid and solid characters are often not clearly separated and viscous and elastic properties can occur in combination. In such viscoelastic materials the relationship between stress and strain also depends on the time scale of the perturbation. Typical properties of a viscoelastic material are for example that for a constant stress the strain increases with time. This is also known as creep. While for constant strain the stress decreases with time which is called relaxation. Under cyclic loading hysteresis will occur indicating that mechanical energy is dissipated. And like for most other materials, too, the effective stiffness will depend on the rate of application of the load. Silly putty, a funny toy, for example bounces if it hits the floor sharply but flows slowly if left at rest.

2.2.3 Properties of flat, particle laden interfaces

In this thesis I consider emulsions which are stabilised by solid particles which are trapped in a deep energy well at the interface between two liquids. Such energetically trapped particles on interfaces form a composite material which shows significantly different behaviour to its individual components: clear ("empty") liquid-liquid interfaces and individual particles. In the following paragraphs I look at the properties of particle-laden interfaces.

A particle-free liquid-liquid interface will deform easily under stress and always assume the lowest interfacial area possible. If a flat liquid-liquid interface is compressed it will scarcely resist a decrease in its surface area. When such interfaces occur in the form of droplets they will always assume a perfectly spherical shape to reduce the interfacial area. A pure liquid-liquid interface does not have the means to support a non-spherical shape. On the other hand a $2\%_v$ dispersion of hard spheres flows like a liquid. However, the situation changes when these particles are trapped on liquid-liquid interfaces.

In this section I will consider planar examples like a flat water-air interface containing uniformly spread particles, also known as a particle raft [48]. Provided the particles wet both, the air and the water, then the particles are reducing some of the expensive air-liquid interface as discussed before. The particles are therefore held at the interface and a displacement perpendicular to the interface will be opposed by the interfacial energy cost. By contrast, movement within the plane of the interface is not restricted as long as there is unoccupied area. However, on a densely particle-laden interface horizontal movement is physically hindered due to the presence of other particles. This physical barrier can be very strong since the particles can be considered as undeformable. If the particles are pushed close enough together it will eventually be energetically favourable for the particle raft to deform as a whole, for example, by forming wrinkles in the particle raft (valleys and hills) but with the particles still trapped at the interfaces. Forming these valleys and hills comes at the cost of the creation of some extra liquid-liquid interface. If the force pushing the particles together is removed the stored energy in the additional interface returns the particle raft back into a flat interface. This experiment has been carried out by Vella and co-workers [48, 49] using monolayers of particles in a Langmuir trough. These monolayers buckle under sufficient static compressive loading and relax once the loading is removed. The support of such an anisotropic stress is evidence for a non-zero shear modulus indicating that the particle raft has solid character. The relaxation shows that these particle rafts also have elastic character which is driven by the changes in interfacial area.

Vella et al further analyse the situation and arrive at an expression for the non-zero shear modulus G given by:

$$\begin{aligned} G &= \frac{1-\nu}{1-\Phi}\frac{\gamma}{d} \\ &\propto 4.54\frac{\gamma}{d} \end{aligned} \tag{2.5}$$

where ν is the Poisson ratio, Φ the solid area fraction, γ the interfacial tension and d the particle diameter [48].

The result that physically jammed particles on liquid-liquid interfaces have a solid character leads to the conclusion that jammed particle-laden interfaces should be able to withstand Plateau-Rayleigh instabilities therefore non-spherical droplets should be able to be stabilised by solid particles.

2.2.4 Properties of curved particle-laden interfaces

Emulsion droplets stabilised by solid particles resist coalescence very effectively for periods up to years [2]. Although the wetting properties of particles induce a preferred curvature in emulsion droplets this fact can be violated. A catastrophic phase inversion can be obtained by varying the volume ratios of the two emulsifying liquids. In doing so a water-in-oil emulsion stabilised by partially hydrophobic particles can be inverted into an oil-in-water emulsion when adding more water. This leads to a change in the droplet size but does not affect the stability against coalescence [39]. It shows that it is possible to stabilise two different types of curvature with a single type of particle. For particles with more extreme wetting properties (a clear preference for one of the two liquids) the efficiency of collecting at the oil-water interfaces is reduced during the attempt to stabilise inverted emulsions [39]. This indicates that to stabilise a system where different types of curvatures are concurrently present will be more readily successful for particles with near neutral wetting.

Ramsden [32] has already observed in 1903 that “sharply angular and grotesque shapes” can occur in particle-stabilised emulsions. Such non-uniform curvatures imply anisotropic stresses within the interface and can only be supported when the interfaces are solid and therefore static over time. Evidence of the solid character of particle-laden interfaces is, the verified existence of a finite Young’s modulus in particle rafts [48], but also the static nature of particle-stabilised droplets which have a non-spherical geometry or show cracking and crumpling behaviour if the internal volume is reduced [45, 50, 51]. It

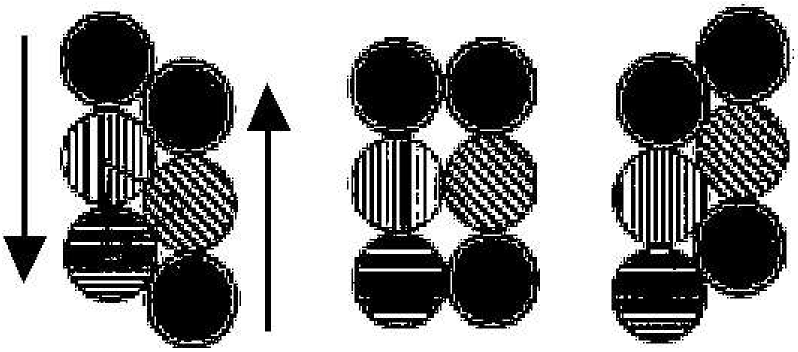

Figure 2.3: For particles to slide past each other the surface needs to dilate to accommodate this rearrangement leading to a plastic deformation [3].

has been shown that various different non-spherical shapes like a torus [52] or cylinder [53] can be stabilised by particles trapped on interfaces. All these particle-covered structures are static over time. While Subramaniam et al [3] have shown that small inhomogeneous stresses on such particle laden interfaces lead to collective particle rearrangements resulting in a plastic deformation as shown in figure 2.3, they also show that homogeneous stresses evoke a rigid, elastic response. Depending on the nature of the stress on the material particle-laden interfaces these either respond plastically or elastically [3].

2.2.5 Dynamics of glassy systems

In the last few sections I have shown that particles trapped at a liquid-liquid interface change the mechanical properties of this interface. Consequently, a system starting its evolution from a point far from equilibrium will no longer behave in the same way as without particles. The driving force towards equilibrium is the energy cost of the interface. The system will therefore decrease its area pushing the trapped particles closer together until their resistance to being further compressed will oppose the drive towards equilibrium (provided that expulsion of the particles from the interface is not possible). However, the particles on the interface are likely to jam and build up resistance to being

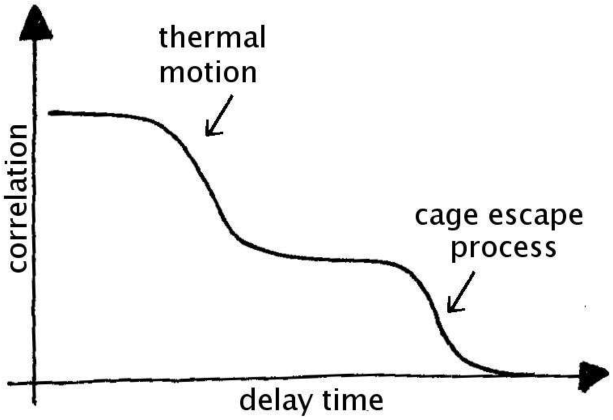

Figure 2.4: Typical correlation function for a fluid system described by the mode coupling theory. The graph shows a decrease in correlation due to the thermal motion of the particles eventually followed by a second relaxation due to the cage escape process leading to full decorrelation.

compressed before they are maximally packed leaving possibly room for slow rearrangements.

To improve the understanding of material properties it is of interest to find out whether the system will be able to undergo these rearrangements and if so in which manner these occur. Such glassy materials occur widely in various industries like that of pharmaceutics, food, paints, cosmetics and in oil-recovery. An insight into the rheological and mechanical properties and their behaviour over long time scales will help smart product design and a better prediction of their shelf life.

Research so far has shown that many arrested out-of-equilibrium or jammed systems exhibit very slow relaxations. The theoretical assumption of the dynamic behaviour of particles in a fluid near the glass transition is that these particles will exhibit thermal motion but are confined to cages formed by their neighbours. However, for the fluid state the particles will eventually be able to escape this cage and move on to jiggle around in the next cage. While for a glass this cage-escape process is not taking place or is at least dramatically delayed. This behaviour is described by the correlation curve shown in figure 2.4[2]. Here the correlation in

---

[2] For a more detailed explanation of correlation see section 3.4.2.

particle positions is considered over time. If the arrangement has not changed much the correlation will be high, while if the positions have changed a lot, decorrelation leads to a lower signal. For very short times the particle locations are fixed and the correlation is high. Mode coupling theory (MCT) describes how, for example, colloidal particles behave when approaching the glass transition coming from the liquid state. In this theory the first decorrelation in figure 2.4 is due to the particles moving within the cages while the second decay leading to a full decorrelation is due to the cage escape process. Upon approaching the glass transition the characteristic decay time of the second relaxation in the MCT is expected to diverge implying a complete dynamical arrest [54]. Both these decorrelating processes are diffusive in origin and the decays can be fitted to extract a diffusion constant D or the mean squared displacement of the constituents using the following function:

$$f(q,t) \sim exp(-Dq^2t^b), \tag{2.6}$$

where f(q,t) is the dynamic structure factor which is the correlation curve shown in figure 2.4, q is the scattering vector which indicates the examined length scale, t is time, and b is a stretching exponential. If the typical decay time of such a decay is proportional to q^{-2} as it is the case if the dynamic structure factor can be fitted with equation 2.6 and $b \leq 1.0$ this implies that the dynamic process leading to the decorrelation is of a diffusive origin. Recent experiments on soft glassy materials like colloidal systems have shown that contrary to the postulates of the MCT a second decorrelation can occur even deep into the glass state. However, this decay has an unusual shape that rules out a diffusive cage escape process. This final relaxation can be on observable time scales in soft glassy materials and is characteristic of many different types of materials. The typical signature of this slow relaxation is that the typical decay time is no longer proportional to q^{-2} but is most often found to be proportional to q^{-1} although exponents of 0.5 or 1.3

have also been found. An extensive review on this topic is given by Cipelletti and Ramos [54]. Additionally the decay is regularly found to be faster than diffusive. The dynamic structure factor is therefore fitted with a function proportional to:

$$f(q,t) \sim exp(-t/\tau_c)^{\beta}, \tag{2.7}$$

where β is a stretching or compressing exponential, t time, and τ_c is the characteristic decay time. Compressed exponentials, $\beta > 1.0$, leading to faster than diffusive decays are observed and are typically around 1.5 but lower values occur as well [55]. The third characteristic of slow dynamics in soft glassy materials is a significant dependence of the second decay on the sample age. A slowing down of the dynamics with sample age is observed in a wide variety of materials [54]. Contrary to the second decay, the first decay is still found to be of diffusive origin in these soft glassy system and does not change over time [55]. The dynamic structure factor is a time averaged quantity. If the underlying signal is instead resolved with respect to time it is possible to see a heterogeneous behaviour of the signal for the slow decays discussed above. At the same time diffusive processes show homogeneous behaviour if analysed in a time resolved manner. It therefore seems that heterogeneous dynamics give rise to compressed exponential decays with a variety of exponent values and q-dependencies. This time resolved correlation (TRC) method [56, 57] will hopefully help to understand the dynamic behaviour of soft glassy systems better in the future. There are different microscopic mechanisms which might be responsible for these heterogeneous dynamics, for example excluded volume interactions or elastic deformations of constituents giving rise to internal stresses which then eventually relax leading to rearrangement events heterogeneously distributed in time. In solid stabilised droplet emulsions gravity continuously acts on all the droplets in the sample making them cream into a densely packed layer. Like the jammed particles on the interface these droplets will continuously be pushed together and rearrange over time. In chapter 7 I will examine the dynamic behaviour of such a system over time.

2.3 Phase separation in binary liquids

Phase separation occurs in a broad variety of materials often leading to very specific and reproducible arrangement. Such a mechanism can be exploited in self-assembly processes. If two liquids are added together some liquids mix, some do not and some exhibit both phenomena depending on temperature or pressure. Here I briefly show how this behaviour is noted in phase diagrams and then give an overview of how the different shapes of phase diagrams arise before explaining the kinetics involved in phase separation, the process a system needs to undergo when going from a one-phase state into a two-phase state.

2.3.1 Phase diagrams

Two important parameters which determine whether two liquids mix or not are the composition of the liquids and the temperature. To describe the behaviour of a binary-liquid a phase diagram is drawn which indicates for which values the liquids are miscible. Figure 2.5 shows such a system with the composition of the two liquids plotted versus temperature. The solid curve, the binodal, indicates the phase boundary above which the system is in the miscible state and below which it will phase separate. These phases will not necessarily be the pure liquids, but the original liquids will still be mixed to some extent, i.e. they are partially miscible. The composition of the separated phases is determined by the location of the phase boundary at the current temperature. To obtain the volume ratios of the separated phases the Lever rule is applied. Considering the phase diagram shown in figure 2.5, then mixing 60% of liquid A with 40% of liquid B at temperature T_i will result in a miscible binary liquid. When changing the temperature to T_f the system prefers to be in a demixed state. It will separate into two phases, phase α and phase β. Phase α consists of 20% of liquid B and

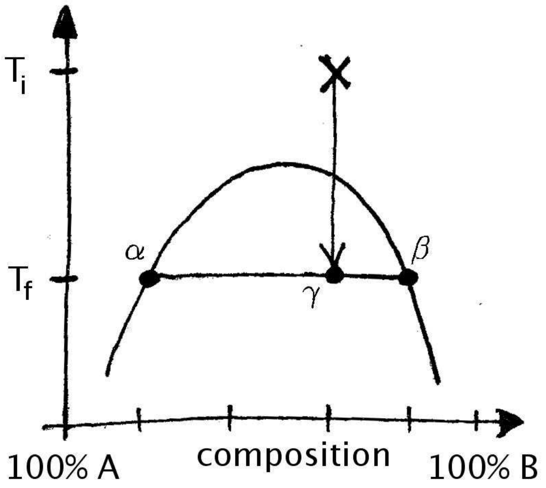

Figure 2.5: Typical phase diagram of temperature against composition. On the left hand side liquid A makes up 100% of the sample, while on the right it is 100% of liquid B with linearly varying mixtures in between. The lever rule determines the volume ratios when a binary mixture is quenched from T$_i$ to T$_f$ at composition γ as explained in the text.

80% of liquid A (A-rich) and phase β consists of 80% of liquid B and 20% of liquid A (A-poor). The respective volumes of these two separated phases is given by the ratio of the lines connecting α & γ and γ & β, where the left hand side of γ refers to the volume of the β-phase and the right hand side of γ to the volume of the α-phase. This swapping is due to the fact that the closer γ moves towards β, the less of liquid A will initially be added to the system. Consequently the A-rich phase α must decrease in volume. This is the Lever-rule and shows that in figure 2.5, the A-poor phase would have a third of the total volume while the A-rich phase would make up the remaining two thirds.

Whether two liquids mix or not depends on molecular interactions and the entropy of the system [58]. For a system to be in equilibrium it needs to minimise its Gibbs free energy

$$G = H - TS. \tag{2.8}$$

This can be done by reducing the enthalpy and by increasing the entropy S. Enthalpy is defined as H=E+PV, where E is the internal energy and depends on bond interactions between the molecules, while the entropy S is a measure of the disorder in the system. Ordered molecules have a lower entropy than randomly distributed ones. P is pressure and V is the volume.

At low temperatures the enthalpy term determines the free energy while at high temperatures a small change in entropy substantially influences the free energy. To understand the behaviour of a binary-liquid system at different temperatures I first consider the situation at high temperature. If T is large then, because it multiplies the entropy in the free energy equation 2.8 a small change in entropy, S, will have a larger effect on G than a small change in the enthalpy H. Entropy is highest if there is the highest disorder which is the case if the two different types of molecules are randomly mixed and orientated in random directions. For high temperatures the two liquids will therefore be miscible. If the temperature is lowered the enthalpy term slowly gains importance. The enthalpy of a system is determined by the interaction of the molecules. All systems will have Van-der-Waals forces acting between molecules, i.e. if the molecules move close to each other they will shift their electron clouds leading to attractions between the oppositely charged parts. For most systems the Van-der-Waals forces between like molecules are stronger than between different molecules. This implies that the energy between like molecules is generally lower which will result in a demixed system where like molecules surround each other at lower temperatures.

This will result in a phase diagram with an upper critical solution temperature (UCST). The liquids demix at low temperatures but at high temperatures they are miscible.

However, there are also systems where further cooling induces another miscible region leading to a lower critical solution temperature (LCST). This can be attributed to intermolecular attractions, for example, the formation of hydrogen bonds. These form when lobes of unshared electrons from an electronegative atom attract the nucleus of a hydrogen atom. They are stronger than Van-der-Waals forces and therefore lower the enthalpy more. Although compositional entropy

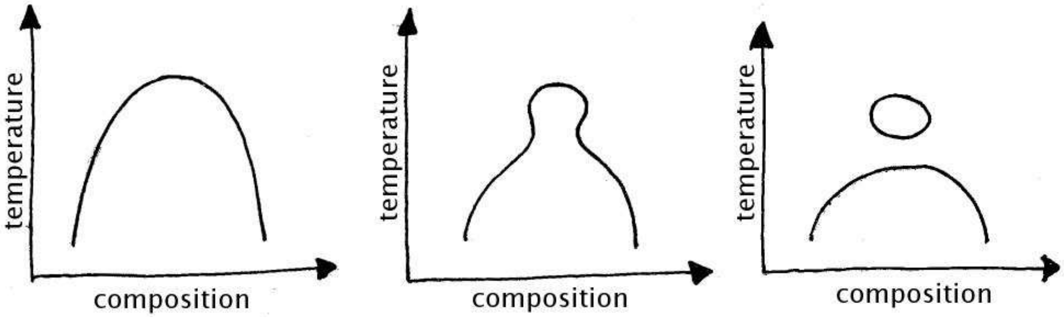

Figure 2.6: The shape of a simple phase diagram with UCST will change to one with an immiscibility loop if association forces (e.g. hydrogen bonds) are present. From left to right the effect of increasing association forces is demonstrated [4].

is gained when the molecules mix to form hydrogen bonds with unlike molecules this also implies that the molecules need to align. Hence orientational entropy is lost and this can be greater than the gain in compositional entropy resulting in a lowered net entropy. While for low temperatures the lowered enthalpy dominates and the lowered entropy does not play such an important part, hydrogen bonds can be formed leading to a miscible state for low temperatures. However, at higher temperatures the low orientational entropy is an unfavourable effect resulting in the absence of hydrogen bonding at higher temperatures. Through the formation of hydrogen bonds it is possible for the system to re-enter miscibility at low temperatures leading to a phase diagram with a closed immiscible loop. If the strength of the hydrogen bonds increases this loop gets smaller until it disappears. If there are very weak or no hydrogen bonds no reappearance of miscibility occurs upon decreasing the temperature (see figure 2.6). This increase of hydrogen bonds can be promoted for example by applying pressure to a system.

The methanol/hexane and ethanol/dodecane system used in chapter 5 are examples for standard binary systems with a single UCST. The 2,6-lutidine/water system, however, is an example of a system with an immiscibility loop. For experimentally accessible temperatures this system exhibits a phase diagram with a LCST which is actually the bottom part of an immiscibility loop as described above. The 2,6-lutidine/water system is also well studied under pressure and as predicted by this theory an increase in pressure will (at least initially) raise the LCST. This fact is exploited later in chapter 6.

On closer investigation the competition between enthalpy and entropy actually results in three different states. Figure 2.7 shows an example of the free energy curve for a certain temperature T_x. Three different regions can be distinguished. Depending on the shape of the free energy curve the net free energy of the liquid mixture will be lowered or raised when thermal fluctuations occur. If such fluctuations result in a lowering of the free energy the system will be unstable and start separating. This is the case when $\frac{\partial^2 G}{\partial c^2} < 0$. This can be easily understood when looking at the special case of critical composition where the free energy G has a maximum and therefore spontaneous fluctuation to either side (into phase critical - α and critical + α) will lower the total free energy. But the total free energy is also still lowered if the original composition is off-critical and between compositions b and c in figure 2.7. This is because the magnitude of the slope of G increases towards b and c implying that the total free energy of any fluctuation in composition will lead to a net reduction in the free energy resulting in an unstable state between b and c. By contrast if $\frac{\partial^2 G}{\partial c^2} > 0$ any fluctuations in composition will increase the net free energy. Therefore fluctuations in that region will be damped by the free energy cost. This damping becomes more pronounced the steeper the free energy curve and leads to an increase of stability for the system. However, between a and b as well as between c and d metastable regions exist where after overcoming an initial energy barrier the system can reach a lower energy minimum by phase separating into compositions at a and b where the free energy is minimised, i.e.$\frac{\partial G}{\partial c} = 0$. Finding $\frac{\partial G}{\partial c} = 0$ for all temperatures produces the solid curve in the top sketch of figure 2.7 which is called the binodal and separates the miscible region of the phase diagram from the immiscible region. The set of points where $\frac{\partial^2 G}{\partial c^2} = 0$ is called the spinodal and separates the metastable from the unstable state (dashed line in figure 2.7).

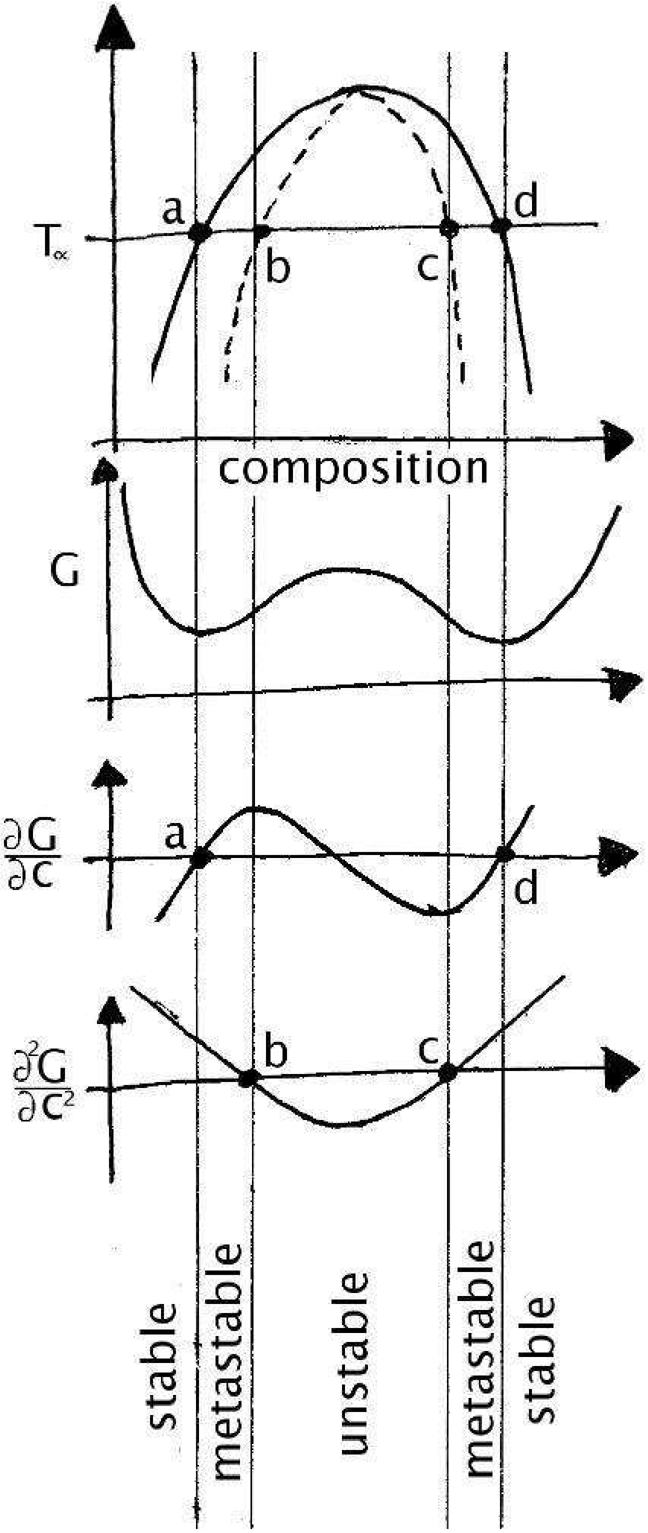

Figure 2.7: The free energy of the system determines which regions are stable, metastable and unstable. The free energy and its derivatives are plotted below the phase diagram for temperature T_{alpha} [5].

2.3.2 Separation kinetics

When entering the immiscible region of a binary liquid phase diagram there are different kinetic pathways to the demixing of the liquids. In the metastable region demixing occurs via nucleation while spinodal decomposition occurs in the unstable region.

In the nucleation process nuclei of the final phase are formed which grow and coalesce until the system has fully separated. Such nuclei form spontaneously due to concentration fluctuations. However, while the interactions between the molecules inside such a nuclei have a free energy minimum, the molecules at the surface of the nuclei have high free energy interactions with the remaining liquid. Therefore the nuclei must grow larger than a critical size before such a nucleus is energetically stable and can grow further. At this critical size the surface cost (growing with radius^2) is compensated by the free energy reduction of the volume term (growing with radius^3) [4]. The nucleation process described here is also called homogeneous nucleation. In experiment it is likely that there are preferential sites, e.g. colloids, for nucleation to occur leading to heterogeneous nucleation. Apart from coalescence another process can lead to droplet growth called Ostwald ripening. The large droplets grow at the cost of the small droplets and material transfer is via diffusion through the surrounding phase. The driving force behind this process is the interfacial tension per unit volume which is higher for smaller droplets. This process can be responsible for emulsions to fall apart very slowly if droplets can shrink. In solid-stabilised emulsions shrinking of droplets is inhibited by the solid nature of the stabilising particles and therefore Ostwald ripening is inhibited.

While there is an energy barrier for phase separation via nucleation this energy barrier vanishes for spinodal decomposition. Separation will immediately occur spontaneously at all points throughout the sample. A dominant wavelength in the fluctuations develops which determines a typical domain separation. Initially the separation process is governed by diffusion of the two types of molecules. The

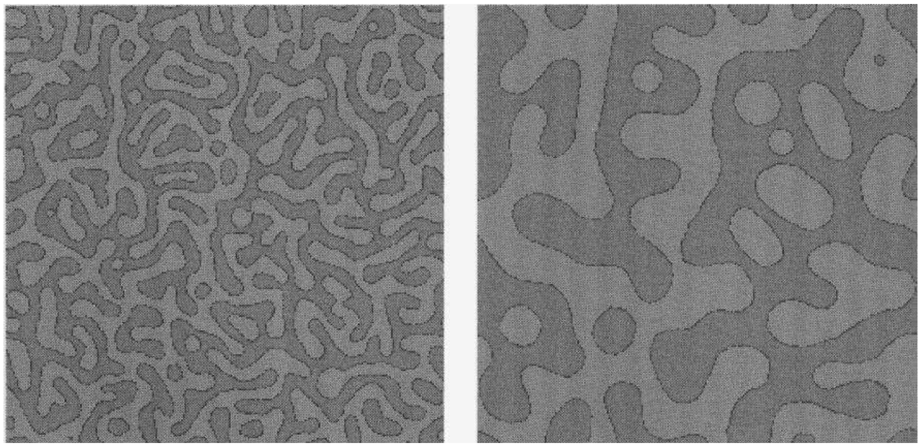

Figure 2.8: The coarsening of a system separating via spinodal decomposition happens in a self-similar manner. Although the typical domain size increases the morphology remains the same. Left: early stage, right: later stage. From [6]

liquid gradually demixes into two phases which gradually grow more diverse in composition. Parallel to that the energy cost associated with these developing interfaces increases. The need to retain a low free energy eventually requires the system to coarsen, i.e. to reduce its interfacial area. The reduction of interfacial area is driven by the interfacial tension and is called hydrodynamic coarsening [4]. The local curvature of the interfaces causes stresses which drive the fluid motion. The stronger the curvature of the interface the higher the associated Laplace pressure given by $\frac{2\gamma}{R}$ where γ is the interfacial tension and R the radius of curvature.

There are significant differences between nucleation and spinodal decomposition. Most apparent is the difference in morphology. While nucleation produces many individual droplets spinodal decomposition has a characteristic, bicontinuous and convoluted pattern. During the growth and coarsening of the nucleation process the nucleated phase will always aspire to maintain a spherical shape to reduce the interfacial area between the two separated phases leading to a range of droplet sizes during coarsening. In spinodal decomposition the characteristic separation pattern is self-similar. This means the morphology obtained at different times only changes by a scale factor as shown in figure 2.8 [6].

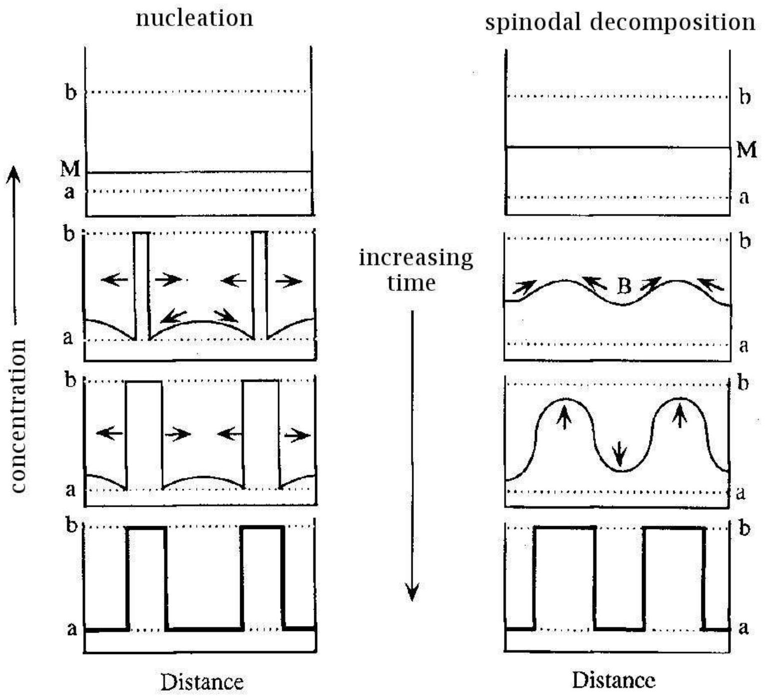

Figure 2.9: The compositions of the final phases develop in a different manner for nucleation and spinodal decomposition. From [7].

At constant temperature nucleation will produce droplets of the final composition so that the droplet phase has the same composition throughout the phase-separation process. This leads to sharp interfaces between the nuclei and the surrounding liquid at all times. The majority phase serves as a reservoir from which the appropriate composition of molecules is extracted to form the droplets until the majority phase has also reached the final composition at which the system continuous coarsening by coalescence. In contrast to this, concentration fluctuations throughout the sample separating via spinodal decomposition imply a gradual change of composition in both phases which slowly grow more diverse in composition. The composition of the two separating phases is therefore continuously changing leading to initially diffuse (not sharp, but with a finite width) interfaces with the effective interfacial tension initially being very low but increasing over time until the system has obtained its final compositions. Figure 2.9 illustrates these two contrasting mechanisms nicely [5].

How quickly the separation process occurs depends mainly on the interfacial tensions involved and the viscosity of the binary system. For low molecular weight liquids separation can happen in a fraction of a second. However, close to the critical point the system will experience critical slowing down and the separation process can last for many seconds instead. To understand critical slowing down concentration fluctuations need to be considered once more. These fluctuations can be described by a small perturbation, say ζ which oscillates and has a time dependent amplitude:

$$\zeta \sim exp(\mu t)exp(i\omega t). \tag{2.9}$$

If the system is stable towards concentration fluctuations then $\mu < 0$ and the oscillations of the perturbation will be damped within a characteristic time

$$\tau \equiv \mid \mu \mid^{-1} . \tag{2.10}$$

When the system is unstable the oscillations due to the perturbation will grow with time, implying that $\mu > 0$. This implies that at the critical point, the only location where the system goes from the stable directly to the unstable state, μ must be zero implying that the characteristic relaxation time of perturbations diverges (equation 2.10). Because the damping at the critical point is extremely slow there is an unlimited amplification of fluctuations resulting in critical slowing down [59]. For experiments this means that the separation process will occur on a much longer time scale than usual.

Chapter 3

Experimental methods

In this chapter I first discuss the properties of Stöber silica and how their surface properties can be modified. Then I briefly mention the basic principles of confocal microscopy before I show the design and working of the temperature control system used in the critical quenches in chapter 4. In the last section I give an introduction to light scattering and in particular the method of x-ray photon correlation spectroscopy (XPCS).

3.1 Particle preparation

The solid particles used here to stabilise the various emulsions are silica particles. These solid spheres can be produced with a chosen diameter and very good monodispersity. Additionally, they can be labelled with fluorescent dyes which can improve the imaging of the resulting structures. But the most crucial point is the possibility of altering the surface properties of these silica spheres because this influences their wetting behaviour which is essential in my experiments. In this section I briefly describe the Stöber method which is used to produce such monodisperse silica spheres and then I show how the surface chemistry of these colloids can be changed by chemically altering their surfaces and I point out the difficulties with this approach.

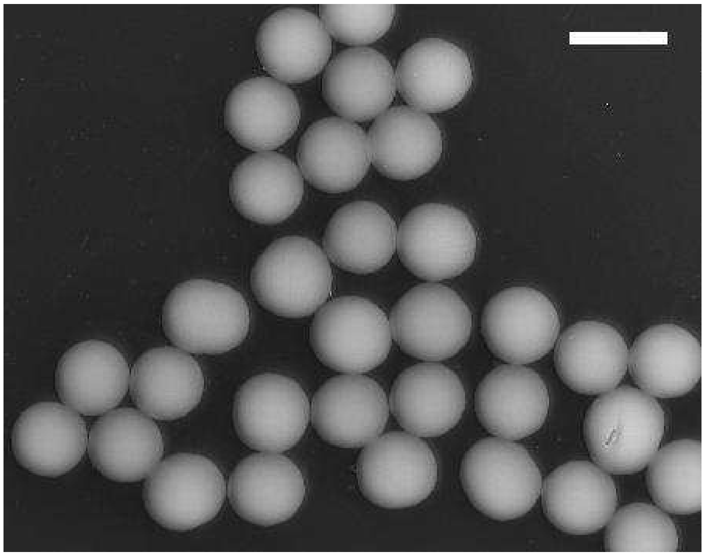

Figure 3.1: Electron microscopy image of Stöber silica doped with FITC. Image taken by Andrew Schofield. Scale bar 0.5 μm.

3.1.1 Stöber silica

The spherical silica particles are prepared by Andrew Schofield after the Stöber technique [60]. Silica acid which is formed by the hydrolysis of tetraethyl othosilicate is polymerised in a solvent mixture of ethanol and ammonium hydroxide. This polymerisation process forms homogeneously sized, spherical silica colloids. The size is determined by the time and efficiency of the reaction which gives a handle on the colloid size. However, exact reproducibility of size is difficult and therefore the diameters of spheres of different batches can slightly vary in size. To obtain fluorescently doped particles the fluorophore fluorescein isothyocyanate (FITC) is added during the Stöber process [61]. The silica spheres used in the alcohol/oil experiments (Assi 9) presented here have a typical radius of 260 nm ±13 nm as obtained from fitting electron microscopy images. The FITC-doped particles used for the lutidine/water experiments are slightly smaller with 200 nm ±10 nm (size also obtained from electron microscopy images). Both sets of particles have a polydispersity of 0.05. The electron microscopy images presented in figure 3.1 are the FITC-doped batch of (Assi 16) particles showing

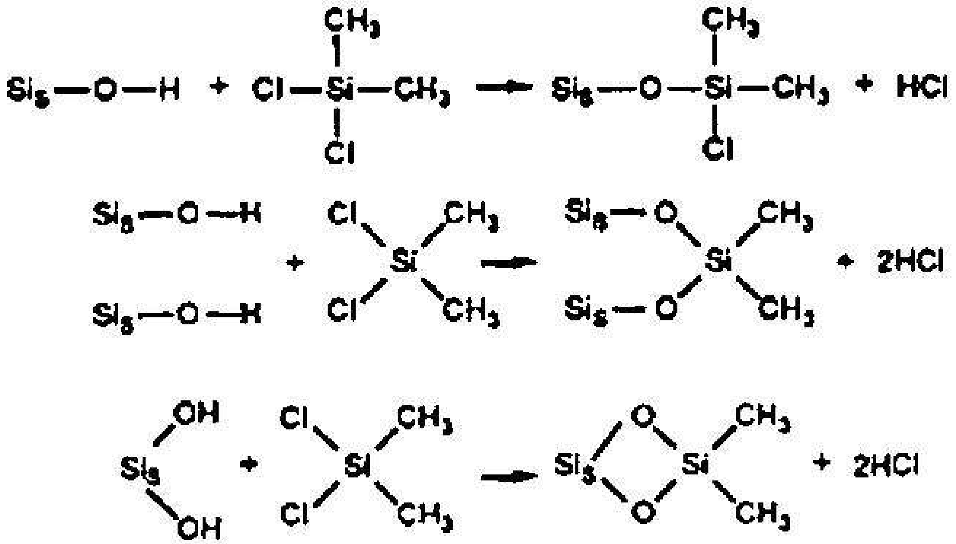

Figure 3.2: Different binding possibilities for DCDMS to the silica surface [8]

how nicely spherical the particles are. The particles (Assi 12) used in the x-ray experiments are again plain Stöber silica particles with a radius of 243 ± 7 nm implying a polydispersity of 0.03 as obtained from x-ray scattering data. For such low polydispersity systems it is possible for the particles to crystallise on the interfaces when jammed together.

3.1.2 Surface chemistry

Originally the surface of Stöber silica particles is covered with OH-groups (silanol groups). This implies a very hydrophilic behaviour because water will be able to easily form hydrogen bonds with the free OH-groups [62]. But it is possible to chemically alter this surface by exchanging the silanol groups with inactive methyl groups, a less hydrophilic compound. By silanising different fractions of the surface hydroxyl-groups with dichlorodimethylsilane (DCDMS) it is possible to tune the wetting behaviour of the particles.

Silanisation of silica with DCDMS

Dichlorodimethylsilane (DCDMS) consists of two methyl groups and two chlorine atoms individually bound to a silicon atom. The chlorine end can react with a surface hydroxyl group of the silica to bond the molecule to the silica surface by eliminating HCl. This is proposed to happen either monofunctionally, i.e. only one chlorine atom is involved in the reaction binding the methylsilyl group with a single bond to the surface or difunctionally where both chlorine atoms get reduced such that the silicon of the methylsilyl group is bound with two bonds to an oxygen atom each. [8] As is illustrated in figure 3.2 this can happen with two isolated surface hydroxyls (vicinal hydroxyls) or two geminal hydroxyls which in the latter case means that they are both bound to the same silicon atom.

When researching the literature I found interesting information on trichlorosilanes, in particular octadecyltrichlorosilane (OTS) a larger molecule. While DCDMS has two chlorine end-atoms trichlorosilanes have three. Sagiv [63] and Silberzan [9] suggest the following mechanism in which the surface hydroxyl groups of silica surfaces are silanised but no experimental evidence is given. The authors claim that OTS is strongly attracted to the clean silica surface via the trichlorosilanes. The surface silanol groups are very hygroscopic and easily attract water from the surrounding air and are therefore covered with a water layer unless good care is taken to remove this surface water. As soon as the trichlorosilane groups get close enough to the silica surface they get hydrated by the surface water producing HCl. These newly created OH-ends of the molecule are then hydrogen bonded to the surface hydroxyls. This relatively unstable situation is followed by water elimination, bonding the silane molecule to the silica surface or linking adjacent molecules as shown in figure 3.3. It would not be surprising if the silanisation process for DCDMS occurs in a similar manner.

The initial set of particles was silanised in Hull with the help of Tommy Horozov. However, I encountered problems with the reproducibility of the silanisation process. In an effort to obtain reproducible particle wettabilities I

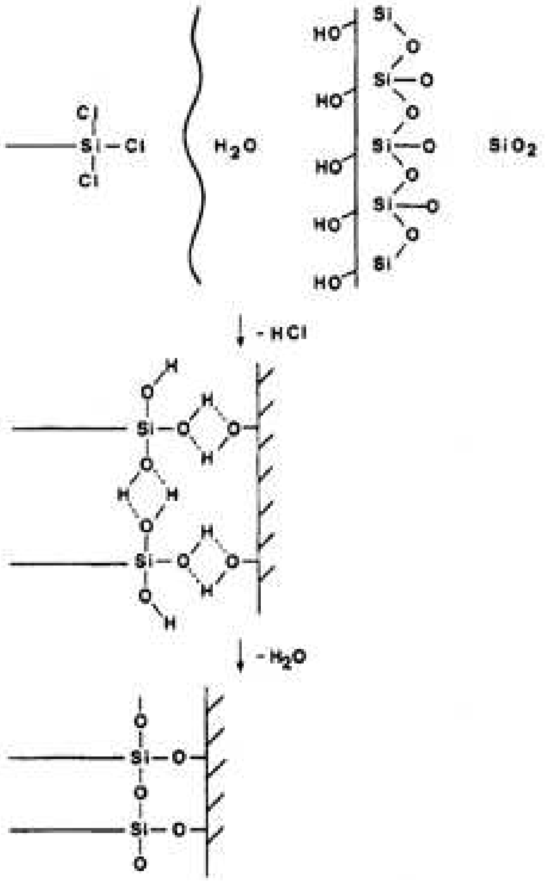

Figure 3.3: Water catalysing the silanisation process of OTS [9].

studied the effect of water on the silanisation process. As mentioned before, the silica surface has a high affinity for water due to the surface hydroxyl groups which physically adsorb water, i.e. bind the water via Van-der-Waals forces to the silica surface. Depending on the amount of water present several layers of water molecules can be found adsorbed in this way [62]. This surface water can be removed by drying the silica under vacuum but care has to be taken that the chemical structure of the surface is not altered. Young [37] showed that drying silica leads to the condensation of hydroxyl groups at temperatures above 150°C, i.e. water condensing out of the bound silanol groups. While this process is reversible below 400°C it turns irreversible above 400°C. To only remove the surface water it is therefore important to dry the silica below the condensation

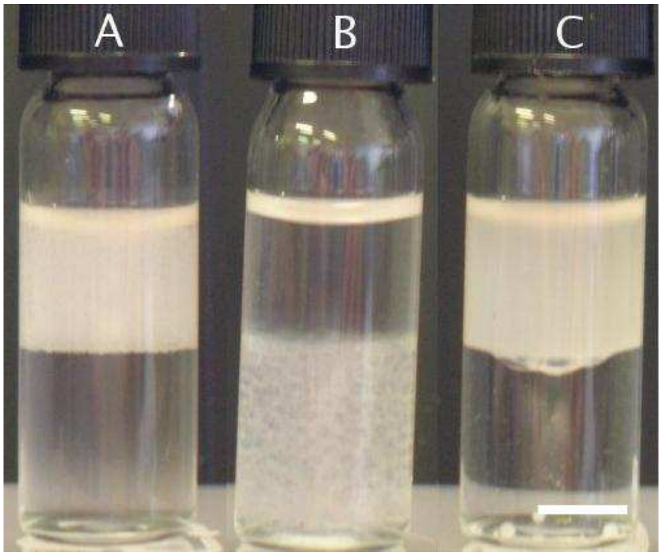

Figure 3.4: A wide range of wetting behaviour is obtained for the same DCDMS concentration depending on the presence of water in the system during the silanisationprocess. Methanol/hexane mixtures containing (A) particles silanised under dry conditions, (B) particles that were "contaminated" with water prior to the silanisation process and (C) particles where the water "contamination" was in the silanising solvent during surface modification. While the particles in A stabilise hexane droplets, they stabilise methanol droplets in B and in C don't stabilise droplets at all but are only found in the hexane-rich phase. Scale bar 5 mm.

temperature of 150°C.

To test whether water activates the silanisation process I silanised (see next section) three sets of particles from the same Stöber process and examined the behaviour of the particles in off-critical methanol-hexane mixtures (see section 5.2.1). Sample A was prepared under conditions where all reagents of the silanisation process were kept as dry as possible. For sample B the desiccated solvent (cyclohexane) was deliberately rehydrated by adding 43 μl of purified water, while for sample C the same amount of water was directly added on the dried particles. All three samples were left to equilibrate under shaking for 5 hours before the silanisation process was carried out in the same way for all three samples. Figure 3.4 shows a drastic change in the wetting behaviour although the amount of DCDMS is constant for all three samples. This shows that any water present during the reaction will influence the reproducibility of the silanisation process. The particles in A which had no water added remain very hydrophilic and stabilise oil droplets. For the particles in B the reaction was stronger (more HCl was produced) and the particles have turned slightly hydrophobic now stabilising alcohol droplets, while in C the particles behave very hydrophobically and go straight into the oil-phase without stabilising droplets. In C the HCl production was very strong, indicating a much larger hydration efficiency of the DCDMS than in the other two samples. Controlling the efficiency of the silanisation process by the water content is, however, not a very good method because it will most likely also lead to uncontrolled polymerisation of the DCDMS. But this test shows that care has to be taken to achieve reproducible conditions.

Experimental silanisation procedure

The silanisation procedure described here was obtained from Tommy Horozov at the University of Hull. The particles are dried over-night under vacuum at 100°C. Then 0.3 g of these silica particles are dispersed in 10 ml solvent containing DCDMS in dry cyclohexane at different molar concentrations typically ranging over 3 orders of magnitude. The cyclohexane is dried with molecular sieves for weeks prior to being used in the silanisation process and is kept under a nitrogen blanket to reduce possible water contamination. The DCDMS is stored in the fridge. The relative quantities are determined by weighing the liquids prior to mixing with the particles. Before the particles are brought into contact with the DCDMS they are dispersed in half of the cyclohexane with the ultrasound probe. Then the remaining cyclohexane is added containing the relevant amount of DCDMS. After a reaction time of one hour under continuous stirring at room temperature the particles are spun down. Care is required as HCl is produced during the silanisation reaction. The supernatant is replaced by chloroform to stop further reactions in an effort to control the reduction of the hydroxyl groups in a reproducible manner. Subsequently the particles are washed repeatedly in alternately dry cyclohexane and ethanol before being dried under vacuum.

Determining wettability of the particles

After the silanisation process each set of particles is tested for its degree of hydrophobicity. This is done by mixing 0.1% volume fraction of the relevant silica in a methanol/hexane mixture with an ultrasound probe at a minimum of 3W. After mixing there are several possible outcomes. The two extremes are that the particles are found in only one of the two liquids. The suspended particles will make the solvent opaque compared to its former transparent appearance. If the particles are found in the bottom liquid they are in the alcohol and therefore still very hydrophilic. If they are dispersed in the less dense oil, the top liquid, the surface is now covered with more methyl groups and the particles therefore behave hydrophobically and prefer the oil to the alcohol. In intermediate cases the particles stabilise the methanol/hexane mixture by forming a Pickering emulsion. Depending on the wetting properties either oil-in-alcohol or alcohol-in-oil emulsions are formed [40]. If the droplets cream they contain the less dense oil, if they sediment they contain the alcohol. Because the interfaces curve depending on the wetting behaviour (see figure 2.2) the surrounding liquid will be the one the that preferentially wets the particles. Oil droplets will therefore be stabilised by more hydrophilic particles, while alcohol droplets will be stabilised by more hydrophobic particles. If the particles have neutral wetting they are particularly strongly bound at the liquid-liquid interface. A high stability of the emulsion therefore indicates appropriate wetting conditions. The particles leading to the longest stability are therefore chosen for the subsequent experiments; they are found near the inversion point.

It is important to note that reproducibility of the silanisation process is a problem. Many factors can influence the efficiency of the silanisation process. The period for which the cyclohexane has been dried over molecular sieves, the drying time and temperature of the particles as well as the use of dry glassware can influence the result. I have established that the preparation temperature has an observable influence and therefore mixing by ultrasound where local heating occurs will lead to a different outcome than using stirrer bars. Furthermore the age of the DCDMS or the recipe used to prepare the Stöber particles will have an effect. It would therefore be desirable to have a more quantitative method to determine the wetting angle of the particles than the one described above. Thanks to our collaborators in Hull I was able to attempt this using their equipment. By observing sessile methanol drops in hexane I tried to study the change of contact angle with temperature. Unfortunately, the partially miscible character of this system makes this experimentally very challenging because already small variations in temperature lead to a change in volume of the observed droplet. This and undesired, heterogeneous nucleation masking the main droplet led to this approach being abandoned. A more stable environment is required before the wetting angle can be measured systematically.

3.2 Confocal microscopy

Microscopy is a very powerful tool and developments in the last century have led to a variety of techniques allowing the observation of different features of a huge range of samples. The majority of my observations have been carried out using confocal and fluorescent confocal microscopy. In the following section I will outline the principles of this microscopy technique which allows the three-dimensional sectioning of a sample without physical intrusion. Prior to the advent of confocal microscopy samples had to be physically cut into sections which then were examined by conventional microscopy. Such an invasive technique is not appropriate for samples which are evolving over time or have insufficient structural stability. Standard bright-field microscopy is unsuitable for most of my samples since they are too opaque due to their internal structure. In the following section I briefly introduce confocal microscopy and then show how the resolution of such a system is determined before describing typical aberrations.

3.2.1 Basic principles

In a typical microscopy set-up the sample is illuminated and the objective collects the light and subsequently forms a magnified image using an array of lenses. This image formation process has been adapted and improved for many situations over recent years. The key point in confocal microscopy is that most of the collected light is discarded. Doing this so as to isolate light from a single plane leads to a powerful method for imaging the sample in three dimensions. This is achieved by illuminating only a single spot of the sample at a time. The reflected light from this point is collected and passed through a pinhole which only selects the light that is in focus in the chosen image plane. All the light from other focus planes is blocked and does not contribute to the formed image. This mechanism is shown schematically in figure 3.5. Scanning the whole image, point by point in this manner, builds up a full image which only contains information from a selected image plane. Repeating this for different image planes allows three-dimensional sectioning of the sample. For this reflected light method the condenser lens of the microscope does not need to be adjusted and therefore it is not necessary to carry out the Köhler illumination alignment.

The image quality depends very much on the objective lens and how well it is matched to the sample and environment. Conventional microscopy is carried out on a thin specimen covered with a standard coverslip of grade 1.5 which has a thickness of 160 to 190 μm [64]. Standard objectives are optimised for such a situation. To obtain good image quality it is important to understand the objective design parameters. These details are written on the outside of the objective. Especially for higher magnifications it is important to know which working distance (WD) the objective has. Usually the WD decrease with increasing magnification. The WD is the spatial separation between the objective and the focal point as shown in figure 3.6. The angle θ in the same figure

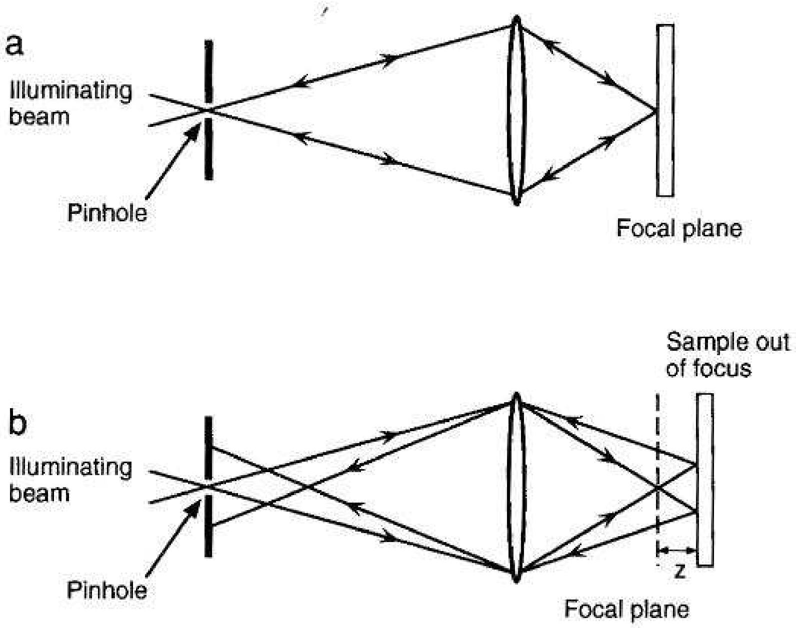

Figure 3.5: Schematic diagram of confocal microscope showing the sample (a) in the focal plane and (b) out of focus. The out of focus contributions are blocked by the pin hole so that only the signal coming from the focal plane is imaged. From [10].

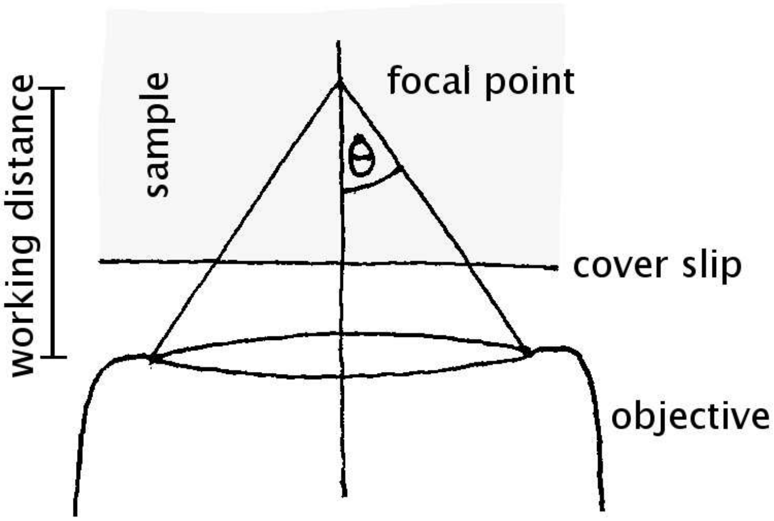

Figure 3.6: The objective collects a cone of light originating in the focal point characterised by the angle θ. The distance between the objective and the focal point is called the working distance (WD).

determines the maximum cone of light the objective can collect. The larger this angle the higher the achievable resolution and intensity. The refractive index n between the lens and the cover slip can effectively increase this light cone and therefore the numerical aperture (NA) is used instead of the cone angle to quantify the objective performance:

$$NA = nsin(\theta), \tag{3.1}$$

where n is the refractive index surrounding the objective. The larger the numerical aperture the higher the resolution. Therefore the space between objective and coverslip is sometimes filled with a high refractive index oil to make possible values of NA > 1. Oil immersion objectives are usually used for high magnifications and short working distances and can be very powerful. More detailed information on the set-up of the confocal microscope and microscopy in general can be found in various books on this topic. For example [10] or [65].

In fluorescence microscopy the ability of certain molecules to emit light when illuminated is exploited. Due to some energy loss prior to emission the emitted light has a longer wavelength than the light used to excite the molecule. This is known as the Stoke shift. The fluorophore used here is fluorescein isothyocyanate (FITC) which is excited very efficiently at 488 nm and then emits around 512 nm. Using a filter which blocks light for wavelengths below 500 nm will lead to an image formation with light only emitted by the sample. This method can improve image quality significantly (see chapter 6).

3.2.2 Resolution

To carry out successful microscopy it is necessary to find a sensible compromise between resolution and contrast. The various apertures inside a confocal microscopy set-up (including the NA of the objective) determine the contrast. To explore the spatial resolution limit in the x-y plane an image is considered which is produced by a point source. In an experiment this point source can be

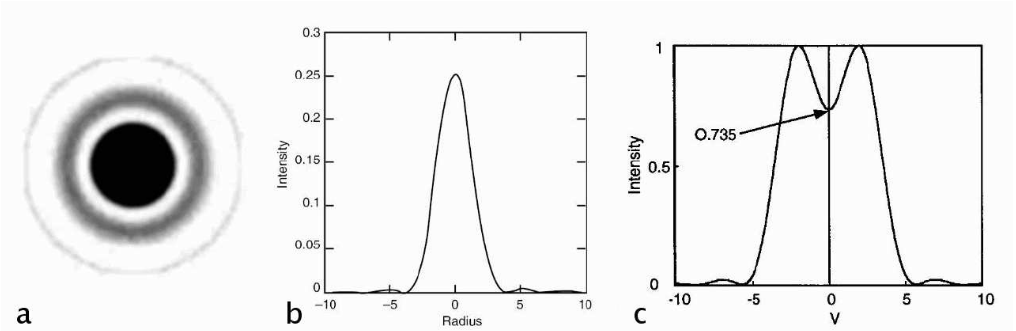

Figure 3.7: An overexposed airy disk is shown on the left with a cross section through its pattern in the centre [11]. Two objects producing airy disks will only be separated if they are far enough apart such that a minimum of 26.5% less intensity exists in between them as shown on the right [10].

approximated by examining an object smaller than the resolution limit. The image of a point source will, in the absence of any aberrations, produce an Airy disk. As seen in figure 3.7a and b this is a circularly symmetric intensity pattern and its exact shape depends on the wavelength and the image forming components. The actual resolution in an image, i.e. the smallest distance two points can be apart while still being distinguished, is determined by the Rayleigh criterion:

Two points will be resolved if the first dark ring of the Airy disk of one point coincides with the bright point of the Airy disk of the other point.

This results in an image with two bright peaks and local minimum between them which has approximately 26.5% less intensity than the two peak values as demonstrated in figure 3.7c. This minimum is strong enough to make the two points distinguishable although the definition of what is resolvable is somewhat arbitrary. In experimental systems the Airy function is known as the point spread function (PSF).

From this relation between different Airy disks the lateral resolution for a confocal microscope is given by

$$R_{xy} = K\frac{\lambda}{NA}, \tag{3.2}$$

where NA is the numerical apertures of the objective. The constant K depends on the coherence of illumination. For standard microscopy K = 0.61, but for confocal microscopy where the side lobes of the airy pattern are modified this reduces to K=0.56 [10, 66].

The Airy pattern (or point spread function for real systems) is three dimensional and behaves similarly along the z-axis (the vertical of the sample). The Rayleigh criterion can therefore also be used to determine the axial resolution which is also known as the depth of field. In this case

$$R_z = \frac{0.62\lambda}{n(1 - cos(\theta))}, \tag{3.3}$$

where n is the refractive index, θ the angle determining the numerical aperture and λ the wavelength used. If θ is small this can be approximated by $R_z \approx 1.24$ n $\lambda/(\mathrm{NA})^2$. In a fluorescence microscopy experiment the full expressions for the lateral and z-axis resolutions depend on the incident and fluorescent wavelengths. Here the values are sufficiently similar for the effect to be negligible. Especially when aiming to create three-dimensional reconstructions it is important to obey the Nyquist sampling theorem which requires to record confocal slices separated by $\Delta z = \frac{1}{2}R_z$. The effect of a finite depth of field on the image formation process is demonstrated in figure 3.8.

The pinhole of the confocal system can also have effects on the resolution. There exits an optimal setting of the pinhole for each combination of wavelength, magnification and NA. The confocal microscopy software calculates this automatically and this value is used here.

The time resolution of recording confocal slices is set by the scanning rate given in lines per second and can be set from 125 lps up to 700 lps. The scanning speed is limited by the adjustment speed of the mirrors guiding the laser and determines the exposure time for each pixel. To record an image the sample is continuously scanned line by line and therefore time evolves from the top to the

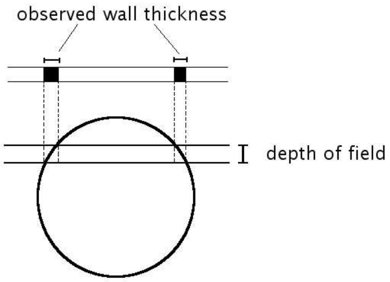

Figure 3.8: If a finite depth of field exists then curved objects like the schematically drawn droplet will appear to have thicker walls than they actually have. This is due to the fact that information from a three-dimensional space (the section slice with height R_z) is represented in a two-dimensional image.

bottom of the image. The sample will therefore be younger at the top of the image than at the bottom. It is important to keep this in mind especially when recording fast processes.

Aberrations

There are common aberrations which will influence the image quality, like chromatic aberration and curvature of field. They apply to most systems and therefore a correction method is incorporated in research objectives. Chromatic aberration arises because different wave lengths will refract differently. Hence an objective will only perform optimally for a single wavelength. However, concave and convex lenses have chromatic aberrations of opposite senses and can therefore be combined to form an achromatic doublet to correct for chromatic aberration. Different correction mechanisms work for different wavelength ranges. The one used here is the Apochromat working for orange, green and blue light (470 - 620 nm). Curvature of field arises naturally since the image produced by a perfect lens will always be curved in space. A compound lens can produce a flat focus field and is known as Plan. An objective combining both these correction methods is known as PlanApo or short PA.

Another factor determining the resolution, particularly the depth of field,

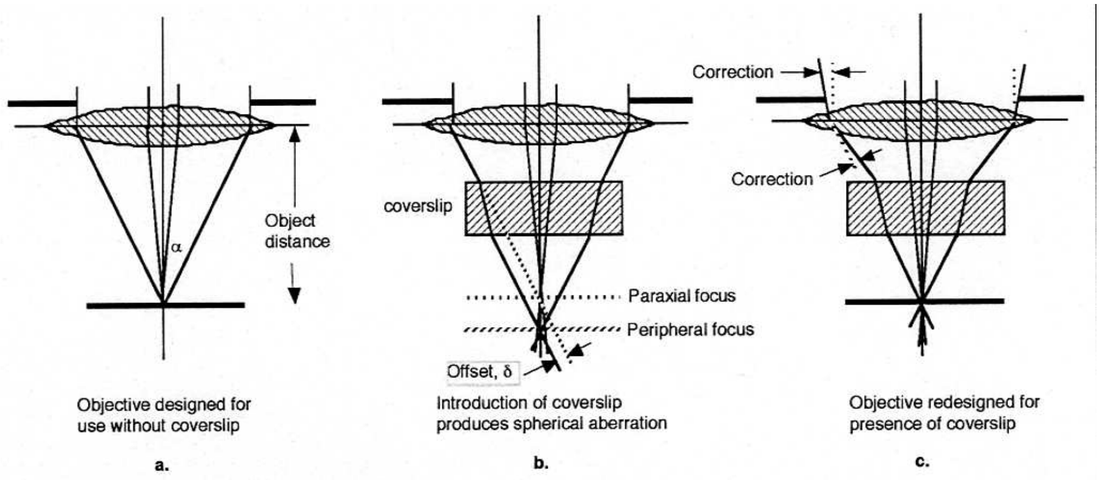

Figure 3.9: Peripheral rays with a larger angle of incidence bend more than central rays if travelling through a medium with different refractive indices. Therefore spherical aberration occurs when introducing a coverslip (b) but objectives correcting for spherical aberration are available (c) [12].

(important for three-dimensional sectioning) is spherical aberration. If light travels from one medium into a medium with a different refractive index it is bent. This bending is stronger the larger the angle of incidence. If materials with different refractive indices have a finite thickness this leads to different optical path lengths depending on the angle of incidence. As a result the peripheral rays will be in focus at a different depth compared to the axial rays, leading to a blur. This effect is shown schematically in figure 3.9b. If an objective is built to correct for spherical aberration the refractive index and thickness of the materials in the light path need to be known. Because these might vary in real situations, especially when working with larger working distances, these objectives are often equipped with collars that allow the movement of the lenses inside the objective to adjust for example for different coverslip thicknesses.

3.3 Temperature control

In chapter 4 I study temperature induced quenches in binary liquids. The temperature of the binary liquid sample determines whether it is in a miscible or immiscible state. If it it is immiscible, the temperature also determines the composition and volume of the two separate phases. To carry out systematic studies it is important to have control over the rate of temperature change. At the same time it is important to suppress oscillations of the temperature once the final temperature is reached to avoid fluctuations in composition and volume. In the following two sections I first describe the experimental set-up for heating samples contained in rectangular glass cuvettes and then explain how the temperature controlling mechanism works.

3.3.1 Experimental set-up

During the course of the various different quenching experiments it became apparent that it is very important to avoid convection within the sample due to temperature gradients. These movements within the sample are very strong and significantly disturb any structures that have previously been formed. Therefore a heating element is required that avoids such temperature gradients. I have therefore designed a sample holder that almost fully surrounds the sample. The samples that require a thermally controlled environment are contained in rectangular glass cuvettes that are sealed with a teflon stopper. The following set-up is used to carry out temperature quenches at different rates or to maintain a steady temperature environment during observation. For the pressure work in chapter 6 a copper heating brace (heat conductivity of copper is 401 W/mK) was built to heat the pressure cell. To use this already developed experimental heating set-up I only designed a new module to satisfy my needs for the temperature quenches instead of building a completely new set-up. A large enough thermal mass is necessary for steady temperatures while a high thermal conductivity is important to achieve fast temperature adjustments. Aluminium is easy to machine, is cheap and has a satisfactorily high thermal conductivity of 237 W/mK [24]. Figure 3.10 shows the central unit: a 1.9 cm high aluminium cylinder with a diameter of 5 cm. A rectangular recess at the bottom of the

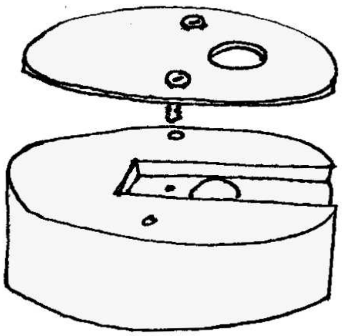

Figure 3.10: An aluminium block is used to heat uniformly the sample contained in a rectangular glass cuvette. The sample is placed into the rectangular groove inside the block below the lid which is held in place by screws.

block with the outside dimensions of the cuvette is closed with a thin (1 mm thick) aluminium lid that is screwed on tightly. This forms a cavity that entirely surrounds the sample with temperature controlled aluminium. Only the end of the cuvette with the teflon stopper remains exposed to room temperature and the cuvette can be quickly inserted and removed. The high thermal conductivity of the Aluminium allows the heat to be quickly distributed throughout the block resulting in uniform temperatures surrounding the cuvette where the large thermal mass of the block acts as a heat bath for the initially cooler sample. To start with a heat sink paste was used in between the lid and the block but the effect temperature control performance was unnoticeable and was therefore not repeated. To observe the sample under the microscope there is a 7 mm diameter hole in both, the aluminium block and the lid, which act as windows allowing the illumination of the sample from top and bottom. The lid must be thin enough so that the required working distance of the objective is not increased unnecessarily. The opening is chosen that it is large enough for it not to reduce the effective numerical aperture of the objectives used. A smaller hole drilled vertically through the aluminium block allows the insertion of a thermocouple which then touches the outside of the cuvette. This is the closest I can reasonably get to the sample to measure and control its temperature. The thermocouple is clamped in place by a screw prior to inserting the block into the copper brace. Should a direct measurement of the sample temperature be vital at some stage, a special teflon lid could be machined that holds the thermocouple wire. The current set-up however, is satisfactory for temperature stability purposes and no external mechanical or chemical disturbances influence the sample. In the final set-up this central unit is surrounded by the heating element, a copper clasp with built-in heating wires. This in turn is surrounded by rubber tubing through which cooled water (typically at 10°C) is circulated to provide cooling power. Being able to heat quickly does not suffice when controlled temperatures are needed. It is equally important to have significant cooling power so the system can regulate the temperature in both directions.

3.3.2 PID controller

The temperatures of interest lie in between 32°C and 40°C. This is above room temperature and will require heat input to reach and maintain such temperatures. To stabilise accurately the system needs to be able to effectively cool as well as heat the object. Here I use a system which has a constant cooling power (provided by circulating cold water at a constant temperature) but varying heating output. A medium heating setting will cancel the cooling power, a high heating setting will raise the temperature while a low or no heating output will cool the sample. To manage the heating output in a controlled manner the heating element and a temperature sensor are connected to a proportional-integral-derivative (PID) controller. The temperature sensor, a Type K thermocouple, measures the temperature of the sample holder. The PID controller compares this measured temperature to the desired temperature and changes the power output to the heating element accordingly. In practice the sample is constantly heated and cooled in quick iterations. The name PID arises from the control algorithm which consists of proportional, integral and derivative terms:

$$\text{heater output} = P[\mathrm{e} + I\int \mathrm{e}dt + D\frac{d\mathrm{e}}{dt}] \tag{3.4}$$

where e is the error or deviation from the desired temperature defined as e=setpoint - feedback reading [13]. The first term in equation 3.4 is the proportional contribution to the output which will decrease the output as soon as the difference of the feedback temperature to the desired temperature decreases. This always requires some error to give heating and therefore proportional only control will result in unsatisfactory behaviour as plotted in figure 3.11. This is why another term looking at how the error develops over time is added, the integral term. The error is zero when the set point temperature is reached and therefore the proportional term no longer contributes but the integral contribution will lead to a constant output which is necessary to maintain that temperature. When a fast heating rate with a low overshoot is important as it is the case for the experiments here, the derivative term can reduce the overshooting. It reacts to how quickly the feedback temperature is changing resulting in a reduced overshoot and faster reaching of the set point.

Choosing appropriate proportionality constants (P,I,D in equation 3.4) is essential for satisfactory performance and depends delicately on the load, sensor and controller. The process of finding the correct settings is called tuning and there are different manual techniques or for the new Lakeshore 331 controller the auto-tuning works very well. Instructions on how to tune such a system can be found in the manuals of the controllers [67, 13].

3.4 X-ray photon correlation spectroscopy

X-ray photon correlation spectroscopy (XPCS) is based on dynamic light scattering but carried out with x-rays instead of light from the visible spectrum.

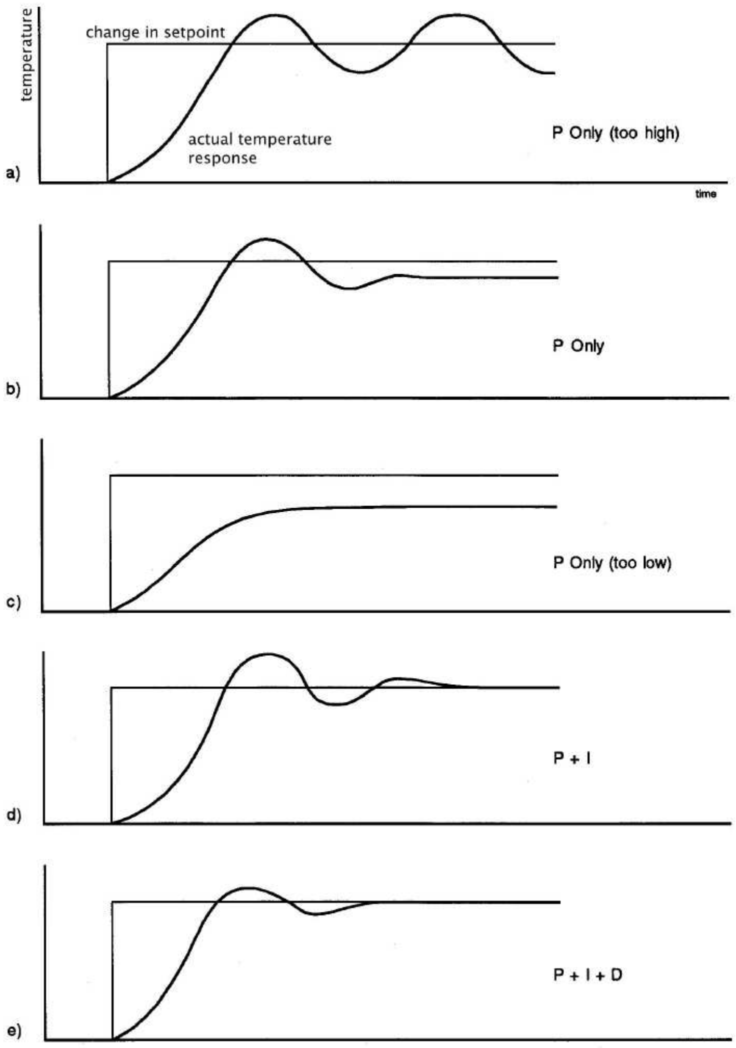

Figure 3.11: Response curves for different contributions of a PID controller. Labels refer to equation 3.4. From [13].

Using x-rays has the pivotal advantage that most materials have a refractive index very close to one. This fact allows opaque emulsion samples to be measured in the single scattering limit which would not be possible for visible light. Diffusive wave spectroscopy (a multiple scattering technique) is also possible with opaque samples although this technique requires more assumptions to be made about the nature of the sample.

This section briefly discusses the relevant key concepts of static and dynamic

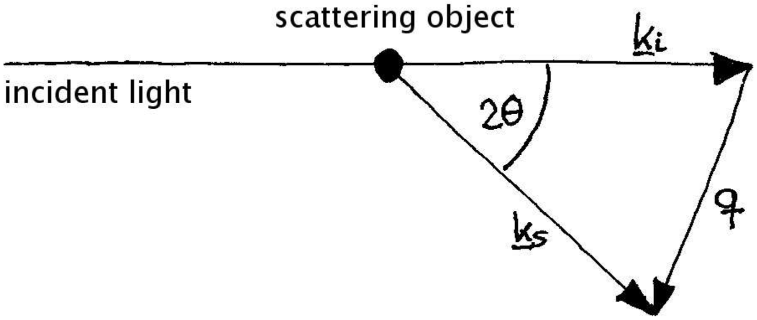

Figure 3.12: A photon initially travelling along $\underline{\mathrm{k}_i}$ will change its direction if it is scattered. The scattering vector q is defined as the difference between $\underline{\mathrm{k}_s}$ and $\underline{\mathrm{k}_i}$.

light scattering for XPCS experiments. To study the dynamics in a particle-stabilised emulsion system small length scales need to be probed and therefore coherent light with a small wavelength is needed. X-rays have such short wavelengths. To carry out XPCS the x-rays need to be coherent. The concept of coherence is explained followed by the experimental realisation of coherent x-ray beams in synchrotrons and the experimental set-up (TROIKA I beamline at the ESRF in Grenoble) used in the experiments in chapter 7 is presented.

3.4.1 Basic light scattering principles

As in conventional light scattering the x-rays pass through the sample and are scattered by the silica particles because these have a higher electron density than the two liquids. While visible light would scatter multiple times in the emulsion samples here, the samples are quite transparent for the x-rays such that only single scattering events take place. This is essential to the technique. This scattering introduces a change in the direction of light propagation. Provided the x-rays are coherent (i.e monochromatic and in phase) the emerging wave fronts will interfere and create a speckle pattern which is characteristic of the sample at that instant. Recording this speckle pattern over a longer time (or averaging over subsequent frames) recovers the average scattering intensity recorded in conventional scattering techniques. In the XPCS experiment here, a

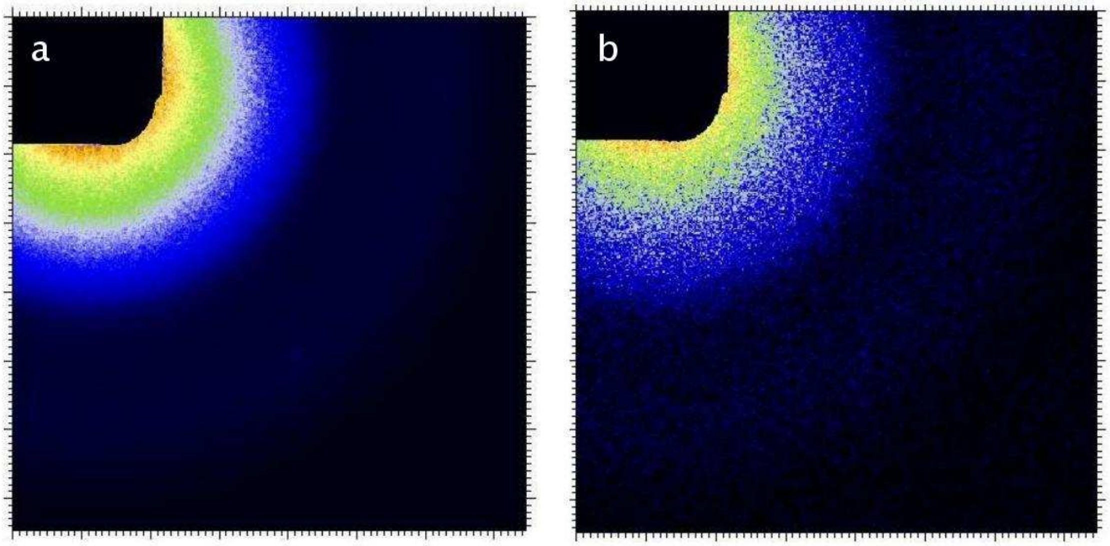

Figure 3.13: The two dimensional scattering pattern obtained from particle stabilised droplet emulsion recorded by the CCD camera. (a) average over 100 frames (b) single frame (exposure 0.7 sec).

2-dimensional detector records the speckle pattern over time.

Figure 3.12 shows how one photon is scattered. The light formerly travelling in the direction of $\underline{\mathrm{k}}_i$ travels in the direction of $\underline{\mathrm{k}}_s$ after the elastic scattering process. The magnitude of the scattering is defined by the scattering vector q, where

$$\underline{q} = \underline{k_s} - \underline{k_i} \tag{3.5}$$

$$|\underline{q}| = 4\pi n \frac{sin\theta}{\lambda}. \tag{3.6}$$

Provided the light is coherent (see next section) the superposition of many such scattering events produces a two-dimensional speckle pattern which depends on the shape of the individual scattering elements (the silica particles) and how these are arranged within the sample (forming shells around the droplets). Such a two-dimensional pattern is shown in figure 3.13a. The measured intensity varies with

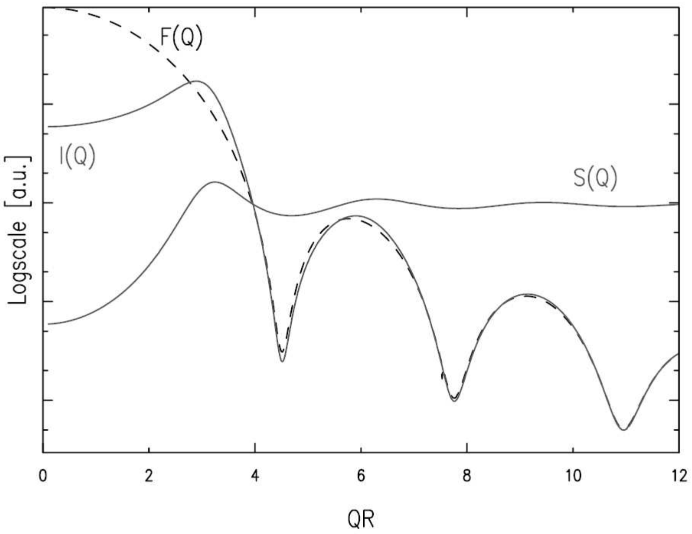

Figure 3.14: Typical scattering intensity of a dispersion of interacting spheres. The structure factor describes the arrangement of the particles while the form factor describes the shape of the particles. The intensity in arbitrary units is plotted agains the product of wave vector q and particle radius r. From [14].

the scattering vector q and can be expressed as

$$I(q) \propto F(q)S(q). \tag{3.7}$$

The form factor F(q) describes the shape of the individual particles and the structure factor S(q) their arrangement in the sample. Figure 3.14 shows the contribution of each to the observed intensity for an assembly of interacting spheres in a colloidal suspension. This figure shows that for large q the dominant contribution is the form factor. The structure factor for scattering shells (particle stabilised emulsion droplets) is proportional to q^{-2} for small q [68] but for the large droplets this is found at much smaller q than measured here and is therefore not observed.

Using Bragg's Law of diffraction $\frac{\lambda}{n} = 2\ d\ \sin(\theta)$ gives the useful expression

$$d = \frac{2\pi}{q} \tag{3.8}$$

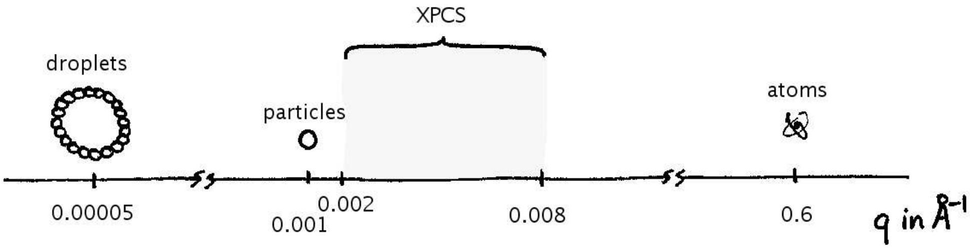

Figure 3.15: Length scales probed in the XPCS experiment on emulsion droplets stabilised with silica particles. The particles are half a micron in diameter while the droplets range between 10 to 15 μm.

where d can be viewed as the length scale probed by the scattering vector q. Figure 3.15 shows the length scale probed in this experiment in relation to atomic, stabilising particle and emulsion droplet size.

3.4.2 Dynamic light scattering

The speckle pattern obtained when the x-rays are scattered from the sample fluctuate over time. Since the speckles arise from the scatterers in the sample the fluctuations of the speckles are directly related to the motion of the scatterers. By analysing the intensity fluctuations at each pixel it is possible to infer the motion of the particles. This technique is called x-ray photon correlation spectroscopy (XPCS).

Figure 3.13b shows that for short exposure times the scattering pattern recorded during an XPCS experiment consists of individual speckles. These speckles move over time and when averaged build up the pattern seen in figure 3.13a. To analyse the motion of the speckles and therefore the motion of the scatterers the intensity at a single pixel is observed as shown in figure 3.16. It is possible to quantify these fluctuations by correlating this function with itself which evaluates how similar the signal is to the original intensity value after a certain delay time τ. Analysing the way the intensity decorrelates over time allows a quantitative analysis of the dynamics occurring within the sample to be carried out. This can be done by calculating the normalised correlation function

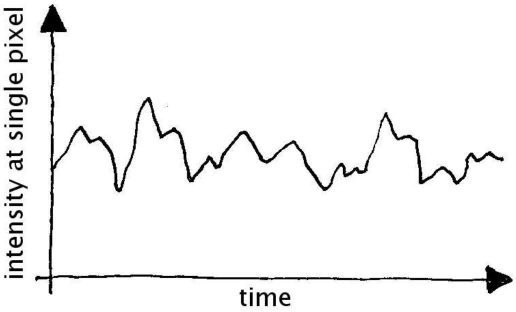

Figure 3.16: Intensity fluctuations over time at a single pixel of recorded CCD images.

g_2-1 from the observed intensity.

$$g_2 - 1 = \frac{\langle I(\mathbf{q},0)I(\mathbf{q},\tau)\rangle}{\langle I(\mathbf{q})\rangle^2} \tag{3.9}$$

where $\langle ... \rangle$ denotes an ensemble average which is the average of the intensity over many different realisations of the system and I($\mathbf{q}$,t) is the measured intensity at time t. In XPCS this concept is used after having obtained a time series of scattering patterns produced by x-rays scattered from the examined sample.

3.4.3 Time resolved correlation

Many soft glassy materials comparable to the particle stabilised emulsions here have been found to change their dynamics with age and to exhibit heterogeneous dynamics. It is therefore desirable to examine the evolution of the correlation function over time to establish if such ageing and heterogeneity is present. To do so, c_I(t,τ) is calculated for a set of fixed delay times τ at a fixed wavevector q.

$$c_I(t,\tau) = \frac{\langle I_p(t)I_p(t,\tau)\rangle_p}{\langle I_p(t)\rangle_p \langle I_p(t,\tau)\rangle_p}. \tag{3.10}$$

I_p denotes the intensity at pixel p and τ is the delay time between the two signals while $\langle ... \rangle_p$ denotes the average over all pixels of the selected area of the CCD image. Figure 3.17 shows the different information we can obtain from this

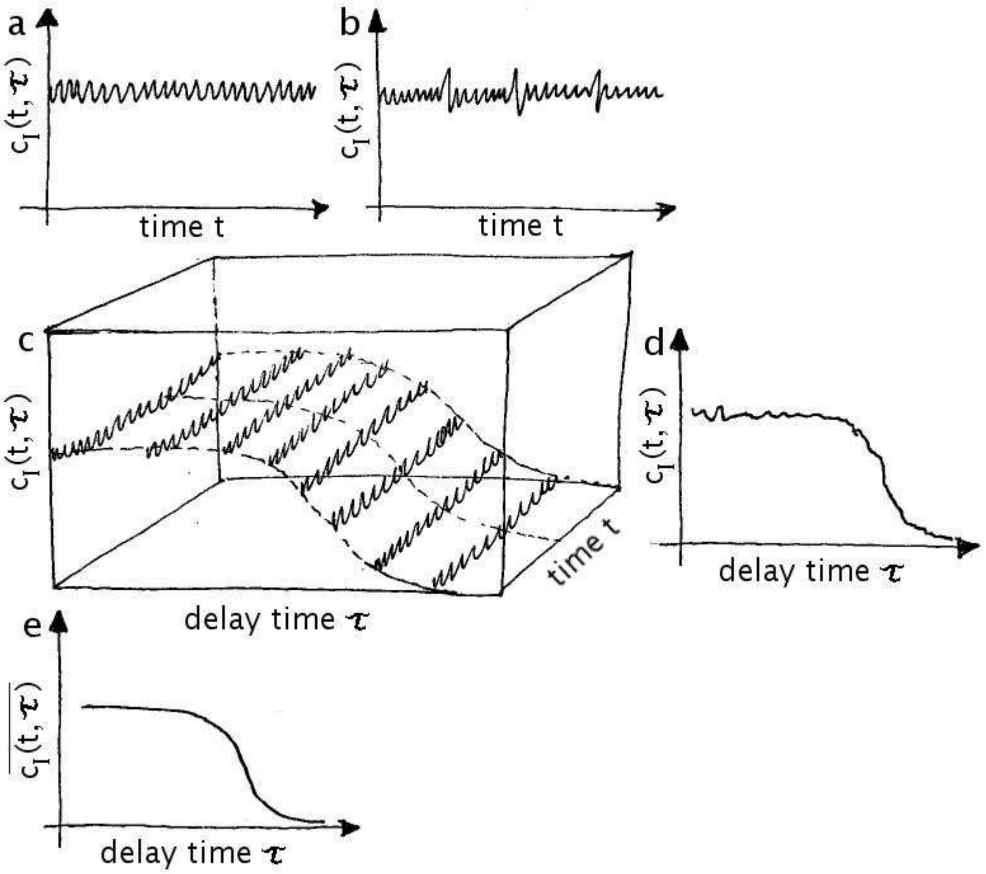

Figure 3.17: The time resolved correlation function c_I(t,τ) is plotted in various ways. (a) shows homogeneous signal at fixed τ, (b) shows heterogeneous signal at fixed τ, (c) behaviour of c_I(t,τ) with time t (=age) and delay time τ, (d) correlation function for single frame (fixed t), (e) correlation function averaged over time (region of t) equivalent to g_2-1.

quantity. Figure 3.17a shows c_I(t,τ) for a small, fixed τ plotted against time with homogeneous dynamics as would be expected for example when examining a colloidal suspension where the particles are moving under Brownian motion and are slowly diffusing through the system. In contrast figure 3.17b shows a sample with heterogeneous dynamics which has random spikes and troughs. Spikes indicating a slowing of the dynamics and troughs a speeding up. If several c_I(t,τ) functions are calculated for different delay times τ the central figure can be produced (figure 3.17c) and figure 3.17d can be extracted for any time t so that the correlation can be viewed with respect to the delay time τ showing for which characteristic time τ_c the system loses its correlation. Averaging over a range of times t_1 to t_2 will then produce figure 3.17e which is basically g_2-1 as shown in equation 3.9.

$$g_2(q,\tau) - 1 = \overline{c_I(t,\tau)} \tag{3.11}$$

where $\overline{(\ldots)}$ implies an average over time. The advantage of examining c_I(t,τ) instead of the time averaged quantity g_2-1 is that it is possible to see changes over time easily and to distinguish between heterogeneous and homogeneous dynamics.

3.4.4 Synchrotron radiation

To obtain a speckle pattern when attempting to carry out photon correlation spectroscopy a longitudinally and spatially coherent light source is needed. While this has been achieved for visible light with lasers it is much more difficult for x-rays since appropriate filtering in wavelength and phase to make the beam coherent will always decrease its intensity. However, partial coherence can be sufficient and combined with a high enough brilliance x-ray beams can be used to obtain a speckle pattern of the sample. High brilliance beams can be produced in third generation synchrotrons such as at the ESRF in Grenoble, France. The underlying principle is that any accelerating charge must radiate electromagnetic energy. If electrons are accelerated to high velocities they will radiate high energy radiation, the x-rays. In this way a discrete spectrum of intense synchrotron radiation is is produced. In the third generation synchrotrons the efficiency of producing x-rays was improved drastically by using undulators. This leads to a much higher beam intensity and beam stability. In third generation synchrotrons the electrons are accelerated to velocities near the speed of light before entering an undulator. The undulator consists of a periodic magnetic structure producing a sinusoidal magnetic field along the electron path. In the frame of reference of the electron which has a velocity close to light this magnetic field looks like a plane wave. The magnetic field of these plane waves force the electrons to

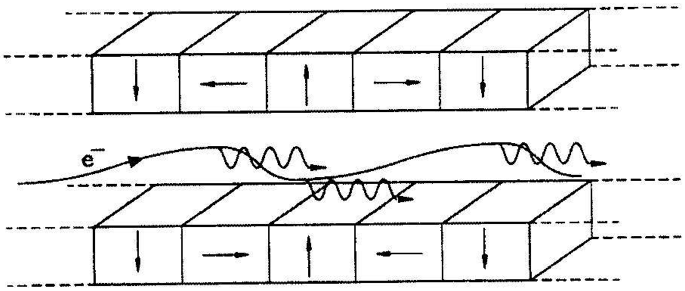

Figure 3.18: Diagrammatic representation of a multipole undulator from [15]. The sinusoidal magnetic field forces the fast electrons to oscillate which emit x-rays as a result of being accelerated.

oscillate. This in turn leads to radiation being produced which are the desired x-rays. This mechanism is illustrated in figure 3.18.

3.4.5 X-ray coherence

In synchrotrons x-rays are created at many different instances in space and time and the beam available at the experiment is a superposition of many different, individual waves with a spread of wavelengths and phases. For XPCS experiments coherent x-rays are needed. This implies the x-rays need to be monochromatic and in phase with each other. The term coherence describes how close the superposition of waves resembles a single wave.

If x-rays all have the same wavelength and in phase they are called longitudinally (=temporally) coherent, while if they are all in phase across the beam they are spatially (=transversely) coherent (see figure 3.19). An undulator produces x-rays with a wavelength that depends on a mechanical parameter called the undulator gap. The spread around this wavelength is too broad for XPCS without further conditioning. Filtering in wavelength and phase can pick out an appropriate subset of the x-rays which are coherent. Of course the higher the coherence obtained in this way, the more rigorous filtering is needed and the smaller the fraction of the remaining x-rays. However, partial coherence can be sufficient and combined with a high enough brilliance from 3rd generation

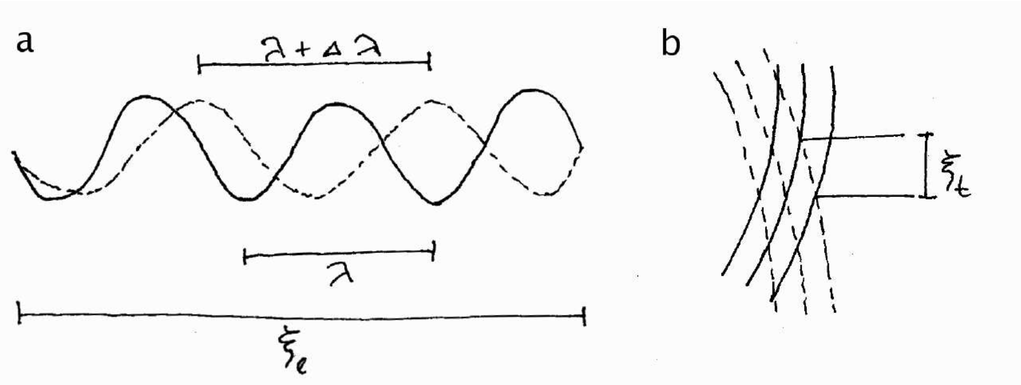

Figure 3.19: (a) The longitudinal coherence length is the distance over which the phases of the different light waves do not differ by more than π. (b) The transverse coherence length is the length over which the light is not more than π out of phase.

synchrotron sources can be used to obtain a speckle pattern of the sample.

The longitudinal coherence length ζ_l describes the temporal coherence of the x-ray beam and is the distance over which the beam can be assumed to be more or less monochromatic:

$$\zeta_l = \frac{\lambda}{2}(\frac{\lambda}{\Delta\lambda}). \tag{3.12}$$

where $\frac{\Delta\lambda}{\lambda}$ is the monochromaticity of the beam which is 1×10^{-4} for the Si(111) monochromator used at the Troïka beamline at the ESRF [69]. The spatial coherence ζ_s depends on the wavelength λ and the angular source size $\Delta\Theta = \frac{s}{R}$, where s is the source size (or if the beam is collimated the pinhole size) and R, the distance between source (or pinhole) and sample.

$$\zeta_s \approx \frac{1}{2}\frac{\lambda}{\Delta\Theta} = \frac{\lambda}{2}\frac{R}{s} \tag{3.13}$$

At the TROIKA I beamline (ID10A) at the ESRF in Grenoble we used λ=1.5$\mathring{A}$ and R=46m with a pinhole having dimensions 10×10 μm. Hence ζ_s is 0.75 μm. In an optimal XPCS set-up the sample should be illuminated coherently. This is the case if the maximum path length difference (PLD) for all x-rays passing through the sample is smaller than or equal to the longitudinal coherence length and if at the same time the lateral illumination width (LIW) of the sample is smaller than or equal to the spatial coherence:

$$PLD \leq \zeta_l \qquad \text{and} \qquad LIW \leq \zeta_s. \tag{3.14}$$

The path length difference (PLD) can be approximated by [70]:

$$PLD \approx 2Tsin^2(\theta) + LIWsin(2\theta) \tag{3.15}$$

where θ is the scattering angle (Q=$(4\pi/\lambda)$sin(θ)), T is the thickness or width of the sample while LIW $\leq \zeta_s$ is the beam size illuminating the sample. The diameter of the capillaries containing the sample implies T=1.5 mm and the pinhole determines the illuminated sample dimensions so that LIW=10 μm. A PLD for the largest q wavevectors used in this experiment is only about 30 nm. In the set-up used here the ζ_l and ζ_s are 345 μm and 0.75 μm respectively. Whereas the PLD which lies well below the required ζ_l=750 nm indicating that the sample is coherently illuminated under the experimental conditions. However, LIW $> \zeta_s$ and this will degrade the speckle contrast in our experiments.

The angular speckle size can be determined by [70]:

$$D_s = [(\frac{\lambda}{LIW})^2 + (\Delta\Theta)^2]^{1/2} \tag{3.16}$$

where $\Delta\Theta$ is the angular source size $\frac{s}{R}$ as given above for equation 3.13. With a sample-detector distance of 233cm this leads to an actual speckle size on the detector of 35 μm which is larger than the detector pixel size of 20 ×20 μm. Hence there will be one or fewer speckles per pixel.

3.4.6 Experimental set-up and procedure

The experimental XPCS set-up used in the experiments in chapter 7 is located at the ESRF, Grenoble in France on the Troïka beamline. Figure 3.20 shows a

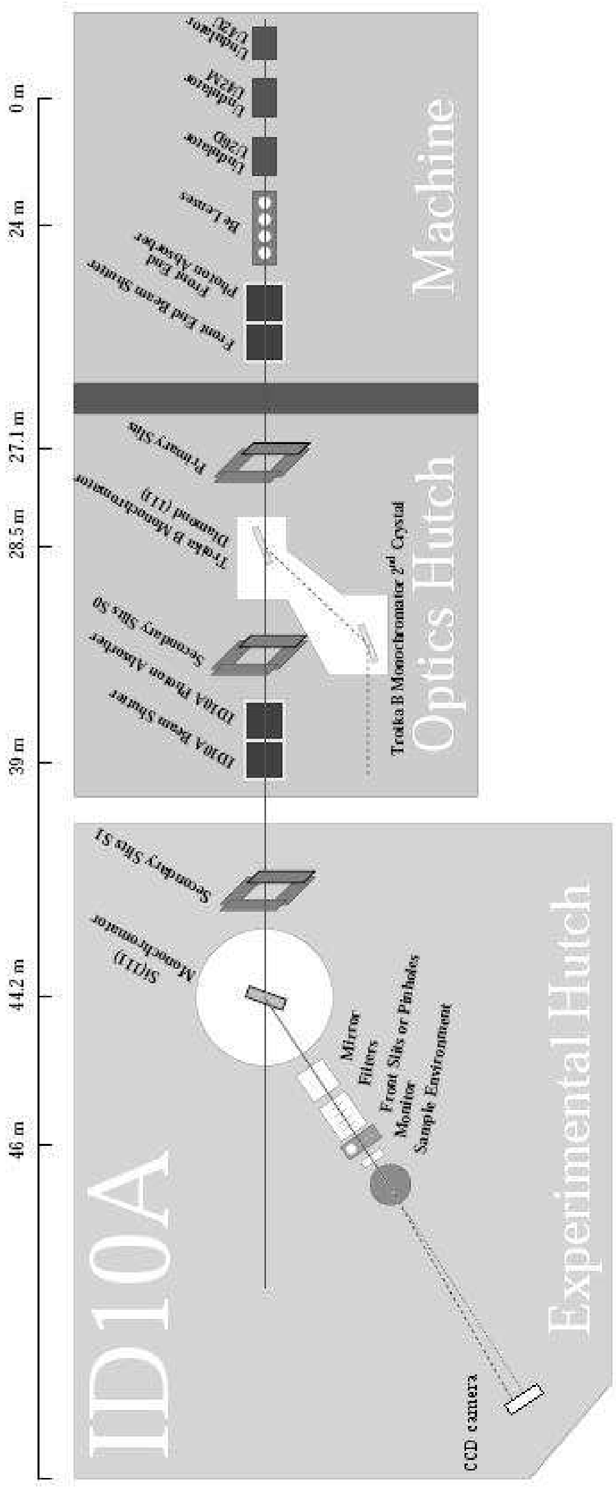

Figure 3.20: The x-rays are produced in the undulators. Various selection mechanism ensure that partially coherent x-rays are present in the experimental Hutch where the sample is mounted in the beam path. The scattering pattern is recorded with a CCD camera.

schematic layout of the beamline.

At the beamline we worked with instrument scientist Aymeric Robert who adjusted the set-up to yield good speckle contrast for our samples. For the experiments here the selected x-ray energy was 7.979 keV and with a pin hole of 10×10 μm the photon count was at 10^{10} photons/sec. Once the sample is mounted the beam and sample position as well as various shields needs to be optimised. Then the exposure time for recording the scattering images can be established. After this the principal experimental challenges concern preparing and studying samples with heterogeneous dynamics. For analysis purposes the beam centre is recorded and a series of dark images. The latter are collected when the beam is blocked in an effort to establish the background activity of the CCD camera.

Chapter 4

Bijel formation and properties

In the following chapter I will examine in detail the formation and properties of bijels. In the introduction I will present the computer simulations motivating this work and the current understanding of colloids at liquid-liquid interfaces. Then I present spinodal decomposition in the presence of particles after which I examine the three-dimensional structure as well as its behaviour over time, followed by the influence of parameters such as quench rate, volume fraction and liquid composition.

4.1 Introduction

Stratford et al [71] have presented computer simulations postulating the feasibility of an intriguing new material they call bijel (**bi**continuous **i**nterfacially **j**ammed **e**mulsion ge**l**). They simulate an instantaneous quench into the demixing region of a symmetric binary liquid in the presence of neutrally wetting particles. They observe that the particles sequester to the interfaces created during spinodal decomposition and eventually slow down the coarsening process. As the domains coarsen the particles jam into each other on the interfaces. This results in a bicontinuous material where two low molecular-weight phases are kept in a convoluted arrangement within the matrix formed by the interfacially jammed particles. The stability arises from the fact that neutrally wetting particles are exceptionally strongly and therefore irreversibly trapped to the liquid-liquid interfaces [2]. However, the computer simulations access only very short time scales that are less than 1 μsec in the laboratory time frame and therefore it is not possible to determine whether the structure fully arrests although a drastic slowing down of domain size growth is observed. The authors suggest that slow rearrangements between the particles or the expulsion of particles could be responsible for not reaching a steady plateau at this time. To support their claim that this structure will arrest out-of-equilibrium they examined smaller, typical subsets of the structure over a longer period of time. This way they could show that the presence of the interfacially trapped and jammed particles increases the life time of bumps and necks at least ten-fold compared to their finite life time when no particles are present. The particles trapped and jammed on the liquid-liquid interfaces seem to be able to prevent liquid necks from undergoing Plateau-Rayleigh instabilities (see section 2.1) if they are coated with an interfacial layer of particles. In experiments this stability has been shown for much longer time scales by the longevity of non-spherical droplets [45] or bubbles [52, 3] and extended structures [53, 72] (see also chapter 5). The ability to sustain the anisotropic stresses which are present in systems with varying mean curvature is due to the fact that such particle-laden interfaces acquire solid-like properties [48, 50, 51, 45, 3]. Composto et al [73, 74, 22] have shown that for thin films particles can halt the coarsening process when polymers phase separate via spinodal decomposition.

I will use low molecular-weight binary liquids and silica particles to produce a three-dimensional sample of the postulated bijel. Before this can be achieved different issues have to be addressed. Firstly it is important to have the binary liquid undergoing phase separation via spinodal decomposition. The approach in this chapter is to quench the system through the critical point because this is the only point in the phase diagram where the miscible region meets the spinodal demixing regime without a nucleation region intervening (see section 2.3). Next it is necessary that the particles are trapped at the interfaces. This can either happen during spinodal decomposition while the interfaces are still diffuse or at a later stage when sharp interfaces have already formed and the particles are picked up by moving interfaces. The latter process has been extensively studied in the context of froth flotation [41]. Clegg et al [45] have shown that during nucleation, where the interfaces are sharply defined at all times, particles with appropriate wetting properties successfully sequester to the interface. In the following chapter I will show in detail how bijels are formed using temperature quenches through the critical point and which parameters can be used to tune the resulting structure.

That similar composites have benefits in every day life is shown by Si et al [75] who use clay in polymer mixtures to increase the miscibility of the polymers on a macroscale. They have successfully demonstrated that this overcomes the stability issues of recycled polymers and can be used on impure systems typically obtained during recycling.

4.2 Experimental system

To study bijel formation I use a binary-liquid at critical composition because quenching through the critical point directly accesses spinodal decomposition. The binary liquid system has a lower critical solution temperature (LCST) such that heating induces phase separation. The particles used to stabilise the liquid-liquid interfaces are monodisperse, hard spheres tagged with a fluorophore to improve observation by confocal microscopy.

Liquids and particles

The binary liquid system used here is 2,6-lutidine and water (lut/w) with a LCST at atmospheric pressure of 34.1°C and a critical lutidine mole fraction of x_l=0.064 [21, 76]. To induce phase separation the lut/w system needs to

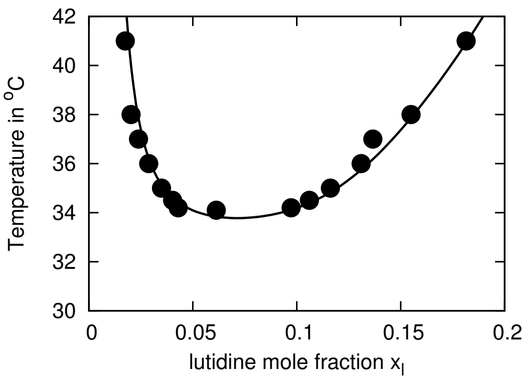

Figure 4.1: 2,6-lutidine-water phase diagram from [16]. The system is miscible below the solid curve and separates into 2 phases inside the solid curve.

be heated as shown in figure 4.1. The interfacial tension grows from zero on quenching through the critical point. At 40° the two phases have an interfacial tension of 0.22 mN/m [16] between each other and a volume ratio of 38.9:61.1 which will result in sufficiently symmetric quenches. The 2,6-lutidine used here is from Sigma Aldrich, $\geq$ 99%, used as received, while the water is purified using a MilliQ system (18MΩ).

Using dried, fluorescently tagged silica particles can form stable emulsions without the need of further surface modifications. The fluorescent dye is fluorescein isothyocyanate (FITC) which excites at 488 nm and emits at 512 nm, ideal for microscopy studies using an Ar-ion laser. Since the fluorophore is also present at the surface of the particles it influences the surface chemistry of the silica which no longer consists purely of silanol-groups. During the course of the lut/w experiments there are indications that the wetting properties of these particles depend on the surface bound water. Studies on examining this behaviour with the ultimate aim to control the wetting properties systematically are currently carried out by Kathryn White. The particles were prepared by Andrew Schofield using the Stöber technique [60, 61] with this particular batch number being Assi16 and have a radius of 200 nm ±10 nm.

Sample preparation

An ultrasound (Sonics & Materials) probe is used to disperse the particles in the miscible liquid. During the mixing with the ultrasound probe acoustic cavitation is exploited. Under the influence of acoustic waves bubbles form, grow and rapidly implode. This induces shock waves which disperse the particles. However, the rapid implosions also lead to very high, localised temperatures so that the sample heats up [77]. The lut/w system demixes upon heating. Even if the mixing is carried out in short bursts such that the overall sample temperature stays below the LCST of the system, the increase of the local temperature near the tip of the sample will still rise into the demixing region. Therefore the particles cannot be dispersed using ultrasound in the lut/w mixture. Instead the particles are first dispersed in the water only. After a homogeneous, aqueous suspension has formed and has cooled back down to room temperature (or lower temperatures when working with high volume fractions of particles) the appropriate amount of lutidine is added. Mechanical shaking of the sample is then sufficient to create a miscible lut/w-particle suspension. Because I wish to work as close to the critical point as possible it is important to measure the quantities of the liquids carefully. I do this by first weighing the particles (ρ_{silica}=2.2g/cm^3) [1], then adding 0.694 ml water which will eventually result in 1 ml of solution. I use an electronic pipette, but its volume accuracy and reproducibility is not high enough for this work here. Therefore, I also weigh the water. After the sonication process I then add the amount of lutidine that is needed for the given water mass to create a critical composition of 0.064 lutidine mole fraction. This way only the lutidine needs to be added very accurately. Again, I use the electronic pipette but measuring less than the required amount. Then slowly more lutidine is added drop by drop with a glass pipette while weighing the sample until the composition is as close as possible to the critical one. If too much lutidine is added it is possible

---

[1] Fused silica has a density of 2.2 g/cm^3. This value has been used throughout this project for silica density. However, Stöber silica actually has a density of 2.03 g/cm^3 [61].

to re-calculate the required amount of water and add the difference. This way the accuracy of the volume fraction is reduced but can be easily re-calculated. Additionally, a small change in the liquid-liquid composition will have a more significant effect on the experimental result than a minor change in the volume fraction of the particles. My observations show that lutidine mole fractions in the range from at least 0.0611 to 0.0660 ± 0.0001 (x_c=0.064) produce spinodal demixing as the first separation process.

The lutidine is a very pungent and not very healthy chemical. It is therefore necessary to work in the fume hood when preparing the sample and to wear nitrile gloves. Because the work on the microscope cannot be carried out in a fume hood it is important to seal the sample very tightly for the sake of the experimenter's health and that of any people working in the vicinity. At the same time lutidine is very aggressive towards many materials like rubbers, plastics and glues as discussed in section 6.2.1. Glass and teflon are some of the few materials I found to resist reliably. I therefore choose rectangular glass cuvettes as sample holders sealed with a teflon stopper (Optiglass) which are usually used in spectrophotometry experiments. These cuvettes have a path length of 1 mm and a window thickness of 1.25 mm. This is very thick for microscopy purposes but on the other hand the glass walls are polished to less than 4 Newton fringes per centimetre and have a varying thickness throughout of less than 1 μm. Provided an objective is used that can handle extra thick coverslips (such as the ELWD × 20 objective discussed in section 6.2.1) and no particle resolution is required then the optical imaging conditions for such a cuvette are better than for the small capillaries used for the eth/dod and meth/hex systems discussed in chapter 5. Using the rectangular spectrophotometry cuvettes seals the samples securely while obtaining satisfactory imaging conditions but at the cost of a low heat conductivity of the surrounding glass (1.1 W/mK). Once the sample is prepared it should be kept at low enough temperatures to avoid aggregation due to pre-transitional wetting[2] or even a premature phase separation. Room temperature is sufficiently low apart for volume fractions higher than 3%. The quench should occur soon after filling the cuvette to avoid unnecessary sedimentation of the particles. If the particles sediment while other preparations are carried out then mechanical shaking of the sample can restore the suspension.

Quenching method

To quench the sample it is filled into a glass cuvette and then inserted into a heating block which is described in section 3.3.1. Uneven heating will induce convection inside the cuvette where the warmer liquid rises under gravity. This leads to turbulent flow within the sample that greatly interferes with structure formation and should therefore be avoided. The heating block used here for the critical temperature quenches is designed in such a way that it almost fully surrounds the sample leading to very uniform temperature conditions reducing unnecessary convection inside the sample and allows at the same time the observation of the sample under the microscope before, during and after the quench.

Initially, the temperature was controlled by a Honeywell UDC 3000 Universal Digital Controller which resulted in insufficient control over temperature stability and in overshooting. However, replacing it with a new PID controller (Lakeshore 331) meant very accurate heating rates and stability can be achieved with negligible overshooting. I use a range of heating rates between 0.1°C/min up to 17°C/min, where the latter quench rate is not driven by the temperature controller. For this highest rate the aluminium block is maintained at 40°C and the room temperate cuvette is quickly inserted into the block. The working of the temperature controller is explained in more detail in section 3.3.2.

---

[2] Near the phase boundary a layer of one of the liquids can form on the surface of the particles although the system is still in the one-phase region [18]. This leads to the aggregation of particles and is explained in section 5.1 in more detail.

4.3 Spinodal decomposition in the presence of particles

The first essential step for bijel formation is the creation of interfaces in a convoluted, bicontinuous arrangement. Here this is achieved by letting a binary liquid undergo phase separation by spinodal decomposition which is a demixing process that creates domains with the desired morphology.

Aim and context

The initial question I need to address is whether the lut/w system can be quenched in such a way that it demixes via spinodal decomposition. At the critical point the barrier for nucleation vanishes and the spinodal decomposition regime can be directly accessed when crossing the binodal (see section 2.3.2). Therefore I will use a sample close to the critical composition and heat it into the demixing region. The critical point is associated with critical slowing down (see section 2.3.2) and it remains to be seen whether this effect is helpful in bijel creation or not. More importantly I need to establish whether the presence of the particles influences the phase-separation process. Beysens claims that small amounts of particles ($\Phi_v \sim 0.1\%$) do not alter the shape of the phase diagram significantly [78], however, experiments by [79] and Narayanan [80] observe a lowering of the phase boundary when larger amounts of particles are added ($\Phi_v \sim 1\%$). Jayalakshmi et al [79] interpret this as an indication that the phase diagram is determined by all three components. Contrary to this argument Narayanan et al [80] point out that the shift in temperature might be due to impurities being released by the particles and the system is still described by a binary phase diagram and inspite of any shift in temperature should still show the usual spinodal demixing. However, Tanaka has found that the separation process can be significantly influenced by capillary effects if the sample holders are very thin [81] and that the wetting of spatialy fixed particles can also have influence on the demixing morphology [82, 83]. In the phase separation of polymers where the separation process is much easier observed due to the much slower time development there is evidence that the coarsening mechanism is not altered by the presence of particles apart from a slowing down due to the increased viscosity of the particle containing phase [73]. Unless the particles segregate at the interfaces in which case the particles can stop the coarsening process on the observerd time scale (120 h) [74, 22].

Once the interfaces are created with the desired morphology it is then necessary for the particles to be successfully trapped at these interfaces. For liquids phase separating via spinodal decomposition the interfacial tension is initially very small and Gallagher and Maher [43] found that only above a wetting temperature T_w which is a few mK higher than the critical temperature T_c the particles were trapped at the interfaces. This is likely to be due to the low interfacial tension close to the phase boundary. Since the sample will be quenched through the critical point with rates of ~ 1 °C/min it will only spend a limited time that close to the critical temperature. The successful trapping of the particles will strongly depend on their wetting properties [2] but can be prevented if other mechanisms dominate. Should particles be joining an already well formed interface instead of segregating onto still diffuse interfaces during the separation process then other issues need to be considered. Upon approach or collision of particles with sharp interfaces the liquid film separating a particle and the interface first has to thin and eventually rapture before the particle can then attach to the interface. This process is thoroughly studied in the context of froth flotation and a review is given in [41].

Sample and method

I aim to compare a very small and shallow quench with a deep and faster quench through the critical point into the demixing region of the lut/w system. I examine how the phase separation is modified by the presence of the particles. Firstly, a critical 2,6-lutidine-water mixture containing 2% volume fraction of FITC doped silica particles is heated quasistatically through the critical point (T_c=34.1°C) by increasing the temperature by 0.5°C at a time, waiting a few minutes to let the temperature inside the cuvette equilibriate, then repeating this until the separation occurs. Secondly, a different sample with the same specifications is rapidly quenched to 40°C at a rate of 17°C/min. The quenches were carried out using the aluminium heating block in conjunction with the Honeywell controller. The separation processes are observed using fluorescence confocal microscopy focused just inside the cuvette. The slow quench is imaged at a rate of 0.7 sec per image while the fast quench was recorded at 1.44 seconds per image. Each image is rastered from top to bottom. A new frame begins every 0.7 (or 1.44) seconds but time also progresses during the scanning of each frame. The particles appear white while the liquids appear dark in these images.

Results and discussion

Figure 4.2 shows the quasi-static quench while figure 4.3 shows the faster temperature ramp. From these images it is qualitatively evident that the system directly undergoes spinodal decomposition. The initial stages of the spinodal decomposition are not resolved and it is not possible to determine the role of the particles in the early stages [83]. The dominant pattern at mid to late stages, however, has spinodal characteristics: the typical cross-sectional pattern and the self-similar coarsening process are clearly observable. Later when using higher volume fractions up to 4% I observe a significant lowering of the separation temperature in accordance with references [79, 80]. My microscopy images show clearly that in all samples spinodal decomposition is the initial separation mechanism independent of the volume fraction. For the time scales where imaging is possible this suggests that the spinodal demixing is still the dominant process although particles are present. The spinodal pattern in my experiments confirms that the particles do not hinder spinodal decomposition to occur in this low viscosity system which could be possible if for example the particles induced

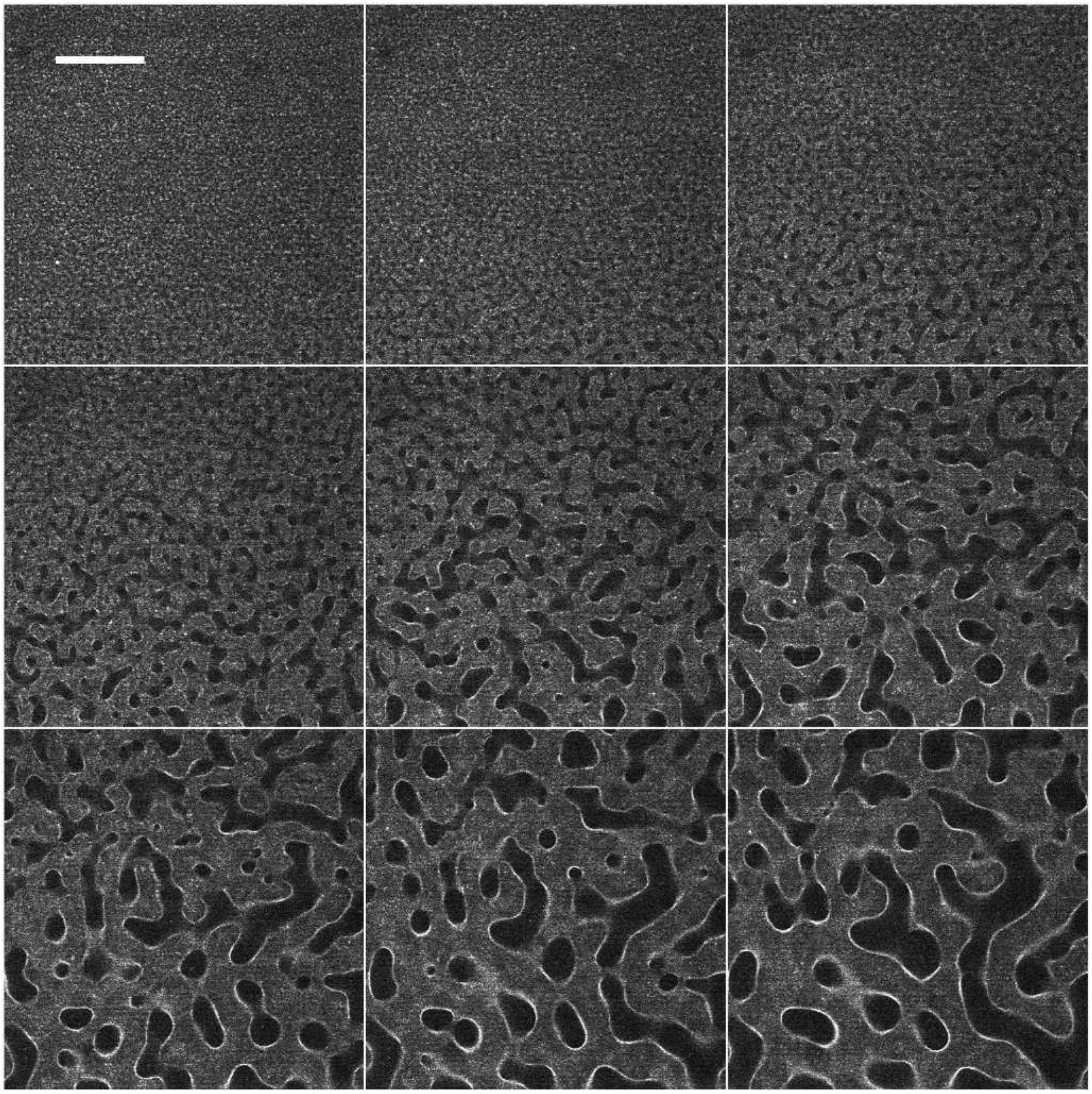

Figure 4.2: Time series of fluorescence confocal microscopy images of a 2,6-lutidine-water sample at critical composition with Φ_v=2% particles, slowly quenched from 33.5°C to 35.3°C. Only images around the separation are shown. Δt between images is 0.7 seconds. Particles appear white while liquids appear dark, scale bar 100 μm, time progresses from left to right for each subsequent row. The separation via spinodal decomposition is clearly visible.

strong heterogeneous nucleation. The microscopy images do not have a high enough time resolution to obtain a quantitative analysis of domain size with time.

While the presence of the particles do not influence the kinetics of demixing,

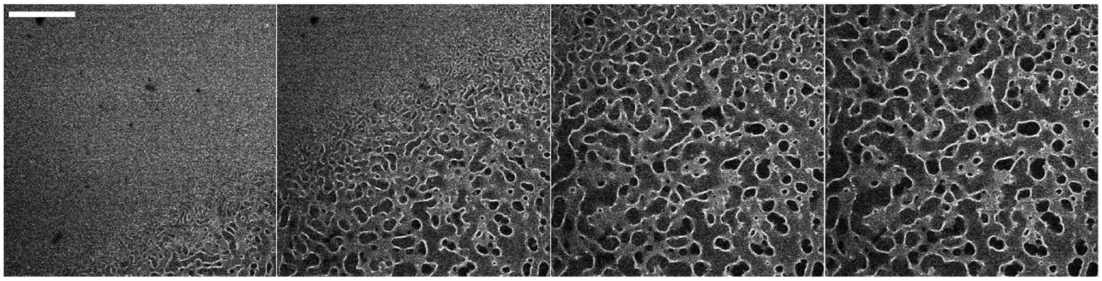

Figure 4.3: Fluorescence confocal images, taken Δt=1.44 sec apart, on a critical lut/w system containing 2% FITC doped silica particles heated with 17°C/min. The particles appear white, the liquids dark. Scale bar 100μm.

they do hinder the coarsening process if they sequester to the interfaces such that further phase-separation is halted. The interfaces are seen to grow bright during the course of the separation process indicating an increasing density of colloids which are being swept up by the interfaces. This is particularly well resolved in the quasi-static quench. For this slow quench the interfaces move slowly but have a very low interfacial tension because the temperature is only a few tenths of degrees above the critical temperature. Despite the low interfacial tension the particles are trapped which is in agreement with Gallagher and Maher's [43] observation because the temperature is at least several 100 mK higher than the critical temperature. For the fast quench the interfaces move faster but at the same time also develop a much higher interfacial tension (0.22 mN/m at 40°C compared to 0.017 at 34.5°C [16]). Nevertheless the particles are still sequestering to the interfaces indicating that even at this higher speed of the interfaces the reduction in the free energy is stronger than the inertial effects proposed by West et al [42] for related systems. It is possible to estimate a force related to the trapping potential well given by equation 2.2. For neutral wetting particles (θ_{ow}=90°) this reduces to G=πr$^2\gamma$ [2].

$$\begin{aligned} F &= \frac{\Delta G}{\Delta x} \\ &\sim \frac{\pi r^2 \gamma}{x} \\ &\sim \pi r \gamma \end{aligned} \tag{4.1}$$

When the particle has moved by x = r (its radius) then G=0. The particle radius is 200 nm so that the involved forces holding each particle on the interfaces are between 10 pN and 100 pN for 34.5°C and 40°C respectively which is very large. For comparison the particle trapping forces here are about 10 to 100 times larger than the pico newton forces used in optical tweezers.

The slow and fast quenches show that for all quench rates ranging from very slow up to 17°C/min the dominating trapping mechanism is that of the reduction in interfacial area which is strong enough to neglect other influences. This observation is also true for polymer systems where particles also segregate at interfaces [74, 22] and consequently slow down the coarsening mechanism. Because the particles are clearly seen to trap at the interfaces here, an upper bound on the line tension τ can be estimated. The line tension is the one-dimensional analogue of surface tension γ and can create a barrier to particle adsorption. It arises as a result of the excess free energy associated with the formation of a 3-phase contact line and can be either positive or negative contrary to the surface tension which is always positive. Positive line tension can form an energy barrier to adsorption because it is most dominant where the circumference to area ratio of the displaced interface is large which is the case when the particle initially adsorbs onto the interface. :

$$\begin{aligned} \Delta G_{line} &\lesssim \Delta G_{surface} \\ 2\pi r\tau &\lesssim \pi r^2\gamma \\ \tau &\lesssim 0.5r\gamma \sim 1\times10^{-12} - 1\times10^{-11}\ [N] \end{aligned} \tag{4.2}$$

for interfacial tensions between lut/w ranging from 0.017 mN/m (34.5°C) to 0.22 mN/m (40°C) and maximum radius of 200 nm. As expected these values are smaller than the respective trapping forces shown before (equation 4.1) and are on the lower side of expected line tensions for low molecular weight binary liquids [28].

	interfacial tension (mN/m)	viscosity (Pa·s)
polymer system	≤ 0.9	4×10^3
lut/w system	≤ 0.22	2×10^{-3}

Table 4.1: Comparison of interfacial tension and viscosity of polymer systems examined by Chung et al [22] and the lut/w system [16] used here.

In both figures (figures 4.2 and 4.3) it is apparent that the presence of the particles successfully slows down the coarsening process. This confirms the computer simulations [71]. Although the particles prefer one of the liquids which appears greyer than the other phase in the confocal images, the reduction in the coarsening rate is due to the interfacially trapped particles. I found that quenching the system with the same volume fraction of inappropriately wetting particles does not halt the coarsening process. This is contrary to polymer systems where the coarsening can be slowed by either the particles being in one of the phase [73] or on the interface [74, 22] due to the already extremely high viscosity of the polymers.

So far I have shown several parallels between related experiments on polymer systems and the experiments carried out here. This might be surprising at first because the viscosities can differ by six orders of magnitude between the lut/w and polymer systems suggesting that the behaviour could be very different. However, at the same time the interfacial tensions are relatively similar for both systems (see table 4.1). The relevant time scales involved are that of the colloid motion and that of the fluid during demixing. While the time for a colloidal particle to diffuse one radius is given by

$$\tau_p \sim \frac{6\pi\eta r^3}{k_B T}, \tag{4.3}$$

where η is the viscosity of the surrounding liquid. The time scale for the motion of the fluids during most of the demixing process is given by

$$\tau_p \sim \frac{\eta r}{\gamma} \tag{4.4}$$

with γ being the interfacial tension between the two liquid phases. Hence both time scales change linearly with viscosity which could imply that all behaviour slows down in concert.

When comparing the fast and slow lut/w quenches it is apparent that the separation process takes significantly longer for the quasistatic quench than for the fast, deep quench. Near the critical point critical slowing down is taking place. The slow and shallow quench is influenced by this effect and its separation process therefore takes a longer time to occur. This slow time evolution allows me to capture the process using confocal microscopy which has been tremendously helpful while trying to build up understanding of how bijels form. For deeper quenches the chemical potential difference between the two separating phases is larger leading to an increase in the interfacial tensions and implying a stronger driving force for the coarsening process with increasing quench depth. Provided the particles are still trapped on the interfaces then critical slowing down is not necessary to successfully produce bijels. For the faster, 17°C/min quench the sample is less influenced by critical slowing down but still shows that the particles are efficiently trapped on the interfaces and I therefore see no reason that the slowing down is essential for the actual bijel formation unless even faster moving interfaces may eventually trap particles less efficiently.

The diagonal temperature gradient moving through the sample visible in the faster quench shows that bijel formation is still taking place even for moving phase separation fronts leading to different domain sizes in very close vicinity to each other. This can be of interest for work where different morphologies are obtained by moving a controlled temperature gradient through a sample.

These two critical lut/w quenches presented here show clearly that spinodal demixing is taking place when the system is quenched through the critical point and that appropriately wetting particles sequester to the interfaces resulting in a dramatic slowing down of the coarsening.

4.4 3-dimensional structure

After having demonstrated that bicontinuous interfaces can be created and particles can be trapped on these interfaces it is now of interest to examine whether this can result in a stable bijel structure.

Aim and context

This section examines the structural stability and morphology of a bijel. The spinodal decomposition is expected to lend the bijel a bicontinuous and convoluted morphology. The liquids making up this morphology cannot by themselves maintain the necks occurring in such a structure. The system would therefore coarsen by undergoing Plateau-Rayleigh instabilities (see section 2.1), i.e. by breaking of the necks. Increasing the viscosity of the liquid components which is the case for phase separation in polymer systems will lead to a much slower coarsening process but cannot avoid such instabilities. There are only two ways in which a neck filled with liquid can be stable. First of all the reason for the instability can be removed. This is the interfacial tension and it can be dramatically reduced by the presence of surfactants. Surfactant systems can exhibit a similar convoluted and bicontinuous morphology as that of the postulated bijel [26]. The near-zero interfacial tension in a surfactant sponge phase leads to a supple structure which rearranges continuously while being in thermodynamic equilibrium. The second way of avoiding the collapse of liquid necks is to give the neck enough mechanical strength to withstand the Plateau-Rayleigh instability. This can only be achieved if the material supporting the neck is able to stabilise two signs of curvature concurrently. This in turn is only true

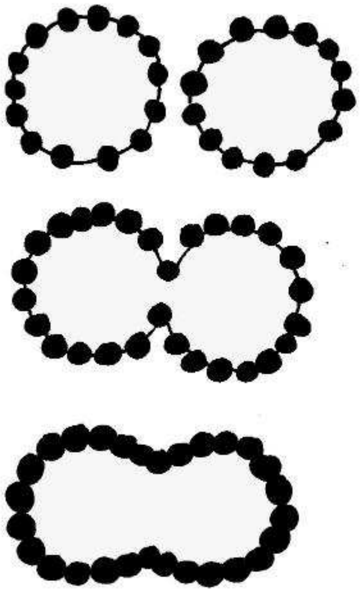

Figure 4.4: For particles preferring the continuous phase droplets can merge as long as the particles are still free to rearrange on the interfaces. Schematic sketches with evolving with time from top to bottom.

for a solid which does not dissipate forces like a liquid but rather has the ability to sustain anisotropic stresses. A material is said to have solid-like character if it exhibits a finite Young's modulus. There are several experiments which indicate that particles energetically trapped on liquid-liquid interfaces and jammed against each other can exhibit a finite Young's modulus. Buckling of flat particle-laden interfaces [48] or of droplets where the internal volume is decreased [51, 45] shows the existence of a Young's modulus as well as cracking of such interfaces [45]. The stabilisation of a single curvature has been shown in various experiments on solid-stabilised droplet emulsions and their properties and behaviours have been widely studied [2]. Although the wetting properties of stabilising particles induces a preferred curvature [28] it is also known that the opposite curvature can be stabilised if the system is forced to [39]. Therefore accompanied by jamming, particle-laden interfaces should also be able to sustain anisotropic stresses and this is demonstrated by the existence of particle stabilised, non-spherical droplets [45], bubbles [52, 3] and extended structures [53, 72]. It is important to note that while the particles are not jammed on the interface such non-spherical structures are not stable. For example two not fully coated, spherical droplets can start merging together in an effort to reduce their total interfacial free energy (see figure 4.4). However, on the way towards this low final free energy the interfacial area is continuously reduced driving the particles on the interface closer together. It is possible that the particles are so closely packed at some point that they inhibit a further reduction of the interfacial area although the minimum is not yet reached so that the end product is not a larger spherical droplet but a peanut shaped, non-spherical droplet. This transition of the interfacially trapped particles from a state where they happily rearrange their positions to the point where they are stuck between their neighbours must occur before the interfaces can resist Plateau-Rayleigh instabilities. This method of stabilisation will lead to a structure which is static over time.

Chung et al have shown that nanoparticles in phase-separating polymers can indeed prevent Plateau-Rayleigh instabilities if the particles segregate to the interfaces [73, 74, 22]. This has been shown for thin films of highly viscous polymers where the sample is only about a domain size in height and therefore two dimensional. The following section examines whether this method of stabilisation also works for low molecular fluids with a low viscosity and in a three-dimensional geometry. For this purpose the full depth of the sample needs to be examined to establish firstly, if spinodal decomposition is taking place throughout the sample and secondly, whether the structural stability is strong enough to support the bijel morphology over several domains.

Sample and method

A standard lut/w sample at critical composition containing Φ_v=2% particles is quenched to 40°C with 17°C/min. The sample is subsequently studied using fluorescence confocal microscopy. This yields satisfactory results for imaging up to 50-80 μm into the sample depending on the sample. Further into the sample the brightness decreases and aberrations degrade the image. The aberrations are due to the fact that the two separated liquid phases have different refractive indices. At 41°C these are 1.44 and 1.35 for the lutidine and water rich phases respectively. This difference is large enough to induce a lensing effect. Each time the light enters a material of different refractive index the light is refracted. Therefore the image degrades when the focus moves past the first domain. To circumvent this problem there are two approaches. For x-rays most materials have a refractive index close to 1. Therefore x-rays will not encounter the lensing effect and will be able to examine much further into the sample. X-ray tomography can be used to reconstruct 3-dimensional images and I was able to use the Skyscan 1076 from the Molecular Medicine Department[3]. The x-ray contrast is reasonable as tested on a droplet emulsion but the resolution for this machine is limited to 9μm/pixel under optimal conditions and in the test run this was not achieved by far. There are other x-ray tomography systems with resolutions up to 150 nm (NanoCT, Skyscan) but not available within the UK and in the mean time I found another way of imaging throughout the sample.

The problem for confocal imaging is the refractive index mismatch. By reducing the difference between the refractive indices of the two liquids, however, this problem can be overcome. This can be achieved by lowering the temperature so that the composition of the two phases becomes more similar as well as their refractive indices (see figure 4.5). Another way of moving the phase boundary is to add a third component to the system. Serendipitously I found that a copper wire suspended in the sample releases ions into the lut/w phases inducing a halo around the wire. In this region the liquids are refractive index matched and the confocal microscopy can be successfully carried out more than half way through the sample. I propose that the copper ions make the immiscibility loop of the lut/w phase diagram contract analogously to the salting-out effect described in [84]. As a

---

[3] contact person: Dr. Rob van't Hof, Western General Hospital

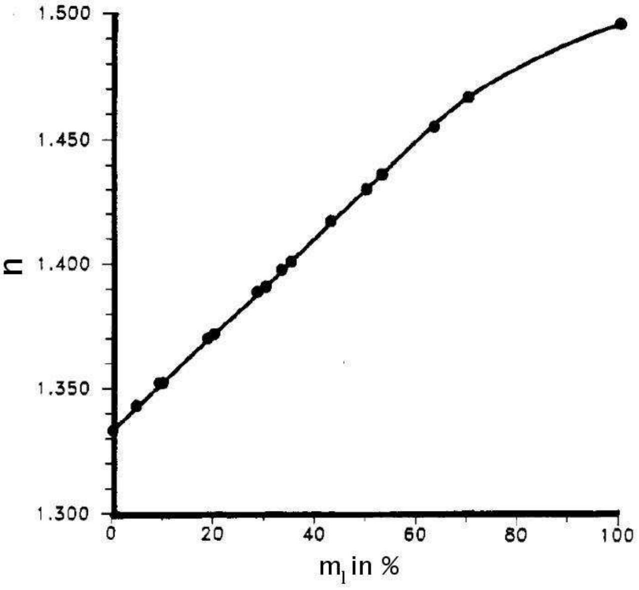

Figure 4.5: The refractive index n of 2,6-lutidine water mixtures plotted against m_l, the mass fraction of lutidine [16].

result of this refractive index matching it is possible to use fluorescence confocal microscopy to image through the whole depth of the 1 mm sample by examining it from both sides. Figure 4.6 shows a 5 day old sample which is refractive index matched using copper, so that good imaging quality is obtained several hundred microns into the cuvette. An easier way to carry out the refractive index matching is to simply cool the sample to reduce the difference in refractive index. Of course, when lowering the refractive index match this will also lead to a reduction in the interfacial tension. The effects of this will be discussed in section 4.5. In figure 4.5 the refractive index of lut/w mixtures is shown depending on composition.

Results and discussion

Confocal slices taken at different depths into the sample are shown in figure 4.6. The particles appear white while the liquids appear dark. The particles are mainly seen on the interfaces and show no preference for either of the liquid phases indicating that their wetting behaviour is neutral. The characteristic spinodal pattern is seen throughout the depth of the cuvette. Similar stacks can

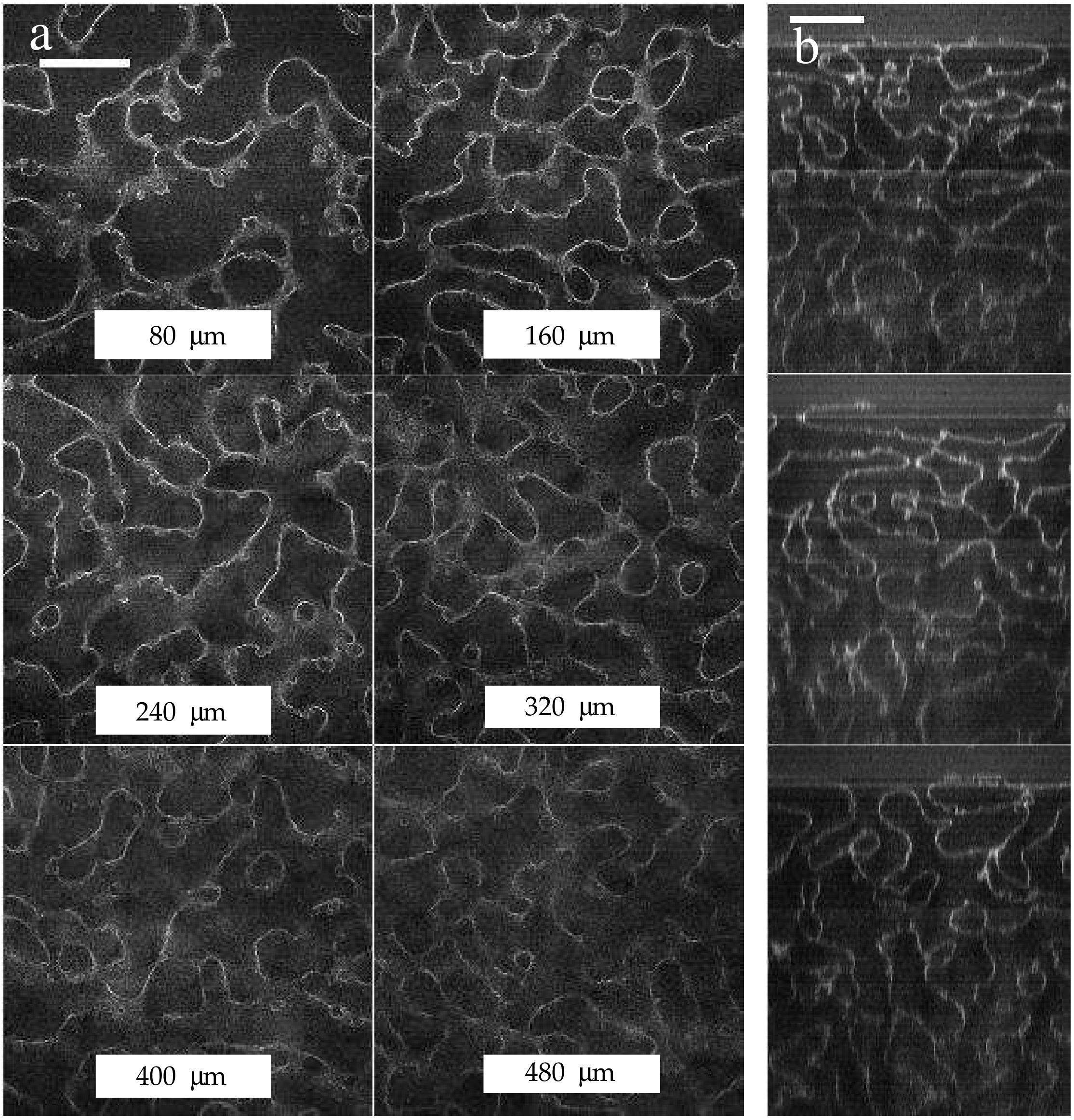

Figure 4.6: Left: Fluorescence confocal microscopy images at different depths into the sample of 2,6-lutidine-water at critical composition with Φ_v=2%, quenched from room temperature to 40°C at 17°C/min. Depth into sample is shown on labels. Right: Reconstructions along z-axis for bottom, centre and top of images on the left reaching 500 μm into the cuvette. In both cases scale bar is 100 μm. Actual sample thickness is 1 mm and the age of the sample is 5 days.

be obtained when the cuvette is turned by 180° and imaged from the other side of the sample therefore examining the complete depth of the sample. In figure 4.6b a reconstruction along the z-axis is shown through the top, centre and bottom of the images on the left.

Also along the z-axis the morphology is clearly spinodal and undistorted. The z-reconstruction shows that the sample is many domains thick making this confocal microscopy analysis to my knowledge the first demonstration of a properly three-dimensional composite material of this kind. The particle laden interfaces arrest within seconds of the spinodal decomposition process and are static from then on supporting a whole series of necks without further coarsening. From this I conclude that the particles must have jammed against each other and are seemingly not expelled from the interface and therefore produce a finite Young's modulus in the interface. With these images here I have proven that particles trapped at liquid-liquid interfaces can build up enough strength to prevent liquid necks undergoing a Plateau-Rayleigh instability and have enough mechanical resistance to also carry the weight of the whole bulk of the sample. Furthermore these images show that the bijel morphology is determined by the spinodal demixing pattern throughout the sample. For images taken close to the glass of the cuvette some surface effects as suggested by Tanaka [17] are occasionally visible as in figure 4.7, but these do not extend into the bulk of the material where the pattern is fully determined by the spinodal separation process confirming the computer simulations [71].

The imaging problems described above arise from domains containing liquids with different refractive indices. Consistently not being able to image much further than one domain into the sample implies that each domain is surrounded by the other liquid implying bicontinuity of the system. To demonstrate the bicontinuous character of the bijel further I have reconstructed a three-dimensional representation of the sample from the z-stacks shown in figure 4.6. By slicing the sample diagonally the bicontinuous character throughout the bijel is revealed (figure 4.8).

These experiments here show that spinodal decomposition is taking place throughout the sample and that the interfacially trapped particles have jammed

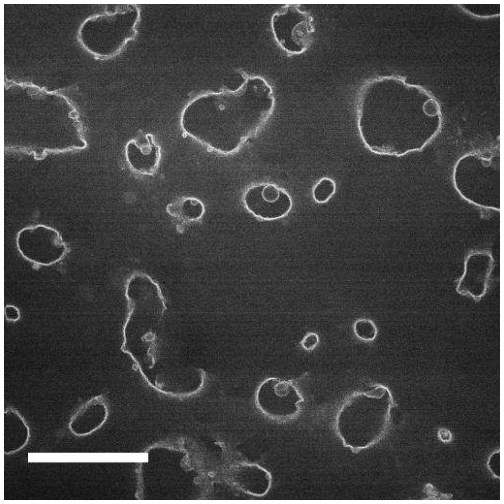

Figure 4.7: An image taken close to the surface of the cuvette shows wetting tubes as proposed by Tanaka [17] in a 2% bijel. Scale bar 100 μm.

and now arrest the system out-of-equilibrium inhibiting further coarsening and at the same time giving the sample enough structural strength to support its own weight.

4.5 Ageing effects

Structural stability is essential for the bijel to exist in the first place but whether the structure truly arrests on the length scale of these studies is established in the following section.

Aim and context

This section examines the behaviour of the bijel over time. The computer simulations by Stratford et al [71] suggest that the reason for structural stability will be due to the particles jamming on the interfaces. Like them I observe a drastic slowing down of the coarsening. However, from their data it is not clear whether a full arrest occurs because although the growth of the typical domain size significantly slows down, the domain size does not reach a plateau by the end of

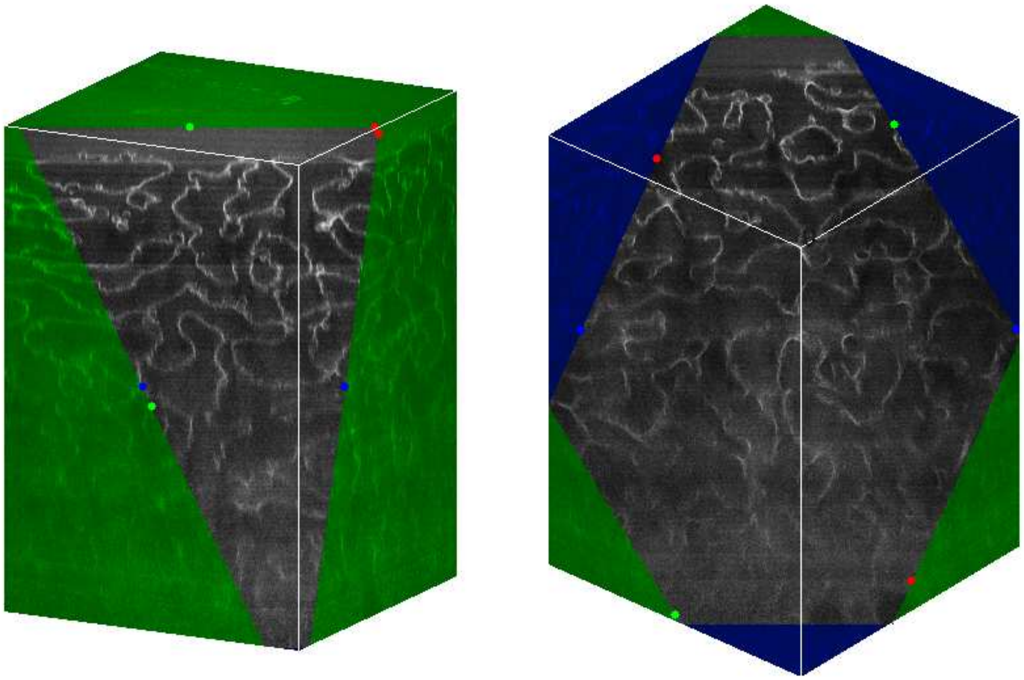

Figure 4.8: This three-dimensional reconstruction shows the bicontinuous nature of the bijel. Domains can clearly be traced into the depth of the sample. Confocal microscopy stacks are rendered using ImageJ and cut diagonally to reveal the inner structure. Same data as figure 4.6.

the simulation. The simulation times are very short in the laboratory time frame and only reach a few hundred nanoseconds [71] or just below a microsecond [85]. Stratford et al therefore suggest that the slow increase in the domain size at the late stages of the simulations could be due to particle rearrangements leading to a denser packing on the interfaces or it could happen because particles are slowly expelled from the interface. It is impossible for particle expulsion to occur when the particles are trapped with $\theta_{ow} \sim 90°$ because the free energy gain is too large compared to thermal fluctuations within the system. Simulations show, however, that although the particles have neutrally wetting properties their effective wetting angles can significantly deviate from 90° leading to lower or higher contact lines especially at strongly curved patches of the interface [85]. For such exposed particles the trapping is much weaker and it could be possible that mechanisms exist to expel particles over the course of time. I am therefore looking at the experimentally created bijels to find out whether they resemble a truly arrested system. Signs of arrest will be the stabilisation of necks and bumps in the structure over a long time scale, i.e. the stabilisation of curvatures much larger than the lengthscale of the particles. A long life time of a system is of course desirable when considering possible applications. But it is also of interest to study such metastable states because although the bijel might be static, it is still out-of-equilibrium. In addition to establishing whether the bijel arrests I would like to gain insight into how the stability arises. I have established that the main driving force in the formation process is the interfacial tension. It now needs to be found out whether it is only due the interfacial tension that the structure gains strength or whether other particle-particle interactions play a role as well. These can be electrostatic interactions, Van-der-Waals attractions, hydrophobic interactions or monopolar and bipolar interactions or combinations thereof [86].

Sample and method

With the following experiments I want to examine on which time scale the structure arrests and to test how the interactions between the particles vary over time. Firstly, the sample examined in section 4.4 is kept in an incubator at 40°C for seven months along with a second sample. Secondly, it is possible that particle stabilised droplets are present inside the fluid domains (see section 4.7) and the interaction of these droplets with the bijel walls shortly after their formation is examined. And thirdly, the effect of reducing and removing the interfacial tension by cooling the lut/w system back to room temperature is studied qualitatively for different sample ages.

Results and discussion

The same sample that was analysed in figure 4.6 has been kept in an incubator at 40°C for seven months. Confocal images after such a long time are shown

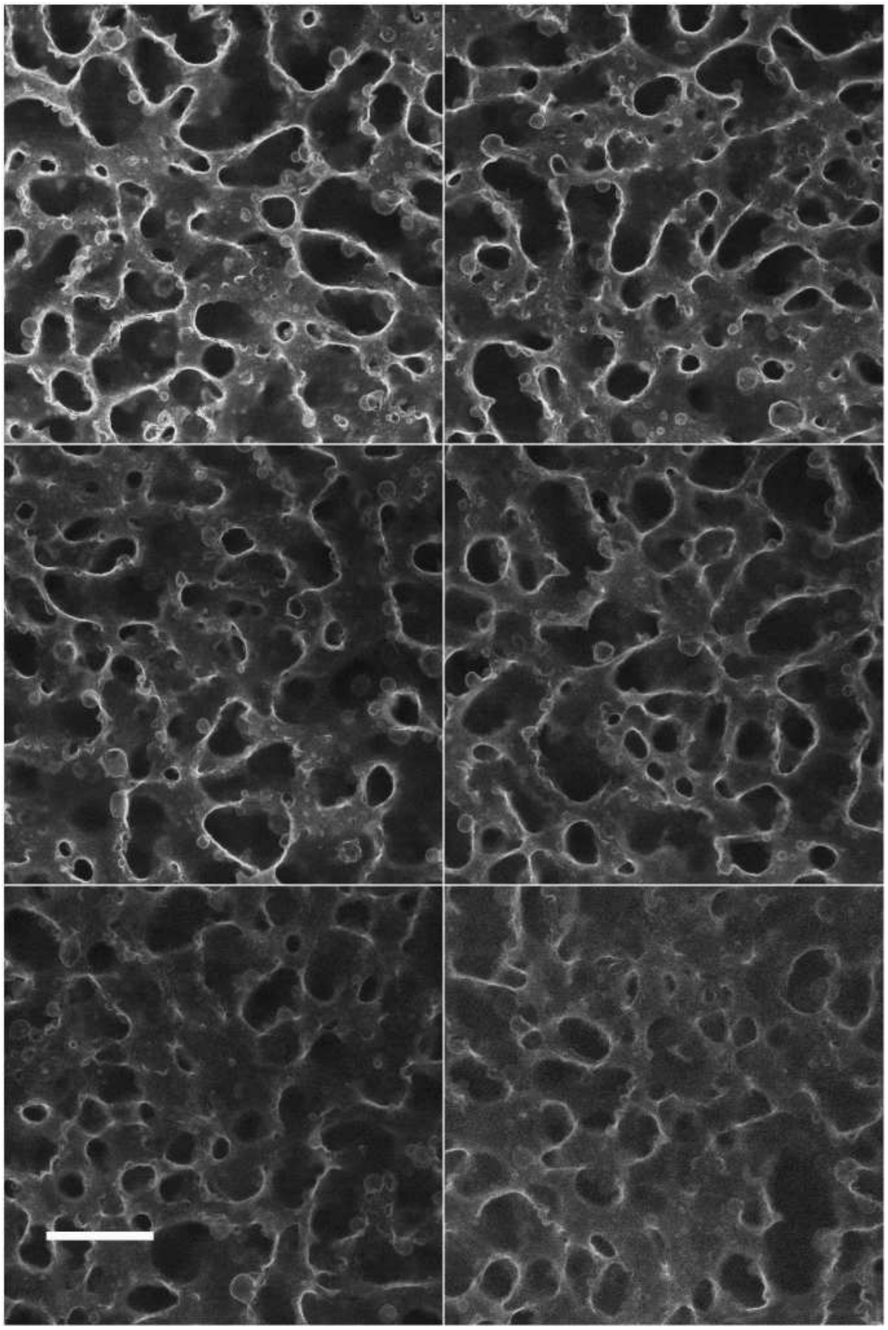

Figure 4.9: These fluorescent confocal microscopy images show a 7 month old bijel. The first image (top left) is 80μm into the sample, the following images are each taken 80μm further towards the centre of the sample with the final one on the bottom right. Scale bar = 100μm.

in figure 4.9. Although it is not possible to examine the exact same spot the morphology of the sample clearly has not changed even over such a long time.

The characteristic spinodal pattern is present with no evidence of having changed significantly in structure or domain size. The particles are hence able to sustain anisotropic stresses within the various necks for extended amounts of time as well as bumps in the walls of the bijel structure. The bijel can therefore be considered as a static structure which although being in an out-of-equilibrium state has a life time of many months. With the cuvette as a sample holder it is not possible to resolve individual particles and I cannot examine whether the particle packing has changed over time. However, it is unlikely that particles are expelled over time since this would have certainly changed the domain size over the course of months which is not observable by eye. As an extension to the computer simulations I therefore conclude that the particle stabilised bijel arrests in a metastable state for at least many months.

Experiments where the interfacial tension is reduced or removed by cooling the lut/w system shows that the age of the bijel has an influence on the behaviour of the particle-laden interfaces. When cooling a freshly created bijel below T_c only seconds after the coarsening has stopped the bijel structure quickly falls apart. However, if the sample is left for some time (from several minutes up to days) and then cooled below T_c the structure does not fall apart and can be stable for days at room temperature. It might seem surprising that these particles still keep their integrity although the interfacial tension is removed but the same effect has also been observed for particle stabilised, cylindrical structures [53] and droplets [45]. This indicates that other mechanisms than the interfacial tension must be present. Because this effect has been observed for PMMA [53] as well as silanised [45] and the FITC-doped silica particles here, I propose that the interactions are chemically non-specific. The combination of repulsive and attractive forces between particles [51] will lead to an attractive potential well in the interaction energy between interfacially trapped particles for distances close to the particle. This minimum must be shielded by a repulsive contribution for slightly larger distances because the particles are not seen to aggregate unless they are jammed into each other. While this repulsion is enough to keep particles away from each other if they interact thermally, the huge interfacial energy can overcome this barrier and push the particles into the attractive Van-der-Waals minimum. Once the particles have reached this minimum they are trapped in close contact. The stability over days shows that the energy barrier needs to be higher than 10's of k_BT. At the same time the energy stored in the interfaces (5000 k_BT) is sufficient to overcome this barrier and puts an upper limit on the repulsion. Fernández-Toledano et al [86] calculate Van-der-Waals interactions of the order of 100 k_BT confirming the feasibility of the above concept. The walls of the bijel structure which are held together just by particle interactions within a miscible liquid can be shattered by hitting the cuvette briefly. Bits of the structure then break off but keep their integrity. This indicates solid behaviour in the walls due to particle-particle interactions.

Examining the behaviour of the bijel upon the reduction or removal of interfacial tension indicates that two different regimes are in play concerning the properties of the particle-laden walls. This is further supported by the observation that droplets present in the bijel channels can merge into the walls of the bijel just after the formation of the bijel while this has not been seen at later times. Fuller et al [51] have systematically studied the merging of various droplets. They found that a droplet can merge into a particle-laden interface if the wetting layer between particles is overcome and provided rearrangements of the particles can occur on the interfaces. For the bijels here this implies that the particles on the bijel interfaces can undergo rearrangements in the early stages while this is not possible or significantly slower at later times.

These latter observations indicate that there are two regimes: for freshly formed bijels rearrangements in the walls are possible and a removal of the interfacial tension destroys the bijel while at later times the possibility of rearrangements is significantly reduced and interparticle forces lend the bijel stability even in the absence of interfacial tension. This indicates that once the bijel is created and no coarsening is any longer visible by eye there are still small rearrangements going on slowly altering the properties of the particle-laden interfaces.

I have shown here that the bijel arrests out-of-equilibrium for the course of months and that there are indications that a transition in the rheological character is associated with this arrest with evidence for slow dynamics in this system. To understand the behaviour of such jammed systems in more detail dynamic studies are carried out using x-rays in chapter 7.

4.6 Mechanical strength

To examine the mechanical strength of the bijel the response to an external force is observed over time.

Aim and context

The response of a material is very dependent on which time scale it is probed. For example, mixing maize starch in some water will result in a material which behaves like a solid on short time scales (punching it quickly makes it break) while if left just sitting in the pot it flows like a liquid. Hitting an aged bijel makes it break indicating solid behaviour when tested on short time scales while examining the long life time of the sample tests a much longer time scale on which the sample still shows the ability to maintain anisotropic stresses. A Young's modulus [48] has been inferred from studies of interfacial buckling [87, 50, 88] for particle-laden interfaces. Subramaniam et al [3] showed that where possible, local rearrangements tend to be preferred to large-scale rearrangements because less bare liquid-liquid interface is exposed. For jammed particles on an interface to slide past each other it is necessary for the interface to locally dilate to allow a plastic deformation to occur [3, 89]. This is shown in figure 2.3. The bijel, too, exhibits macro-scale variations of mean curvature in a static liquid-liquid interface. Since the interface extends through the entire sample its solid-like character makes the bijel a soft solid. Here I want to examine the structural strength of the bijel more quantitatively by testing its response to a defined external force.

Sample and method

To demonstrate the load-bearing properties of the bijel I compare two samples of the same composition as in Fig. 4.6. While the particles stabilise extended domains in the bijel the second sample contains an emulsion consisting of individual droplets. This droplet sample was produced in the same way as the bijel samples apart from the fact that it was vigorously shaken during the quench to avoid the formation of bicontinuous domains. Prior to the experiment I used microscopy to confirm that spherical droplets make up the second sample and no extended structures are present. For both samples a cylindrical wire of 0.2 mm diameter and total mass 1.9 mg is dropped into the cuvette and the path the weight takes is recorded with a digital camera at 15 frames per second. The images are subsequently analysed tracking the position of the weight using an image analysis software (Vision Assistant). Using thresholding and edge detection algorithms the location of the tip of the wire is obtained in each frame.

Results and discussion

Here the response of the bijel is tested when an external force is exerted on it in the form of a falling wire. The droplet emulsion provides little resistance: the weight sinks to the bottom with a speed of about 1 cm/s (see figure 4.10a, dashed line). To estimate the speed at which the wire would drop in a lut/w mixture without emulsion droplets the final Stoke's velocity for an elongated ellipsoid of

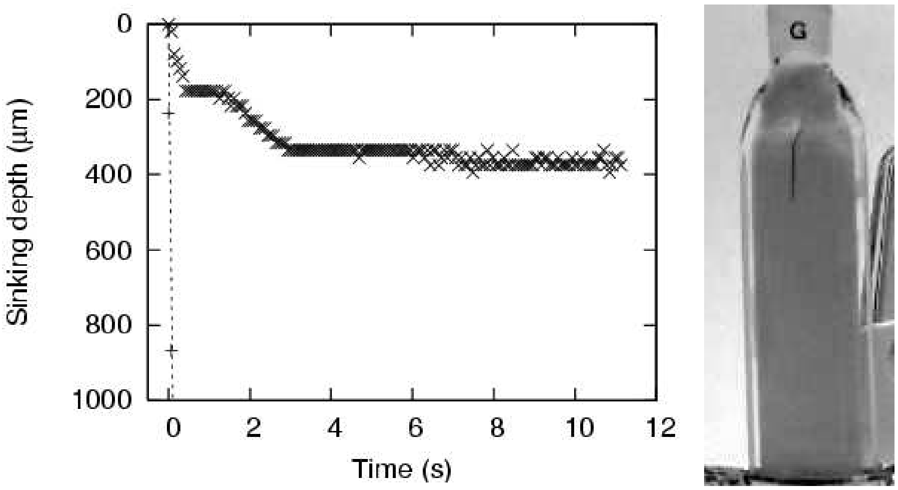

Figure 4.10: Left: Sinking depth of cylinder with mass of 1.9 mg and 0.2 mm diameter dropped over time in both droplet emulsion (dashed line) and bicontinuous emulsion (×) with compositions as above. The cylinder drops quickly through the droplet emulsion, and much more slowly through the bicontinuous sample with plateaus of zero sedimentation rate. Right: Cylinder 12 sec after being released under gravity into a bicontinuous emulsion (cuvette is 1 cm wide). The wire remains at this location for weeks confirming that there is a yield stress.

length 2a and radius b can be used.

$$\begin{aligned} v_d &= \frac{\Delta mg}{8\pi\eta a}(ln(\frac{2a}{b})+\frac{1}{2}) \\ &\sim 500\frac{cm}{s} \end{aligned} \tag{4.5}$$

with a viscosity of the lut/w mixture of around 2 mPas [16], but this speed would only be achieved after falling for about 0.5 sec under the influence of gravity which would require much longer distances than the length of the cuvette. The droplets increase the effective viscosity of the lut/w mixture but do not prevent the wire from falling continuously through the sample. In contrast, the weight in the bicontinuous emulsion sinks even more slowly and becomes stuck after travelling only a few millimetres (see figure 4.10a and figure 4.10b) and occasionally sinks further. Because the pixel resolution is 4-5 domain sizes the breaking through

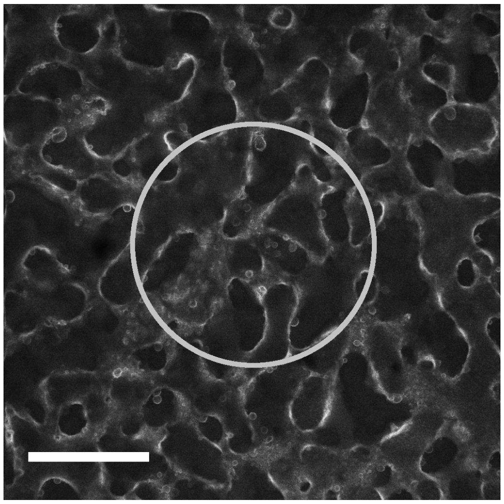

Figure 4.11: The circle shows the size of the wire which is being dropped into the bijel (critical, 2% lut/w) which extends over several domains.

individual domains cannot be observed. Figure 4.11 shows the relation between the wire diameter and the bijel structure. When the wire is halted by the bijel from further dropping the wire will rest on several domain boundaries at the same time. Over a period of several weeks the weight remains supported against gravity with little further movement.

While the slowing and stopping of the weight in the bijel suggests viscoelastic properties, the zero-sedimentation rate plateaus in Fig. 4.10a are clear evidence for a yield stress beyond which the material has fluid character. The occasional descent from one plateau to another may be due to local rearrangements in the interfaces in response to the stress exerted by the wire. Such intermittent behaviour is generic to many soft solids [54].

The lower bound on the yield stress for this bijel (Fig. 4.10b) can be estimated as σ_s = (cylinder weight) / (cylinder area) = 600 Pa while the Young's modulus for a flat interface can be estimated as E $\approx \frac{\gamma}{d}$ [48] where d is the particle diameter and γ the interfacial tension of a lutidine-water interface which is 0.22 mN/m at 40°C [16]. The Young's modulus is therefore about 550 Pa which is of the same magnitude as the exerted pressure and the bijel can therefore sustain the

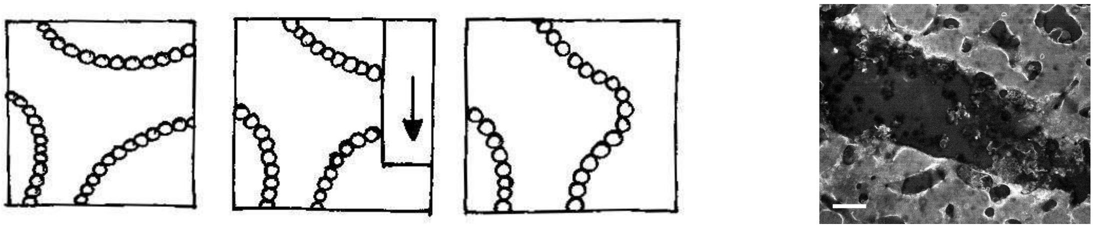

Figure 4.12: The moving wire can rip channels of the bijel open but subsequently the exposed interfaces are recovered with particles. Scale bar 50 μm.

load. Stratford et al [71] suggest that such percolating interfaces should give the structure a static modulus proportional to $\frac{\gamma}{\xi}$ on length scales larger than the typical domain size ξ. Here this would result in the modulus being around 6 Pa which would not be able to account for the stability against the wire.

It is important to note that the strength of the bijel structure is initially dominated by the interfacial tension holding the particles together. After several days however, the copper ions of the wire induce refractive index matching which implies that the interfacial tension is significantly lowered if not vanishing entirely. This implies that days after the start of the experiment the bijel is stabilised against the load of the wire solely by the Van-der-Waals interactions between the particles.

Combining all this information I conclude that the convoluted, particle-laden interfaces give solidity to the sample. While the interfacial tension is essential during the formation of the bijel and to give it a particularly large strength, the Van-der-Waals interactions alone can also lend the structure significant strength once the particles are jammed together closely enough.

Confocal images examining the path within the bijel taken by the cylinder show that after the fall of the weight a ‘healing effect’ takes place. When the wire passes through the bijel some of the structure is broken to make room for the wire. This inevitably leads to ripped-open domains now exposing empty interfaces but it is observed that these exposed areas are re-covered with particles creating a self-supported tunnel through the structure. This mechanism is shown in figure 4.12.

With the experiments here I have shown that the bijel has structural strength due to the interfacial tension trapping the particles on the interfaces as well as due to interparticle interactions. A more quantitative rheological analysis will be carried out by Job Thijssen in the near future.

4.7 Influence of quench rate

Composition and interfacial tension both change with temperature which are essential parameters during spinodal decomposition. In the next section I examine how the heating rate affects the formation of bijels.

Aim and context

Theoretical models of spinodal decomposition suggest that in the early stages of spinodal decomposition diffuse interfaces exist while the system separates via diffusion and that by the time sharp interfaces have formed the composition within the separated domains has already reached its final composition. Then as soon as the sharp interfaces are formed they will drive a fast hydrodynamic coarsening process in which the interfacial area between the two liquid phases is reduced [4]. While this can be true for an instantaneous quench it cannot be achieved in the laboratory where all quenches will be continuous. For such a continuous quench the system will already start to coarsen hydrodynamically before the final compositions are obtained [90]. Tanaka found that for systems undergoing spinodal decomposition where the coarsening happens faster than the diffusion of the liquids, secondary phase separation can occur [91, 82, 92]. These double phase separations are initiated in situations where the hydrodynamic coarsening exceeds the speed of diffusion significantly like in superfluid 2D mixtures [91] or in thin capillaries where surface wetting effects dominate [82, 17] and Tanaka refers to this mechanism as *interface quench*. Rüllmann and Alig [93] found that in the examined polymer systems the phase separation process including a secondary phase separation scales with the quench rate. This implies

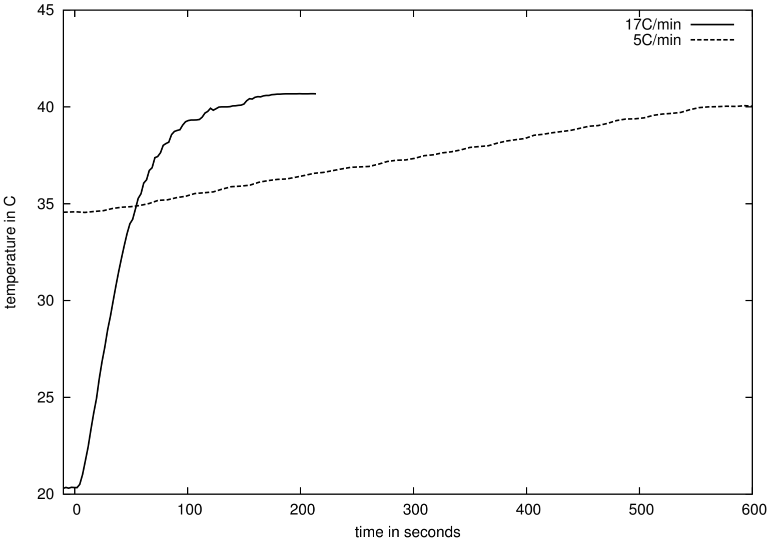

Figure 4.13: Heating rate measured inside cuvette with a K-type thermocouple. When inserting the cuvette into the aluminium block preheated to 40°C the resulting rate is 17°C/min. Also shown is the steady heating performance of the new Lakeshore 331 temperature controller for the rate set to 1°C/min.

that the separation pattern will evolve at different speeds but the underlying mechanism driving the different separations does not change with the quench rate.

Sample and method

To test the influence of heating rate I have employed different rates of 17°C/min, 1°C/min and 0.1°C/min for samples with 2% volume fraction of particles at critical water-lutidine composition. With the new Lakeshore 331 PID controller very steady heating rates can be achieved without overshooting once the final temperature is reached. That no overshooting takes place using this controller is demonstrated in figure 4.13 where the temperature was measured inside the sample holder. The temperature environment is now much more stable than previously when using the Honeywell controller. This is important because the separation behaviour which will be observed using the Lakeshore controller will be produced by steady rates and does not produce unknown fluctuations which

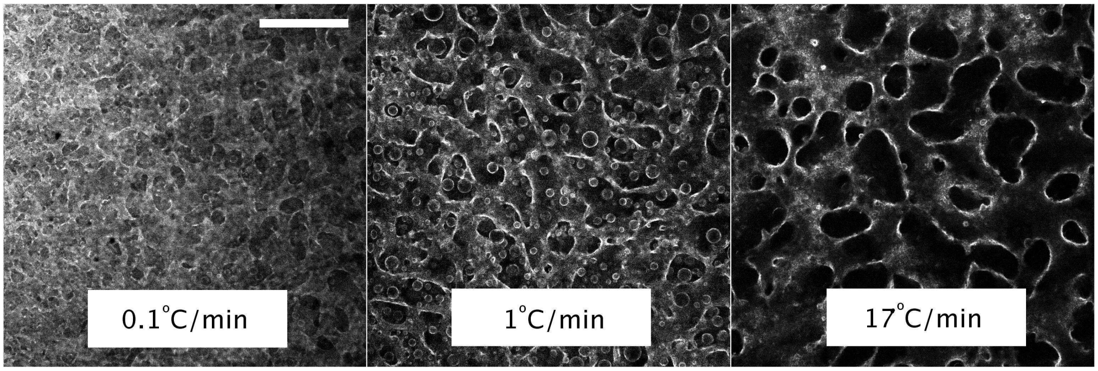

Figure 4.14: Fluorescence confocal microscopy images of 2,6-lutidine-water samples at critical composition with Φ_v=2% particles, heated from room temperature to 40°C with different heating rates as labelled. Particles are shown in white while liquids appear dark; scale bar 100 μm.

could lead to unwanted phase separations. The Honeywell controller will fluctuate by up to ± 0.5°C while the Lakeshore controller controls the temperatures up to 0.001°C for constant temperatures and up to 0.01°C during heating which is a significant improvement.

Results and discussion

Figure 4.14 shows the dependence of the sample morphology on the heating rate. In all cases spinodal decomposition is the initial separation process (see figure 4.2). However, subsequently I observe that droplets appear as soon as the spinodal decomposition pattern stops coarsening even for the fastest 17°C/min quench. I find that slowing the heating rate to 1°C/min increases the proportion of droplets at the final temperature (centre in figure 4.14). In a more extreme development decreasing the heating rate even further to 0.1°C/min results in a collapsed structure with thinned necks also containing droplets (left in figure 4.14).

Phase separation will only take place when the system is out of equilibrium. I use this deliberately when changing the temperature to induce spinodal decomposition. Due to the finite heating rate the temperature is continuously changing even once the liquids start separating. Therefore the desired composition changes continuously and the system needs to constantly adjust the composition of the two liquid phases on its way towards equilibrium. To obey these constant changes in composition 2,6-lutidine and water molecules need to be exchanged between the domains while the system simultaneously coarsens. This exchange happens via diffusion and if it is inhibited the system will need to find a new route towards equilibrium. There are two ways how the molecular exchange between the domains can be stalled. In these experiments here characteristics of both mechanisms are found and it is therefore not possible to assign the secondary phase separation to one of the mechanisms.

Competition between domain growth and diffusion of molecules through domains A reason for molecular exchange between domains to fail is simply if the domains grow too large for the particles to diffuse that distance quickly enough. This is possible because the coarsening happens hydrodynamically and can therefore be faster than diffusion. This has been observed in viscous polymer systems [93, 92], superfluid 2-D liquids [91] or in polymer systems in thin capillaries [82]. In these cases a stage is reached during coarsening at which the domains grow faster than diffusion takes to equilibrate the domain compositions even for these non-laden interfaces. A secondary phase separation, a so called interfacial quench [82, 92], within the domains will help the system to reach equilibrium via a new route. This would imply that there is a maximal domain size that can be reached with our method putting a limitation on the tunability of the system. Tanaka [82] predicts that an interfacial quench happens when diffusion cannot keep up with the hydrodynamic coarsening anymore. To compare these two mechanisms he calculates the time τ_h to hydrodynamically form a domain of size ξ as

$$\tau_h \sim \frac{\xi\eta}{k\gamma} \tag{4.6}$$

while the characteristic diffusion time for the same distance will be

$$\tau_D \sim \frac{\xi^2}{D} \tag{4.7}$$

where ξ is the viscosity, γ the interfacial tension, k a constant that is 0.04 in bulk spinodal decomposition and D is the diffusion constant. As soon as $\tau_h < \tau_D$ the interfacial quench would start. This can be solved for the domain size at which that would happen in the system here:

$$\xi > \frac{D\eta}{k\sigma} \sim 4\ [\mu m] \tag{4.8}$$

with D=$15\times10^{-10}\frac{m^2}{s}$ [94] and average viscosity of 1.65 mPas and γ=0.017 mN/m at 34.5°C [16]. This is smaller than what I observe here but it does not take into account that the particles on the interfaces will slow down the separation process. These will slow down the hydrodynamic coarsening and reduce the difference to the diffusion process which therefore leads to a larger ξ before the interfacial quench will occur. The speed of the interfaces for the hydrodynamic coarsening after Tanaka would be $\frac{k\gamma}{\eta} \sim 400$ μm/s while I observe speeds of interfaces in the region of 5 to 100 μm/s. Multiplying equation 4.8 by a slowing down factor of 4 to 10 will get us exactly into the range of domain sizes where I observe such a secondary phase separation.

Particles reduce diffusion across interface Another effect which increases the discrepancy between diffusion and hydrodynamic coarsening is that particles jamming on the interface before the final temperature is reached can dramatically decrease the exchange of molecules between domains. Temperature cycling of particle stabilised droplets [45] shows that diffusion across interfaces populated with jammed particles is slow and can lead to an independent phase separation inside the particle stabilised droplets. If the particles reduce the exchange of the liquids while the system is still heating up, the composition in the domains cannot be adjusted quickly enough. Instead the system will undergo a second phase separation within the domains in an effort to reach equilibrium on a different route. This also ties in with Tanaka's model of the interface quench, because the difference between hydrodynamic coarsening and diffusion is increased when

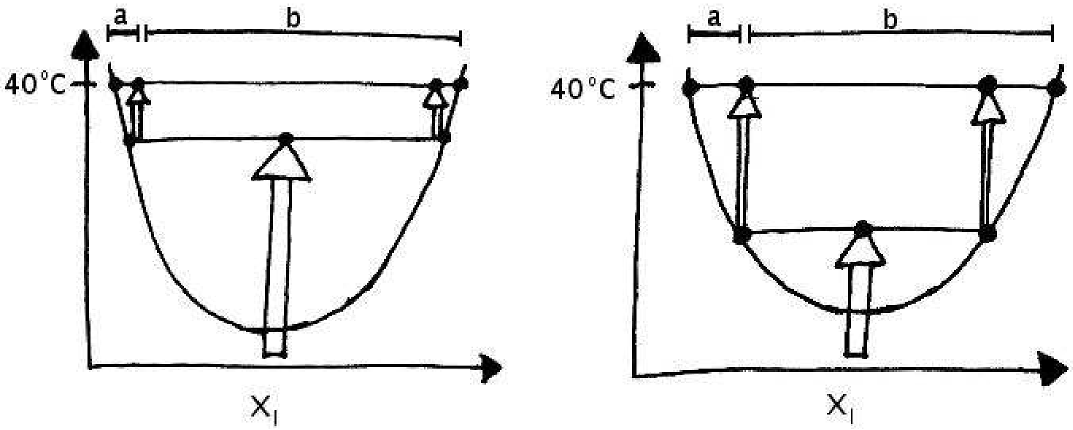

Figure 4.15: Assuming the faster the quench rate the higher the temperature when the secondary separation will occur then the final droplet volumes will vary. The Lever rule (a:b = $V_{minorityphase}$:$V_{majorityphase}$) shows that the volume of the nucleating phase is smaller for the fast quench than for the slow quench.

the diffusion is slowed down. If the reduction of the diffusion is the dominating process then this would decrease ξ from equation 4.8. Since experiments show that ξ is much larger it seems that the reduction in diffusion is not the dominating process if assuming that an interface quench takes place.

It is of course possible that the slowing down of the coarsening process due to the particles on the interfaces slows down the hydrodynamic coarsening sufficiently so that diffusion can keep up and therefore Tanaka's model which is developed for clear interfaces does not take place in the first place. The second phase separation can then be induced simply because the particles lock and reduce the diffusion across the interfaces sufficiently before the final temperature is reached that a secondary phase separation is preferable. This would tie in with the observation that the secondary phase separation is observed to occur close to or after the coarsening has stopped and the fact that different amounts of droplets are observed in the final bijel. In contrast, if the interface quench is the responsible mechanism the scaling property of the mechanism observed by Rüllmann [93] would then imply that the secondary separation would occur at the same temperature and produce the same amount of droplets. While the secondary phase separation for the fast 17°C/min quench would then occur not too far from reaching the final temperature at 40°C the secondary phase separation for the much slower 1°C/min quench will occur at a lower temperature. This will lead to a much deeper secondary quench and result in a larger volume of the minority phase compared to the faster quench and therefore in more droplets (see figure 4.15).

It is important to note that although diffusion is reduced, molecular exchange can still take place across the particle laden interfaces. Evidence for this is the observation that when a bijel is slowly cooled the composition changes without destroying the structure. Additionally, copper ions which induce the refractive index matching in figure 4.6 must have been able to diffuse through the bijel, too.

Independent of the origin, the 'secondary quench' is now off-critical and will therefore occur via nucleation leading to droplet formation. If using particles with sub-optimal wetting properties excess particles are found in the separated phases. These excess particles are picked up by the interfaces during the secondary nucleation and stabilise the droplets. Because particles are usually predominantly found in one phase there are generally more stable droplets in one of the phases. The more ideal the wetting properties the less droplets are found in the system. However, this does not imply that the secondary separation does not take place. It rather shows that there are less particles available to stabilise the secondary phase separation.

Shortly after their creation the secondary droplets can fuse into the walls of the bijel. At later times this is no longer observed (see section 4.5). The opposite, that the bijel buds off droplets from its structure does not seem to occur and has so far not been captured.

The structure of the sample heated at 0.1°C/min collapses (see figure 4.14) and the necks thin. This has also been observed for the step quench in figure 4.2 at later stages than shown in the figure but was initially thought to be due to temperature fluctuations due to inaccurate heating control. Like for the other quench rates I heat through the critical point where the interfacial tension is very low [16]. For rising temperature and the associated increasingly distinct phases the interfacial tension increases. But when the heating rate is very low the interfacial tension increases very slowly. Vella et al [48] have shown that the strength of the interfaces is proportional to the interfacial tension, therefore, if the interfacial tension is very low the stabilised interfaces are initially very supple and as seen here not strong enough to support the weight of the jammed structure. At 34.5°C this would lead to a Young's modulus of about $\frac{\gamma}{d} \sim 40$ Pa [48] which is more than ten times less than at 40°C.

The need to increase the interfacial tension quickly enough to obtain sufficient structural strength is important when considering the possibility of creating larger volumes of bijel. When heating a sample from the outside the centre of the sample will always heat more slowly than the outside. Although, quenching through the critical point allows direct access to spinodal decomposition for larger samples the heating rate will reduce towards the centre of the bulk leading to weak structures in the centre which would be squashed by the surrounding weight. Critical pressure quenches, using metallic colloids to heat the sample in situ or having heating wires within the sample are just a few suggestions to circumvent this problem for large bijel productions.

4.8 Influence of particle volume fraction

Here I show that by varying the amount of particles it is generally possible to tune the pore size of a bijel while the behaviour is more subtle for the lowest volume fractions.

Aim and context

The spinodal pattern coarsens in a self-similar way, i.e. throughout the process of reducing the interfacial area the intrinsic bicontinuous character of the separated liquids is maintained [95]. Minimisation of the free energy drives the reduction of the interfacial area during spinodal coarsening. Initially the amount of interface is very large and the domain separation very small. Over time the interfacial area decreases and the domain size consequently grows larger while at the same time the overall morphology does not lose its bicontinuous character. In earlier sections I have established that particles present during spinodal decomposition can be picked up by the interfaces (section 4.3 and arrest the demixing pattern when they jam against each other (section 4.5). Combining these properties with the coarsening mechanism it is possible to tune the domain size of a bijel.

Since the silica particles cannot overlap the stabilised interfacial area A is directly related to the number of particles N$_p$ on the interface with A $\propto N_p \times \frac{\pi d^2}{4}$ where d is the diameter of the colloids. By choosing a larger amount of particles I can therefore expect to stabilise a larger amount of interface which in turn implies smaller domain separations.

Testing how the system behaves when adding different amounts of particles will show how efficient the picking-up of particles is and whether the packing of the particles on the interfaces is reproducible. Ultimately, the volume fraction of particles can then be used to tune the domain separation of bijels.

Sample and method

To test the influence of particle volume fraction on the typical domain separation I prepare standard bijels and use a range of different particle volume fractions from 0.5% to 4%. Each sample is quenched through the critical point to 40°C with 17°C/min and is characterised by vertically scanning it at different positions. It is known that the addition of particles can influence the separation temperature [78, 80, 79] and I have tested this trend for the ethanol/dodecane system with silanised silica particles of similar size than the ones used here. The outcome is presented in the next chapter in figure 5.5. This effect needs to be taken into account when preparing the $\Phi_v = 3$ and 4% samples and to avoid pre-transitional wetting [18] these samples are kept below 20°C prior to the quench.

Results and discussion

By varying the amount of added particles the effect on the domain size is examined in the following experiments. Figure 4.16a shows a selection of the resulting confocal images demonstrating qualitatively that the domain size decreases with increasing particle volume fraction. For the higher volume fractions the change in interface separation occurs without a change in morphology while for 0.5% and 1.0% the system has very similar curvature and droplets dominate over the spinodal pattern.

While simple length measurements applied by hand using an image processing software like ImageJ [96] can give a good idea of the situation it is not statistically satisfying and neither feasible for a large number of images. To analyse this observation more quantitatively I extract the typical length scale from the confocal microscopy images using a Fourier transform method.

The created structures are static analogues of sponge mesophases [26] and their scattering pattern is well known. A knee in the log-log plot of the scattering intensity will indicate the wave vector corresponding to the characteristic length scale. To extract the dominant length scales of our confocal microscopy images we calculate the structure factor by radially averaging the squared Fourier transform. To improve statistics I average structure factors for several different images. A standard method used for example in the related computer simulations is to take the following integral which finds the expectation value of q:

$$L = \frac{\int_0^\infty qS(q)dq}{\int_0^\infty S(q)dq}. \tag{4.9}$$

However, this only works if the structure factor has a proper peak so the expectation value is found at the location of the peak. In our case the images are quite noisy and a very washed out knee instead of a clear peak is visible. Instead

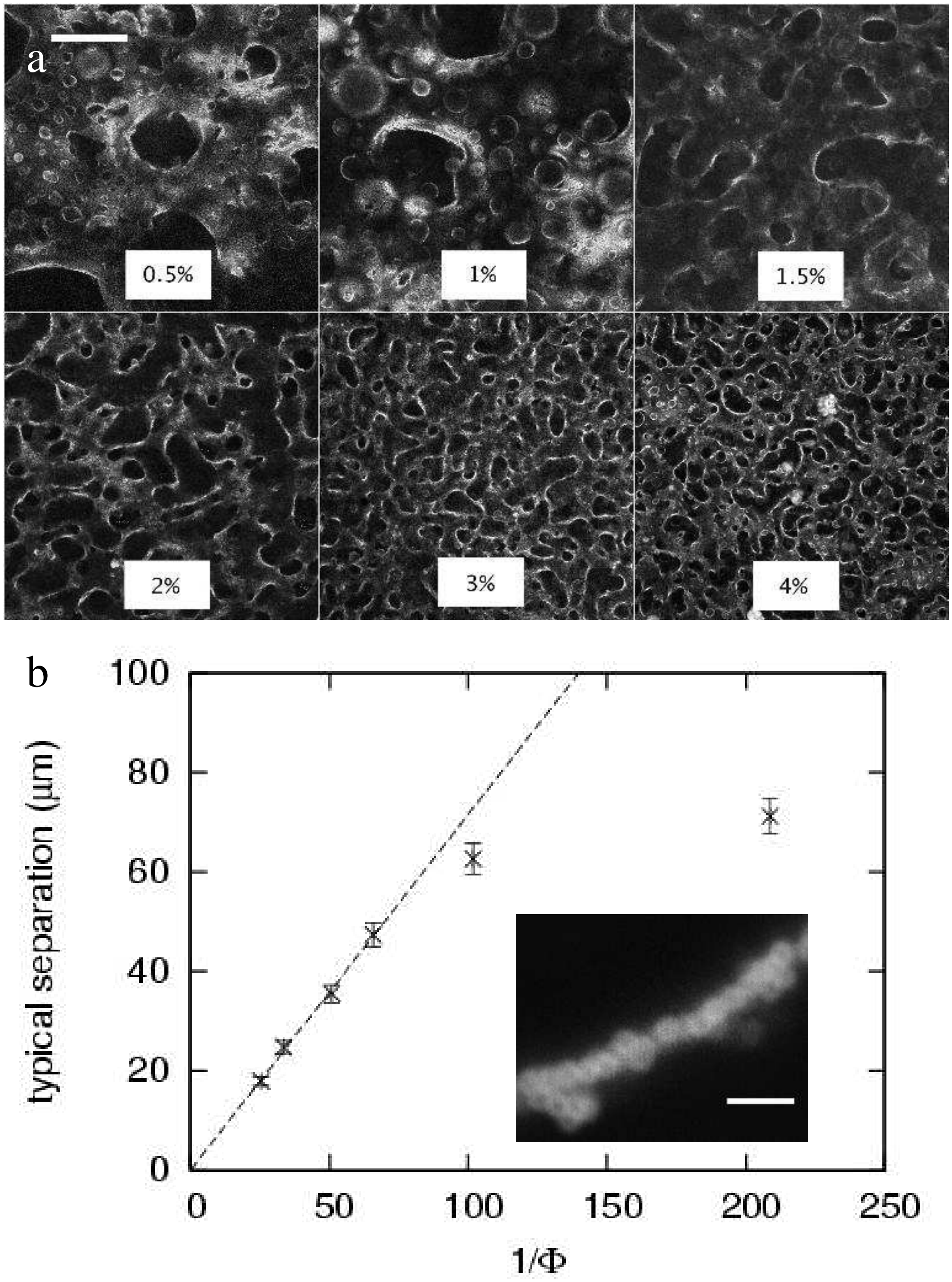

Figure 4.16: Top: Fluorescence confocal microscopy images of 2,6-lutidine-water samples at critical composition, quenched from room temperature to 40°C at 17°C/min with varying particle volume fractions Φ_v (scale bar 100 μm). Particles are shown in white while liquids appear dark. Bottom: Typical separation between domains (see Methods) plotted against inverse of particle volume fraction. Inset: High resolution image of colloid packing, scale bar 1 μm.

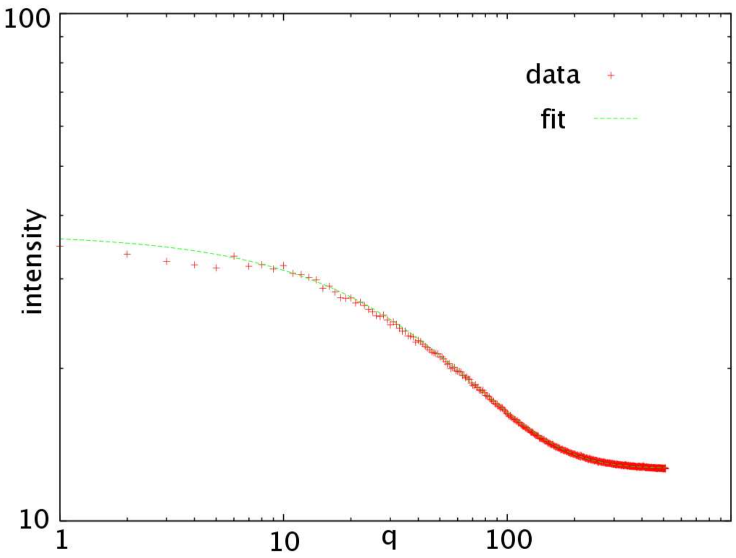

Figure 4.17: A typical structure factor obtained after radially averaging several Fourier transformed images. The fit is a compressed exponential as shown in equation 4.10.

I fit a compressed exponential

$$I(q) = b_1 + b_2 * exp(\frac{0.22q}{b_3})^{b_4} \tag{4.10}$$

and extract b_3 as q_{knee} for when the curve has decayed by 20% (a small increment on the log scale). A typical structure factor is shown in figure 4.17 with the solid line indicating the compressed exponential fit. The results obtained from the Fourier transformations agree with values obtained for several test samples by measuring domain separations in ImageJ [96] by hand but has the advantage of being automated and statistically more reliable.

Plotting the obtained domain separations against the inverse of volume fraction shows a linear relationship between these two quantities. By assuming a situation with minimised surface area and a typical domain separation I can find a mathematical expression to relate the volume fraction of particles to a typical length scale. I take a sphere with diameter ξ (corresponding to the typical domain separation) filled with a volume $V_i=\frac{4}{3}\pi(\frac{\xi}{2})^3$ of the internal phase and surrounded

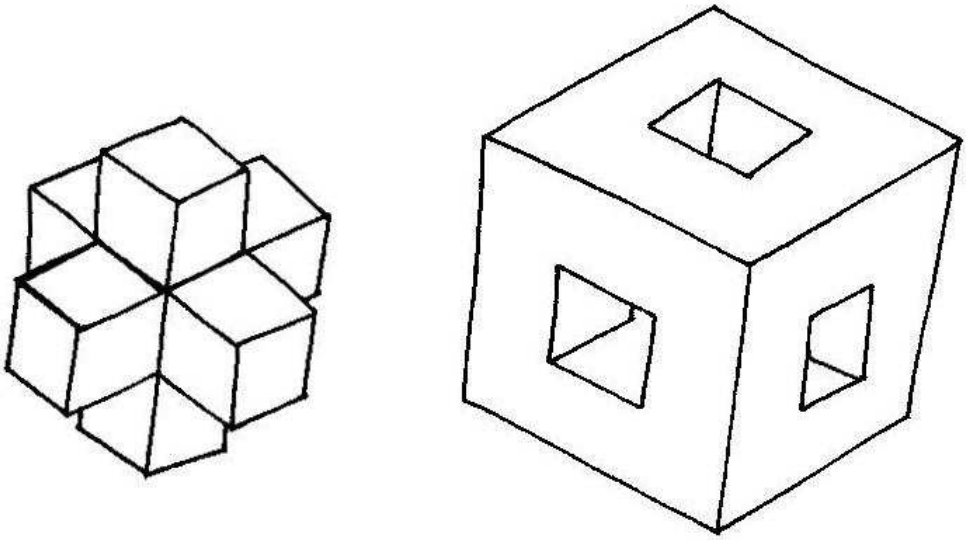

Figure 4.18: Simple geometrical representation of a convoluted bijel with equal volumes consisting of regular dice. This geometry can be used to obtain a relationship between typical domain separation and volume fraction. Diagram shows phase A on the left which is surrounded by phase B on the right.

by the same volume of the external phase. The interface available to be covered with particles is the surface of that sphere. The stabilising particles itself are spherical, hence the total area that needs to be covered is $\mathrm{A}_{tot}=\frac{A_{part}}{\nu}$ where ν is the particle packing fraction in two dimensions. The total area is also equivalent to the surface of the sphere with diameter ξ.

By describing the volume fraction Φ_v as $\Phi_v = \frac{Volume_{colloids}}{Volume_{total}}$ and I find that

$$\xi = 2\nu d\frac{1}{\Phi_v}. \tag{4.11}$$

Instead of using a sphere I also calculated the relationship between ξ and Φ_v for a regular bicontinuous geometry built from equally sized cubes. Figure 4.18 shows a part of this geometry approximating the bijel structure and by using the fact that on average each cube has three of its sides forming interfaces with the other liquid this can be used to carry out the same calculation as for the sphere above. This leads in both cases to the same relationship between ξ and Φ_v and shows that I appropriately model a convoluted structure with minimised interfacial area. If the interfaces are stabilised by more than one layer of colloids then equation 4.11 will change to

$$\xi = 2n\nu d\frac{1}{\Phi_v}, \tag{4.12}$$

where n is the number of particle layers.

Plotting the experimental data of the typical domain separation against the inverse particle volume fraction results in a linear relationship for volume fractions above 1%, the slope of which is 0.72 ± 0.02 μm. Andrew Schofield carried out electron microscopy on the fluorescent silica beads from which we can obtain a good measurement of the physical size of the particles which is $0.40 \pm 0.02\mu$m in diameter[4]. Using equation 4.11 this gives an estimate on the packing fraction ν to be ≈ 0.9. This is around the maximum packing of disks on a plane which is $\frac{\pi}{2\sqrt{3}} \approx 0.907$ for a highly ordered, face centred packing which is unlikely to occur here. But taking into account that some of the particles are still in the liquids, that will reduce the packing into the region of 0.8 which then would be in good agreement with random close packing disks in 2 dimensions [97]. This implies that the particles are in contact with at least 2-3 particles at a time but the packing will most likely not show any significant short or long range order. These numbers also indicate that the particles form a monolayer on the interfaces. This is supported by high magnification microscopy kindly provided by Kathryn White. These show bijel walls at particle resolution which clearly consist of a monolayers of particles in close contact to each other (see inset to figure 4.16b) [5]. This evidence of particle monolayers is an important observation because it shows that the key element in the formation of bijels is the interfacial

---

[4] Because of thresholding during the analysis this is rather underestimating the real size. Light scattering measurements yield a hydrodynamic radius of the same particles of 290 nm ± 7 nm which is known to be larger than the physical size.

[5] A near critical lut/w mixture containing Φ_v=1% particles was quenched to 40°C inside the aluminium block contained in an open cuvette (Starna, 20/C/Q/1) which was subsequently cooled to room temperature and, covered with a coverslip, examined on the upright microscope using an oil ×100 objective

tension and not direct interactions between particles. The possibility of the latter cannot be excluded in the alcohol/oil systems in chapter 5.

Sources of uncertainties in the experimental pre-factor include the density of the silica particles which is used to calculate the volume fraction. Throughout this work a value of 2.2g/cm^3 is used which is the density of fused silica, measurements on Stöber silica have shown that a more appropriate value is 2.03g/cm^3 for the particles here [61]. Correcting for this will then lead to a slope of 0.78 ± 0.01 μm which indicates even higher packing. Other factors include inhomogeneous distribution of particles within the sample, for example, due to sedimentation, or heterogeneous wetting properties leading to some particles with inappropriate wetting conditions. However, the linear relationship for higher volume fractions further indicates that the process of picking up the particles during interface formation and the resulting packing is independent of the volume fraction and we can indeed use the amount of particles to tune the typical interface separation.

For 0.5% and 1.0% droplets appear and interfere with the image analysis. The typical separation decreases because the droplet sizes cannot be excluded during the analysis. The underlying structure is nevertheless still bicontinuous and possible reasons for the occurence of droplets have been discussed in section 4.7.

4.9 Role of kinetic pathways in phase-separation

Here I explore the role of the kinetic pathway during phase-separation for bijel formation and compare the result to emulsion inversion behaviour.

Aim and context

Throughout this chapter I have claimed that the kinetic pathway of the phase-separation process is responsible for bijel formation. Here I want to further support this claim and show that varying the kinetic pathway changes the emulsion type. Depending on the 2,6-lutidine mole fraction different regions of the phase diagram are accessed upon heating. The system will directly enter the spinodal decomposition region only for near critical compositions. Off-critical quenches will separate via the nucleation of the minority phase. The interfaces created in these two processes have a significantly different morphology.

Extensive work on particle-stabilised droplets has shown that phase inversion can occur under different conditions. Using the same particles but varying the liquid ratio of two immiscible liquids can lead to catastrophic phase inversion [39]. Transitional phase inversion can be achieved by changing particle surface chemistry or by using mixtures of particles with different wetting properties [40]. In both cases the emulsions are at all times in the form of droplets. The emulsions here have the longest stability at the inversion point in the form of a bijel which does not consist of droplets but has a bicontinuous character where it is not possible to distinguish between internal and external phase.

Sample and method

To test the behaviour of the lut/w + silica particles system under different separation mechanisms I probe the different compositions shown in figure 4.19. All samples contain 2% particles and are quenched with 17°C/min from room temperature to 40°C. To distinguish the type of droplet emulsions between lutidine-in-water and water-in-lutidine droplets I check whether the sedimentation or creaming occurs. However, for $\Phi_v = 2\%$ the weight of the shell makes all droplets sediment. Therefore, the droplets were re-made using a lower volume fraction of colloids for which the difference in sedimentation and creaming is now possible.

Results and discussion

Only for the critical liquid composition a bicontinuous emulsion emerges after the quench. All off-critical quenches result in particle-stabilised, individual droplets

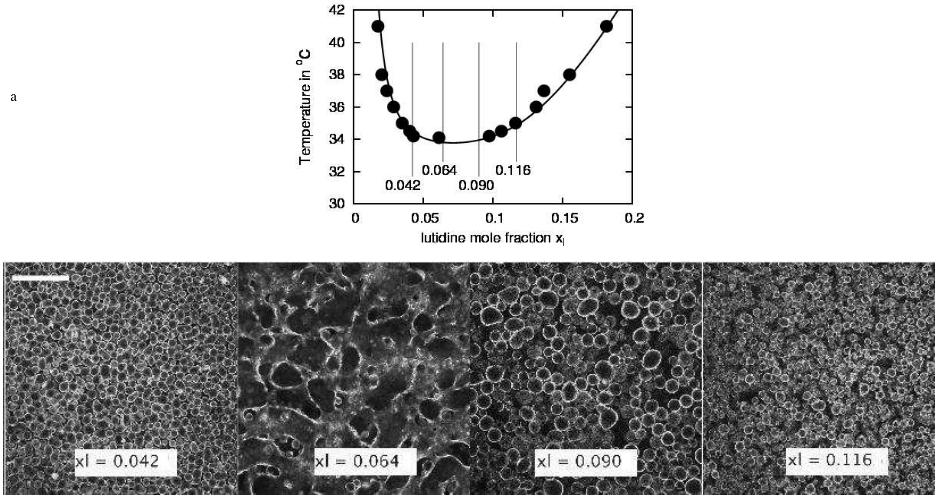

Figure 4.19: Left: Phase diagram of 2,6-lutidine-water system from [16]. Vertical lines indicate quench composition for images on the left. Right: Fluorescent confocal microscopy images of water-lutidine samples with Φ_v=2% particles, quenched from room temperature to 40°C in preheated aluminium block with varying lutidine mole fraction x_l as labelled. A catastrophic phase inversion occurs with the bicontinuous emulsion in the inversion region. Particles are shown in white while liquids appear dark; scale bar 100 μm.

which decrease in size away from the critical composition. While left of the critical point the internal phase is lutidine-rich, it changes to water-rich on the right hand side demonstrating that a phase inversion is taking place with the inversion around the critical composition. At the critical composition the two phases cannot be categorised into external or internal phase.

The spinodal decomposition regime can only be directly accessed through the critical point. At off-critical composition the quench will access the nucleation region. Therefore spherical interfaces are created and pick up particles. The droplets randomly merge until the interfaces are completely covered and have reached their final size. The observed phase inversion confirms that the emulsification is entirely determined by the liquid demixing process because on the left hand side of the critical point lutidine-rich droplets will nucleate while on the right hand side of the critical point the water-rich phase is the nucleating component. Since the volume fraction of colloids is the same for all four samples, the interfacial area that can be stabilised is constant ($A=N\times4\pi r^2$, N = number of droplets). However, we vary the liquid compositions and hence the final volumes of the phases will differ ($V=N\times\frac{4}{3}\pi r^3$). Further away from the critical composition the internal phase decreases in volume, hence

$$\begin{aligned} V_2 &< V_1 \\ N_2 \times \frac{4}{3}\pi r_2^3 &< N_1 \times \frac{4}{3}\pi r_1^3 \\ r_2 &< r_1. \end{aligned} \tag{4.13}$$

Therefore the sample furthest away from the critical composition will only have the same amount of interface if the droplet size is decreased as is the case in figure 4.19.

While the surface chemistry of the particles and the chemical composition of the final phases remains the same throughout the inversion series, the volume ratios and more importantly the kinetic pathway of the phase-separation change throughout. Because here the particles are able to support two types of curvatures concurrently it is for the first time possible to stabilise the solid-stabilised emulsion at the inversion point itself not just on either side of the inversion as in the catastrophic and transitional inversion [39, 40].

4.10 Summary and outlook

These experiments here show to my knowledge the first ever experimental creation of bijels. Key to emulsification is the interplay between particle trapping and the creation of a complete surface layer. Direct particle interactions can aid in structure stability when the interfacial tension is removed. The bijel morphology is formed during phase separation via spinodal decomposition. Other separation processes also lead to emulsification but with a different morphology. It is essential to use particles with appropriate wetting properties so that the irreversible trapping process occurs reliably and that the particles do not induce a preferred curvature in the interfaces but can support two signs of mean curvature on length scales larger than the particles themselves. Quenching through the critical point slows down the kinetics and permits the study of the phase-separation process using a confocal scanning microscope. Additionally, a critical quench allows the creation of properly three-dimensional sample volumes because spinodal decomposition is directly reached even for slow quench rates which is not the case for off-critical quenches. But reducing the quench rate too much will result in too low interfacial tensions during the formation leading to a lack of structural strength because the interfacial tension is responsible for the stability of the structure. If the interfacial tension is not high enough the bijel will lose its integrity. Faster quench rates up to 17°C/min are therefore preferable. The spinodal coarsening process is scaling invariant and therefore the pore size can be chosen by the amount of stabilising particles added to the system. The more particles are used for stabilisation, the smaller the typical pore size. Confocal microscopy scans into the depth of the sample shows that the bijel morphology extends throughout the sample holder which is 10's of domains thick demonstrating for the first time that an extended, three-dimensional structure can be stabilised solely by jamming solid particles which are trapped at interfaces. The stability of such a bijel is many months which is in accordance with the life time of standard pickering emulsions. Probing the mechanical strength of this new material reveals viscoelastic behaviour and a certain solidity obtained by the convoluted, sample-spanning, particle-laden walls. Extracts of this chapter are published in Nature Materials [98]

Overall, these experiments show that bijel formation is possible but requires a highly tuned system. Particularly the particle wetting behaviour is crucial. For reproducibility it is therefore important to find a way of controlling the particle wetting in a systematic manner. Kathryn White is currently working on this task. To further improve the attractiveness of this new material for industrial purposes she will also examine the behaviour of the bijel when the liquids inside the channels are counter-flowing. This will open up potential applications, for example as microreaction medium. At the same time a more quantitative examination of the rheological properties are currently under way. It will be particularly interesting to observe the rheological behaviour for different sample ages. So far it is not clear how the individual particles behave on the interfaces. Experiments shown here, however, indicate that rearrangements are still taking place after the system has visually stopped coarsening which are evidence for slow dynamics. The behaviour of particle dynamics on particle-laden liquid-liquid interfaces is examined in the next chapter.

Chapter 5

Off-critical temperature quenches

In this chapter I present studies of particle-stabilised emulsion formation in thin capillaries. These experiments rely on fast cooling and lead to a new route to bijels.

5.1 Introduction

An alternative way of accessing spinodal decomposition is to use fast quenches at off-critical compositions. At off-critical compositions the miscible regime of a binary-liquid system is separated from the spinodal decomposition region by a nucleation region as shown in figure 5.1. Fast temperature quenches are required so that the sample spends as little time as possible in the nucleation region. Experimentally this is a tricky task because heat transport is a diffusive mechanism and therefore intrinsically slow. To achieve fast quenches temperature baths are used which have a significantly higher or lower temperature than the sample. The steep temperature gradient will then lead to a relatively rapid quench. However, the quench rate will decrease towards the centre of the sample and therefore to obtain high quench rates the sample should be as thin as possible. Two experimental systems with an upper critical solution temperature (UCST) were chosen.

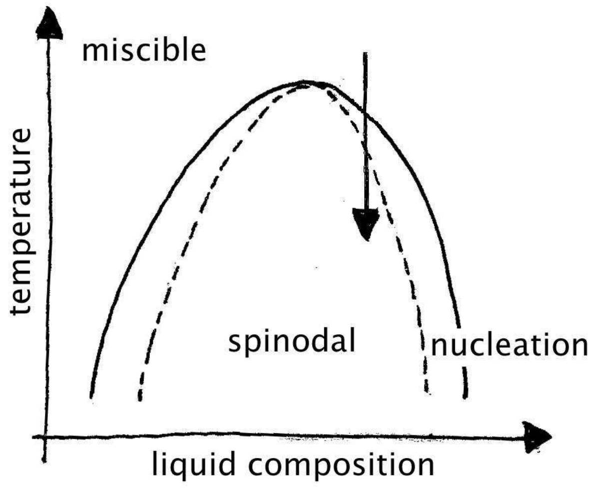

Figure 5.1: A typical phase diagram with UCST showing the miscible region outside the solid curve (binodal), the spinodal demixing regime inside the dashed curve (spinodal) and the two nucleation regions on each side between the dashed and solid curve.

For off-critical quenches pre-transitional wetting is more significant than for critical quenches. On approaching the binodal [99, 18] a wetting layer can form around the particles and this induces aggregation (see figure 5.2). The formation of aggregates in an initially homogeneous suspension of particles inside the miscible region of the phase diagram will lead to rapid sedimentation of the particles and is therefore not desirable during particle-stabilised emulsion preparation. To achieve fast cooling rates it is important to keep the sample volume small. However, it is known that for samples in capillaries the phase-separation mechanism can be affected by one of the liquids preferentially wetting the surface of the sample holder [81, 17]. If the sample holder is very thin this effect can dominate the separation process and therefore interfere with the spinodal demixing pattern that is necessary for bijel formation. A typical wetting-dominated pattern would involve the formation of tubes near the surface which speed up the separation process by transporting the more wetting phase to the sample holder surface.

It is not only the geometry of the sample holder that influences the phase

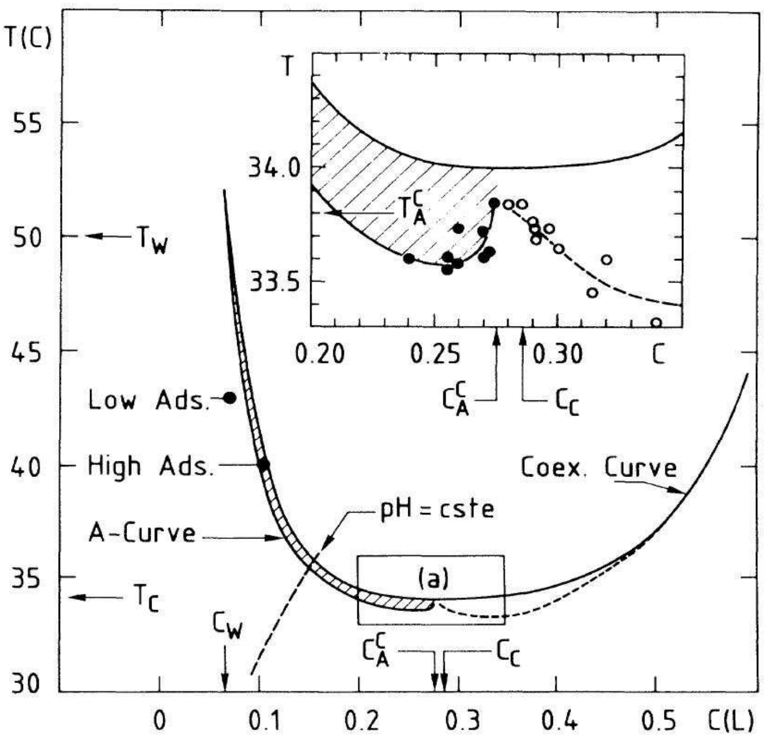

Figure 5.2: Phase diagram of lut/w system (lutidine mass fraction versus temperature) indicating the regions of pre-transitional wetting leading to aggregations. Left of the critical point the aggregation is significantly stronger than on the right hand side. At the critical point itself this effect is reduced. From [18].

separation process, the presence of the particles can also affect the observed pattern of the separated phases. Iraqi and Tanaka [83] have used computer simulations to study pattern evolution due to wetting effects on particles in a 2D system and found that whether the resulting pattern is bicontinuous or not depends strongly on the number of particles present and their mobility. They also show new attractions arising between particles within the demixed region of the phase diagram. For polymer systems Chung et al have shown that the presence of nanoparticles only adds to the effective viscosity of the system slowing down the separation kinetics but not altering the kinetic process itself, unless the particles sequester to the interfaces [73]. The jamming of particles on the interfaces can halt the separation process in these thin polymer films [74]. In the previous chapter I pointed out that although the viscosities differ for the polymer and lut/w system the interfacial tensions are similar, 0.9 mN/m and 0.22 mN/m respectively. The off-critical quenches, in contrast, explore the bijel formation process for higher interfacial tensions (of the order of 10 mN/m)at very low temperatures. The properties of the particle-laden interfaces are pivotal for the behaviour of any particle-stabilised emulsions. For example, the ability of particle-stabilised droplets to maintain non-spherical shape is controlled by the mechanical properties of the interfaces. These mechanical properties of solid-stabilised droplets can be probed indirectly by changing the internal volume [51], the interfacial tension [45] or by mechanically forcing them [52, 3]. More controlled experiments can be carried out in a flat trough [48, 87]. All these studies show that the behaviour of such interfacially jammed interfaces is determined by the cost of creating new liquid-liquid interfaces and the particle-particle interactions.

5.2 Experimental set-up

To examine the use of off-critical quenches for bijel formation I use two different alcohol/oil binary liquid systems which both have an upper critical solution temperature (UCST). Both phase diagrams exhibit their miscible and immiscible regions in an experimentally accessible temperature range but neither is entirely symmetric. The interfaces created during spinodal decomposition will only coarsen in a bicontinuous manner if the volume of the separated phases is similar. Since the separation will occur at very low temperatures for which it is assumed that the separated phases have almost pure compositions the ideal volume ratio of alcohol:oil would be 50:50. However, considering the phase diagram it is apparent that the further the quench is away from the critical point the larger the nucleation region will be through which the sample has to travel prior to reaching these low temperatures. Nucleation must be avoided if a bicontinuous coarsening is desired

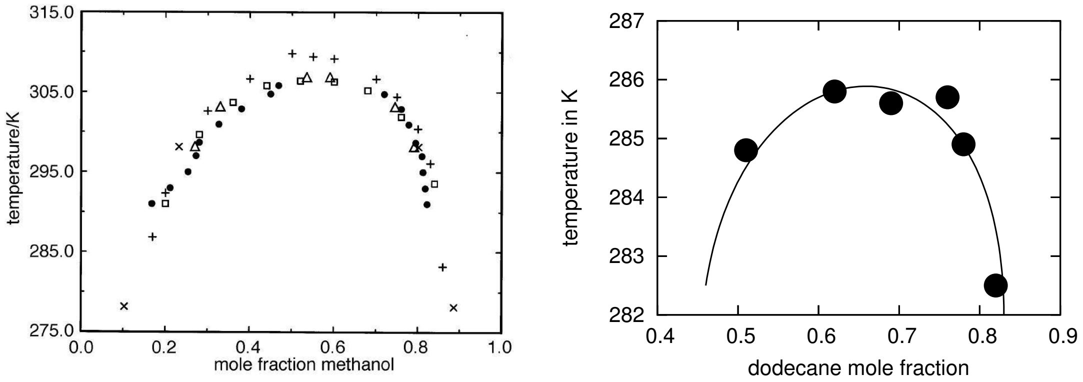

Figure 5.3: Left: Methanol-hexane phase diagram from [19] with mole fraction of methanol versus temperature showing data from several different groups. Right: Ethanol-dodecane phase diagram data from [20] with the dodecane mole fraction versus temperature.

and therefore I choose a volume ratio half way in between 50:50 and the critical volume ratio resulting in off-critical quenches. To avoid the nucleation region of the phase diagram the samples are rapidly and deeply quenched from the miscible into the immiscible region. Fast cooling rates into the demixing region can be achieved when exposing the sample to very low temperatures.

5.2.1 Liquids and particles

This first set of experiments is carried out using two different alcohol-oil systems, methanol-hexane (meth/hex) and ethanol-dodecane (eth/dod). Both have an UCST, but while the meth/hex system is immiscible at room temperature (UCST=36.4°C [19] with critical volume ration of alcohol:oil of 27.5:72.5 [100]), eth/dod is miscible at room temperature and only separates below 12.5°C (critical volume ratio of alcohol:oil at 36.1:63.9) [20]. This makes the meth/hex system easier to study, because observations can be carried out at room temperature, but it requires the sample preparation to be carried out in an incubator. The eth/dod system must be observed on a cold stage (as described below) but can be prepared in ambient conditions. For both systems cooling will induce phase separation. The volume ratios used for the off-critical quenches are 38.7:61.3 for meth/hex

	Freezing points
methanol	-97.6°C
hexane	-95°C
dodecane	-9.6°C
ethanol	-114.1°C

Table 5.1: Freezing points for the individual components of the alcohol-oil systems [23, 24].

and 43:57 for eth/dod. The phase diagrams of these two systems are shown in figure 5.3. The liquids used here are methanol (Aldrich, $> 99.9\%$), ethanol (Fisher, 99.8%), hexane (Fluka, $\geq 99.5\%$) and dodecane (Aldrich, $> 98\%$).

The freezing points of the liquids are given in table 5.1. Reliable data on the interfacial tension for alcohol-oil systems is sparse in the literature. Jańczuk et al [101] have measured the interfacial tension between dodecane and ethanol with various methods, however, surprisingly at a temperature of 20°C ±0.1°C at which point the system should be fully miscible unless the solvents are not very clean. Since it does take a finite amount of time for a pure dodecane droplet to equilibrate within the pure ethanol especially for larger droplet sizes, the authors might not have been aware that the experiments are not carried out at equilibrium conditions. The obtained results vary dramatically for the different methods between 23.20 down to 4.01 mN/m. These values give a good indication for the interfacial tension at very low temperatures where the system is assumed to separate into its almost pure components, but in my opinion overestimates significantly the interfacial tensions at the observation temperature of 0°C for the eth/dod system. For the meth/hex system the interfacial tension between the two equilibrated phases was measured in the range from 20°C up to T_c where it vanishes as shown in figure 5.4. At room temperature the interfacial tension between meth/hex is 0.35 mN/m. For fully immiscible liquids usual interfacial values are several 10 mN/m [2].

To stabilise emulsions by solid particles using interfacial trapping, the particles need to have appropriate wetting properties at the created interfaces. This

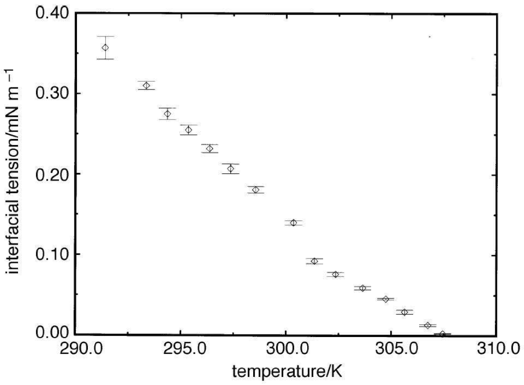

Figure 5.4: Interfacial tension of the binary methanol-hexane system for various temperatures [19].

implies that the particles need to have an affinity for both liquids. Silica particles produced with the Stöber technique have silanol groups (=OH-groups) on their surfaces which have a high affinity for polar liquids. As shown in section 3.1 the surface can be tuned such that the particle develops an effective affinity for the oil phase. To choose particles that are closest to neutral wetting from a range of different surface chemistries I create a series of standard Pickering emulsions by mixing. This leads to a set of emulsions that show a phase inversion [40]. I choose the sample closest to the phase inversion with the longest stability for the experiments that are described in this discussion here. For the meth/hex system this is straight forward since the emulsions are created and observed at room temperature. The eth/dod emulsions need to be observed at 0°C in an ice-bath which is slightly more tedious. The latter system also requires more hydrophobic particles implying that an emulsion inversion is not necessarily observed but the highest hydrophobicity is chosen. As described in section 3.1.2 the silanisation procedure was associated with difficulties and the wetting angle should therefore not be seen as well controlled.

The surface of the silica beads is very hygroscopic therefore it is important to store the samples in a desiccated environment to avoid the development of layers of surface water which can influence reproducibility of the experiments.

5.2.2 Sample preparation

Prior to the quench the samples are mixed in a small glass vial. The silica and the two liquids are all weighed to ensure an accurate composition. The constituents are combined in the miscible region which necessitates the the working at elevated temperatures which can be achieved inside an incubator. For the meth/hex system this is 40°C and 28°C for the eth/dod system. First, the liquids are left to reach the incubator temperature and are mixed to assure they are miscible before being brought into contact with the particles to avoid any hysteresis effects due to either liquid wetting the particles first. Once all three components are added I use an ultrasound probe (Sonics & Materials) to agitate the sample for 2 minutes at 3 Watts. To reduce the unavoidable heating of the sample obtained during mixing by ultrasound the sample bottle is kept in a water bath at the incubator temperature during the mixing. This procedure allows the particles to always be wetted by the miscible fluid first. Working at elevated temperatures also reduces the risk of premature phase separation. If either meth/hex or eth/dod particle suspensions in the miscible liquids are viewed under the microscope the dispersed particles are seen to undergo Brownian motion. This is a good test to check whether the sample preparation has been successful.

The cooling rate is determined by the temperature and cooling efficiency of the cryogen. For fast cooling rates it is important that the sample has as little bulk as possible. Therefore I use rectangular glass capillaries with a path length or inner height of 200 μm, a width of 4 mm and a length of 5 cm (Vitrotubes W3520, VitroCom Inc.). These capillaries have a flat surface of only about 150 μm thickness which should allow for good microscopy imaging. Unfortunately there are substantial variations in the thickness of the glass which reduces the imaging quality due to the occurrence of fringes. For an increased sample depth similar capillaries are used but with double the path length, i.e. 400 μm inner height, which is associated with an increased wall thickness of 300 μm no longer allowing microscopy with single-particle resolution.

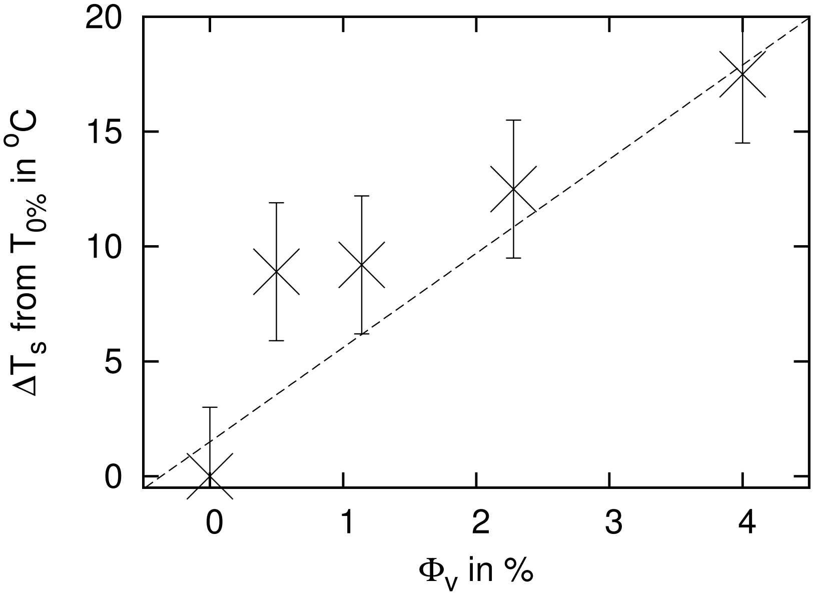

Figure 5.5: Ethanol-dodecane system with increasing particle volume fractions changing temperature starting in the miscible region until separation occurs. Separation temperatures are given in relation to separation temperature for binary liquids containing no particles. The line is a guide for the eye only indicating the increasing trend of the phase separation temperature.

To fill the pre-warmed capillaries one end is dipped into the prepared particle suspension and capillary forces will fill the sample holder. Once it is filled the top end is sealed with a finger so that no liquid is dropped out when the sample is removed from the reservoir. Both sample ends are subsequently dipped into two component araldite glue (either Araldite Rapid or Araldite Instant clear [1]), preferably in such a way that some of the araldite penetrates into the capillary to ensure good sealing. The sticky ends are wrapped in aluminium foil and the sample is left until the glue has set. It is important to try and avoid large air bubbles during the filling and sealing process. These can later perturb particle-laden interfaces when moving the sample holder to carry out observations.

When particles are added in large amounts to a binary liquid as is the case here, this can lead to a shift in the phase boundary. For a system with an

---

[1] Araldite Rapid was used at higher temperatures while Araldite Instant Clear was used at room temperature, both leading to setting time around 1 minute.

UCST the more particles are added the higher the separation temperature. I tested this trend for the eth/dod system. Using the cooling stage to reduce the temperature at 5°C/min from the incubator temperature (50°C) until separation occurs, gives a crude indication of this effect. Figure 5.5 shows how the separation temperature increases with volume fraction compared to separation without any particles being present. If I want to avoid premature phase separation I need to take this effect into account and an appropriate temperature must be maintained during the sample preparation and filling of the capillary which can be achieved inside an incubator.

A premature phase separation can be easily induced during sample preparation by accidental cooling. To avoid this, especially for samples containing higher volume fractions of particles it is therefore important to warm up all components, the capillary, glue, fingers touching the sample, etc before they come in contact with the liquids. When handling either of the two systems, care should be taken not to smudge the glass. Cleaning the glass surface with any solvent will induce phase separation when the solvent evaporates.

It is important to avoid any contaminations during the sample preparation since these will influence the separation behaviour and interfacial tension. Only fresh liquids should be used and glassware needs to be clean. The ultra-sound probe is carefully washed in water and the alcohol prior to its use. The bottles containing the hygroscopic solvents are sealed with a crown cap to keep any water and other contaminations present in air away from the solvents. To extract the liquids the needle of a syringe is pierced through a rubber seal in the crown cap. These needles and syringes are usually obtained from the medical industry. It is important to note that often these hypodermic needles are sold greased with silicon. While this improves the performance in medical situations it will contaminate the systems used here. It is therefore necessary to wash the needles thoroughly in the solvents before use.

When sealing the capillaries with araldite as described above, the liquids of

	Boiling point
$\ell\mathrm{N}_2$	-195.8°C

	Sublimation point
CO_2	-78.5°C

Table 5.2: Temperatures of the cryogens used for the deep quenches [23].

the sample are in direct contact with the glue. Although the two types of araldites used are oil and chemical resistant, this is not ideal, however, other methods have failed. By far the cleanest method, sealing the edges off by melting, cannot be done due to the flammability of the liquids and their sensitivity to temperature. It is possible to seal the ends with wax. Unfortunately, in the extreme cooling conditions used in these experiments the wax cracks and fails to seal the system properly over an extended period of time. Although the samples sealed by wax did not have a long life time, there were no observable differences in the quench results between the use of wax and araldite shortly after the quench indicating that sealing with araldite is an appropriate method.

5.2.3 Cooling method

To quench the miscible sample into the immiscible region I use a cooling bath into which the sample inside the capillary is submerged. The cryogens have a very low temperature which is advantageous for achieving fast cooling rates. When cooling so deeply the reheating process cannot be neglected and must be carried out with care. To achieve fast quenches a liquid nitrogen ($\ell\mathrm{N}_2$) bath (-195.8°C) or dry ice in hexane (-78.5°C) can be used (see table 5.2). To measure the effective cooling rates for the different cryogens, a small Type K thermocouple is inserted into the capillary and the quench protocol is carried out as usual. The output of the thermocouple was digitised using an acquisition card (National Instruments). The cooling behaviour measured for different cryogens is presented in figure 5.6. The associated rates for the initial cooling speed can be found in table 5.3. Although $\ell\mathrm{N}_2$ has the lower boiling point and results in deeper quenches, the quench speed

cooling rates	Sample holder	
	200μm	400μm
ice bath	65°C/sec	
CO_2 bath	143°C/sec	
ℓN_2 bath	55°C/sec	24°C/sec

Table 5.3: Heating rates for different cryogens measured inside the two types of holders used.

is actually slower than that for the sample in a hexane bath cooled by dry ice. This is due to the fact that liquid nitrogen has a very low heat capacity. The consequence is that when the -196°C cold nitrogen touches the room temperate sample it heats up very locally and dissipates the heat from the sample only slowly into the bulk of the nitrogen. As soon as the liquid nitrogen heats up at the surface of the sample it will change into the gas phase. Therefore a gas layer develops that surrounds the sample which decreases the heat transfer even further and acts as an insulating layer reducing the cooling rate experienced by the sample. Using basic heat transfer theory [102] to get an estimate on the situation shows that the effective cooling rate depends strongly on the thickness of this insulating gas layer and if this gaseous layer exceeds around 70 μm cooling by CO_2 will actually be faster. The measurements show that the dry ice in hexane bath indeed cools about three times as fast. Both, cooling in the CO_2 and the ice bath, results in very reproducible cooling rates while for the liquid nitrogen the rates can vary more. This is understandable since moving the capillary within the nitrogen bath (which happens when submerging the capillary) will change the thickness of the gaseous layer. However, if dunked in straight away using a pair of tweezers and if the capillary is released quickly, the cooling rates are reproducible. To obtain a gentle reheating, the samples are kept in a CO_2 or ice bath after the initial quench so any rearrangements can happen under steady temperature conditions. After this the meth/hex system is brought to room temperature for observation while the eth/dod system is observed on a temperature stage (Linkam Scientific Instruments) at 0°C.

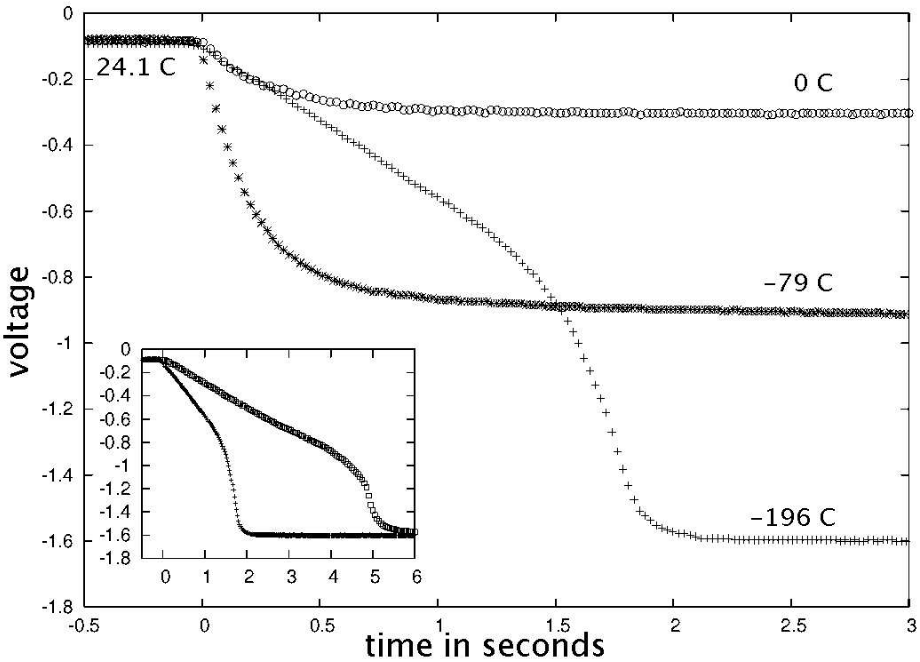

Figure 5.6: Cooling rates inside sample holder for different cryogens: ○= ice bath, +=ℓN_2, ∗=CO_2 in hexane bath; inset: comparison between thin (+) and wider (square) capillary for ℓN_2.

Slow cooling (and also heating) up to 30°C/min can also be carried out using this temperature stage. However, with most objectives, it is not possible to use the lid on the stage in the set-up used here. This leads to temperature gradients inside the sample and can have significant effects on the structure formation. While the bottom of the sample is at the chosen temperature, the top part of the sample is surrounded by air at room temperature. The thermal mass of the objective can also influence the behaviour of the sample. Especially when using oil objectives, the objective is very close to the surface of the sample. Particularly at the beginning of observations the objective can transmit a lot of heat into a cooled sample or vice versa. At the same time care must be taken not to damage the objective by exposing it to an inappropriate temperature environment which can permanently damage the delicate optics inside the objective.

5.3 Effect of interfacial tension on particle-laden interfaces

Aim and context

Before focusing on bijel formation in off-critical quenches I want to show the importance of the interfacial tension for the case of a binary liquid droplet emulsion. This demonstrates the properties of the particle-coated interfaces that underpin bijel formation.

As discussed in the previous chapter the Young's modulus of a jammed, particle-laden interface is proportional to $\frac{\gamma}{d}$ where γ is the interfacial tension between the two liquids and d the particle diameter [48]. The interfacial tension determines how strongly the particles are held on the interface. The balance between the surface pressure created by particle-particle repulsions and the cost of interfacial area determines the extent of jamming. An additional force pushing the particles closer together will eventually cause buckling when the surface pressure becomes equal to the interfacial tension [49]. In examining the lut/w bijel system the particle-particle repulsions appear to be short ranged and it has already become apparent that the character of the particle-laden interfaces changes upon jamming because particle rearrangements are restricted. Subramaniam et al [52, 3] have shown that for such an interfacially jammed system to rearrange extra interfacial area needs to be created so that individual particles can slide past each other. If large external stresses are applied particle-scale rearrangements will occur to accommodate for these stresses leading to a plastic deformation. For two emulsion droplets to coalesce two mechanisms have to occur first: the droplets need to approach each other and the liquid film of the external phase between them needs to thin to make coalescence possible. At the same time a hole needs to nucleate in the particle covered interfaces. For this to occur the particles need to be able to rearrange [51]. If the droplets are fully covered by particles this does not occur under normal circumstances. Coalescence, however, can then be forced mechanically [52]. Since the barrier to rearrangements amongst the particles is determined by the interfacial tension I will examine the behaviour of droplets in contact with others when the interfacial tension and the internal volume of the droplets is decreased. A binary liquid system is suitable for such an experiment because increasing the temperature will lead to a decrease in composition and therefore a change in interfacial tension and volume. Near the phase boundary the change in volume will be dramatic for non-symmetric systems as the one here.

Sample and method

A shallow temperature quench from the mixed region using a 0°C ice bath using a sample containing Φ_v=2% particles silanised with 10^{-1}M DCDMS at standard off-critical composition of the dod/eth system results in the formation of a droplet emulsion as seen in the top frames of figure 5.7. The majority of these droplets are spherical and although they are in close contact with each other they are stable against coalescence. From this state the sample is heated on the Linkham temperature stage while at the same time being observed by confocal microscopy. The sample is warmed from 0°C to 41°C at 30°C/min and the images in figure 5.7 start at 9°C with each frame being 1.5°C warmer than the next with the last frame at 30°C. The time between frames is 3 seconds.

Results and discussion

Figure 5.7 shows the response of a droplet emulsion to heating from the immiscible region across the binodal into the miscible region. For the first few images not much change is visible although the critical temperature (T_c=12.5°) has been exceeded by the fourth image. This indicates that the particle-laden interfaces slow the exchange of molecules. During the first few images the system has therefore not yet reached the equilibrium composition for that temperature and

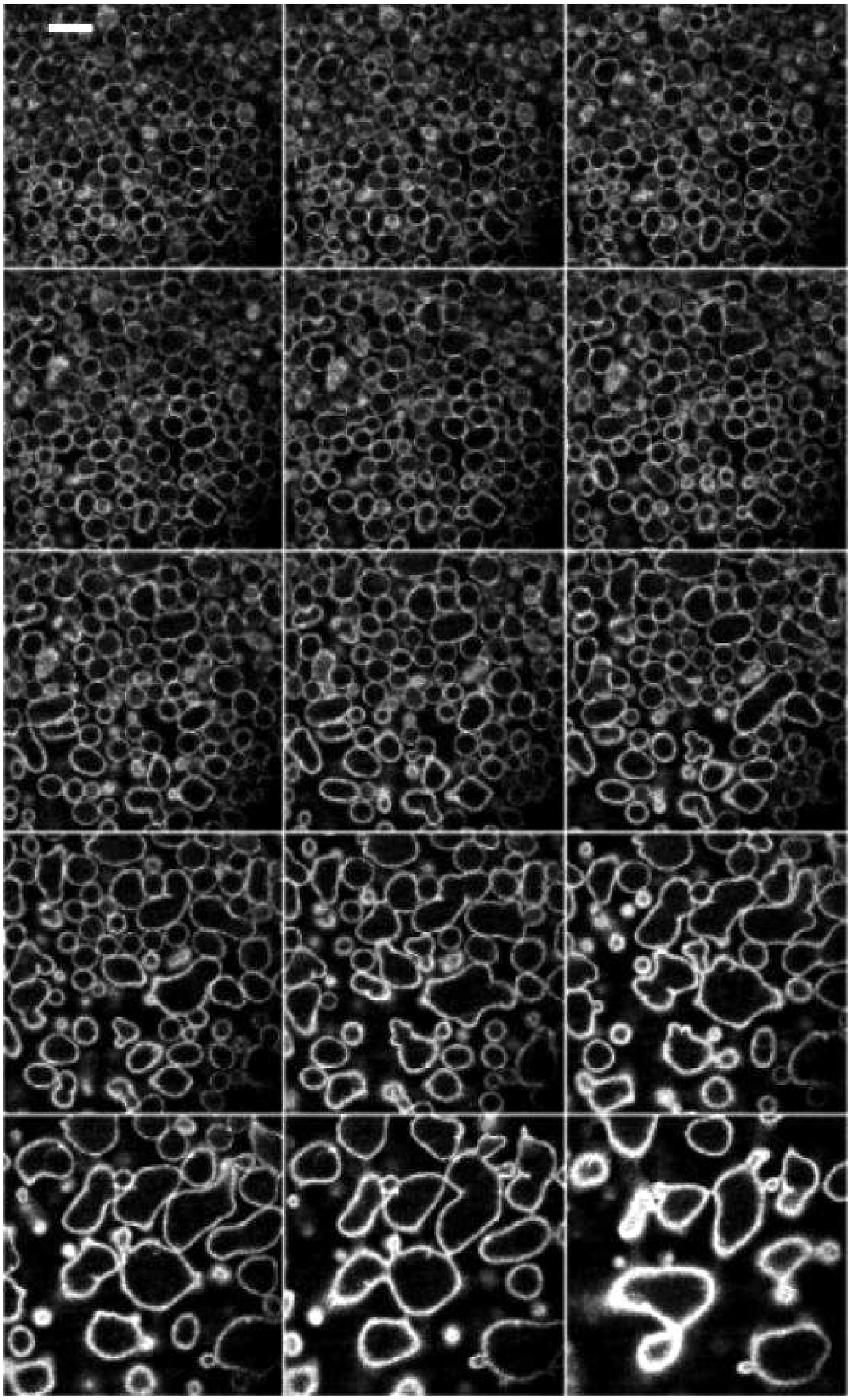

Figure 5.7: Off-critical eth/dod droplets heated into miscible region at 30°C/min. Sample contains Φ_v=2%, images start at 9°C with a change of 1.5°C (or Δt=3 sec) between images with time progressing from left to right for each subsequent row. Scale bar = 100 μm.

consequently the interfacial tension is still high giving the droplets stability against coalescence. Eventually, with a further raise in the temperature the interfaces seem to become more supple and droplets start to coalesce. As discussed previously the particles prefer the alcohol to the oil, they therefore prefer the surrounding ethanol-rich phase in contrast to the dodecane-rich phase inside the droplets. The coalescence process is therefore in accordance with the mechanism proposed by Fuller et al [51]. For the coalescence to take place the particles need to be able to rearrange on the interfaces. The images show that this is only possible once the interfacial tension has decreased. Evidently the particles are initially jammed on the interfaces at high interfacial tension (touching droplets are clearly visible in the early frames of figure 5.7) and when the interfacial tension gradually decreases this jamming is decreased. To complicate matters the internal volume is decreased at the same time. Overall the energy cost of rearrangements reduces with the interfacial tension, the particle-coated interface "unjams" and particle-free holes on the interfaces can be nucleated. Due to the presence of surrounding droplets this leads to coalescence. Furthermore it is visible that the merged droplets relax their appearance towards a more spherical shape although this takes place over several frames. This supports the picture of more mobile particles because the particle-laden interfaces lose the ability to sustain non-isotropic stresses when the interfacial tension is reduced. By contrast for high interfacial tension non-isotropic stresses can be supported as demonstrated by the existence of non-spherical droplets [45] or necks and bumps in the bijel (section 4.4). In the last image a temperature of 30°C is achieved and a broadening of the interfaces is clearly visible. By this time the phases have reached equilibrium with the interfacial tension vanishing so that the particles can diffuse away from the original interface leading to the observed broadening. Eventually all walls disappear by the time 41°C is reached.

From research on blood cells and vesicles it is known that a system with high bending modulus will always try and maintain smoothly curved surfaces when

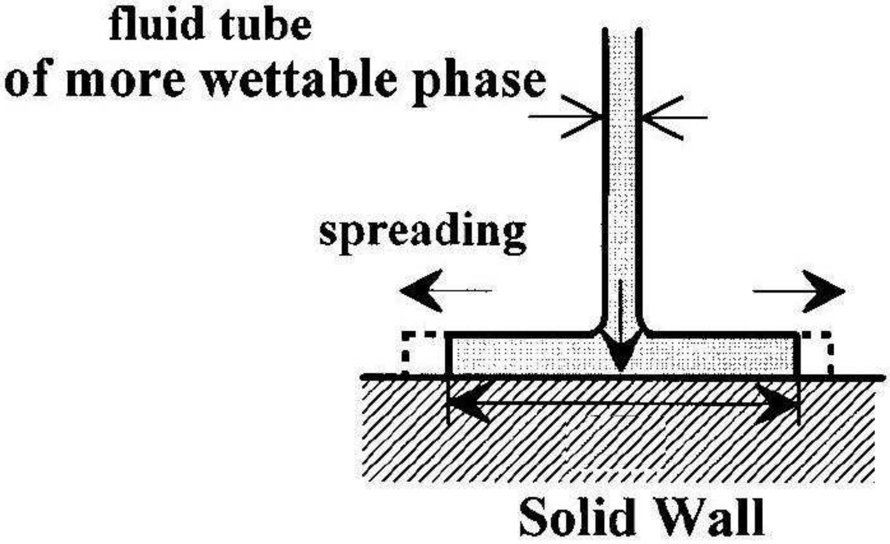

Figure 5.8: Schematic figures explaining the wetting dynamics of bicontinuous tubes to the strongly wetting wall which is dominated by the hydrodynamic tube instability. From [17].

deforming. Individual particle-stabilised droplets, however, can reach a point where the decrease in internal volume leads to catastrophic failure so that they crack or crumple [45]. This implies that the mechanical properties of particle-laden interface are dominated by the cost of extension and hence the creating of new interfaces. If droplets are in close contact during heating no crumpling or cracking is observed because a decrease of the interfacial energy cost can be gradually achieved via coalescence.

Although the eth/dod system containing silanised silica particles forms multilayers of particles on the interfaces the particle-laden interfaces still behave analogously to the monolayers observed during the lut/w bijel formation with FITC-doped silica. In both systems a transition seems to occur between a jammed state where no rearrangements of the particles are preferred and a more supple liquid state that allows particle-scale rearrangements to occur such that anisotropic stresses cannot be maintained. In both cases interparticle interactions are present. In the eth/dod these lead to the formation of multilayers, most likely due to capillary condensation of polar impurities from the oil phase. This phenomenon has been studied by ellipsometry [103] and cannot be avoided in this alcohol-containing partially miscible liquid system. In the lut/w systems I have shown that for large enough interfacial tensions jammed particles can be attracted by Van-der-Waals forces. Nevertheless, in both systems the interfacial tension ultimately determines the behaviour of the particle-laden interfaces. It controls not only structure formation but also induces the important jamming of the particles which then lends particle stabilised emulsions their mechanical stability.

5.4 Wetting effects for thin samples

Aim and context

In bijel formation it is essential to form bicontinuous domains. To reach the region where demixing occurs via spinodal decomposition and therefore yielding bicontinuous domains requires fast quench rates for off-critical compositions. To achieve such fast rates the bulk of the sample needs to be as small as possible and therefore thin capillaries are chosen as sample holders. For such thin, quasi-2D sample holders the phase-separation kinetics can be modified from bulk behaviour. Tanaka suggests that the spinodal demixing can be dominated by hydrodynamic wetting tubes [81, 17]. When a wetting layer forms on the sample holder surface and spinodal decomposition follows in the middle of the sample the wetting layer will be fed by a supply from the bulk delivered through a tube as shown in figure 5.8. The growth of the wetting layer can occur much faster than by diffusion. For thin samples this will lead to the formation of tubes from the top to the bottom of the sample. If such tube formation occurs this will influence the spinodal demixing pattern and possibly dominate the resulting morphology and could jeopardise bijel formation.

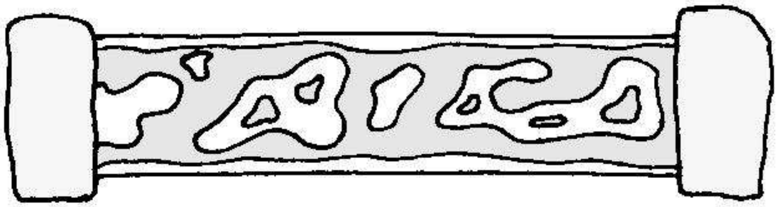

Figure 5.9: Sketch of a sample showing that the formed structure macroscopically spans the sample. 5 cm long holder, 4 mm inner width, 200 μm inner height.

Sample and method

To investigate the effect of wetting on the separation mechanism two different sets of samples are prepared. Firstly, deeply quenched off-critical samples are examined. Using the meth/hex system containing Φ_v=1.3% of particles silanised with 10^{-2}M DCDMS or Φ_v=1% silanised with 5×10^{-1}M DCDMS are quenched for 5 seconds in a CO_2 bath followed by 5 minutes in an ice bath. Secondly, slower quenches at critical composition are carried out for the eth/dod system containing Φ_v=2% particles silanised with 10^{-1}M DCDMS and cooled at 30°C/min on the Linkham temperature stage from room temperature to 0°C.

Results and discussion

For the fast off-critical quenches the sample cannot be observed while the separation is taking place. Only after the sample has separated and rested for 5 minutes in an ice bath is it moved underneath the microscope and examined there. These samples show that extended domains have formed throughout the capillary as shown schematically in figure 5.9. Figure 5.10 shows sections of two similar samples. It is possible to see stabilised necks and bumps (see arrows in figure 5.10) but more importantly the tube like formations which have formed from top to bottom inside the capillary. The typical domain size is several hundred microns and therefore the sample is not expected to be thicker than one domain size in the 200 μm thick holders. It seems, however, that apart from the connected

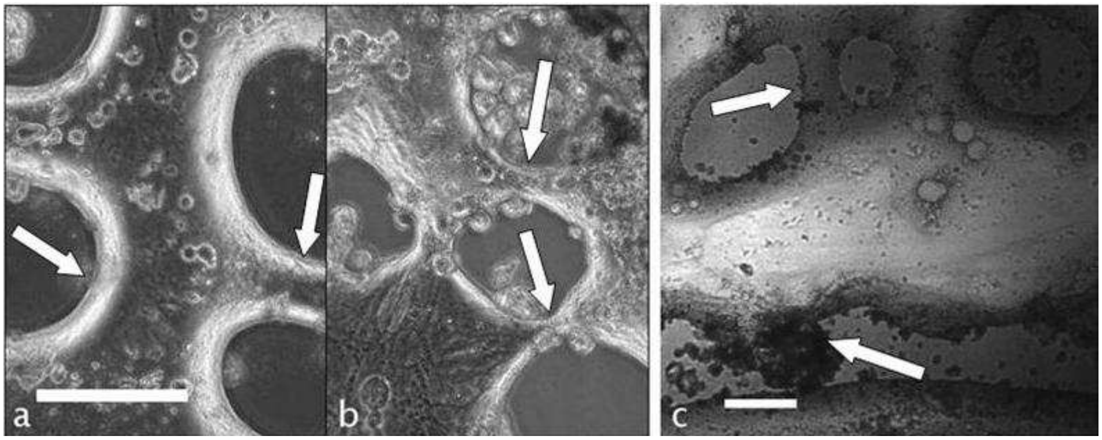

Figure 5.10: Tube formation between the top and bottom of off-critical meth/hex samples quenched with CO_2 followed by a 5 minute ice bath. Arrows indicate particle-stabilised necks and bumps. **a** and **b** are Φ_v=1.3% with scale bar = 500 μm and **c** has Φ_v=1.0% with scale bar = 100 μm.

nature the pattern does not resemble that of spinodal demixing, but is dominated by the more polar phase wetting the inside of the capillary. Nevertheless these images demonstrate that extended structures with variations in mean curvature on length scales larger than the particle size can be stabilised by solid particles.

From the second set of experiments it is clearly visible in figure 5.11 that the eth/dod system undergoes spinodal decomposition when it is quenched through the critical point. The particles are preferentially wet by the ethanol-rich phase making the spinodal pattern discernible in the reflected confocal images but the particles do not sequester to the interfaces. The spinodal pattern is also clearly visible in the bright field images. It is seen to coarsen until the appearance of droplets obscure the view.

How is it possible that spinodal decomposition is taking place, creating its typical morphology for the critical quench but not for the off-critical, deep quench although the same thin capillaries are used as sample holder? The wetting effect described by Tanaka is driven by the lower Laplace pressure for the flat wetting interface compared to that in the tube ($\sim \frac{\gamma}{R}$) as seen in figure 5.8. At the start of the demixing process this effect is therefore stronger when the interfacial tension

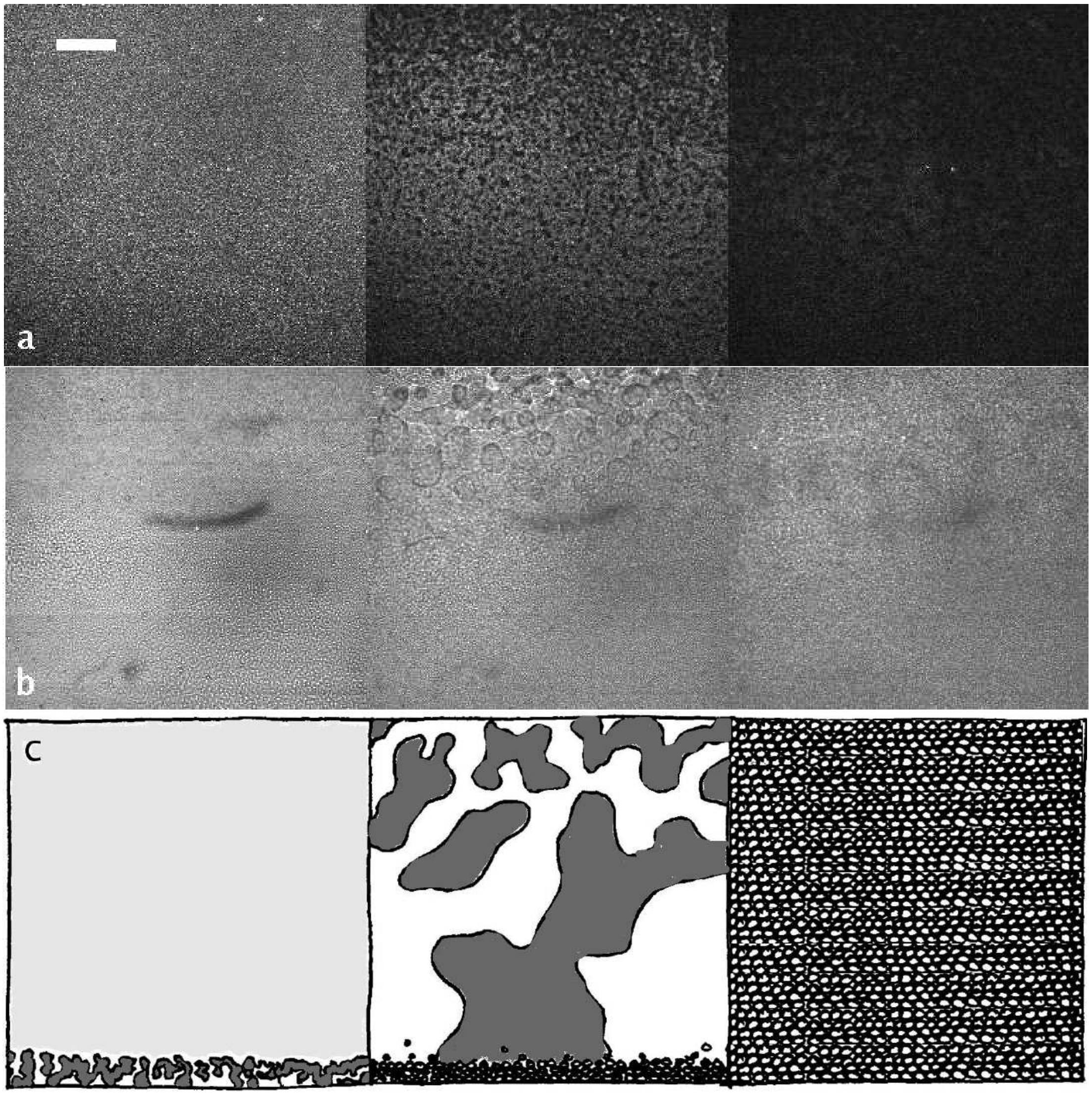

Figure 5.11: Two critical eth/dod Φ_v=2% samples each quenched at 30°C/min. **a** recorded with reflected confocal microscopy, **b** recorded with bright field microscopy, **c** cartoon showing that initially the system separates via spinodal decomposition, then coarsens unhindered by the particles and finally small droplets appear obscuring the rest of the sample. Scale bar = 100 μm.

is higher. However, at a later stage when the tubes coarsen (radius increases) during the demixing process the pressure difference will decrease and slow down the tubewetting process. For the deep, off-critical quench a very high interfacial tension is achieved very shortly after the sample is submerged into the cryogen while for the critical quench the composition and therefore the interfacial tension increases much more slowly and not to such high values. This is partly due to the slower quench rate and depth but also supported by the critical slowing down occurring near the critical point. However, the dewetting via tube formation cannot only be due to the high interfacial tension since it is also observed in polymer systems [22] where the interfacial tension is similar to the dod/eth system. Another reason for tubes occurring preferably in the CO_2-quenched systems is that extreme temperature differences enhance condensation. CO_2 very quickly cools the glass of the sample holder such that the sample holder surface will be initially significantly colder than the sample itself. The condensation on the surface can then encourage wetting and subsequently tube fed wetting to occur.

Furthermore the critical eth/dod system undergoing spinodal decomposition under conditions where the particles are not sequestering to the interfaces can give insight on double phase separation as discussed in section 4.7. Although the particles are not sequestering to the interfaces droplets occur during the coarsening of the system. Because the densities of the liquids are very similar the capillary length[2] which determines the typical length scale the domains can obtain before gravity takes over is several hundred microns. Droplets occur far below this domain size. In this case here the interfaces are not laden with particles, therefore the secondary quench that is occurring will be due to an interfacial quench as proposed by Tanaka [92] and discussed in section 4.7 and not due to the diffusion being reduced across the interfaces because of the presence of the

---

[2] The capillary length is given by $l = \sqrt{\frac{\gamma}{g\Delta\rho}}$ where γ is the interfacial tension, g gravitational acceleration and $\Delta\rho$ the density difference of the liquids.

particles.

5.5 Spinodal decomposition for off-critical quenches

Aim and context

To reduce the dominating effect of wetting for off-critical quenches there are two ways. Firstly, a slower quench rate can be used since the wetting effect is stronger for the quickly cooled sample holder due to extreme temperature differences inducing condensation. A less rapid quench will also increase the interfacial tensions less quickly reducing the wetting effect at early times. Secondly, more bulk can be added to the sample by using a 400 μm thick sample holder instead of the thin capillaries with 200 μm inside height. This increase in depth will reduce the chance of the wetting tubes forming all the way through the sample. At the same time the use of thicker sample holders is an attempt to form bijels that are deeper than 1 domain size. Chung et al [73, 74] have shown that for high viscosity polymers it is possible to trap particles at the interfaces which, once jammed, will prevent the further separation of the polymers. In the previous chapter I argued that the formation of bijels in the lut/w system is very similar to this polymer system because the high viscosity slows down diffusion and hydrodynamic coarsening in the same manner making the interfacial tension the controlling variable. While the interfacial tension of the lut/w system (up to 0.22 mN/m [16]) is comparable to the polymer system (0.9 mN/m [22]) the interfacial tension is expected to be significantly larger for the deep, off-critical quenches (several 10mN/m). It is therefore of interest to see whether the off-critical system still behaves like the other two critical systems although the interfacial tension is increased during the bijel formation process.

Sample and method

Slower, but still deep quenches are carried out in the 200 μm thick samples using the off-critical meth/hex system containing Φ_v=2% (10^{-2}M DCDMS particles). The first sample is quenched for 5 seconds in ℓN_2 and then for 5 min CO_2 before being observed at room temperature, while another sample is quenched for 30 seconds in ℓN_2 prior to observation at room temperature. Both samples are characterised using reflected confocal microscopy. The recorded z-stacks are rendered into 3-d images using ImageJ [96]. To examine spinodal decomposition in a thicker sample holder an off-critical eth/dod sample containing Φ_v=2% particles silanised with 10^{-1}M DCDMS is quenched in ℓN_2 for 30 seconds followed by a 5 minute ice bath and is then examined on the Linkham cold stage at 0°C. A z-stack is taken through the first 100 μm of the sample using reflected confocal microscopy.

Results and discussion

Liquid nitrogen quenches in thin sample holders show that extended bicontinuous domains can be formed. Tube formation is no longer as apparent as for the CO_2-quenched samples although this is difficult to distinguish since these samples are only a single domain in thickness. The 3-d reconstructions in figure 5.12 show that both samples form freestanding necks. Although the two samples shown in the figure are identical in preparation prior to the quench the resulting structures have very different particle-stabilised interfaces. The short ℓN_2-quench has a much lumpier surface than the smooth appearance of the long ℓN_2-quenched sample. These emulsion structures show bicontinuity but are only one domain size in depth.

Figure 5.13 shows a z-stack through the deeply quenched eth/dod sample at off-critical compositions in a thicker 400 μm sample. The images in the figure are separated by 6 μm in depth starting near the sample surface. In the central

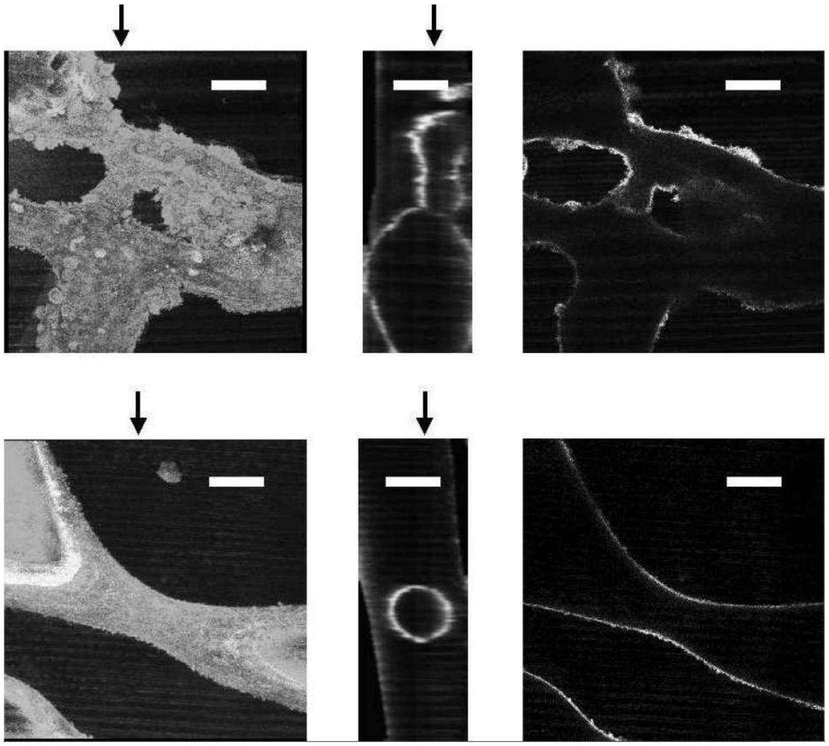

Figure 5.12: Left: Three-dimensional projections obtained from confocal z-stacks on meth/hex system. Both samples have Φ_v=2% (102 particles) and are cooled in ℓN_2 but for different lengths of time. Top: 5 sec ℓN_2, 5 min CO_2, bottom: 30 sec ℓN_2. Observation carried out at room temperature. Centre: side view, right: cross section through centre. Scale bar = 100μm.

images a spinodal pattern is clearly recognisable stabilised by particles. Near the surface of the sample holder no tube formation is observed at this location in the sample, while towards the centre of the sample the spinodal morphology is replaced by the appearance of droplets. It seems that the use of ℓN_2 as a cryogen combined with the larger geometry of the sample holder reduces the tube wetting formation proposed by Tanaka sufficiently to allow the sample to separate via bicontinuous domains. Further into the sample this bicontinuity is lost and is replaced by a droplet morphology. This can be explained by taking into account that the cooling rate decreases towards the centre of the sample. If the cooling rate is too slow demixing will happen via nucleation for off-critical quenches and not via spinodal decomposition.

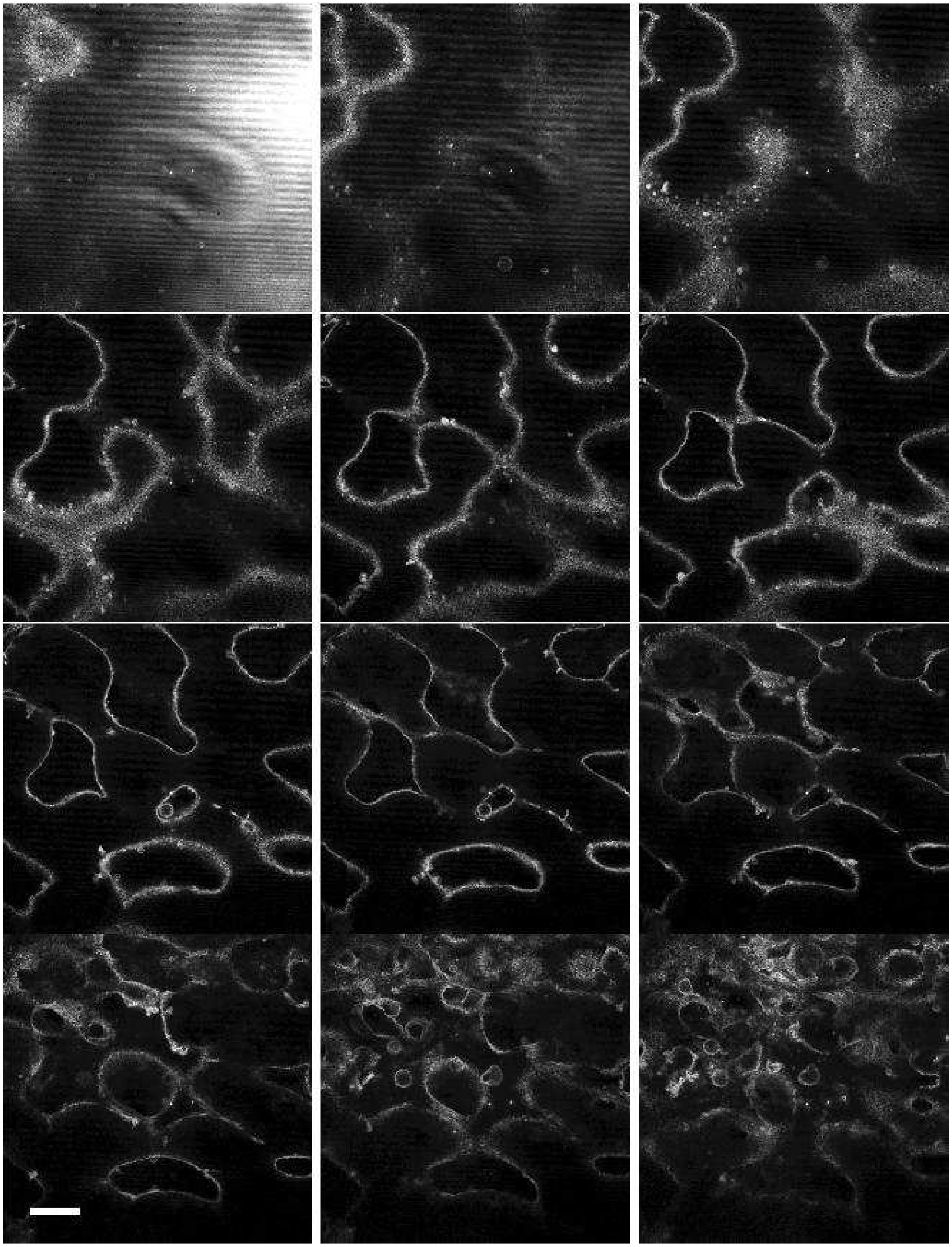

Figure 5.13: Eth/dod system containing Φ_v=2% 10^{-1}M DCDMS particles in larger 400μm thick holder, quenched for 30 sec in ℓN_2 followed by a 5 min ice bath before observation on cold stage at 0°C. Confocal microscopy images taken through the first 60 μm of the 400 μm thick sample in 6μm steps. Depth increases from left to right for each subsequent row. Scale bar = 100μm.

Taking all these observations as well as those from the previous section into account I conclude that for off-critical compositions there is an optimal quench rate. For too fast quenches wetting effects gain in importance while for too slow quenches the sample does not demix bicontinuously.

These samples furthermore show that the particles, although present in multilayers on the liquid-liquid interfaces are still able to stabilise a bicontinuous geometry. Deviations from a constant mean curvature on a scale much larger than the particles are stable for at least the duration of the sample examination. The interfacial tension is supposedly much larger during the formation process than for the bijel formation in the lut/w system or that in the polymer systems [73, 74] and the particles are shown to successfully trap under these different conditions.

The slow quench on the critical dod/eth system shows how effective a high interfacial tension can be for improving particle trapping. Comparing the critical and off-critical eth/dod quenches it is possible to see that while the particles stabilise the bijel in figure 5.13 the same particles clearly do not sequester to the interfaces during the critical quench (figure 5.11). Near the critical point the interfacial tension is very low. In contrast for the deep quenches the interfacial tension is much higher. Although the particles do not change their wetting properties they are trapped much more efficiently in the latter case showing that a large interfacial tension can also trap particles that do not have ideal wetting properties.

5.6 Comparison of 2-D alcohol/oil and 3-D lut/w bijels

The main difference which leads to successful three-dimensional bijel formation in the lut/w system but not in the eth/dod or meth/hex system is the difficulty of achieving a bicontinuous demixing pattern. For the latter systems an optimum quench rate has to be reached. Even if this optimum quench rate has been determined it is not straight forward to quench exactly at this rate throughout the sample. In laboratory experiments there will always be some temperature gradients towards the bulk of the sample when changing the temperature from the outside. This heat transport issue limits the size of samples significantly because spinodal decomposition does not take place for slow off-critical quenches. In contrast the critical quenches in the lut/w system lead to bicontinuous structures for a tested range of quench rates that spans two orders of magnitude. In reality this range is slightly reduced to make the bijel self-supporting after the formation process. Nevertheless, the thin bijel created in the 400 μm sample or the thinner bicontinuous extended domains do contribute to understanding bijel formation although they are only about one domain size in depth. In contrast to the polymer systems [73, 74] and the bijel in the previous chapter the interfacial tension here is about two orders of magnitudes higher. The free energy gain for particles located on the interface is therefore very large and the particles become trapped at the interfaces created during the phase separation process. This shows that the trapping of the particles is successful for a large range of interfacial tensions. While it might be obvious to assume that an immediate high interfacial tension will be beneficial due to the large gain in the free energy upon trapping, a high interfacial energy will also lead to a much faster coarsening of the system with the consequence that interfaces are moving much more rapidly through the sample. West et al [42] suggests for related systems that the success of particles being picked up on moving interfaces will depend on the speed of the interfaces. The different quench methods here show a certain independence of the particle trapping efficiency from the speed of moving interfaces indicating that either the increase in surface tension leads to an equal increase of the speed of an interface with which particles can still be successfully trapped or it shows that the majority of particles are trapped during the initial separation process and do not get picked up at a later stage during the coarsening. This is an interesting point because other methods apart from demixing via phase separation can be used to create bicontinuous interfaces. However, this will only lead to successful bijel formation if the particles also sequester to already sharply defined interfaces.

The apparent increase in domain separation for a Φ_v=2% sample in the eth/dod system compared to the lut/w system is most likely due to the fact that in the alcohol-oil system the particles form multilayers on the interfaces while the lut/w system exhibits jammed monolayers. The presence of multilayers in general does not seem to have a large impact on the actual bijel formation. However, it is likely that the multilayers may lead to a different jamming behaviour which would only become apparent in ageing studies which have not been carried out and therefore the solidity of these multi-layered interfaces and their associated stability is questionable. The multi-layered system also shows much less reproducibility. This is partly due to the difficulty of producing appropriately wetting particles but also due to the delicate dependence on the quench route.

5.7 Summary and outlook

Off-critical quenches can induce bijel formation but only for a limited sample depth. The limitation in depth is due to the necessity of having an optimum quench speed. On the slow quench side this is limited by the fact that at off-critical compositions the phase diagram exhibits a nucleation region upon crossing the phase boundary, while wetting effects dominate for rapid quenches leading to a maximum quench rate. The resulting quasi-2-D samples obtained by the deep, off-critical quenches show that bijel formation is also possible for systems with a much higher interfacial tension than in the lut/w or in the two-dimensional polymer systems [74]. As for the lut/w system the wetting properties of the particles are crucial for bijel formation and only small changes in the wetting behaviour can stall the stabilisation of bicontinuous structures. The alcohol-oil systems presented here additionally require that the particle surface is tuned using a silanisation process. This has not been achieved in a controlled enough manner while the FITC-doped particles worked well for the lut/w system without modification.

Experience led to the abandonment of the alcohol-oil system and switching to the lut/w system where it was possible to gain, to some extent, control over parameters like particle wettability and quench rate.

Parts of this work are published in Langmuir [72].

Chapter 6

Pressure quenches on 2,6-lutidine-water system

This chapter describes the development of a pressure cell suitable for sample imaging using confocal microscopy. After showing the reason for interest in a pressure cell like this, its design is presented, followed by improvements that had to be carried out. Finally, some results using this pressure cell are presented.

6.1 Introduction

To experimentally create bijels I have already shown that the 2,6-lutidine/water (lut/w) system is very suitable when quenching through the critical point. Here I present the attempt of using pressure on the lut/w system to reach phase separation via spinodal decomposition. As discussed in the previous chapter temperature cannot be used to achieve fast and deep quenches for samples thicker than a few hundred micrometers. This is due to the fact that temperature changes spread diffusively throughout the sample which is a rather slow process. A much faster quench can be achieved when using pressure as the changing variable. Changes in pressure are distributed at the speed of sound resulting in a sub-millisecond adjustment of the pressure (on the mm-lengthscale used here) in

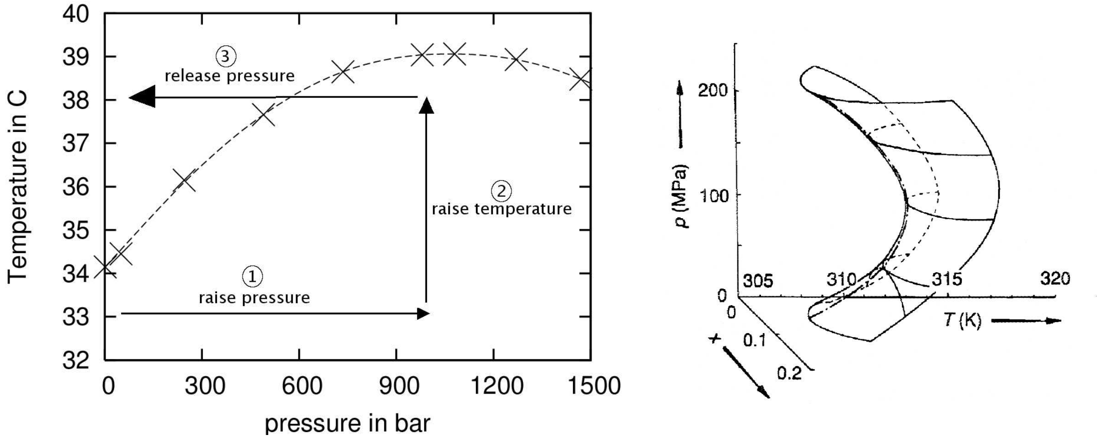

Figure 6.1: Pressure-temperature phase diagram for critical composition (left) and phase boundary surface for 2,6-lutidine-water mixtures in concentration-temperature-pressure space (right) [21].

contrast to the slow diffusive changes during temperature quenches.

To reach spinodal decomposition via a fast and deep pressure quench, a binary liquid system must be chosen that phase separates when the pressure changes. Mixtures of 2,6-lutidine and water exhibit this property. A transition from the miscible to the immiscible regime can be achieved when releasing the pressure from 1kbar to atmospheric pressure at a selected constant temperature in the range of 34.15 °C to 38.5°C [21]. These pressure and temperature values are in an experimentally accessible range. Figure 6.1 shows the phase boundary between the miscible and immiscible regime. Another advantage is that the 2,6-lutidine/water system is miscible at atmospheric pressure for temperatures below 34°C. This is valuable because it allows the preparation of the sample at ambient temperature and pressure. Therefore the experimental challenges are limited to the actual quenching procedure.

I aim to perform pressure quenches in the 2,6-lutidine/water system and wish to directly image the phase transitions as well as the final quench product using microscopy. This is a challenging task because pressure set-ups are inherently bulky. Nevertheless microscopy under pressure has been achieved for example for phase transition experiments on polymer systems. In this case the sample itself is in contact with the pressurising oil [104]. While this is acceptable for polymer systems this will not work for our system. Carboni et al [105] working on liquid crystals use Argon instead to avoid contamination in their liquid crystal system. But for the binary liquid system here a sample-compressing, contamination free approach is needed as for the light scattering pressure cell by Kohlbrecher et al [106] where the sample is concentrically compressed but sealed from the pressurising medium. The pressure cell developed here achieves this for pressures up to 1.5 kbar using a sample compressing piston. Magnifications up to × 20 are possible with a required working distance of 4 mm or larger.

A general feature of adiabatic pressure changes is the fact that the temperature will change if the pressure changes. For binary liquid systems it has been shown that this leads to changes of the order of 5 m°C/bar for shallow quenches [107, 108]. This can possibly have an effect of several degrees for the 1 kbar pressure release I am planning to carry out. Therefore the quenching temperature has to be chosen appropriately to remain in the demixed region. If a system is quenched into the demixing region the accompanying enthalpy change can have an increasing effect on the temperature reducing the change in temperature due to the pressure quench [107].

6.2 Pressure cell design

To realise fast and deep pressure quenches on the 2,6-lutidine/water system I collaborated with Hugh Vass, a specialist in designing and building pressurising equipment. He designed the prototype of the pressure cell which we adapted progressively during the course of the project to the version presented here. We started our collaboration when the cell was able to withstand pressures up to 5 kbar for water based samples with a single window potentially allowing the use of basic reflected light microscopy.

To develop the prototype of the pressure cell towards a system suitable for my needs there are three main points which need to be addressed. Firstly, it must be possible to obtain pressures of at least 500 bar, preferably up to 1 kbar and to hold these pressures at a stable enough level. Secondly, it is necessary to heat the sample in a controlled manner avoiding overshooting and fluctuations of the final temperature. Since we are working close to a phase boundary, both, fluctuations in temperature or pressure, can move the system into the immiscibility region and lead to an undesired, premature quench and must therefore be avoided during a successful experiment. Thirdly, to observe the sample before, during and after the quench the design of the pressure cell needs to allow optical imaging. Additionally, it turned out that the chemical aggressiveness of the lutidine is another major problem that needs to be dealt with during the course of development.

My most significant contribution to the work is the optimisation of the imaging quality which in return reduced the maximum achievable pressure from 5 kbar to 1.5 kbar. However, this is still well within the necessary pressure range. Additionally I carried out repeated test runs to iteratively discover and solve problems in pressure and temperature stability as well as testing different materials to improve chemical resistance of the components. I modified the heating set-up to increase the control over the sample temperature and encouraged the development of the grease-free sealing technique. Hugh Vass has carried out all mechanical work and used his vast knowledge and experience in pressure related projects to accommodate my requirements.

A schematic layout of the final pressure cell is shown in figure 6.2. The set-up consists of two main components. The surrounding ram with a ram piston and the actual pressure cell with a smaller sample piston. Both, the titanium pressure cell and the sample piston have a diamond window fitted to permit imaging. To pressurise a sample the pressure cell is loaded while still separated from the ram and sealed with the smaller sample piston. This combination is then screwed into the ram. A hand pump is used to insert oil into a chamber (not shown on diagram) to move the ram piston downwards which in turn pushes the sample

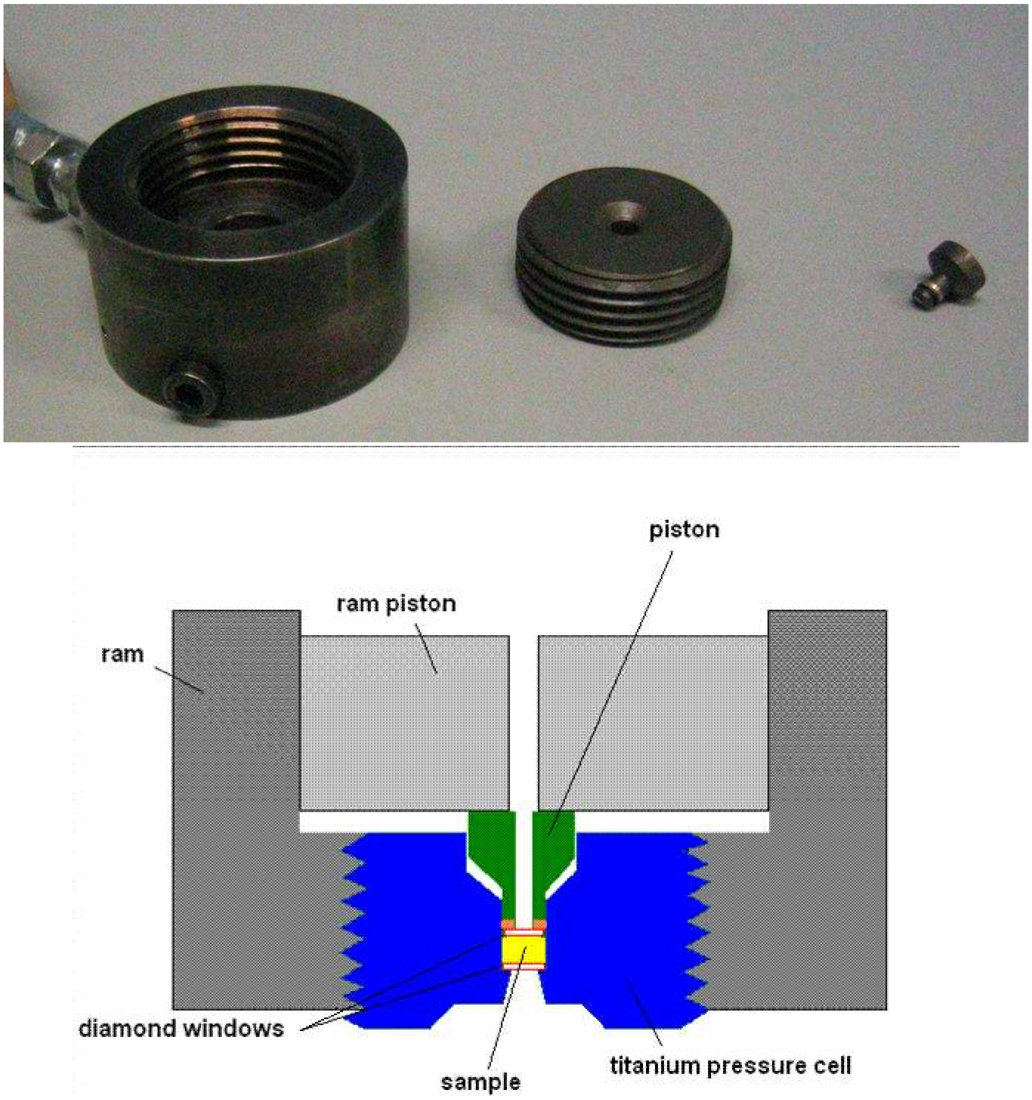

Figure 6.2: Top: photograph of ram, pressure cell and sample piston. Bottom: schematic diagram of pressurising system. Pushing the piston downwards raises the sample pressure.

piston into the pressure cell compressing the sample and thereby increasing the pressure of the sample itself.

In the following sections I discuss the different components of the pressure cell and how they were optimised for the 2,6-lutidine/water system. The result is a pressure cell that allows satisfactory fluorescent confocal imaging before, during and after applying pressure while maintaining control over pressure and temperature changes and fluctuations.

6.2.1 Pressure control

In this section I discuss the pressurising mechanism. In particular how to optimise applying, keeping and releasing the pressure in this particular cell.

The sample is pressurised by pushing a cylindrical piston into a cylindrical cavity thereby compressing the volume of the sample trapped in the cavity. Pressure will only build up in this way if the piston seals firmly against the cavity walls preventing any leakage of the sample material. Naturally, the piston needs to have a smaller diameter than the cavity within the cell so that the pressure can be adjusted by changing the position of the piston. A sealing mechanism at the tip of the piston is responsible to seal the sample against any leakage. The pressure is therefore maintained by the seals. Originally, the piston was designed to apply pressures up to 5 kbar. It therefore consisted of a conventional three seal system which has three seals in series made of different material to act in adjacent pressure ranges. Closest to the front with the embedded diamond window was a greased rubber seal responsible for sealing at low pressures. Next in line was a teflon seal that can hold pressures up to 3 kbar. To seal at pressures higher than 3 kbar a third seal of phosphor bronze was used. However, to improve imaging we deliberately reduced the maximum pressure to 1.5 kbar (see section 6.2.3) which made the phosphor bronze seal unnecessary. Additionally, there were significant problems with the rubber seal. All tested rubber materials suffer in contact with lutidine and quickly break. Teflon in contrast was found to keep its performance in contact with lutidine. Using a single teflon seal which fits the cavity tightly does perform very well under these conditions. A significant advantage of the teflon seal is that greasing of the seal is unnecessary and therefore contamination of the sample can be avoided. The teflon is soft enough that it adapts to the shape of the cavity already at low pressures. To ensure the reliable performance of the seal a system is used that increases its sealing ability with increasing pressure.

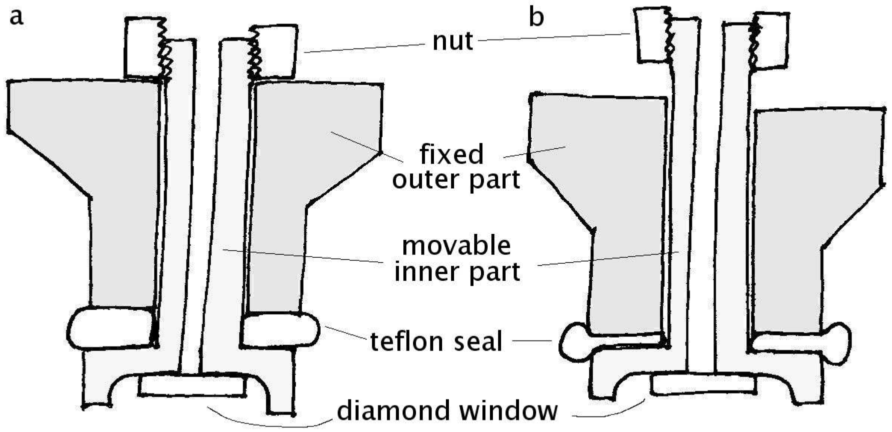

Figure 6.3: The sample piston is built in such a way that it seals increasingly with increasing pressure. Two movable parts make the teflon seal bulge at higher pressures.

The schematic diagram in figure 6.3 shows the beautiful self-sealing mechanism. The piston actually consists of two separate parts which move with respect to each other. Only the outer part is pushed down into the pressure cell by the ram piston. The component holding the window, however, is pushed upwards by the pressure inside the sample cell. The teflon seal is consequently squeezed between the two. The higher the pressure inside the cell, the harder the two piston parts are pushing together and the more the teflon seal is getting compressed in between. The teflon seal therefore bulges towards the cavity wall increasing the strength of the seal. A screw on top of the piston can set the minimum bulging of the teflon at the start of the experiment so that the piston seals even at low pressures. The teflon will slowly deform under pressure requiring the seal to be replaced eventually. This is, however, a slow process and a new teflon seal is not only cheap but also easily replaced. Such a replacement is only necessary after several sessions.

Apart from the necessity of containing the sample material inside the pressure cell it is also important that the sample chamber does not deform like a balloon if pressure is to be kept constant. This would not only reduce the pressure but more importantly would lead to material failure and abruptly destroy the pressure cell.

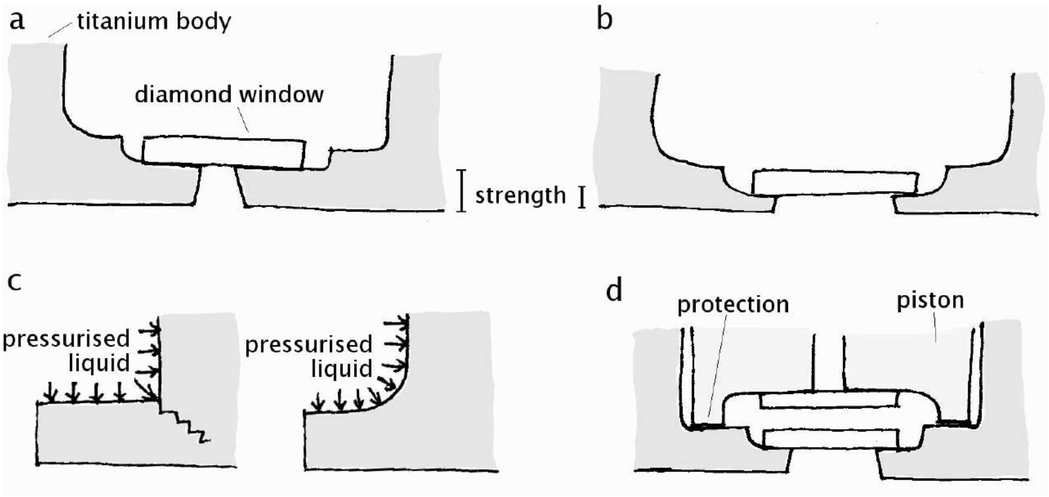

Figure 6.4: The amount of pressure the cell can contain reduces with the thickness of the titanium and for larger window openings. Rounded edges are less prone to break than sharp ones. The windows are set in such a way that if the seal fails the windows are not destroyed.

The main body of the pressure cell consists of titanium which is a very strong material. The bulk material will easily withstand pressures up to 1.5 kbar without deformation. The failure prone areas are where the material is required to be less bulky. As discussed in section 6.2.3 it is important for imaging purposes to have the objective as close to the diamond window as possible. However, this implies that the titanium which holds the window in place needs to be as thin as possible. The thinner the titanium at this point, the lower the pressure which the cell can maintain before the material fails. Figure 6.4 shows the points where failure is most likely to occur. Rounding off any sharp edges helps to distribute the strain in the weak region reducing the risk of breaking.

Another advantage of titanium is that it is chemically very inert. This is necessary to deal with the lutidine and it simplifies the cleaning of the cell, and is also useful because the cell will not rust in contact with water.

To observe the sample inside the pressure cell under the microscope, light must be allowed into the the sample cavity. Therefore the pressure cell needs windows. These need to be large enough (see section 6.2.3) and at the same time very strong. Diamond is a good choice in this situation. The strength of the diamond exceeds that of many other materials and allows for a relatively wide window opening while at the same time keeping the window thin which is important for imaging. Diamond windows perform optically very well under pressure without introducing birefringence or other artefacts and are additionally very scratch resistant which is a huge advantage when cleaning the cell. The windows used here are made from 0.5 mm thick, circular diamond disks with a diameter of 2.5 mm. To hold the windows in place, the opening in the titanium is smaller than the diamond window. The larger the diamond-titanium overlap (see figure 6.4) the higher the pressure that can be sustained.

Both diamond windows (in the piston and at the bottom of the pressure cell) are set in such a way that if pressure is applied they are pushed into their sockets. This method alone is, however, not sufficient to seal against material and pressure leakage and it is necessary to glue the windows in place. While the initial design has achieved pressures up to 5 kbar with water based samples, the lutidine samples pose a new challenge. Various different apoxy adhesives (Araldite 2014), high temperature curing and UV glues did not withstand exposure to lutidine and pressure. However, eventually Hugh Vass found a specialist high pressure glue (M-Bond GA-61, M-Line, cured at 150°C) to hold the windows in place even after long lutidine exposure [1]. To obtain maximum performance of the diamond windows they need to sit in the socket very evenly. If the base is not flat enough the window will bend leading to green and red stripes in the transmitted image, a sure indication that the window will loosen shortly which results in the pressure being lost. At a few hundred pounds a piece the diamond windows are quite valuable. Because a sudden pressure loss is possible, especially during the development phase, the piston and cavity are designed such that the diamond windows will not smash onto each other and break. Instead part of the metallic

---

[1] Kathryn White also found that the instant adhesive TakPak 382 by Loctite performs well in contact with lutidine. This is useful for high resolution microscopy at ambient pressure because samples can be sealed with standard coverslips.

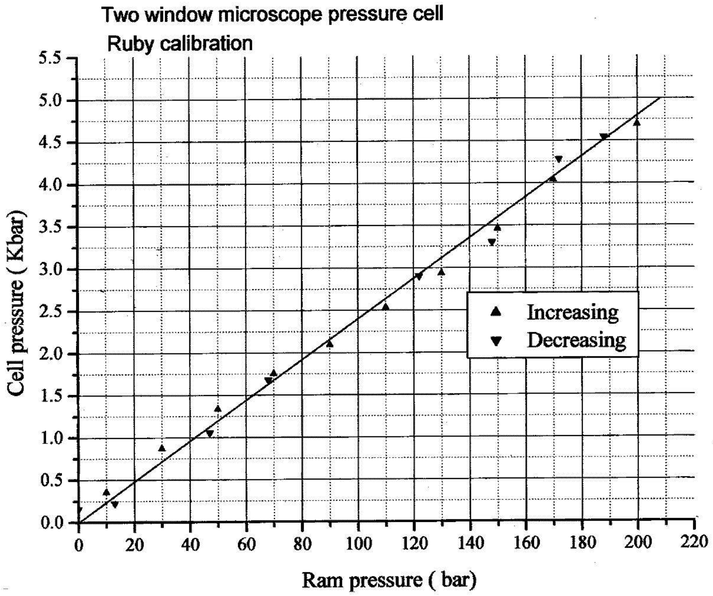

Figure 6.5: Calibration curve for pressure cell relating ram pressure to the pressure inside the cell. Using He-Ne laser a speck of a ruby inside the pressure cell is excited. The ruby emission lines shift linearly with pressure. Calibration carried out by Hugh Vass.

piston will hit the bottom of the sample cavity leaving the windows intact (see figure 6.4d).

While these points are essential to build up and maintain a constant pressure it is equally important that the external force applying the pressure does not drop over time to achieve a satisfactory pressure control. To push the piston into the cavity, a handpump is used to pump oil into a chamber inside the ram piston which in turn pushes the mushroom piston into the cavity. This requires very little effort and the pressure can be read off the gauge once the system has been calibrated using the linear shift of ruby-emission lines under pressure (see figure 6.5). The handpump and gauge are connected via a 1 m long, standard flexible hydraulic pipe to the ram. When applying pressure in the cell the hose contains the compressed oil as well. It turns out that the pressure inside the cell continuously drops because the driving pressure is gradually lost. This is most probably due to the hose expanding slowly or possibly due to effects inside the pump and leads to a drop of the overall pressure inside the system requiring regular pressure top-ups. We managed to circumvent this problem by introducing an additional valve (valve II) between the ram and the hose. Unfortunately, this also implies that it is no longer possible to tell the pressure inside the sample cavity. However, the stability of pressure is more important than knowledge of the exact value of the pressure for the experiments here rendering this a minor issue. Moreover, this additional valve also increases the quench speed.

Now that the pressure can be raised to the appropriate level and held there I can now look at the pressure release rate. Initially the pressure was released by simply opening the valve at the pressure pump and letting the pressurising oil expand back to its original state. The manual and therefore slow opening of the valve and the long hose do not allow for a very fast quench speed. To increase the speed of the pressure release, a new exit with a larger cross section was fitted between valve II and the ram. Fitted with an electronic valve this new exit allows very fast opening and dumping of excess oil in an external container instead of leading the oil back into the pump. To improve the response of the oil we changed to break oil (DOT 4) used in standard cars. It is important that any o-rings used in the various components (valves, ram piston) need to be resistant to this oil. If for example the o-ring in the ram piston degrades, the ram piston will not move smoothly and the pressure release will be slowed. If o-rings in the valves break, the pressure will be lost prematurely. For valve II it is important to note that this valve only keeps pressure from one side. Increasing the pressure on the side of the pump while the valve is closed will destroy the o-ring.

Overall, Hugh and I have achieved a lutidine resistant pressurising system that drops less than 100 bar on the timescale of at least minutes. We also increased the speed at which the raised pressure drops to atmospheric level during a quench. Estimates using the scanning rate of the confocal microscope show that the quench is achieved on the order of $\sim$ 10 milliseconds.

6.2.2 Temperature control

To carry out a pressure quench in the 2,6-lutidine/water system, the sample needs to be heated to a fixed temperature at elevated pressure. If the temperature rises higher than the selected value an unwanted, premature phase separation can take place (see figure 6.1). When working so close to a phase boundary it is important that the temperature does not overshoot, while the rate at which the temperature changes is less important.

To keep the pressure cell design as simple as possible the temperature control unit is designed as an external add-on. A copper coil containing heating wires is fitted around the stainless steel ram body. Heat conducting fabric wrapped around the copper ensures good thermal contact between the two components. Later a copper brace with embedded heating wires was used instead to simplify the set-up and optimise thermal contact. But this is more important for controlled heating like in the previous chapter and less crucial here. A PID (proportional-integral-derivative) controller regulates the power output to the resistive heater using the feedback from a thermocouple mounted on the pressure cell.

For the development of the pressure cell an old Honeywell UDC 3000 PID controller was available which is set by trial and error. Depending on the setting of this PID controller (discussed in more detail in section 3.3.2) the temperature will rise quickly with a large overshoot or slowly with less overshoot. I found the best way to heat the sample inside the pressure cell quickly enough (to reduce the risk of pressure drops) was to first heat at a fast rate to a temperature a few degrees below the necessary temperature and then to change the settings to a slower speed to approach the final temperature much slower to reduce overshooting oscillations. For the new modern PID controller (Lakeshore 331) this precaution is not be necessary.

The heat conductivities of the ram (heat conductivity of stainless steal is about 16 W/mK) and the titanium body (22 W/mK) are relatively low. This does not worry us since we are not interested in fast temperature changes. It is,

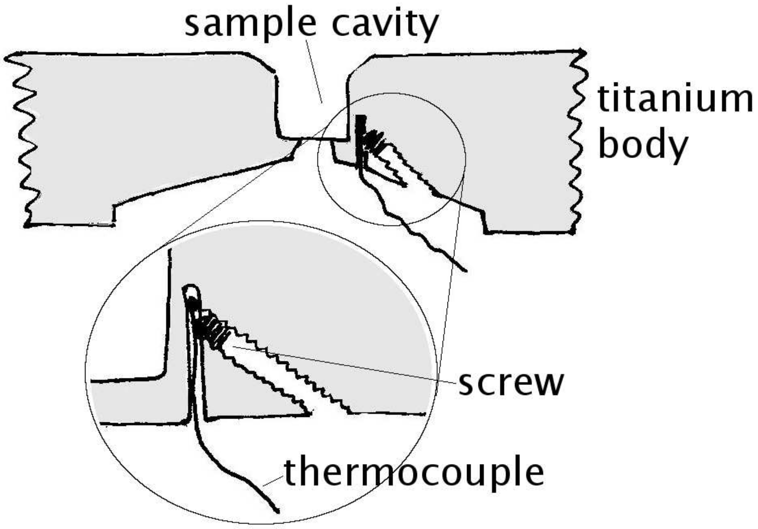

Figure 6.6: The thermocouple is positioned as closely to the sample cavity as possible. Good thermal contact is achieved using a sunk screw to clamp the thermocouple in place.

however, important to realise that there will be a finite delay in the distribution of the temperature from the outside of the ram to the inside of the titanium cavity where the sample is situated. To control the temperature of the sample, ideally, the thermocouple which regulates the heating mechanism should be placed inside the pressurised cavity. This would, however, lead to complications in pressure control and cleaning of the sample. Alternatively, I have placed the thermocouple in a small hole as close as possible to the sample cavity (see figure 6.6). The PID controller therefore controls the temperature in the vicinity of the thermocouple which is as close to the sample as experimentally feasible. This is a significant improvement to the initial position of the thermocouple outside of the ram or later on top of the titanium cell. Having the thermocouple closer to the sample and therefore having a better knowledge of the sample temperature reduces the amount of accidental phase separations due to wrongly estimated temperatures. If the temperature is measured further away from the sample there is an offset of temperature inside the sample cell from the measured one which will change over time and makes the actual sample temperature a very unpredictable value.

Apart from optimising the heating set-up the most important point learnt during the temperature work on the pressure cell is that temperature gradients within the sample are extremely damaging for structure formation. When observing slow quenches in thin capillaries on a microscopy heating stage where one side of the capillary is cooled while the top side is at room temperature, strong currents are observed which are able to rip particle covered interfaces. Such an evident temperature gradient is an extreme situation, however, the opposite is achieved here. The sample sits in a cavity that is almost entirely surrounded by a large block of metal. Once the temperature of the block is established this leads to a very uniform temperature distribution inside the sample. This successfully suppresses temperature fluctuations so that no convection is going on within the sample cell. As a result a slow pressure quench that leads to nucleation results in very uniformly sized droplets (see figure 6.7. This indicates that the coalescence process is not disturbed. Arditty et al [109] have shown that emulsion droplets that are not yet fully covered with particles coalesce more quickly the smaller they are. This leads to a surprisingly small size distribution which is also expected from computer simulations [110]. When obtaining droplet emulsions inside the small capillaries used in chapter 5 an inhomogeneous size distribution is obtained indicating that convection is present within the sample. The process of coalescence is then more encouraged for some of the droplets and not for others leading to a less homogeneous size distribution of droplets. For bijel formation these fluctuations could lead to the loss of the characteristic bicontinuity. This points out how important it is to avoid any changing temperature gradients that induce convection when trying to produce bijels.

The experiments on pressure quenches have been carried out when the temperature was stabilised using the old PID controller and without a cooling unit. Further development of the system from the temperature quench set-up will give more control over heating rate and temperature stability but more importantly here, will reduce temperature overshoots.

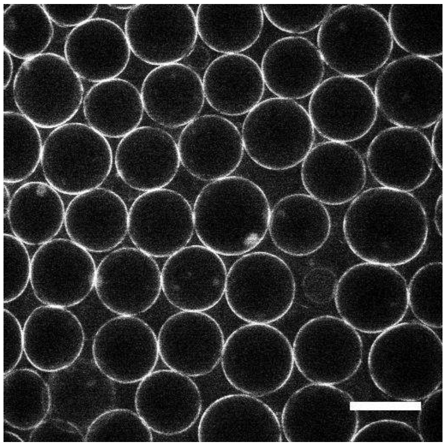

Figure 6.7: Fluorescence confocal microscopy images after a slow off-critical pressure quench leading to nucleation of droplets. In the absence of temperature fluctuations the droplets have a very uniform size. Quench from 1 kbar at 36°C containing Φ_v=0.1% particles. Scale bar = 100 μm.

6.2.3 Imaging requirements

I want to study pressure quenches of the 2,6-lutidine/water samples to observe the behaviour of colloids during and after their host liquid undergoes a phase transition. To systematically study this process it is important to be able to check the state of the sample before the quench, as well as while the separation and coarsening process is happening and to have the means to examine the end product in situ. Confocal microscopy is a suitable method.

While confocal microscopy can be a straight forward matter when working under standard conditions, imaging inside the pressure cell poses significant challenges. As discussed earlier in the experimental methods chapter (chapter 3) microscopy is generally optimised for biological samples resulting in the following typical situation:

- the objective can get arbitrarily close to the coverslip
- none of the light travelling between the sample and the objective is blocked
- sample and objective are separated by a coverslip of 170μm thickness

- the coverslip is made of glass with a refractive index of n_{glass}=1.51

- the sample is suspended in water (n_{water}=1.33).

Any violation of these conditions will almost certainly influence the quality of the imaging negatively. In the case of the pressure cell the bulky titanium body does not permit the objective to get arbitrarily close to the window. It also restricts the size of the window opening and therefore part of the light sent into and reflected from the sample is blocked. Additionally, the diamond window has a thickness of 500 μm and a refractive index of 2.41 varying significantly from the standard situation. While the refractive index of the lutidine-water mixture (between n_{water}=1.33 and $n_{lutidine}$=1.50 [16]) does not divert dramatically from that of water, the refractive index will no longer be homogeneous after the binary liquid has phase-separated. Another impairment is the fact that the sample is surrounded by reflecting metal. Light passing through the sample will therefore not only be reflected from the sample but also by the sample walls adding noise to the actual signal.

Microscopy can be carried out in transmitted and reflected mode. Since the phase-separated sample is opaque and the condenser cannot get close enough reflected confocal microscopy is more useful here. Therefore I aim to optimise the optics of the pressure cell for the reflected light mode. However, even if not optimised, the transmitted mode is very valuable for checking the initial state of the sample and for positioning the pressure cell correctly allowing to detect problems prior to the start of the experiment and to reduce setting-up time.

During the course of the project I have addressed the above problems and tried to find an acceptable compromise between pressure concerns and imaging performance. The following considerations and changes lead to acceptable imaging conditions for confocal microscopy inside the pressure cell.

Working distance

As discussed previously in section 6.2.1 the titanium body needs some bulk to be strong enough to withstand the applied pressures. At the same time I wish to bring the objective as close to the window as possible, since the numerical aperture, which is pivotal to the imaging performance, can be larger the shorter the working distance of the objective. The thinner the titanium near the window the lower the maximum pressure that can be achieved inside the cell. By reducing the maximum pressure inside the cell to 1.5 kbar instead of the originally planned 5 kbar the thickness of the titanium can be reduced to 2 mm. However, due to the external mounting of the thermocouple and the need to support the edges of the diamond windows, objectives with a working distance (WD) of less than 4 mm are not able to focus inside the sample. A ×10 objective with a working distance of 16.0 mm and a numerical aperture (NA) of 0.3 is available in the COSMIC lab and was used for initial tests. While this objective and most other ones are optimised for standard situations it is also possible to purchase specialist objectives designed to deal with different situations. We were able to purchase a ×20 extra long working distance (ELWD) objective that although having a large working distance of 7.4 mm still has a numerical aperture of 0.45. It is also equipped with an adjustable collar to compensate for different coverslip thicknesses which is necessary to cope with spherical aberration due to the thick diamond window used here. With this specialist objective I can deal with the current bulkiness of the pressure cell.

Reflections

The shiny titanium metal body surrounding the sample has the disadvantage that it strongly reflects light. Therefore light that is accidentally scattered back into the objective will superimpose and dominate the actual signal. Testing this effect by inserting paper into the cell showed that spurious reflections can be reduced this way.

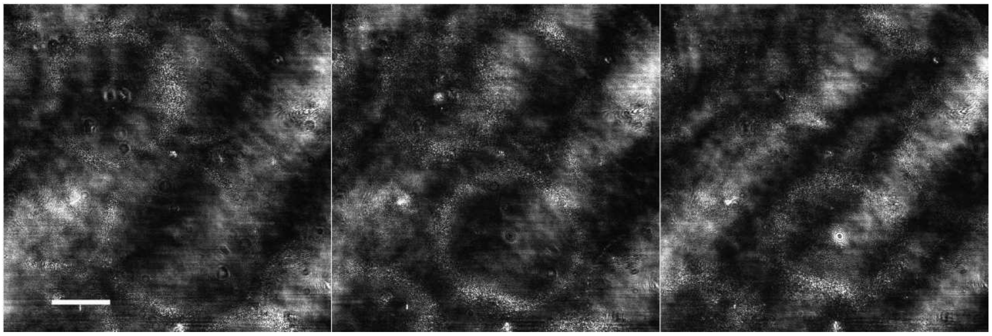

Figure 6.8: Reflected confocal microscopy images of water-dodecane emulsion stabilised with 0.5μm Stöber silica particles inside pressure cell taken with ×10 objective (WD 16.0, NA 0.3). The images are depth wise separated by 15μm. The reflections off the silica particles are dominated by noise. Scale bar 100μm.

Because the inside of the cell needs to remain chemically resistant, painting the surface is undesirable. However, at high temperature the surface of titanium can be annealed rendering the surface a matt black reducing the reflections. Figure 6.8 shows that after the oxidation process some of the sample features are now recognisable. Nevertheless the images are still dominated by noise.

When observing the silica structures inside the pressure cell I am only interested in a fraction of the light that is sent into the sample: the part that is actually reflected by the silica. To select only the light reflected by the silica I use fluorescent particles. The FITC-doped silica absorb light at 488 nm and emit light at 515 nm. This shift in frequency is enough to separate the incoming light and that reflected randomly from the cavity walls from the light which is emitted by the particles. By blocking all wavelengths outside the range of 500 to 530 nm we only observe light produced during the fluorescence process reducing spurious reflections to a negligible amount as shown in figure 6.9.

Effective numerical aperture

Now it is possible to image inside the pressure cell by using an objective with an appropriate working distance and fluorescent particles. To improve the image quality I focus on optimising resolution and contrast. The lateral resolution is

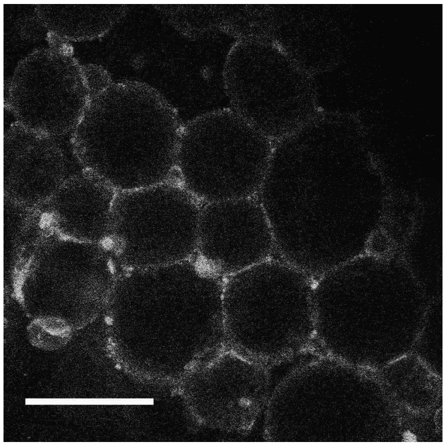

Figure 6.9: Fluorescence confocal microscopy images of water-dodecane emulsion stabilised with FITC-doped Stöber silica particles inside pressure cell taken with ×10 objective (WD 16.0, NA 0.3). The reflections inside the cell are suppressed with the use of fluorescent particles. Scale bar 200μm.

directly determined by the numerical aperture of the objective (see equation 3.2) along with pinhole size, incoming and outcoming wavelength. It implies that light is collected from a light cone characterised by θ, where NA=nsin(θ) as shown in figure 3.6. The light collected by the objective carries information about the different structural characteristics of the sample. All light rays combined together form the optimum image. However, the small opening of the pressure cell blocks a significant fraction of the light the objective could potentially collect. Firstly, this reduces the intensity of the observed light and therefore the contrast. Secondly, the light that is blocked are the peripheral rays which carry information on the smaller variations in the sample. Image formation without the peripheral rays leads to an image appearing blurry because it is lacking small details. In figure 6.10 fluorescent silica beads were observed by blocking the peripheral rays. The effective numerical aperture varies from 0.17 in figure 6.10a over 0.26 in figure 6.10b to 0.34 in figure 6.10c. Initially the opening in the titanium of the pressure cell near the window had a slightly conical shape with a taper of 5° (effective NA = 0.17). This gives the pressure cell strength and allows pressures up to 5 kbar. However, in the experiments here, the image quality is more

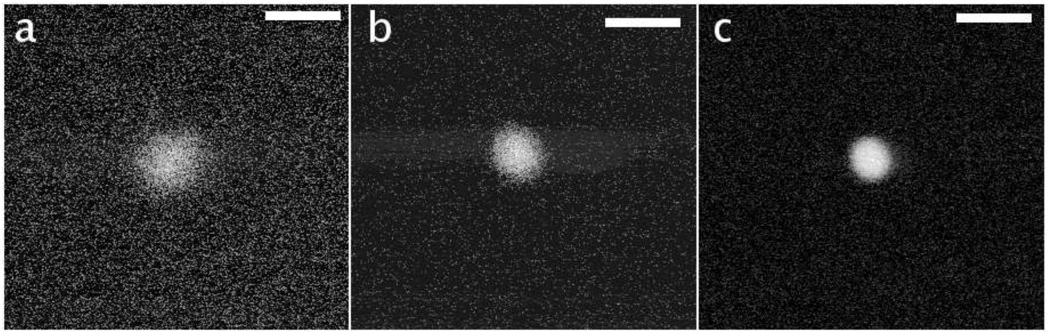

Figure 6.10: Fluorescence confocal microscopy images of different single fluorescent silica beads. The effective aperture varies from 0.17 in (a) over 0.26 in (b) to 0.34 in (c). The contrast and sharpness of the images increase with increasing effective NA. Scale bar = 5 μm. (The recorded intensity is normalised and presented on a logarithmic scale.)

important and lower pressures are still sufficient. Therefore, we deliberately weakened the cell by opening the taper to a larger angle. This reduces the maximally attainable pressure to 1.5 kbar. At the same time it increases image performance as is demonstrated in figure 6.10. An effective NA of 0.34 is still below the possible NA = 0.45 of the objective but the optimum cannot be achieved without further weakening the cell. The pinhole setting was found to be optimal for 1.0. For the lowest effective NA the pinhole size needed to be increased for the signal to be detected. The increase in depth of field in figure 6.10a is therefore also due to a larger pinhole size (figure 6.10b and c have the same pinhole setting).

The numerical aperture also determines the depth of field (see equation 3.3). This is demonstrated in figure 6.11 showing z-scans of fluorescent silica beads for increasing numerical apertures. The larger the effective aperture the shorter the depth of field.

These images show what degrading effect a reduction in the numerical aperture has on the image quality. Opening the taper of the pressure cell has resulted in the most significant improvement in imaging.

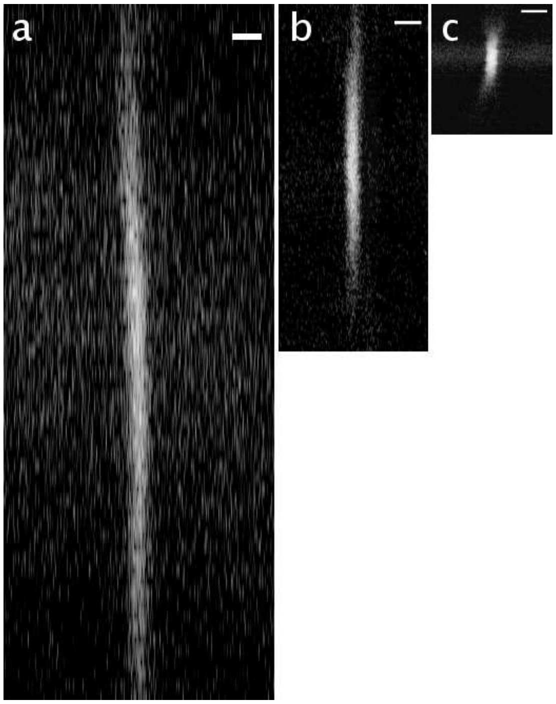

Figure 6.11: Fluorescence confocal microscopy images of different single fluorescent silica beads. The effective aperture varies from 0.17 in (a) over 0.26 in (b) to 0.34 in (c). For reduced effective numerical apertures the depth of field increases significantly. Horizontal resolution given by scale bar = 5 μm, the vertical shows z-direction of sample. (The recorded intensity is normalised and presented on a logarithmic scale.)

Influence of diamond window

The window of the pressure cell consists of a 500 μm thick diamond. As discussed in section 3.2.2 deviations from the standard cover glass thickness can lead to spherical aberration (see figure 3.9). The × 20 ELWD objective has a correction collar which can be adjusted to cope with glass covers with a thickness of up to 1.2 mm. However, for diamond with a refractive index of 2.41 instead of 1.51 for glass, the correction mechanism will not perform optimally. In figure 6.12 I examine the effect of different settings on the depth of field. Compared to the loss in image quality due to a reduced numerical aperture the spherical aberration effects are small. For the extreme collar settings figure 6.12 shows that the depth of field increases and the test bead appears more blurry. The clearest image is

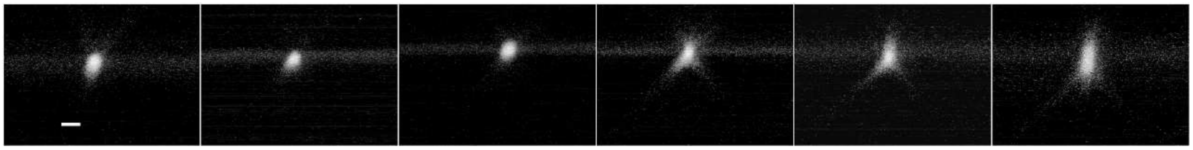

Figure 6.12: Fluorescence confocal microscopy images of the same fluorescent silica bead for different collar settings. From left to right: 0.2, 0.4, 0.5, 0.6, 0.8, 1.0. The streak arises from reflections off the window. Scale bar = 2 μm. (Images are normalised and presented on a logarithmic scale.)

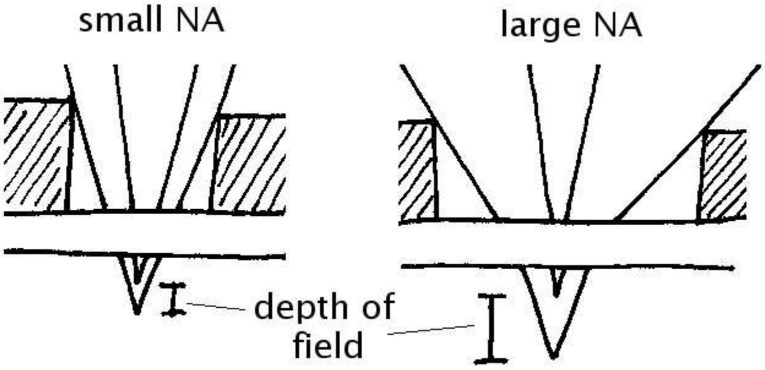

Figure 6.13: The smaller the effective NA, the less important becomes the effect of spherical aberration. Spherical aberration is most significant for peripheral rays.

obtained for a collar setting of 0.5 and is therefore chosen as an ideal setting. The comparison of the effects of spherical aberration and effective numerical aperture shows, however, that to optimise the image quality a larger window diameter is more important than the thickness of the window. This might seem surprising, but as long as the effective numerical aperture is very small all the incoming light rays have a very steep angle. Spherical aberration, however, occurs most strongly if the incident light hits the different refracting material at a shallow angle and therefore does not play a major role if the opening into and out of the sample is too small as shown in the simplified diagram of figure 6.13.

Comparing a standard grid within the pressure cell and behind a coverslip and analysing its size shows that the lateral magnification is not measurably influenced by the diamond window with its high refractive index.

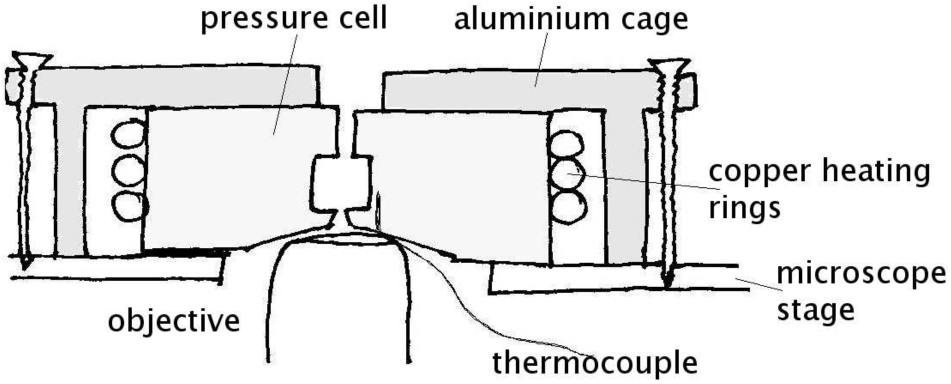

Figure 6.14: Schematic drawing of pressure cell set-up on microscope stage.

6.3 Results with pressure cell

Having achieved a satisfactory imaging quality phase transitions on the lut/w and FITC-doped silica system can be examined. The samples are prepared as outlined in chapter 4. To pressurise a sample the sample chamber is filled with the desired components. The sample piston is tightened so the teflon bulges slightly and seals straight away when it is inserted into the sample chamber. If the sample piston seals properly it will push itself out when pressed into the sample cell, otherwise the piston needs further tightening. Then the titanium cell sealed with the piston, is screwed into the ram and tightened with a purpose made lever. After fitting the temperature control ring the set-up is placed on the microscope. Only now is the thermocouple inserted, coming from below the microscope stage so that the sample cell lies flat on the stage. For safety reasons and to hold the cell firmly in place, an aluminium cage surrounds the set-up and is firmly screwed onto the microscope stage as seen in figure 6.14.

I can use the pressure cell to induce a phase transition in the 2,6-lutidine/water system by either starting with a miscible system and releasing the pressure or by applying pressure to an already separated system making it miscible again.

Figure 6.15 shows a lut/w system that is critical at atmospheric pressure and contains Φ_v=0.5% particles. To induce phase separation the system is pressurised

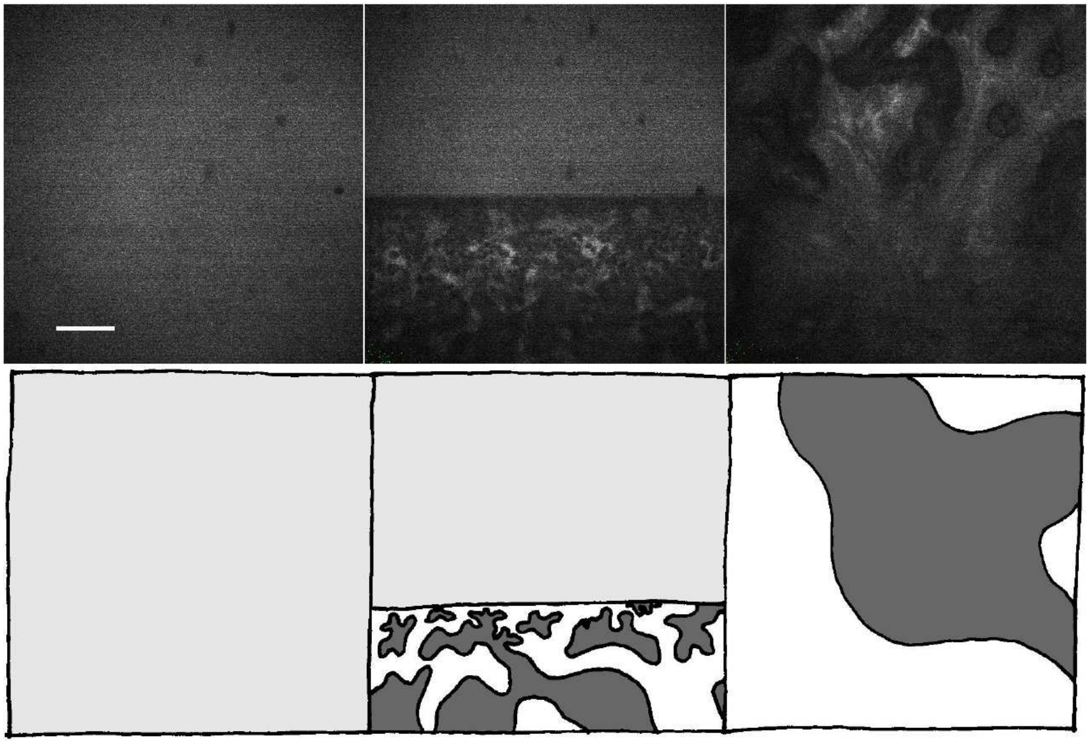

Figure 6.15: Fluorescence confocal microscopy images of phase separation induced by releasing pressure of a 2,6-lutidine/water system that is critical at atmospheric pressure and contains Φ_v=0.5% particles. Time separation between images is 1.034 seconds. Scale bar = 100 μm. The cartoon mimics the process: initially the sample is a homogeneous dispersion, after the pressure drops the liquids immediately separate and the system coarsens quickly.

to 1 kbar at room temperature. Then the temperature is raised to 35.0°C before the pressure is released using the fast electronic valve. The images are recorded a few microns into the pressure cell using fluorescence confocal microsccopy at a sampling rate of 500 lines per second. The time between the beginning of each frame is 1.034 sec. Time progresses while the image is scanned from top left, line by line to bottom right. While the sample is a homogeneous colloidal dispersion in the first image, the separation takes place very quickly in the second image shown by the darkening of the image over just a few lines corresponding to about 10 ms. In the next image it is possible to see how the coarsening has proceeded already very quickly. The wetting properties of the particles used here are not ideal and the particles do not stabilise the system well. Although the separation pattern

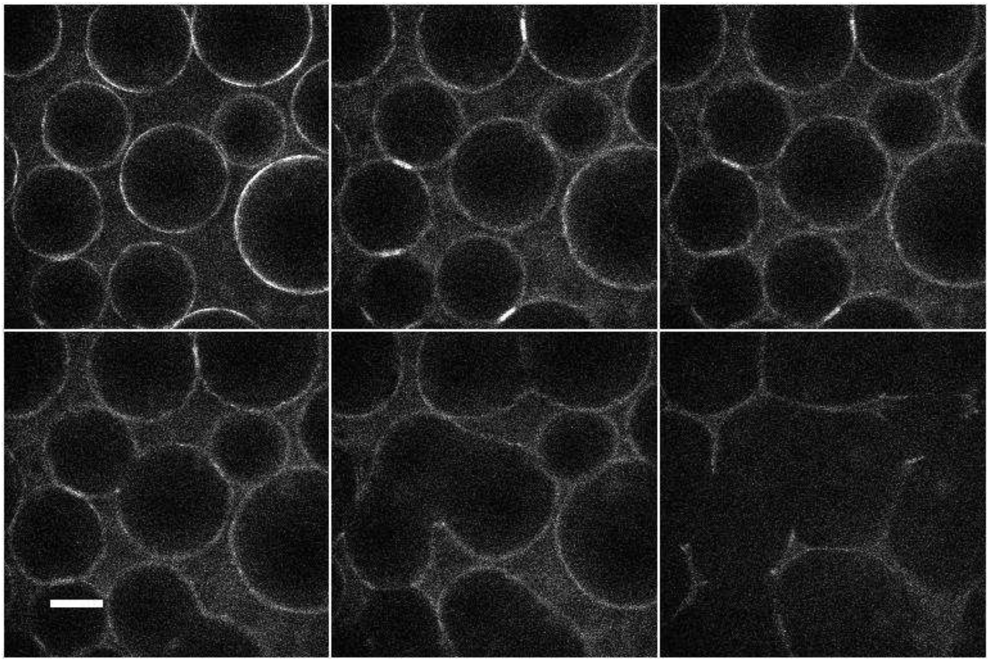

Figure 6.16: Fluorescence confocal microscopy images of phase transition from immiscible to miscible state by applying pressure to an off-critical 2,6-lutidine/water emulsion at 37°C containing Φ_v=0.5% particles. 0.5 frames/sec. Scale bar = 100 μm.

shows some spinodal characteristics, the end result are short lived droplets.

It is also possible to make an immiscible system miscible by applying pressure. Figure 6.16 shows this for an off-critical 2,6-lutidine/water emulsion which was obtained by heating the system to 37.0°C. Once the droplets have formed via thermally induced nucleation, the pressure inside the sample cell is raised to 1 kbar. The images are taken by fluorescence confocal microscopy inside the pressure cell. The pressure is applied slowly after recording the first image. Because the pressure is applied by compressing the samples the droplets slightly deform when pushed into each other (bright sections on touching droplets in second and third image). Similar to the alcohol/oil system in figure 5.7 the droplets do not crack but start merging as soon as the interfacial tension has lowered sufficiently. The droplet walls start blurring once the interfacial tension is reduced. The points of coalescence are where the particles have been pushed into each other. The pressurising system failed at this point, not allowing us to observe the equilibration process any further in this run. It is interesting however, to compare figure 6.7 with the first image of figure 6.16. While the pressure quench (figure 6.7) results in very monodisperse droplets the temperature quench in figure 6.16 has a much wider distribution of droplet sizes showing that the conditions can be more uniform for the pressure quenches. In the absence of convection and other disturbing influences on the system an emulsion coarsening via droplet coalescence is expected to yield a very small size range due to the fact that smaller, not fully particle-coated droplets have a higher coalescence frequency than larger droplets.

The pressure cell project was not carried out to the very end because a simpler way of producing bijels became apparent during the course of the development. However, methods used for the pressure cell were directly transferred to the new temperature quenching set-up. Most importantly the temperature controlling environment, but also essential imaging and sealing techniques. Additionally, my work on the optimisation of microscopy imaging under pressure has led to the development of similar pressure cells for microscopy purposes. These are currently being used by some of the biophysicists of our group to study extremophile bacteria under pressure. These new pressure cells are based on the knowledge acquired during the project described here. For example, the window diameter is increased by putting up with a thicker window since the numerical aperture can then be fully exploited. Also, the window is made of glass to let the spherical aberration correction mechanism work to its strength. Using extra strong steal allows a less bulky window fixture so that it is possible to use a × 60 ELWD objective with WD 2.1-1.5 and NA 0.7 greatly improving the potential resolution.

6.4 Summary and outlook

Initially designed to produce bijels, the pressure cell project aided the development of a more economic route to bijel formation via temperature quenches. Significant advances have been made during the development. The set-up for the temperature quenches discussed in chapter 4 has hugely benefited from the improved temperature control and imaging conditions. Additionally, the chemical aggressiveness of the lutidine has led to the development of a grease free sealing technique avoiding sample contamination. Furthermore the improved pressure stability and establishing the significance of various imaging conditions has contributed to the development of microscopy pressure cells for other purposes.

s

Chapter 7

Dynamic behaviour of emulsion droplets

In this chapter I examine the dynamic behaviour of micron-sized oil-in-water emulsions stabilised by solid particles using x-ray photon correlation spectroscopy. This technique quantifies the variation in particle correlations on the second to many hundreds of seconds time scale.

7.1 Introduction

Soft materials are ideal for studying glassy states because they reorganise on measurable timescales and they can be perturbed by relatively gentle forces. With the advent of new experimental techniques like x-ray photon correlation spectroscopy (XPCS) it is now possible to probe the dynamics of samples up to the order of 1000 seconds. In soft glassy materials a decorrelation in the dynamics of the material constituents is observed within 10's of minutes making XPCS a suitable method to study their dynamics. This decorrelation occurs also in other materials and is usually associated with a diffusive cage-escape process (see section 2.2.5). In various soft glassy samples a linear relationship between the probed length scale and resulting characteristic decay time has been found. This stands, in combination with decorrelations that occur faster than exponential, in stark contrast to a diffusive process but its origin is so far not very well understood. Furthermore, the dynamics of these out-of-equilibrium systems show a delicate dependency on sample age and it has recently been observed that intermittent dynamics are a characteristic feature. An excellent review on this topic with references to a wide range of experiments and the current understanding on these samples has been written by Cipelletti et al [54].

While a few out-of-equilibrium systems exhibit intermittent dynamics as a result of small temperature fluctuations [111] most systems with intermittent dynamics respond to some driving force. Dense colloidal suspensions forced to flow are one example of a driven system that has been studied in some detail [112, 113, 114]. Depending on the volume fraction and the strength of drive the dispersion will enter a transient jammed state. This is a configuration where small fluctuations are insufficient to allow the sample to flow. Eventually, a sudden fracture will occur and flow will recommence. Large, stop-start fluctuations become increasingly common as the fully jammed state is approached [112]. Granular media setting under gravity may have similarities to dense driven colloidal suspensions [115]. In both cases dilation is required to allow motion while in the granular case friction between subunits can be important. Many of the experiments on these systems probe the large scale behaviour of the sample since it is difficult to capture the dynamics of individual subunits in dense heterogeneous samples. XPCS may prove to be a useful tool in this regard.

Here I study the dynamics of a colloid-stabilised emulsion as it is driven to cream by gravity. I observe the samples from an early stage while the droplets are still coalescing. The typical final droplet sizes are on the scale of ten or more microns. This is therefore a non-thermal system. Gravity will drive the droplets to form a high volume fraction cream. For our preparation route there is a broad distribution of droplet sizes which implies that the cream will not tend to crystallise as the volume fraction increases. It is possible to imagine that the

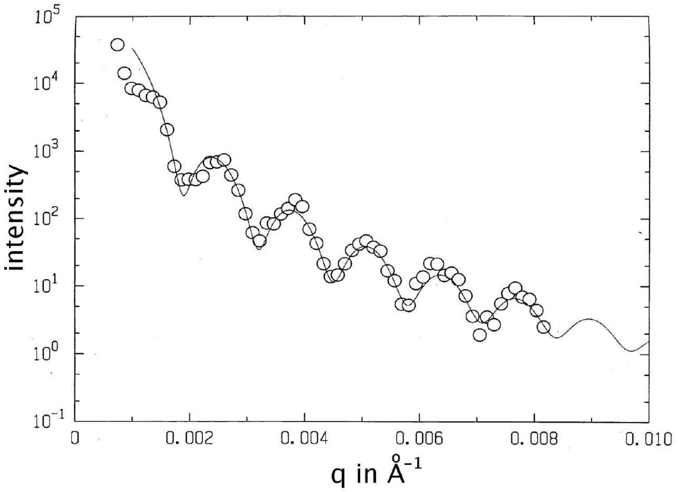

Figure 7.1: Small angle x-ray scattering data on the particles used in the following experiments.

end state of this system would be a disordered random packing of droplets. The experiment presented here shows the very earliest stage where the cream is only just beginning to compact. There is no suggestion of droplet deformation by gravity on this time scale. The colloid-coated interfaces make the droplets quite rigid and additionally give them a rough surface which may create friction. Using XPCS I observe the dynamics of a small number of these droplets, however, the observed droplets will also respond to fluctuations elsewhere in the sample.

7.2 Experimental system

7.2.1 Sample preparation

The liquids forming the emulsion are water and dodecane. The water is purified water obtained from the laboratory at the Troïka beamline. The dodecane is from (Aldrich, >98%) and is used without further purification. Dodecane and water are fully immiscible and have an interfacial tension of 72.8mN/m at 20°C [101] leading to extremely strong trapping of more than 8×10^5 k_BT for wetting angles between 60° to 120°. As documented by Pashley [116] the water-oil interfaces can become charged during emulsion preparation. This is especially true for vigorous mixing in a glass bottle and it can inhibit the trapping of colloids on interfaces. To suppress this effect I add the salt KCl (Aldrich, 99+%).

The particles are undyed silica particles prepared by Andrew Schofield (Assi 12) using the Stöber method [60]. After the initial washing procedure the particles are dried at 50°C before the sample preparation. The particle size is determined by fitting a hard-sphere form factor [14] to the time-averaged small-angle x-ray data as shown in figure 7.1. This results in a particle radius of 243 ± 7 nm.

To prepare the emulsions it is important to adhere to the following protocol. Adding the ingredients in a different order will either lead to the stabilisation of air bubbles or a decrease in the stability of the emulsion. Initially the dried particles are weighed according to the required volume fraction. Then 0.6 ml water is added using the pipette and the weight is checked as well. However, the accuracy of the volumes here is not essential in the way it was for the miscible liquids in the previous chapters. An ultrasound probe is used to disperse the particles in the water for 3 min at 10% of the total power. Only then the dodecane (0.4 ml) is added and before further mixing the KCl is weighed on top of the dodecane. Now all the components are mixed using the ultrasound probe again (2 min, 10% of total power). When the emulsion creams the bottom will clear indicating that all particles are trapped on the interfaces. If, for example, the amount of salt is not sufficient some of the particles will have failed to become trapped on the interfaces and this will make the bottom liquid appear cloudy. Once the emulsion is prepared large bone marrow syringe needles[1] are used to fill the glass capillaries. At the same time some of the same sample is examined using bright-field microscopy to make sure an emulsion has formed. Only once this has been confirmed is the sample measured. The use of the syringe has no visible effect on the emulsion compared to using a spatula to dispense the sample as checked by

---

[1] The syringe is cleaned in both solvents to avoid contamination as discussed in section 5.2.2.

microscopy. Several capillaries are filled at the same time to ensure that, after creaming, the emulsion is in the correct location to be hit by the x-ray beam. If other capillaries are filled at a later point, the emulsion is mixed using the ultrasound probe again before being filled in the capillaries. This reinitialises the emulsion. The sample age is taken to be at zero the moment when the capillary is filled.

A hot gun glue is used to seal the capillaries. If the sample is not sealed properly the evacuation of the x-ray sample chamber will make it explode. It is therefore necessary to properly seal the sample to avoid losing hours of precious beam time - all this while trying to begin measurements for young samples. The capillaries were weighed on at least two occasions to make sure the samples are not drying out since this would induce additional forces on the sample.

7.2.2 Data acquisition

An introduction to the experimental technique of x-ray photon correlation spectroscopy (XPCS) is given in section 3.4.

Prior to carrying out the experiments Aymeric Robert, the beamline scientist we were working with, optimised the necessary parameters on the beamline. The experiment is carried out with an 7.979 keV x-ray beam resulting in a wavelength of the x-rays of 1.5 $\mathring{A}$. The filter selecting the x-ray energies is a Si (111) monochromator. Once the beam line is set-up the capillary is loaded into the sample chamber and the chamber is evacuated. Before the actual measurement starts the position of the beam centre is recorded and the guard slits are brought into position to eliminate any parasitic scattering. Then the exposure time can be determined. A good balance needs to be found between a large photon count and the maximum intensity that is tolerable for the CCD camera. It is also essential to take into account that over the course of each 8 hour slot the incoming beam intensity will slowly drop. If the sample leaks and evaporates the intensity of the scattering pattern will increase rapidly and can destroy the CCD camera. It is therefore necessary to observe the CCD images throughout the experiment to be able to abort the measurement if required. To maximise the measurement time which is limited by the refills of the beam, the dark images are recorded after the measurement has finished because this can be done while the ring is being refilled. The acquisition of CCD-images is limited by the maximum speed of the CCD camera and the necessary exposure time giving a minimum frequency of around 0.8 frames/sec. On the other hand a maximum of 9999 frames can be taken. For long measurements it is therefore necessary to record images with a delay time in between subsequent frames. This increases the lower limit on the delay time that can be probed which is a more important limitation with younger samples. After all settings have been optimised and the measurement is launched no further input is required as long as the intensity stays at an appropriate level. During the measurement the scattering pattern is recorded by the CCD camera which in the end will form a time series of images characterised by the delay time $\Delta\tau$ (time between the start of the recording of two subsequent images).

Each data set is named and all settings are recorded in the lab book which stays on site but can be photocopied. Special care was taken to note down the sample age for each measurement. The data is stored on the network and can be transferred to Edinburgh using the scp command in a terminal. During the course of the experiment more than 120 GB of data was collected which is stored on an external hard drive with a back-up copy on the COSMIC Raid array.

7.3 Analysis

The x-rays scatter from the sample and produce a speckle pattern corresponding to the instantaneous configuration of the sample. The speckle pattern changes over time in concert with the sample dynamics. These speckles are recorded by the CCD camera. Figure 3.13 shows an example of such images. The graininess in an individual frame (figure 3.13b) shows the speckle nature of such a scattering

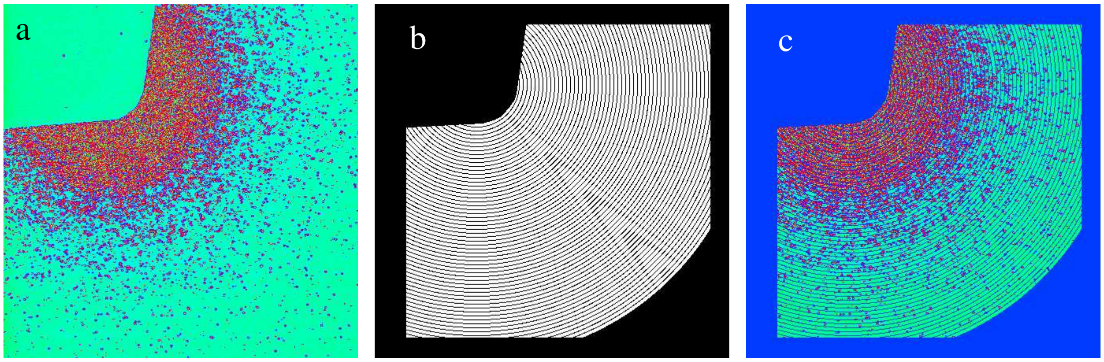

Figure 7.2: (a) is the raw data, (b) shows the pixel selection mask with the circular q-rings and (c) data used for analysis.

pattern. These speckles move over time, hence an average over many subsequent frames leads to a smooth image as shown in figure 3.13a. The fluctuations of the speckles are directly related to the motion of the scatterers in the sample. To quantify the dynamics of the sample the correlation functions for individual pixels are calculated. This is a different situation to standard dynamic light scattering where the speckle is measured at a single point and the correlation function is calculated on a dedicated computer card. To do this for a large number of pixels requires software rather than hardware. An introduction to the concept of correlation is given in section 3.4. Since the scattering pattern is radially symmetric it is possible to average over different q-vector rings to obtain a proper ensemble average as well as good statistics. An example of a selection mask for various q-rings and how it is applied to the data is shown in figure 7.2c. Luca Cipelletti, an expert in this field, has been so kind to let me use his software [117] to calculate the time averaged correlation function $g_2(q,\tau)$-1 as well as the time resolved correlation (TRC) function $c_I(t,\tau)$ [56]. The definitions of these quantities are given in section 3.4. He additionally gave me excellent support in using the software and valuable suggestions on how to tackle the TRC analysis. The programmes were even provided with detailed help files.

Prior to the analysis it is important to check the data for spurious effects or parasitic scattering. ImageJ can be used to assess by eye every frame of the data in sequence. Then a mask shielding all unwanted areas is produced for each data set by hand (0 for unwanted pixels, 1 for wanted pixels) and is an input to the analysis programme which then produces the q-ring mask for all remaining pixels.

After $g_2(q,\tau)$-1 or $c_I(t,\tau)$ are calculated for each q, I use my own programmes to display these functions and to evaluate the best fit of a model. I use shell script to format the data and to automate the process. Then I pipe the data to gnuplot for fitting or plotting. This is not a very elegant or sophisticated approach because the syntax is very basic and therefore sometimes cumbersome but once the code is running it performs reliably.

The challenging part of the analysis is choosing the appropriate region of the CCD detector to use for calculating the correlation functions. This is especially apparent when considering the time resolved correlation $c_I(t,\tau)$. The lack of the time average makes $c_I(t,\tau)$ very sensitive to noise. In contrast $g_2(q,\tau)$-1 which basically is the average over $c_I(t,\tau)$ with respect to t (see equation 3.11) is much more robust.

7.3.1 Sources of noise

Under ideal conditions the fluctuations at one pixel on the CCD camera over time are only due to the dynamics of the scatterers. In reality there are also other mechanisms which can induce variations in the intensity: fluctuations in the incoming x-ray beam, fluctuations in beam coherence, fluctuations of particle number in the coherence volume, background noise of the CCD camera and other noise. Some of these non-idealities can be corrected.

Intensity fluctuations of incoming beam: The intensity of the incoming beam can drop by up to 30% over the course of 5 hours and also fluctuates on a much shorter time scale from frame to frame. It is therefore necessary to normalise the intensity prior to calculating the correlation function so that these fluctuations do not influence the data. This normalisation is discussed in more detail later (see equation 7.4).

Fluctuations in beam coherence: As discussed in section 3.4 coherence of the x-ray beam is a precondition for obtaining speckle patterns. At the same time only partial coherence will be achieved in experiments with x-rays. Fluctuations in the beam coherence will give overlapping speckles and will lead to variations in the scattered intensity. This is due to the fact that an increasing number of coherence volumes will lead to a decrease in the correlation function [118]. If fluctuations in the beam coherence exist these can be observed by measuring a static sample. Vycor glass is a porous material made from a quaternary glass mixture. It scatters relatively uniformly at a broad range of wave vectors. It is a standard static test sample and surprisingly the correlation function of the vycor which is expected to show a constant correlation for all delay times actually decorrelates for characteristic decay times above 1000 seconds. Aymeric Robert confirmed that we were not the first to observe this, especially in the synchrotron 16-bunch mode used for the experiments here. He has furthermore established that while this decorrelation occurs for some experiments and varies with time which is also the case for my vycor measurements, it is not present in other experiments at all. This implies that it is not a stable phenomenon and makes it more tricky to deal with (see appendix B). Fortunately, the characteristic decay time observed with the vycor is large enough that meaningful data can still be collected for two out of three of our samples. The Φ_v=5% and 7.5% emulsions are not affected but this is no longer true for the 2.5% sample. Therefore this latter data set must be discarded.

Variations in number of scatterers: Fluctuations in the intensity can also be due to changes in the number of scatterers. The oil droplets are lighter than the surrounding water and will therefore experience a constant force upwards. There are only 60 to 100 droplets in the scattering volume at a time and these scatter due to the interfacial layer of high electron density colloids. If a rearrangement occurs and a droplet moves out of the beam this changes the number of scatterers in the volume. However, at the same time other droplets will enter the sample volume from below keeping the droplet number roughly constant. This will be a slowly varying fluctuation because, except for very young samples, the droplets are expected to move very slowly if at all due to jamming. The influence of varying particle number in suspensions studied by light scattering has been examined elsewhere [119].

7.3.2 Dealing with noise

All these fluctuations are manifested as a change in the photon number arriving at the detector, because the intensity I(t)$_p$ at pixel p is proportional to the number of photons n. When calculating c$_I$(t,τ) there will be further sources of noise so that it is difficult to determine the origin of the observed fluctuations in c$_I$(t,τ) and therefore due to the dynamics of the sample. But there is a way to see which fluctuations are arising due to the fluctuations in the photon number. The self-correlation of I(t) with zero time delay (i.e. with itself) can be written as follows from equation 3.10:

$$\begin{aligned} c_I(t,0) &= \frac{\langle I(t)I(t+0)\rangle}{\langle I(t)\rangle\langle I(t+0)\rangle} - 1 \\ &= \frac{\langle I(t)^2\rangle}{\langle I(t)\rangle^2} - 1 \\ &= \frac{\langle I(t)\rangle^2 + \sigma^2}{\langle I(t)\rangle^2} - 1 \\ &= \frac{\sigma^2}{\langle I(t)\rangle^2} \\ &\propto \frac{1}{n}, \end{aligned} \tag{7.1}$$

where I have used the relation $\sigma^2 = \langle I(t)^2\rangle - \langle I(t)\rangle^2$. Assuming that the statistics involved are Poisson distributed this implies that $\sigma = \sqrt{n}$ where n is the number of photons, implying that the self correlation varies inversely with the photon number. Comparing c$_I$(t,0) with c$_I$(t,τ) for small τ shows that a majority of the fluctuations in the c$_I$(t,τ) signal are due to photon fluctuations (see figure 3.16).

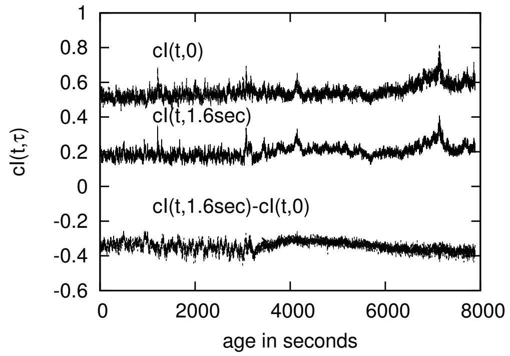

Figure 7.3: c_I(t,0) and c_I(t,τ) at fixed τ plotted against t. c_I(t,0) is expected to be constant and therefore all fluctuations in it will be noise. The difference between the two shows the efficiency of equation 7.2.

For τ's that are much smaller than the characteristic decay time τ_c it is possible to correct the c_I(t,τ) signal to some extent by subtracting the fluctuations due to the varying photon number [57]. If $\tau \ll \tau_c$ then

$$c_{Icor}(t,\tau) = c_{Imes}(t,\tau) - c_I(t,0) + \overline{c_I(t,0)} \tag{7.2}$$

where $\overline{(...)}$ expresses averaging over t and its efficiency for $\tau \ll \tau_c$ is shown in figure 7.3. Unfortunately this is no longer valid for larger delay times and is therefore not a very strong correction method. The reason for trying to correct for the noise is that this would then allow to establish directly whether the dynamics in the droplet emulsion are heterogeneous or homogeneous simply by looking at the fluctuations of c_I(t,τ).

Although this direct observation method fails here it is still possible to detect intermittent behaviour in the c_I(t,τ) signal by an indirect method. This can be done by examining the variation of c_I(t,τ) around its mean for different delay times. While homogeneous dynamics show a variance of c_I(t,τ) that varies with the magnitude of c_I(t,τ) this is no longer true if the underlying dynamics are intermittent. For heterogeneous dynamics the variance will show a peak around the typical delay time, the time when most of the intermittent events take place. Of course this method will only resolve such a peak around τ_c if the fluctuations

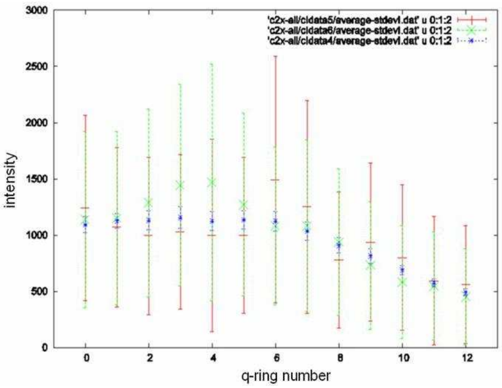

Figure 7.4: Average intensity and its standard deviation plotted against increasing q (q-region is on second peak). red += single pixel 1, green x= single pixel 2, blue ∗= average of all pixels on 1 pixel-wide q-ring (including pixel 1 and 2). The first 8 data points have very similar mean intensity and standard deviation and are therefore taken to form a 16-pixel wide ring which contains 4515 pixels. This is the data that is examined in section 7.4.3.

of the noise are smaller than the signal due to the particle dynamics.

7.3.3 Calculating meaningful correlation functions

When calculating $c_I(t,\tau)$ a certain q-range on the CCD camera needs to be selected. This results in a finite number of pixels that contribute to the outcome. In any experiment, to obtain a reliable average, it is necessary to carry out enough trials on an unbiased sample. A 1-pixel wide q-ring only has several hundred pixels which is insufficient to give a meaningful result for $c_I(t,\tau)$. It is not easy to increase the number of pixels used since for the data here the average intensity is modulated by the strongly varying form factor (equivalent to that shown in figure 7.1) so that the difference in the average of one 1-pixel-wide q-ring to the next can be larger than the actual fluctuations around that average. If the width of the q-rings is increased to obtain a larger number of pixels this will potentially weight the different fluctuations inappropriately.

The correlation function used here

$$c_I(t,\tau) = \frac{\langle I(t)I(t+\tau)\rangle}{\langle I(t)\rangle\langle I(t+\tau)\rangle} - 1 \tag{7.3}$$

is based on the assumption that the fluctuations around I(t) are sampled from the same distribution which has a characteristic mean value and standard deviation. As soon as there are different distributions contributing to the correlation function (which is the case if the mean intensity changes (see figure 7.1)) $c_I(t, \tau)$ described by equation 7.3 no longer gives meaningful information. When evaluating the correlation between two functions meaningful answers will be obtained only if the relative fluctuations are compared. This can be achieved by subtracting the mean value from the actual signal I(t) and then dividing by the standard deviation giving the function D(t) where

$$D(t) = \frac{I(t) - \langle I(t) \rangle}{\sigma}. \tag{7.4}$$

Calculating the correlation of D(t) then gives $c_I(t,\tau)$:

$$c_I(t, \tau) = \langle D(t)D(t+\tau) \rangle. \tag{7.5}$$

It is known that the scattering amplitude, i.e. the intensity measured by the CCD camera, is distributed with negative exponential statistics [120]. This type of distribution has $\sigma=\langle I(t) \rangle$ and hence equation 7.5 will reduce to equation 7.3. At the same time this method of calculating the correlation function compensates for the drop in intensity of the incoming beam which can be up to 30% in 5 hours.

When choosing the q-range to calculate $c_I(t,\tau)$ it is necessary to choose a region with as many pixels as possible to obtain realistic average values but at the same time to make sure that the average intensity is quite constant throughout this region. To do this I examine the first peak of the scattering pattern. Using the circular averages of the intensity I also look at how much the intensity deviates from the mean over time, and repeat the same for single pixels. Plotting the intensities against q then gives a good indication of how the intensity changes. I can then choose a suitable q-range like for the first 8 data points in figure 7.4. For this q-region equation 7.3 holds and the pixel number of 4500 is acceptable.

It is also important to choose a q-range where the signal is not too low, otherwise the background subtraction interferes with the actual data. This favours a q-range closer to the beam-centre.

Using the carefully chosen subset of pixels the correlation function can be calculated. Fitting $g_2(q,\tau)$-1 will give information on the origin of the dynamics leading to the decorrelation. There are well tried and tested ways to analyse the correlations for Brownian particles [121]. Our samples are more unusual although we still use a relatively well known function for g_2-1:

$$f(q,t) = BL + c \times exp(-2(\frac{t}{\tau_c})^{\beta}). \tag{7.6}$$

BL stands for baseline indicating the value to which the curve decays. c determines the contrast between the initial and final level of the curve. And τ_c is the characteristic decay time which determines where the curve falls off indicating how long it takes before the intensity fluctuations decorrelate. β adjusts the slope of the exponential with values greater than 1.0 implying faster than exponential decays (compressed exponential) and smaller than 1.0 slower than exponential decays (stretched exponential). Extracting the fitting parameters for different q allows us to establish a relationship between the wave-vector q and the characteristic decay time τ_c. This can give insight into the process leading to the decorrelation. Since the scattering observed at a certain value of q probes length scales of the order $\frac{2\pi}{q}$ a relationship between q and τ_c where q $\propto \tau_c^{-2}$ will indicate diffusive motion of the particles. The parameters giving the best fit between the function and the data are found using the Levenburg-Marquhardt algorithm implemented within gnuplot.

7.4 Dynamics of solid-stabilised emulsions

In this section I examine the dynamics of particle stabilised oil-in-water emulsion. This is not a primitive system because it has characteristics of two different types of glassy systems. On the one hand there are the particles trapped on the liquid interfaces. After the creation of interfaces and trapping of the particles the initially small emulsion droplets are only partially covered and hence they coarsen over time. During this process the total amount of interface decreases and the particle coverage on the droplet surfaces continuously increases. This implies a continuous increase of the volume fraction of this more or less two-dimensional colloidal system. In analogy with conventional three-dimensional colloidal suspensions a glass transition might be expected for increasing Φ_v leading to an out-of-equilibrium situation for the interfacially trapped particles. On the other hand the oil droplets can be regarded as a driven system because the emulsion creams under gravity continuously pushing the droplets and raising the packing fraction. For the droplets the driving force is gravity while for the interfacially trapped particles it is the interfacial tension that prevents them reaching equilibrium. The samples consist of polydisperse dodecane droplets stabilised by ~ 0.5 μm diameter particles. The typical sizes for the 5% and 7.5% sample are around 16 ± 4 μm and 12 ± 3 μm diameter respectively.

7.4.1 Ageing of sample

First I examine how the dynamics of the sample change over time as manifested by g_2-1.

Aim and context

A commonly observed trait of out-of-equilibrium systems is that the dynamics of such systems slow down over time. Studies have been carried out for dense colloids, shaving foam, surfactant "onions" and many others. Cipelletti et al [122]

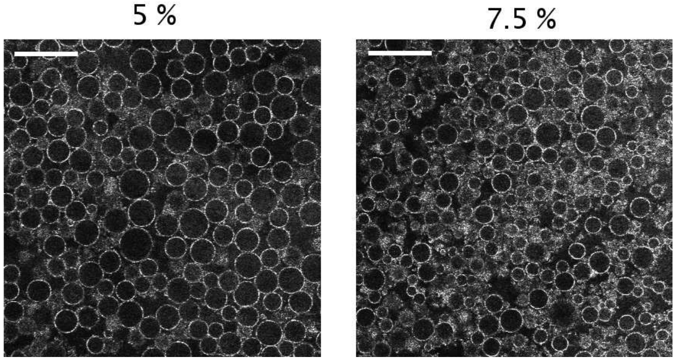

Figure 7.5: Water-dodecane droplet emulsions containing Φ_v=5% and 7.5%. Scale bar 50 μm.

suggest that the dynamics in soft glassy systems are due to the building-up of internal stresses. The slowing down is then due to either a decrease in the rate of change of the stress source strength or the reduction in the number of active stress sources as the sample ages. A large variety of soft glassy systems have so far been examined which show various power laws for the relationship between the characteristic decay time (τ_c) and the sample age (t_a): $\tau_c \propto t_a^{\mu}$, with μ ranging between 0.5 and 1.8 [54]. In some cases there are different ageing regimes or a plateau is reached after some time. The ageing behaviour is seen to depend on the loading of the sample and some samples can be rejuvenated. Here I compare the ageing behaviour of two oil-in-water emulsions containing Φ_v= 5% and 7.5% implying larger and smaller droplets respectively.

Sample and method

A Φ_v=5% and 7.5% with a volume ratio of water:dodecane of 3:2 is prepared as described above with 0.6 ml water, 0.4 ml dodecane, 0.110 g (5%) or 0.165 g (7.5%) and 0.1 mg KCl. Emulsions prepared in the same manner but examined in Edinburgh under the confocal microscope are shown in figure 7.5. The measurements on the system are carried out as close to the preparation time as possible. The speckle pattern of the samples is recorded for over 2 hours and from these images the time-resolved correlation function $c_I(t,\tau)$ is calculated.

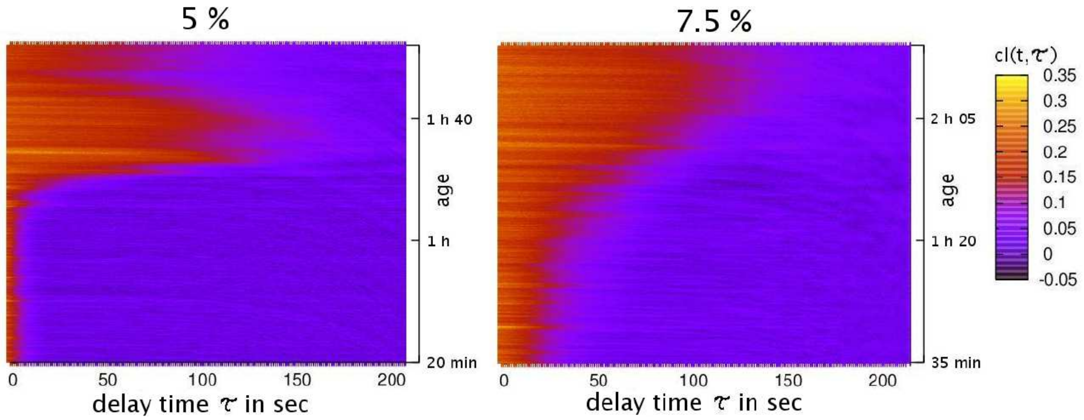

Figure 7.6: Time evolution of 5% and 7.5% sample. $c_I(t,\tau)$ plotted against delay time τ and sample age t.

$c_I(t,\tau)$ is then plotted against τ and t_a in a surface plot with the magnitude of $c_I(t,\tau)$ given by different colours, equivalent to the 3-D plot in figure 3.17c.

Results and discussion

When averaging several hundreds of the speckle patterns a smooth image is obtained as shown in figure 3.13a. The radial averages of the intensity then give the static scattering intensity of the system. Since the chosen q-range probes length scales on a fraction of the particle size the scattering intensity is dominated by the form factor of the silica spheres and can be used to extract the particle size as shown in figure 7.1.

Figure 7.6 shows the time evolution of the two different samples. In both samples a definite change over time is visible. In both cases the behaviour can be divided into three regimes. Initially the characteristic decay time is short, then there is a transition regime where the system starts slowing down and in the final regime it reaches a significantly longer characteristic decay time. For the 5% sample with the larger droplets the intial fast decay is significantly faster than that of the 7.5% sample with the smaller droplets. The onset of the slowing down occurs in both cases after about 1 hour 20 minutes but is drawn out over almost an hour for the small droplets while the change from fast to slow decorrelation happens over 10 minutes for the 5% sample. The first 40 minutes of the final slow regime in the 5% sample are measured and significant fluctuations in the characteristic decay time are observed after reaching an initial plateau. The slower ageing evolution of the 7.5% sample leads to only the first 20 minutes of the final stage being observed which seems to plateau at a similar characteristic decay time as the 5% sample.

The interfacial tension which traps the particles that are responsible for the scattering is the same for both samples. However, during the sample preparation it is apparent that the 7.5% sample has a much higher viscosity than the 5% sample. The force acting on the smaller droplets in the 7.5% sample due to gravity will be smaller than for the larger droplets in the 5% sample. Both these effects will lead to a weaker upward driving force in the 7.5% system compared to the 5% sample explaining the slower evolution of the sample with age. The thermal motion of particles that are not trapped on interfaces and the possible jiggling of particles which are trapped on the interfaces will not be observed since this happens on much shorter time scales which are not resolved in this experiment.

7.4.2 Dynamic behaviour of fast and slow ageing regimes

Aim and context

The XPCS data on the emulsions show a decay that has already been shown to change its characteristic decay time with sample age. For colloidal liquids approaching the glass transition this second decay is due to a so-called cage-escape process (see section 2.2.5) which is a diffusive process. For soft glassy materials, however, this second decay has been shown to have a non-diffusive origin [54]. The cause for such a behaviour is possibly due to stress build-up within the sample [122]. The behaviour of solid-stabilised emulsions is well studied and interactions can be well controlled. Studying such a system can therefore shed light on the current debate concerning the characteristics of this second decay.

Sample and methods

For the same samples as in the previous section the time averaged correlation function is calculated for the recorded q-range within the early and late stages of ageing. These sets of $g_2(q,\tau)$-1 are plotted against the delay time τ and fitted for each q with $f(q,\tau)$ from equation 7.6. The fit parameters are then examined and plotted as they vary with wavevector and sample age.

Results and discussion

Figure 7.7 shows $g_2(q,\tau)$-1 calculated for the early (top) and late (bottom) regime for both samples. The graphs show a significant increase in the characteristic decay time for both volume fractions for all q. At the same time it is apparent that the shape of the decorrelation changes. To quantify these effects all the obtained curves are fitted with $f(q,\tau)$ as given in equation 7.6.

Examining the behaviour of the fit parameters with q allows a more quantitative analysis. $1/\tau$ varies linearly with q for both samples and at all times. This shows that the mechanism(s) leading to the decorrelation is not of diffusive origin. Diffusive motion of the scatterers would imply a $1/\tau \propto q^2$ relationship. The linear relationship observed here has also been observed in many other soft glassy systems [54] and has been attributed to stress dipoles within the sample. Assuming small micro-collapse events are occurring randomly in space and time at a certain rate this leads to a linear relationship between q and τ with an exponent $\beta = \frac{3}{2}$ [123].

Although $1/\tau \propto q$ holds for both samples at all times there is a significant change between the behaviour at early and late times. For early times there is a significant off-set such that the $1/\tau$ behaviour does not go to zero for small q. This is identical for both volume fractions and has also been observed in other data sets not presented here. In addition to this off-set the slope of the $1/\tau$-curve

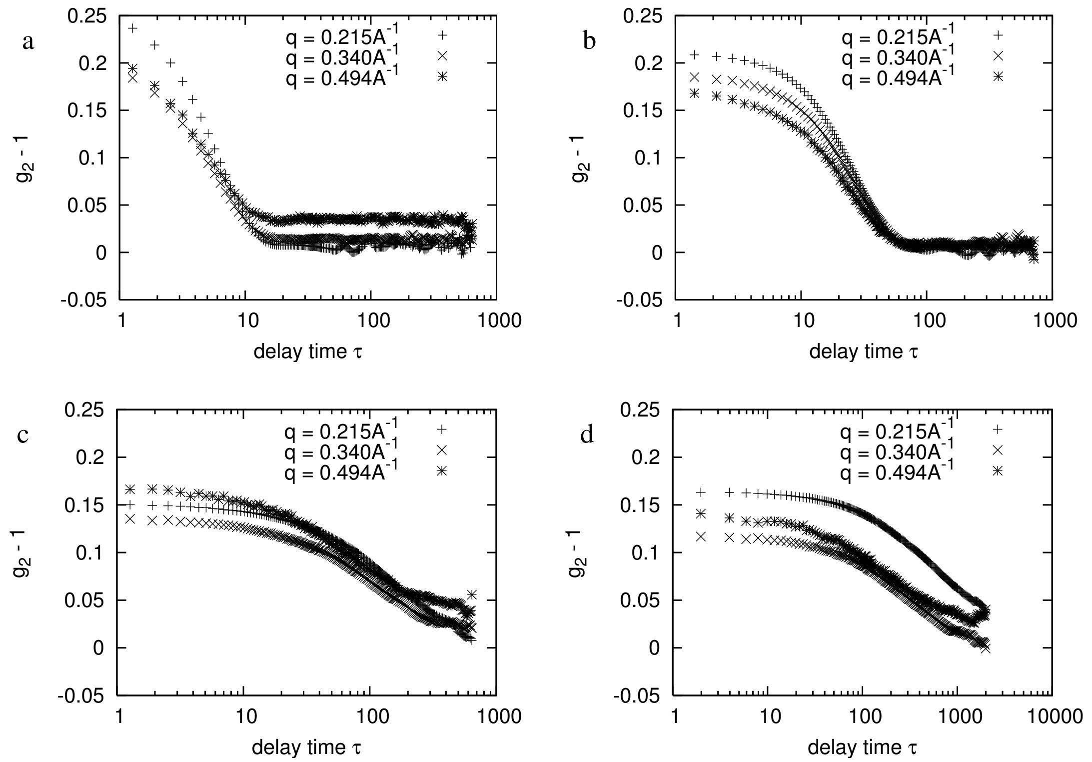

Figure 7.7: The correlation function g$_2$-1 for samples with 5% (left) and 7.5% (right) at young (a,b) and older (c,d) ages at a selection of q-vectors. The characteristic decay time can be seen to extend for older samples.

decreases with time. The speed at which the droplets rise upwards is given by the slope of $1/\tau$ which is in all cases below 1 Å/sec. This effective speed is smaller for the smaller droplets since these are less buoyant. The speed also decreases over time during which the system opposes gravity more and more during compacting of the droplets. It is now of interest to establish whether the rearrangements under gravity are continuous over time, slowly pushing the droplets together, or whether the upward lift of the droplets induces a multitude of separate, small rearrangements.

β behaves very similarly for both volume fractions. At early times β has values around 1.5 for small q which slowly decreases towards one for the largest q-vectors. At later times β is much lower starting at 1.0 for small q's and decreasing further for the larger q-values. These values imply that decorrelation is faster

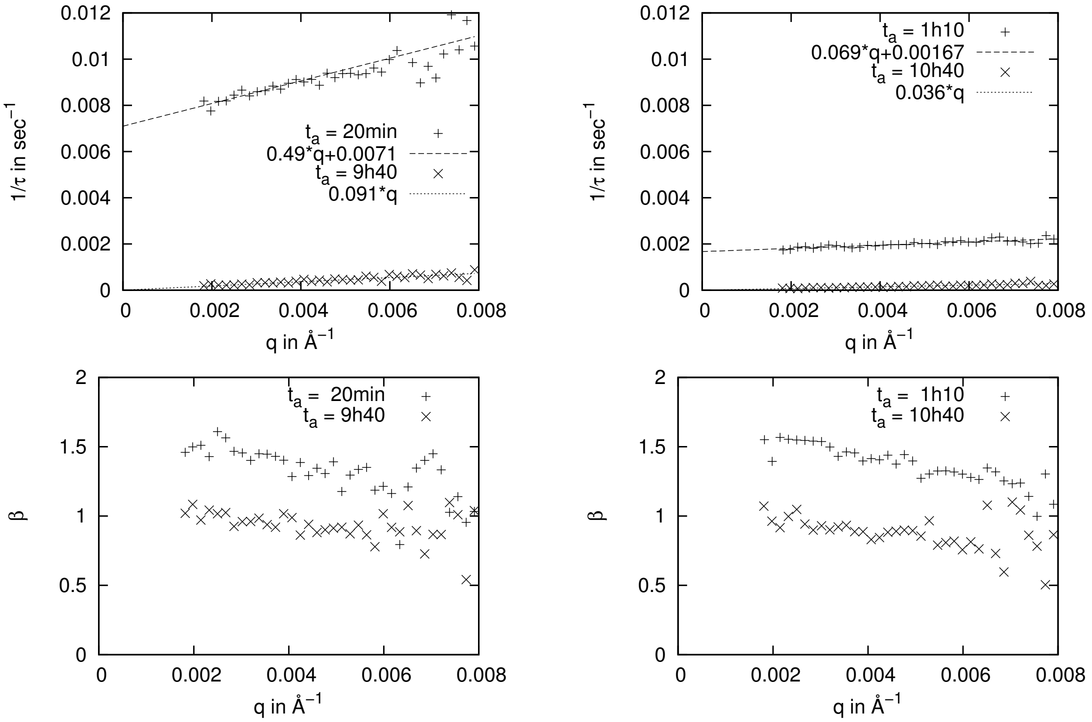

Figure 7.8: Fit parameters τ and β obtained by fitting g$_2$-1 (figure 7.7 and others). Inverse of characteristic decay time $1/\tau$ (top) and compressed exponential β (bottom) plotted against q.

than exponential (compressed) at least at early times. Such behaviour cannot be created from the sum of exponential processes and is as yet not fully understood.

The q-dependence of $1/\tau$ and the changes in β suggest that the origin of the decorrelation for early and late stages is different and I conclude that two main processes are responsible for the decorrelation to occur. A decorrelation for a certain q-vector is observed if the scatterers have moved more than the probed length scale which is $2\pi/\mathrm{q}$ (see equation 3.8). If $1/\tau$ is constant for all q it implies that rearrangements happen on such large length scales that a decorrelation occurs for all q. For the experiment here this means, rearrangements larger than 300 nm are taking place involving all the scatterers and will lead to an immediate decorrelation for all q. This would happen for example if two droplets coalesce somewhere in the sample (not necessarily only inside the observed volume). The coalescence leads to the formation of a new droplet inducing a rearrangement of all the surrounding droplets. Such a rearrangement can easily lead to movements much larger than the particle radius even if the coalescence occurs at a location further away from the observed sample volume. I therefore suggest that the off-set observed at early stages in both samples is due to droplet coalescence taking place. The intersection of the $1/\tau$-line with the y-axis then gives the rate at which these coalescence events take place. This would imply that for the 5% and 7.5% sample droplets coalesce only every 2.3 and 10 minutes respectively indicating that the particle-coverage on the droplets is already quite high. The time average present in g_2-1 is over 800 seconds leading to only 6 or 2 of such coalescence events during the observed time for the 5% and 7.5% sample respectively when the samples are young. Arditty et al [109] have analysed the coalesence behaviour of droplet emulsions over several minutes and find that the coalescence rate significantly decreases the closer the particle-stabilised droplets get to full particle-coverage on the interface until it reaches a low, but non-zero value. My results here are therefore not inconsistent with their observations. Furthermore Arditty et al have demonstrated that initially, when droplets are not fully particle-covered, smaller droplets coalesce more quickly than larger ones. However, for constant surface coverage the coalescence rate decreases with droplet diameter which can account for the coalescence rate decreasing in the 7.5% sample for the same sample age.

The disappearance of the off-set for the $1/\tau$ behaviour for the older samples indicates that eventually the occurrence of such large scale rearrangements becomes too infrequent to still be measured in this way. For these late stages rearrangements smaller than $2\pi/q$ and of linear origin lead to the decorrelation as can be deduced from the $1/\tau \propto q$ behaviour. Although gravity acts on the sample at all times I suggest that at late times, in the absence of coalescence events, the rising of the droplets under gravity becomes the dominant process for decorrelation. This provides a similar drive to a pressure gradient driving a dense colloidal suspension through a capillary [114, 124]. Because in the early times the large scale rearrangements only occur sporadically, it is also possible to observe

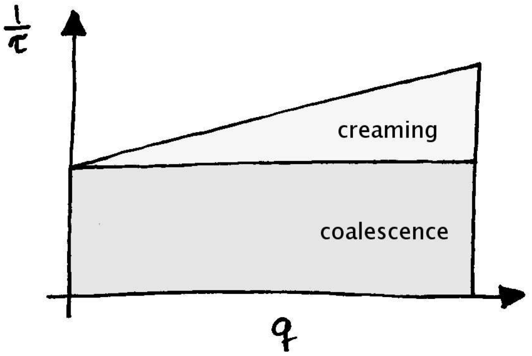

Figure 7.9: For young samples I propose that two different mechanisms are responsible for the decorrelation: sporadic coalescence leads to the same decorrelation for all q and is responsible for the off-set in $1/\tau$; additionally gravity is continuously pushing the droplets upwards inducing a linear slope in $1/\tau$.

this creaming effect due to gravity during this stage. This is the reason why $1/\tau$ still has a finite slope although droplet coalescence will lead to a decorrelation for all q each time such an event occurs and is schematically shown in figure 7.9. At later times the slope decreases indicating that the effective velocity of the droplets decreases during compaction of the droplets.

My models based on the behaviour of τ are supported by the best fit β values. Considering the coalescence events as randomly distributed events in time then Duri and Cipelletti [125, 123] have shown that for dipolar stresses randomly occurring in time this leads to a β-exponent of 1.5 for low q that approaches 1.0 for large q. This is exactly what I observe when the coalescence events take place although it seems surprising that such few events determine the shape of the decorrelation so significantly. For the late stage where creaming is the dominant process the stress source is gravity pushing the particles upwards into each other. Leading to much smaller rearrangements that added together slowly decorrelate the signal and no longer leads to a $\beta = 1.5$ exponent.

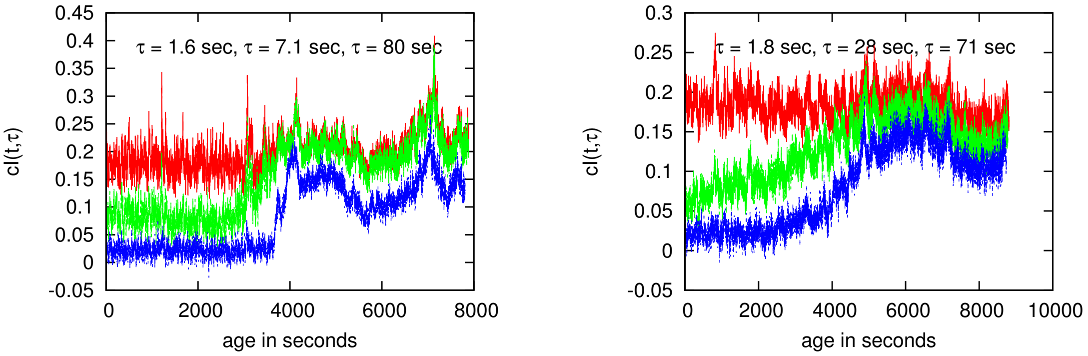

Figure 7.10: The signal $c_I(t,\tau)$ at q=0.0033 ± 0.0003 $\mathring{A}^{-1}$ for different τ values plotted against sample age shows that large fluctuations are present. The distinction between noise and sample signal is not straight forward. left: 5%, right: 7.5%, delay times given for curves from top to bottom.

7.4.3 Testing for intermittent dynamics

Aim and context

In the following paragraph I attempt to establish whether the dynamics leading to the decorrelation in the emulsion system are homogeneous or heterogeneous. Many glasses have also been observed to show intermittent dynamics [54]. In the previous section I have suggested that at least in the early stages the dynamics of the emulsion are understandable in terms of intermittent events. Particularly for the late stage it is crucial to see whether the dynamics are heterogeneous or homogeneous as analysis of g_2-1 cannot illuminate this issue.

Sample and method

Once again the same set of 5% and 7.5% dodecane-in-water emulsions as in the previous paragraphs are observed. As mentioned in the analysis section the $c_I(t,\tau)$ signals are very noisy. It is therefore not possible to distinguish the contributions of the noise from the contributions due to the sample dynamics when plotting $c_I(t,\tau)$ against t. However, while the variance of the noise will scale with the magnitude of $c_I(t,\tau)$ the variance of the dynamics of the sample will show a peak around τ_c. To carry out this analysis an optimised q-ring (large number of

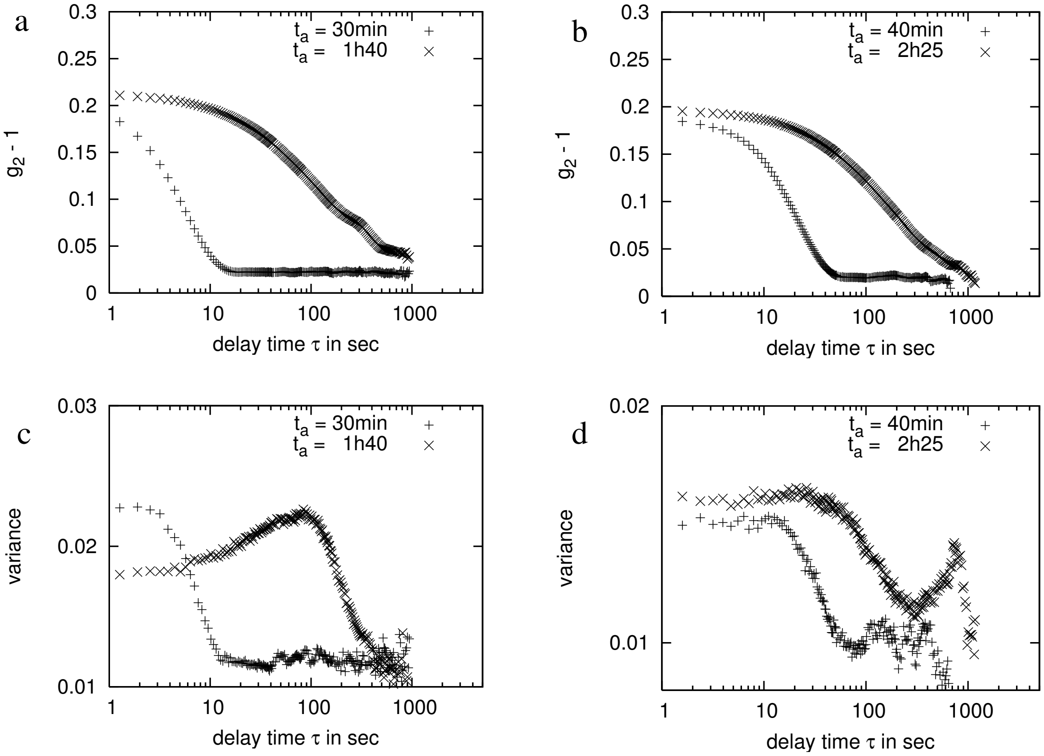

Figure 7.11: A peak in the variance in the region of the characteristic decay time is an indication for intermittent behaviour. top: $\overline{c_I(t,\tau)}$ for optimised q-range (q=0.0033 ± 0.0003 $\mathring{A}^{-1}$) and time segment that does not show strong photon fluctuations, bottom: variance of c_I(t,τ) for different τ. left: 5%, right: 7.5%

pixels, high intensity) is chosen and time sequences where no unnecessarily large fluctuations occur are selected to calculate the variance of c_I(t,τ) over a specific time range for the measured τ-range.

Results and discussion

Figure 7.10 shows the fluctuations present in c_I(t,τ) for different values of τ over the measurement time of the sample even after an optimised q-range is chosen. To detect possible intermittent behaviour of the sample less noisy $\sim$ 20 minute time segments are chosen to calculate the variance of the c_I(t,τ)-signal for the measured τ range. A large variance will indicate that an important role is being played by more extreme events.

Figure 7.11 shows firstly the time averaged correlation functions $g_2(q,\tau)$-1 for 5% and 7.5% from left to right and below the variance of the underlying $c_I(t,\tau)$ signal over time t at each τ. Especially for the late 5% sample a clear peak around the characteristic decay time is visible suggesting that intermittent rearrangements occur at late stages when the emulsion droplets are pushed upwards by gravity. For the early times it is possible that the variance shows a peak but due to the lack of data for small enough τ this cannot be said for certain. It is necessary to confirm whether these peaks are truly due to heterogeneous dynamics or an instrumental effect. It is not hard to imagine that an emulsion which is being compacted by gravity could make occasional sudden rearrangements.

7.5 Summary and outlook

In this chapter I have shown two regimes of dynamics for a dense particle stabilised emulsion. I have also presented evidence that solid-stabilised emulsions could show heterogeneous dynamics during ageing. Using XPCS it is possible to resolve sub-particle movement. However, in the study presented here it is the motion of the droplets that is observed and not the motion of the interfacially trapped particles. Like many other soft glassy systems this micron-scale emulsion has a linear relationship between the characteristic decay time τ_c and the wavevector: $\tau_c \propto q^{-1}$. This excludes the possibility of a diffusive origin in the dynamics and I claim that gravity leads to an upwards motion of the droplets which is seemingly characterised by intermittent events presumably as the droplets re-pack. The colloids follow the motion of the droplets leading to movements on a fraction of the particle size. At early times I suggest that randomly occurring coalescence events result in sudden rearrangements which are larger than 300 nm. The analysis of the intermittent nature of the dynamics in these samples is complicated by a high level of noise. However, there are other methods to further reduce the effect of noise by analysing smaller subsections of the q-range as described by Duri et al [57] when analysing diffusive wave spectroscopy (DWS) measurements. Unfortunately this method is not easily translated to XPCS. The DWS experiments do not have a wavevector dependency and therefore the whole area of the CCD detector can be used to calculate the correlation functions. Duri et al have established that the scattering pattern should contain in excess of 8 000 pixels to yield reliable calculations while the maximum pixel number I have achieved is 4500. To improve the situation it is therefore necessary to first correct for the modulations of the form factor before the q-regions can be subsequently increased to gain larger pixel numbers at the cost of blurring the behaviour of τ with q. Theoretically it should be possible to average the $c_I(t,\tau)$-signal obtained from adjacent q-rings to achieve this as long as the appropriately normalised intensities are used. However, for the steep sections in the form factor it might require q-rings which are very thin such that results might be skewed due to a large ratio of edge pixels to bulk pixels. Trials on 1-pixel wide q-rings did not show an improvement over the current calculations.

The analysis of the XPCS data shows two regimes and a cross-over between them. The early time regime is characterised by an apparent coalescence rate of the droplets which then decreases below the measurable limit for the second regime. For early and late times the creaming of the droplets is characterised by a velocity which is indicative of the steady drive that is imposed by gravity. While the coalescence rate drops dramatically as the samples age a peak in the variance of the correlation function is observed (for Φ_v=5%) with the peak located at the characteristic decay time. This strongly suggests that the droplets are undergoing intermittent rearrangements during compactification. This is likely to be the result of the droplets having “sticky” and rough colloidal surfaces and the fact that the distribution of droplet sizes leads to uneven compaction.

Since gravity is only directed upwards it would be interesting to analyse the data for vertical and horizontal contributions separately to establish whether the system dominantly rearranges in the vertical direction. However, this approach would only take a small subsection of the CCD-detector into account which would increase the statistical problems described above and might not make this method feasible for the TRC method.

Chapter 8

Summary and outlook

8.1 Experimental achievements

In this thesis I have demonstrated for the first time that the experimental formation of bijels is feasible. A successful route to formation is the exploitation of phase separation via spinodal decomposition in the presence of neutrally wettting colloids.

Using critical temperature quenches on the binary liquid system 2,6-lutidine and water I have experimentally confirmed the formation process proposed by computer simulations [71]. Furthermore I have demonstrated the ability to tune the pore size of the system by varying the amount of stabilising particles and the structural stability by exploiting interfacial tension and particle-particle interactions. A simple mechanical test has revealed that the bijel has viscoelastic properties.

Off-critical, deep temperature quenches can also lead to spinodal decomposition. However, the demixing process can be dominated by wetting effects if the sample geometry is quasi-two-dimensional. The need for an optimum quench rate combined with the fact that heat transfer is a slow, diffusive process sets a limitation on the possible bijel thickness for this quench method.

Pressure quenches can also be used to induce liquid-liquid demixing. In collaboration with Hugh Vass I have developed a microscopy pressure cell allowing pressures up to 1.5 kbar in a contamination free environment and with satisfactory confocal microscopy imaging conditions for objectives that have a working distances greater than 4 mm. Phase separation via nucleation (off-critical composition) and spinodal decomposition (critical composition) can be induced. The absence of temperature fluctuations leads to convection free sample evolution. Stable bijel formation via pressure quenches have not been demonstrated but should be feasible. Pressure quenches can possibly overcome sample thickness limitations due to the fact that pressure distributes with the speed of sound throughout the sample.

Dynamic x-ray scattering experiments using XPCS on a related droplet emulsion system have revealed that 10 to 15 μm sized droplets change their dynamic behaviour over time while compacting under gravity. At early stages droplet coalescence events lead to large scale rearrangements throughout the sample. For older samples slow dynamics are observed which have been shown to be intermittent in nature by the use of time resolved analysis methods. These observations tie in with those of various other experiments on soft glassy materials.

8.2 Building on this thesis

The experimental results on bijel formation have shown the potential of using computer simulations to create novel materials. After this first step of demonstrating the experimental feasibility of bijel formation and some of their basic material properties it is now necessary to study this material in more detail to further establish its scientific and industrial usefulness.

To this end the work on bijels is currently being continued by two post-docs. Kathryn White is currently systematically studying the wettability properties of the FITC-doped silica particles to give an understanding of the preparation protocol. She will also be testing the ability of a bijel to resist counter-flowing liquids while Job Thijssen will carry out systematic studies on the rheology of bijels. Other processes producing bicontinuous liquid-liquid domains will be of interest when producing bijels on larger scales.

My work on the pressure cell has been continued by the development of a similar system for higher magnification work which PhD student Lucas Black will use to study extremophile bacteria under pressure.

Following my work with Luca Cipelletti analysing intermittent dynamics in a dense particle-stabilised emulsion, PhD student Danielle Van't Zand is going to take this on to studying dynamics in other novel gels.

Appendix A

Published Papers

- E. M. Herzig, K. A. White, A. B. Schofield, W. C. K. Poon and P. S. Clegg, Bicontinuous emulsions stabilized solely by colloidal particles *Nature Materials*, **6**, 966-971, 2007
- P. S. Clegg, E. M. Herzig, A. B. Schofield, S. U. Egelhaaf, T. S. Horozov, B. P. Binks, M. .E. Cates and W. C. P. Poon, Emulsification of Partially Miscible Liquids Using Colloidal Particles: Nonspherical and Extended Domain Structures *Langmuir*, **23**, 5984-5994, 2007
- P. S. Clegg, E. M. Herzig, A. B. Schofield, T. S. Horozov, B. P. Binks,M. .E. Cates and W. C. P. Poon, Colloid stabilised emulsions: behaviour as the interfacial tension is reduced *Journal of Physics: Condensed Matter*, **17**, S3433-S3438, 2005

Appendix B

Correction for a constant decorrelation

For a constant decorrelation it would be possible to correct the data. Assuming the incoming intensity carries a signal F(t) that decorrelates as observed for the vycor but is uncorrelated to the way the intensity is scattered by the sample then the measured intensity will be I_{mes}(t)=S(t)F(t), where S(t) is the signal arising from the scattering of the sample that we are interested in.

$$\begin{aligned} \frac{\langle I_{mes}(t) I_{mes}(t+\tau)\rangle}{\langle I_{mes}(t)\rangle\langle I_{mes}(t+\tau)\rangle} &= \frac{\langle S(t)F(t)S(t+\tau)F(t+\tau)\rangle}{\langle S(t)F(t)\rangle\langle S(t+\tau)F(t+\tau)\rangle} \\ &= \frac{\langle S(t)S(t+\tau)\rangle}{\langle S(t)\rangle\langle S(t+\tau)\rangle}\frac{\langle F(t)F(t+\tau)\rangle}{\langle F(t)\rangle\langle F(t+\tau)\rangle} \end{aligned} \tag{B.1}$$

where the rearrangement in the last step is valid since F(t) and S(t) are not correlated. A simpler way of expressing this correction is then:

$$g_{2mes} = g_{2S}g_{2F} \tag{B.2}$$

g_{2F} is then the decorrelation function for the instrument and can be extracted from the vycor measurements which itself has a constant signal g_{2vycS}=1+β due to its static nature (β is the contrast of the vycor). In the presence of a decorrelation due to a beam instability a vycor measurement would yield a decorrelating signal $g_{2vyc-mes}$. Then

$$g_{2vycF} = g_{2F} = \frac{g_{2vyc-mes}}{1+\beta}. \tag{B.3}$$

This will be a function between 1.0 and $\frac{1}{1+\beta}$ and I can obtain g_{2S} of the sample of interest via equation B.2 provided that the first equality in equation B.3 holds. However, for my data this is not true because the characteristic decay time for the instrument varies randomly with time and so this correction is not feasible.

Appendix C

Péclet number

The Péclet number is a measure of the relative importance of advection to diffusion. For Péclet numbers Pe $\ll 1$ the system is dominated by diffusion.

$$\begin{aligned} Pe &\sim \frac{v \times l}{D} \\ Pe &= \frac{g\Delta m x}{k_B T}, \end{aligned} \tag{C.1}$$

where the Stoke's velocity is $v = \frac{2}{9}\frac{x^2 g \Delta\rho}{\eta}$ and the diffusion coefficient is given by the Stoke's Einstein relation $D = \frac{k_B T}{6\pi\eta r}$.

For a 10 μm large droplet and a density difference of 240 kg/m^3 between water and dodecane this results in $\delta m = 1.3 \times 10^{-12}$. Taking the particle diameter as a then the water/dodecane emulsions have a Péclet number of Pe $\sim$ 30 000 at room temperature. This clearly indicates that thermal fluctuations are largely irrelevant for this system.

Bibliography

[1] http://www.ichf.edu.pl/spinodal.html.

[2] R. Aveyard, B. P. Binks, and J. H. Clint. Emulsions stabilised solely by colloidal particles. *Advances in Colloid and Interface Science*, 100-102:503–546, 2003.

[3] A. B. Subramaniam, M. Abkarian, L. Mahadevan, and H. A. Stone. Mechanics of interfacial composite materials. *Langmuir*, 22(24):10204–10208, 2006.

[4] Pablo G. Debenedetti. *Metastable Liquids - Concepts and Principles.* Princeton University Press: New Jersey, first edition edition, 1996.

[5] A. K. Varshneya. *Fundamentals of inorganic glasses.* Academic Press Inc., 1994.

[6] Jean-Louis Barrat and Jean-Pierre Hansen. *Basic Concepts for Simple and Complex Liquids.* Cambridge University Press, first edition edition, 2003.

[7] J. E. Shelby. *Introduction to Glass Science and Technology.* Royal Society of Chemistry, 2005.

[8] C. P. Tripp and M. L. Hair. Reaction of chloromethylsilanes with silica: A low-frequency infrared study. *Langmuir*, 7:923–927, 1991.

[9] P. Silberzan, L. Léger, D. Ausserré, and J. J. Benattar. Silanation of silica surfaces. a new method of contructing pure or mixed monolayers. *Langmuir*, 7:1647–1651, 1991.

[10] Timothy R. Corle and Gordon S. Kino. *Confocal Scanning Optical Microscopy and Related Imaging Systems.* Academic Press, San Diego, 1996.

[11] Denis Semwogerere and Eric R. Weeks. *Confocal Microscopy - in: Encyclopedia of Biomaterials and Biomedical Engineering.* Taylor and Francis, 2005.

[12] James B. Pawley. *Handbook of Biological Confocal Microscopy.* Springer-Verlag New York, 3rd edition edition, 2006.

[13] Lake Shore Cryotonics. *User's Manual Model 331 Temperature Controller.* 1.8 edition, 2005.

[14] Aymeric Robert. *Dynamic behavior of charge stabilized colloidal suspensions.* PhD thesis, Université Joseph Fourier, 2001.

[15] http://www.canberra.edu.au/irps/archives/vol12no2/submit.htm.

[16] C. A. Grattoni, R. A. Dawe, C. Yen Seah, and J. D. Gray. Lower critical solution coexistence curve and physical properties (density, viscosity, surface tension, and interfacial tension) of 2,6-lutidine + water. *J. Chem. Eng. Data*, 38:516–519, 1993.

[17] H. Tanaka. Simple hydrodynamic model of fast-mode kinetics in surface-mediated fluid phase separation. *Physical Review E*, 54(2):1709–1714, 1996.

[18] D. Beysens and D. Estève. Adsorption phenomena at the surface of silica spheres in a binary liquid mixture. *Physical Review Letters*, 54(19):2123–2126, 1985.

[19] Shabira Abbas, John Satherley, and Robert Penfold. The liquid-liquid coexistence curve and the interfacial tension of the methanol-n-hexane system. *Journal of the Chemical Society, Faraday Trans.*, 93(11):2083–2089, 1997.

[20] U. Duerr, S. Z. Mirzaev, and U. Kaatze. Concentration fluctuations in ethanol/dodecane mixtures. a light-scattering and ultrasonic spectroscopy study. *Journal of Physical Chemistry A*, 104:8855–8862, 2000.

[21] M. Z. Faizullin and V. P. Skripov. Investigation of the (t,px) surface of phase separation of $xH_2O+(1-x)NC(CH_3)CHCHCHC(CH_3)$ in the visincity of the line of lower cirtical points of dissolution. *J. Chem. Thermodynamics*, 23:561–567, 1991.

[22] H. J. Chung, K. Ohno, T. Fukuda, and R. J. Composto. Internal phase separation drives dewetting in polymer blend and nanocomposite films. *Macromolecules*, 40:384–388, 2007.

[23] D. M. Considine. *Van Nostrand's Scientific Encyclopedia*. Van Nostrand Reinhold Company, 1976.

[24] C. Morris. *Dictionary of Science and Technology*. Academic Press Inc., 1992.

[25] www.science.org.au/nova/059/059key.htm.

[26] D. Roux, C. Coulon, and M. E. Cates. Sponge phases in surfactant solutions. *Journal of Physical Chemistry*, 96:4174–4187, 1992.

[27] D. Shaw. *Introduction to Colloid and Surface Chemistry*. Butterworth-Heinemann, 1992.

[28] B. P. Binks. Particles as surfactants - similarities and differences. *Cur. Op. Coll. Interf. Sc.*, 7(1):21–41, 2002.

[29] K. Shinoda and B. Lindman. Organized surfactant systems: Microemulsions. *Langmuir*, 3(2):135–149, 1987.

[30] D. Roux D. Gazeau, A. M. Bellocq and T. Zemb. Experimental evidence for random surface structures in dilute surfactant solutions. *Europhysics Letters*, 9(5):447–452, 1989.

[31] S. U. Pickering. Emulsions. *J. Chem. Soc., Trans.*, 91:2001–2021, 1907.

[32] W. Ramsden. Separation of solids in the surface-layers of solutions and 'suspensions' (observations on surface-membranes, bubbles, emulsions, and mechanical coagulation). – preliminary account. *Proc. R. Soc.*, 72:156–164, 1903.

[33] M. E. Leunissen, A. van Blaaderen, A. D. Hollingsworth, M. T. Sullivan, and P. M. Chaikin. Electrostatics at the oil-water interface, stability, and order in emulsions and colloids. *Proceedings of the National Academy of Sciences of the United States of America*, 104(8):2585–2590, 2007.

[34] Jos Zwanikken and René van Roij. Charged colloidal particles and small mobile ions near the oil-water interface: Destruction of colloidal double layer and ionic charge separation. *Physical Review Letters*, 99:1783011–1783014, 2007.

[35] C. Zeng, H. Bissig, and A. D. Dinsmore. Particles on droplets: From fundamental physics to novel materials. *Solid State Communications*, 139:547–556, 2006.

[36] B. P. Binks and T. S. Horozov. *Colloidal Particles at Liquid Interfaces*. Cambridge University Press, first edition edition, 2006.

[37] G. J. Young. *Journal of Colloid Science*, 13:67pp, 1958.

[38] P. Aussillous and D. Quéré. Properties of liquid marbles. *Proc. R. Soc.A*, 462:973–999, 2006.

[39] B. P. Binks and S. O. Lumsdon. Catastrophic phase inversion of water-in-oil emulsions stabilized by hydrophobic silica. *Langmuir*, 16(6):2539–2547, 2000.

[40] B. P. Binks and S. O. Lumsdon. Transitional phase inversion of solid-stabilized emulsions using particle mixtures. *Langmuir*, 16(8):3748–3756, 2000.

[41] A. V. Nguyen, R. J. Pugh, and G. J. Jameson. *Colloidal Particles at Liquid Interfaces*. Cambridge University Press, 2006.

[42] J. L.West, A. Glushchenko, and G. Liao. Drag on particles in a nematic suspension by a moving nematic-isotropic interface. *Physical Review E*, 66:012702, 2002.

[43] P. D. Gallagher and J. V. Maher. Partitioning of polystyrene latex spheres in immiscible critical liquid mixtures. *Physical Review A*, 46(4):2012–2021, 1992.

[44] W. Lash Miller and R. H. McPherson. The behavior of colloidal suspensions with immiscible solvents. *J. Phys. Chem*, 12:706–716, 1908.

[45] P. S. Clegg, E. M. Herzig, A. B. Schofield, T. S. Horozov, B. P. Binks, M. .E. Cates, and W. C. P. Poon. Colloid stabilised emulsions: behaviour as the interfacial tension is reduced. *Journal of Physics: Condensed Matter*, 17:S3433–S3438, 2005.

[46] C. W. Lung. *Mechanical Properties of Metals: Atomistic and Fractal Continuum Approaches*. World Scientific, 1999.

[47] R. S .Lakes. *Viscoelastic Solids*. CRC, 1998.

[48] D. Vella, P. Aussillous, and L. Mahadevan. Elasticity of an interfacial particle raft. *Europhys. Lett*, 68(2):212–218, 2004.

[49] R. Aveyard, J. H. Clint, D. Nees, and V. N. Paunov. Compression and structure of monolayers of charged latex particles at air/water and octane/water interfaces. *Langmuir*, 16:1969–1979, 2000.

[50] H. Xu, S. Melle, K. Golemanov, and G. G. Fuller. Shape and buckling transitions in solid-stabilized drops. *Langmuir*, 21:10016–10020, 2005.

[51] E. J. Stancik G. G. Fuller and S. Melle. *Colloidal Particles at Liquid Interfaces*. Cambridge University Press, 2006.

[52] A. B. Subramaniam, M. Abkarian, L. Mahadevan, and H. A. Stone. Non-spherical bubbles. *Nature*, 438(7070):930, 2005.

[53] K. V. Edmond, A. B. Schofield, M. Marquez, J. P. Rothstein, and A. .D. Dinsmore. Stable jets of viscoelastic fluids and self-assembled cylindrical capsules by hydrodynamic focusing. *Langmuir*, 22(21):9052–9056, 2006.

[54] L. Cipelletti and L. Ramos. Slow dynamics in glassy soft matter. *J. Phys.: Condens. Matter*, 17:R253–R285, 2005.

[55] L. Cipelletti et al. Universal non-diffusive slow dynamics in aging soft matter. *Faraday Discussions*, 123:237–251, 2003.

[56] L. Cipelletti, H. Bissig, V. Trappe, P. Ballesta, and S. Mazoyer. Time-resolved correlation: a new tool for studying temporally heterogeneous dynamics. *J. Phys.: Condens. Matter*, 15:S257–S262, 2003.

[57] A. Duri, V. Trappe H. Bissig, and L. Cipelletti. Time-resolved-correlation measurements of temporally heterogeneous dynamics. *Physical Review E*, 72:051401, 2005.

[58] J. S. Walker and C. A. Vause. Reappearing phases. *Scientific American*, 256(5):90–97, 1987.

[59] Michael Bushev. *Synergetics: Chaos, Order, Self-Organization*. World Scientific Publishing, 1994.

[60] W. Stoeber, A. Fink, and E. Bohn. Controlled growth of monodisperse silica spheres in the micron size range. *Journal of Colloid and Interface science*, 26:62–69, 1968.

[61] A. van Blaaderen and A. Vrij. Synthesis and characterization of colloidal dispersions of fluorescent, monodisperse silica spheres. *Langmuir*, 8:2921–2931, 1992.

[62] Sergio Brandriss and Shlomo Margel. Synthesis and characterization of self-assembled hydrophobic monolayer coatings on silica colloids. *Langmuir*, 9:1232–1240, 1993.

[63] Jacob Sagiv. Organized monolayers by adsorption. 1. formation and structure of oleophobic mixed monolayers on solid surfaces. *Journal of the American Chemical Society*, 102(1):92–98, 1980.

[64] Douglas B. Murphy. *Fundamentals of Light Microscopy and Electronic Imaging.* Wiley-Liss, 2001.

[65] C. J. R. Sheppard and D. M. Shotton. *Confocal Laser Scanning Microscopy.* BIOS Scientific Publishers, 1997.

[66] R. Webb in J. B. Pawley. *Handbook of Biological Confocal Micrscopy.* New York: Plenum, second edition edition, 1995.

[67] Honeywell. *Product Manual UDC 3000 Universal Digital Controller.* 51-51-25-07 edition, 1988.

[68] P. Lindner and Th. Zemb, editors. *Neutrons, X-rays and Light: Scattering Methods Applied to Soft Condensed Matter.* Elsevier, 2002.

[69] http://www.esrf.eu/usersandscience/experiments/scmatter/id10a/.

[70] G. Grübel and F. Zontone. Correlation spectroscopy with coherent x-rays. *Journal of Alloys and Compounds*, 362:3–11, 2004.

[71] K. Stratford, R. Adhikari, I. Pagonabarraga, J. C. Desplat, and M. E. Cates. Colloidal jamming at interfaces: a route to fluid bicontinuous gels. *Science*, 309:2198–2201, 2005.

[72] P. S. Clegg, E. M. Herzig, A. B. Schofield, S. U. Egelhaaf, T. S. Horozov, B. P. Binks, M. .E. Cates, and W. C. P. Poon. Emulsification of partially miscible liquids using colloidal particles: Nonspherical and extended domain structures. *Langmuir*, 23:5984–5994, 2007.

[73] H. J. Chung, A. Taubert, R. D. Deshmukh, and R. J. Composto. Mobile nanoparticles and their effect on phase separation dynamics in thin-film polymer blends. *Europhys. Lett.*, 68(2):219–225, 2004.

[74] H. J. Chung, K. Ohno, T. Fukuda, and R. J. Composto. Self-regulated structures in nanocomposites by directed nanoparticle assembly. *Nano Lett.*, 5(10):1878–1882, 2005.

[75] M. Si, T. Araki, H. Ade, A. L. D. Kilcoyne, R. Fisher, J. C. Sokolov, and M. H. Rafailovich. Compatibilizing bulk polymer blends by using organoclays. *Macromolecules*, 39:4793–4801, 2006.

[76] M. Z. Faizullin and V. P. Skripov. Thermodynamic similarity of phase-separation binary solutions with a lower critical temperature. *Zeitschrift für Physicalische Chemie*, 173:53–62, 1991.

[77] Kenneth S. Suslick. Sonochemistry. *Science*, 247(4949):1439–1445, 1990.

[78] B. M. Law, J.-M. Petit, and D. Beysens. Adsorption-induced reversible colloidal aggregation. *Journal of Statistical Physics*, 57(5):5782–5794, 1998.

[79] Yalia Jayalakshmi and Eric W. Kaler. Phase behaviour of colloids in binary liquid mixtures. *Physical Review Letters*, 78(7):1379–1382, 1997.

[80] T. Narayanan, V. Kumar, E. S. R. Gopal, D. Beysens, P. Guenoun, and G. Zalczer. Reversible flocculation of silica colloids in liquid mixtures. *Physical Review E*, 48(3):1989–1994, 1993.

[81] H. Tanaka. Dynamic interplay between phase separation and wetting in a binary mixture confined in a one-dimensional capillary. *Physical Review Letters*, 70(1):53–56, 1993.

[82] Hajime Tanaka, Andrew J Lovinger, and Don D. Davis. Pattern evolution caused by dynamic coupling between wetting and phase separation in binary liquid mixture containing glass particles. *Physical Review Letters*, 72(16):2581–2584, 1994.

[83] T. Araki and H. Tanaka. Wetting-induced depletion interaction between particles in a phase-separating liquid mixture. *Physical Review E*, 73:061506, 2006.

[84] H. Ochel, H. Becker, K. Maag, and G. M. Schneider. Influence of a third component on (liquid + liquid) phase equilibria in (butan-2-ol + water) and in (butan-1-ol + water) at pressures up to 160 mpa. *J. Chem. Thermodyn.*, 25:667–677, 1993.

[85] In discussion with eunhye (grace) kim.

[86] J. C. Fernández-Toledano, A. Moncho-Jordá, F. Martínez-López, and R. Hidalgo-Álvarez. *Colloidal Particles at Liquid Interfaces*. Cambridge University Press, 2006.

[87] R. Aveyard, J. H. Clint, D. Nees, and N. Quirke. Structure and collapse of particle monolayers under lateral pressure at the octane/aqueous surfactant solution interface. *Langmuir*, 16:8820–8828, 2000.

[88] C. Tsamantakis, J. Masliyah, A. Yeung, and T. Gentzis. Investigation of the interfacial properties of water-in-diluted-bitumen emulsions using micropipette techniques. *Journal of Colloid and Interface Science*, 284(1):176–183, 2005.

[89] M. E. Cates, M. D. Haw, and C. B. Holmes. Dilatancy, jamming, and the physics of granulation. *J.Phys.: Condens. Matter*, 17:S2517–S2531, 2005.

[90] H.-O. Carmesin, D. W. Heermann, and K. Binder. Influence of a continuous quenching procedure on the initial stages of spinodal decomposition. *Z. Phys. B - Condensed Matter*, 65:89–102, 1986.

[91] H. Tanaka and T. Araki. Spontaneous double phase separation induced by rapid hydrodynamic coarsening in two-dimensional fluid mixtures. *Physical Review Letters*, 81(2):389–392, 1998.

[92] H. Tanaka. Hydrodynamic interface quench effects on spinodal decomposition for symmetric binary fluid mixtures. *Physical Review E*, 51(2):1313–1329, 1995.

[93] M. Rüllmann and I. Alig. Scaling behaviour of nonisothermal phase separation. *Journal of Chemical Physics*, 120(16):7801–7810, 2004.

[94] A. Stein, S. J. Davidson, J. C. Allegra, and G. F. Allen. Tracer diffusion and shear viscosity for the system 2,6-lutidine-water near the lower critical point. *Journal of Chemical Physics*, 56(12):6164–6168, 1972.

[95] Eric D. Siggia. Late stages of spinodal decomposition in binary mixtures. *Physical Review A*, 20:595–605, 1979.

[96] W. S. Rasband. Imagej, u.s. national institute of health: Bethesda, maryland, usa, 1997-2006; http://rsb.info.nih.gov/ij/.

[97] James G. Berryman. Random close packing of hard spheres and disks. *Physical Review A*, 27(2):1053–1061, 1983.

[98] E. M. Herzig, K. A. White, A. B. Schofield, W. C. K. Poon, and P. S. Clegg. Bicontinuous emulsions stabilized solely by colloidal particles. *Nat. Mat.*, page doi:10.1038/nmat2055, 2007.

[99] D. Beysens and T. Narayanan. Wetting-induced aggregation of colloids. *Journal of Statistical Physics*, 95(5-6):997–1008, 1999.

[100] G. Hradetzky and D. A. Lempe. Phase equilibria in binary and higher systems methanol and hydrocarbon(s). *Fluid Phase Equilib.*, 69:285–301, 1991.

[101] B. Jańczuk, T. Bialopiotrowicz, and W. Wójcik. The surface tension components of aqueous alcohol solutions. *Colloids and Surfaces*, 36:391–403, 1989.

[102] R. H. S. Winterton. *Heat Transfer*. Oxford University Press, 1997.

[103] B. P. Binks, J. H. Clint, A. K. F. Dyab, P. D. I. Fletcher, M. Kirkland, and C. P. Whitby. Ellipsometric study of monodisperse silica particles at an oil-water interface. *Langmuir*, 19:8888, 2003.

[104] T. Reck, E. Sautter, W. Dollhopf, and W. Pechhold. A high-pressure cell for optical microscopy and measurements on the phase diagram of poly(diethlsiloxane). *Rev. Sci. Inst.*, 69:1823–1827, 1998.

[105] C. Carboni, W. K. Robinson, and H. F. Gleeson. A polarizing microscope for high-pressure studies of liquid crystals. *Meas. Sci. Technol.*, 4:1238–1243, 1993.

[106] J. Kohlbrecher, A. Bollhalder, and R. Vavrin. A high pressure cell for sans up to 5 kbar in combination with light scattering to investigate liquid samples. *to be submitted*.

[107] N.-C. Wong and C. M. Knobler. Light scattering studies of phase separation in isobutyric acid + water mixtures. *J. Chem. Phys.*, 69:725–735, 1978.

[108] M. Sieber and D. Woermann. Study of non-equilibrium states of a homogeneous 2-butoxyethanol/water mixture of critical composition in the vicinity of its lower critical point using fast pressure jumps. *Ber. Bunsenges. Phys. Chem*, 95:15–23, 1991.

[109] S. Arditty, C. P. Whitby, B. P. Binks, V. Schmitt, and F. Leal-Calderon. Some general features of limited coalescence in solid-stabilized emulsions. *The European Physical Journal E*, 11:273, 2003.

[110] T. H. Whitesides and D. S. Ross. Experimental and theoretical - analysis of the limited coalescence process - stepwise limited coalescence. *J. Colloid Interface Sci.*, 169:48–599, 1995.

[111] L. Cipelletti S. Mazoyer and L. Ramos. Origin of the slow dynamics and the aging of a soft glass. *Physical Review Letters*, 97:238301, 2006.

[112] D. Lootens, H. Van Damme, and P. Hbraud. Giant stress fluctuations at the jamming transition. *Physical Review Letters*, 90:178301, 2003.

[113] D. Lootens, H. Van Damme, Y. Hmar, and P. Hbraud. Dilatant flow of concentrated suspensions of rough particles. *Physical Review Letters*, 95:268302, 2005.

[114] M. D. Haw. Jamming, two-fluid behavior, and ”self-filtration” in concentrated particulate suspensions. *Physical Review Letters*, 92:185506, 2004.

[115] M. E. Cates and M. R. Evans, editors. *Soft and Fragile Matter Nonequilibrium Dynamics, Metastability and Flow.* Institute of Physics, 2000.

[116] N. Maeda, K. J. Rosenberg, J. N. Israelachvili, and R. M. Pashley. Further studies on the effect of degassing on the dispersion and stability of surfactant-free emulsions. *Langmuir*, 20:3129–3137, 2004.

[117] L. Cipelletti and D. Weitz. Ultralow-angle dynamic light scattering with a charge coupled device camera based multispeckle, multitau correlator. *Rev. Sci. Inst.*, 70:3214–3221, 1999.

[118] I. Sikharulidze. *Dynamics of smectic membranes as studied by X-ray and neutron scattering.* PhD thesis, FOM-Institute for Atomic and Molecular Physics, Amsterdam, 2005.

[119] S. H. Chen, P. Tartaglia, and P. N. Pusey. Light scattering from independent particles – nongaussian correction to the clipped intensity correlation function. *J.Phys.: Math., Nucl. Gen.*, 6:490–495, 1973.

[120] J. W. Goodman. *Laser speckle and related phenomena*. Springer Verlag, 1975.

[121] Bruce J. Berne and Robert Pecora. *Dynamic Light Scattering with applications to Chemistry, Biology and Physics*. Dover Publications, Inc., dover edition edition, 2000.

[122] L. Cipelletti, L. Ramos, S. Manley, E. Pitard, E. E. Pashkovski D. A. Weitz, and M. Johansson. Universal non-diffusive slow dynamics in aging soft matter. *Faraday Discuss.*, 123:237–251, 2003.

[123] J.-P. Bouchaud and E. Pitard. Anomalous dynamical light scattering in soft glassy gels. *Eur. Phys. J. E*, 6:231–236, 2001.

[124] L. Isa, R. Bessling, E. R. Weeks, and W. C. K. Poon. Experimental studies of the flow of concentrated hard sphere suspensions in a constriction. *Journal of Physics: Conference Series*, 40:124–132, 2006.

[125] A. Duri and L. Cipelletti. Length scale dependence of dynamical heterogeneity in a colloidal fractal gel. *Europhys. Lett.*, 76:972–978, 2006.